Numerical modeling of soil-pile interaction considering grain breakage in finite deformations

Luis André Berenguer Todo-Bom

▶ **To cite this version:**

Luis André Berenguer Todo-Bom. Numerical modeling of soil-pile interaction considering grain breakage in finite deformations. Other. Ecole Centrale Paris, 2014. English. NNT : 2014ECAP0018 . tel-01000298

HAL Id: tel-01000298

https://theses.hal.science/tel-01000298

Submitted on 4 Jun 2014

HAL is a multi-disciplinary open access archive for the deposit and dissemination of scientific research documents, whether they are published or not. The documents may come from teaching and research institutions in France or abroad, or from public or private research centers.

L'archive ouverte pluridisciplinaire **HAL**, est destinée au dépôt et à la diffusion de documents scientifiques de niveau recherche, publiés ou non, émanant des établissements d'enseignement et de recherche français ou étrangers, des laboratoires publics ou privés.

ÉCOLE CENTRALE DES ARTS ET MANUFACTURES ÉCOLE CENTRALE PARIS

THÈSE

présentée par

Luís André BERENGUER TODO BOM

pour l'obtention du

GRADE DE DOCTEUR

Spécialité : Modélisation géo-mécanique

Laboratoire d'accueil : Mécanique des Sols, Structures et Matériaux

NUMERICAL MODELLING OF SOIL-PILE INTERACTION CONSIDERING GRAIN BREAKAGE IN FINITE DEFORMATIONS

M. FRANK Roger	Président
M. TAMAGNINI Claudio	Rapporteur
M. BAUER Erich	Rapporteur
Mme. DAGUIAR Sofia Costa	Examinateur
Mme. MODARESSI Arézou	Directeur de thèse
M. SANTOS Jaime	Co-directeur de thèse

Para a Mãe

“ That which can be asserted without evidence,

can be dismissed without evidence ”

Acknowledgments

I would like to express my profound gratitude and sincere thanks to Prof. Arezou Modaressi for her supervision, unlimited availability and trust throughout this PhD work. I would also like to extend my appreciation to my co-supervisor Prof. Jaime Santos for his helpful advice and fruitful discussions.

I am also grateful to the thesis jury: Prof. Roger Frank, Prof. Erich Bauer, Prof. Claudio Tamagnini and Dr. Sofia Costa D'Aguiar. Special thanks to Prof. Erich Bauer and Prof. Claudio Tamagnini for having thoroughly read and critically appraised the PhD manuscript.

Je veux aussi remercier tous mes amis à l'Ecole Centrale Paris pour leurs temps et patience pendant la durée de la thèse. Les pots du vendredi soir vont me manquer beaucoup.

Ich möchte auch bei Christiane für ihre groβe Unterstützung bedanken, sie hat mir in allen schwierigen Situationen beigestanden. Die Aufenthalte in Berlin und Herscheid haben mir geholfen, Perspektive und Ruhe während mancher stressiger Momente in meiner Promotion zu gewinnen.

Finalmente gostaria de agradecer o suporte da minha família durante os quatro anos no estrangeiro durante o mestrado e a tese. A minha mãe Sílvia, e irmãos, Francisco e Guilherme, estiveram sempre disponíveis quando foi preciso.

Abstract

The objective of this thesis is to present a sound mechanical formulation for finite strains and to introduce a rational constitutive model to match realistically the behaviour of the soil near the pile-shaft where high strains localize and the phenomenon of grain breakage is usually observed in granular soil.

Accurate prediction of soil induced forces is crucial for the estimation of axial forces developed in pile foundations. These soil forces depend of numerous factors one of which is the installation procedure of the foundation element. Therefore, the behaviour of surrounding soil when subjected to very high strains during pile installation is of the utmost importance.

A consistent, physically pertinent formulation of finite elastoplasticity considering the inherent inseparability of the total elastoplastic deformation is presented by means of the logarithmic stress rate. This structure combined with adaptations in the finite element formulation is then considered for the numerical simulation of the pile installation procedure.

The performance of the proposed constitutive model for the soil-pile interface is demonstrated simulating monotonic ring shear tests carried out on Ottawa (OT) and Illinois River (IR) sands up to very high shear strains and comparison of the obtained results with laboratory testing data. The study of the phenomenon of shear resistance degradation with shear cyclic loading ("friction fatigue") is then studied in light of both the breakage mechanism in the proposed constitutive model and of the cyclic loading path.

Finally a numerical simulation of different installation procedures as well as monotonic and cyclic axial loading of single isolated cylindrical piles using the finite element code GEFDyn. Parametric calculations are performed to study the influence of the pile geometry, installation type and interface constitutive law during the installation procedure. The effects of installation on the stress path during monotonic loading are summarily analyzed.

Concerning the cyclic axial loading, the validity of the interface constitutive structure to reproduce the shaft resistance degradation phenomenon with increasing number of cycles is also studied.

Keywords : finite deformations, elastoplasticity, grain breakage, soil-structure interaction, pile installation, cyclic loading, friction fatigue

Résumé

L'analyse du comportement des pieux est un problème complexe du fait de la diversité des phénomènes qui gouvernent le comportement du sol et en particulier celui se trouvant au voisinage du pieu. Ce dernier dépend particulièrement du procédé d'installation du pieu qui peut parfois engendrer des déformations de très grande amplitude dans le sol entre autre phénomènes.

L'objectif de ce travail est de mettre en place un outil de modélisation pour évaluer le comportement des pieux sous chargements axiaux en développant des modèles représentant les phénomènes physiques pertinents et de les intégrer numériquement dans un logiciel aux éléments finis utilisant des algorithmes robustes et efficaces.

Pour pouvoir modéliser la phase d'installation statique ou dynamique d'un pieu quelques problématiques doivent être considérées.

Premièrement, étant donné que pendant l'installation d'un pieu des déformations finies (non-infinitésimal) ont lieu au niveau de l'interface, une formulation eulérienne avec un taux logarithmique des déformations a été adoptée pour prendre en compte le fait que l'hypothèse des déformations infinitésimales n'est plus valable. En plus, le modèle constitutive doit prendre en compte le comportement physique du sol lorsqu'il est soumis à des déplacements d'une magnitude élevée. Le dernier est constitué, entre autres, par le phénomène de l'écrasement des grains ce qui influence beaucoup le comportement volumique du sol et finalement sa résistance au cisaillement ou en d'autres termes le frottement mobilisé. Ce phénomène a été modélisé en introduisant une variable d'écrouissage supplémentaire au modèle de comportement élastoplastique de l'ECP.

Les critères d'admissibilité thermodynamique ont été vérifiés pour le modèle constitutive original ainsi que pour le modèle révisé.

Des simulations numériques ont été faites pour les deux types d'installation, monotone et pseudo-dynamique (cyclique) et les résultats ont été analysés en détail. Finalement, la dégradation de la résistance au cisaillement au niveau du ft des pieux est un phénomène typique qui se produit pendant le chargement cyclique des fondations composées par des pieux. Le modèle constitutive pour pouvoir bien reproduire ce phénomène n'est pas simple à définir car le chemin de chargement suivi par l'interface sol-pieu est très dépendant du comportement volumique du sol qui à son tours dépend de l'histoire de chargement et des conditions aux limites du problème. Une étude détaillée de toutes les composantes du comportement du pieu pendant ce type de chargement a été effectuée afin de mettre en évidence l'influence de l'histoire de chargement sur la résistance au cisaillement et l'apparition des phénomènes tels que la fatigue du frottement.

Mots-clés : déformations finies, elastoplasticité, écrasement des grains, interaction sol-structure, chargement cyclique, dégradation cyclique

Contents

1 Introduction **15**
- 1.1 Scope . . . 15
- 1.2 Outline . . . 16

2 Literature Review **19**
- 2.1 Experimental results . . . 20
  - 2.1.1 Experimental pile installations . . . 20
  - 2.1.2 Experimental results of triaxial and ring shear tests . . . 30
- 2.2 Constitutive models . . . 37
- 2.3 Formulations in the Finite Element Method . . . 38
- 2.4 Numerical modelling of pile installation . . . 42
- 2.5 Summary . . . 47

3 Finite Deformations **49**
- 3.1 Hypoelastic-based formulations . . . 51
- 3.2 Hyperelastic-based formulations . . . 53
- 3.3 Elastoplastic Eulerian formulation for finite strains . . . 56
  - 3.3.1 Logarithmic stress rate . . . 61
- 3.4 Elastoplastic Lagrangian formulation for finite strains . . . 64
- 3.5 Numerical Integration . . . 65
- 3.6 Summary . . . 69

4 Constitutive Models **71**
- 4.1 ECP constitutive model . . . 71
- 4.2 Revised ECP constitutive model . . . 77
- 4.3 Constitutive relations from free energy and dissipation functions . . . 83
  - 4.3.1 ECP constitutive model . . . 85
  - 4.3.2 Revised ECP constitutive model . . . 87
  - 4.3.3 Triaxial shear test . . . 89
- 4.4 Summary . . . 94

5 Numerical analysis and validation of the soil behaviour model **95**
- 5.1 Numerical simulation of ring shear tests . . . 95
- 5.2 Numerical simulation of cyclic shear tests . . . 103
- 5.3 Summary . . . 118

6 Numerical analysis of pile foundations **119**
6.1 Numerical simulation of the installation procedure of displacement piles . . 120
6.1.1 FEM - Updated Lagrangian formulation 120
6.1.2 Numerical elements, materials and geometry 122
6.1.3 Calculation procedure 126
6.2 Pile installation results 127
6.2.1 Deformation and displacement patterns 127
6.2.2 Stresses in the soil mass 134
6.2.3 Interface results analysis 140
6.3 Parametric studies 145
6.3.1 Pile diameter 145
6.3.2 Pile length 147
6.3.3 Installation type 148
6.3.4 Interface constitutive law 150
6.3.5 Breakage mechanism 151
6.4 Displacement vs Non-displacement piles 156
6.5 Cyclic axial loading of a single pile 160
6.5.1 Numerical elements, materials and geometry 160
6.5.2 Calculation procedure 163
6.5.3 Result analysis 164
6.6 Summary 174

7 Conclusions and further research **175**
7.1 Conclusions 175
7.2 Further research 177

Appendix **179**

A Concepts of basic mechanics **179**
A.1 Conditions to verify objectivity 182
A.2 Verification of reference frame transformation independence (objectivity) . 183
A.3 Velocity gradient tensor 184
A.4 Objectivity of corotational stress rates 185

B Elastic tests - Objective stress rates **187**
B.1 Simple shear using objective stress rates in hypoelasticty 187
B.2 Elastic deformation cycles using objective stress rates in hypoelasticty . . . 195

C Derivation of constitutive relations **199**
C.1 ECP constitutive model - Monotonic behaviour 199
C.2 ECP constitutive model - Cyclic behaviour 201
C.3 Revised ECP constitutive model 203

D Derivation of free energy and dissipation functions **205**
D.1 ECP constitutive model 205
D.2 Revised ECP constitutive model 210

E Interface elements **215**
E.1 Mechanical formulation 215
E.2 Interface model formulation 216

F Model Parameters **217**

G Ring shear test: Illinois River sand **219**

H Standard mechanical tests in soil mechanics using the ECP constitutive model **221**
H.1 Ottawa sand (OT) (D_r=25%) 221
H.1.1 Ottawa sand: Drained triaxial tests 222
H.1.2 Ottawa sand: Undrained triaxial tests 223
H.1.3 Ottawa sand: Consolidation tests 224
H.1.4 Ottawa sand: Drained cyclic strain-controlled shear test 225
H.2 Illinois River sand (IR) (D_r=30%) 226
H.2.1 Illinois River sand: Drained triaxial tests 227
H.2.2 Illinois River sand: Undrained triaxial tests 228
H.2.3 Illinois River sand: Consolidation tests 229
H.2.4 Illinois River sand: Drained cyclic strain-controlled shear test 230
H.3 Toyoura sand (TY) (D_r=93%) 231
H.3.1 Toyoura sand: Drained triaxial tests 232
H.3.2 Toyoura sand: Undrained triaxial tests 233
H.3.3 Toyoura sand: Consolidation tests 234
H.3.4 Toyoura sand: Drained cyclic strain-controlled shear test 235

References **236**

Chapter 1

Introduction

Numerous physical and numerical modelings have been performed in recent decades to explore the phenomena governing pile behaviour. Despite these achievements pile design still relies heavily on empiricism as design methods are not always based on the physical processes which govern the pile capacity and load settlement relationship [91].

These physical processes include grain breakage due to continued shearing and very high radial confinement among others.

These factors also range from poor extrapolations of correlations from one site to another, to lack of understanding and difficulties in modeling complex physical phenomena such as the type of installation method, initial soil conditions - stress and relative density, soil nature, residual loads, pile-soil interface conditions, type of loading and pile geometry among others [58].

The quantification of installation effects remains one of the most relevant unanswered questions in the behaviour of piles since it may lead to considerable differences in its resistance [59].

1.1 Scope

This work's objective was to develop a valid constitutive model implemented in a robust finite element program which would successfully reproduce the soil behaviour under extreme monotonic and cyclic shear strain. This is done to allow for the numerical modelling of the installation procedure of pile foundations and continued loading of high amplitude cyclic paths.

In order to model the installation phase of a monotonic, jacked or dynamic pile foundation some issues must be addressed.

- Finite deformations take place whilst the pile is put in place requiring an adjustment in the mechanical formulation of the continuum to take into account that the small deformations (rotations and strain) hypothesis is no longer valid.
- The constitutive model must take into account the physical behaviour of the soil when subjected to high order of magnitude displacements. This includes the phe-

nomenon of grain breakage, also referred to as particle crushing, which greatly influences the volumetric behaviour of soil as thus reflecting of shear stress mobilization.

- Numerical issues with large deformation problems require an adaptation in the standard finite element method. Also, an improved numerical integration routine was implemented in the behaviour law for the interface elements in order to obtain a converged solution for the installation during both the monotonic and cyclic loadings cases.

- Cyclic shear resistance degradation at the pile shaft is a commonly occurring phenomenon during continued cyclic loading of pile foundations [32]. The constitutive modelling of this phenomenon, however, is not a straightforward matter. The stress path followed by the thin layer at the soil-pile interface level is dependent of its volumetric behaviour due to the boundary conditions of the problem. A comprehensive analysis of all the components of the behaviour of soil during this stage is also studied in this work.

1.2 Outline

Following this introductory section, the work is divided into 5 Chapters:

The second Chapter presents the literature review on the subject. This consists of laboratory test results of centrifuge piles undergoing installation as well as ring shear and triaxial tests where the behaviour of granular soil subjected to large shear displacements is studied in detail and the ruling physical phenomena are identified and quantified. This is followed by a review of the existing constitutive models defined to describe the behaviour of soil in high strains. Finally the numerical issues in the finite element method for high deformation simulations are described and the existing approaches in numerical modelling of pile installation effects are presented.

The third Chapter is focused on the choice and adjustments of the mechanical formulation in order to cope with finite deformations based on an extensive bibliographic research. The prescribed formulation as well as the numerical integration procedure is detailed in this section.

The fourth Chapter discusses the constitutive modeling issues. First, the conditions at which strain localization may occur are briefly recalled and then the additional mechanism introduced in an incremental elastoplastic model ([2] [57]) to account for the behaviour of granular soil under large shear displacements namely the soil particles "crushability" is presented. Thermodynamic admissibility conditions are formally described in order to ensure the physical consistency of the proposed constitutive model to represent soil behaviour and the distinct phenomena comprised there.

The fifth Chapter consists of an application of the proposed formulation and constitutive model in the form of simulation of shear tests with comparison to existing laboratory results. Different stress paths to which soil in the vicinity of piles is subjected are simulated and the role of grain breakage on the soil response is discussed through finite element computations. Numerical cyclic shear test results are analyzed and the phenomenon known as "friction fatigue" is then studied in light of both the breakage mechanism in the proposed constitutive model and of the cyclic loading path.

The sixth Chapter address the issue of numerically simulating a pile installation and the cyclic axial loading of a non-displacement pile. It includes the full description of the numerical model in terms of its geometry, materials and numerical elements. The calculation procedure to successfully model the process using GEFDyn is detailed. The results of the different calculations are analyzed and parallels are drawn between the ring shear tests and the pile-soil interface behaviour. A parametric study where the effects of different installations, geometrical differences and distinct interface behaviour laws are analyzed is presented.

The seventh and final Chapter consists of the conclusions of the work as well as suggestions for future research on the subject. This is followed by the Appendix and the References.

Chapter 2

Literature Review

The design of pile based foundations has been improved considerably in recent years due better computer modeling describing the physical phenomenon behind pile behaviour. Despite these developments pile design still relies heavily on empiricism for not always design methods are based on the physical processes which govern the pile capacity and load settlement relationship ([91]), due to numerous factors. These factors range from poor extrapolations of correlations from one site to another (most empirical correlations were intended for use with quartzitic sands), to lack of understanding and difficulties in modeling complex physical phenomena such as the type of installation method, initial soil conditions - stress and relative density, soil nature, residual loads, pile-soil interface conditions, type of loading and pile geometry ([58] among others). Of these issues to be addressed the quantification of installation effects remains one of the most relevant unanswered questions in the behaviour of piles since it may lead to considerable differences in its response ([67]) to loading. Implicit modelling of the installation effects based on empirical results and imposition of initial stress conditions on the continuum media exist ([59], [1]) but cannot be considered valid for every case and the complex physical phenomena that occur are not taken into account properly.

This work aims to numerically model the installation process of a pile and its effects on the surrounding media. This media will consist of cohesionless soil. In pursuit of this a literature review is presented in this chapter concerning this topic including various types of experimental data, numerical modelling methods and constitutive models for the soil behaviour. This chapter has been divided into four parts:

1. Laboratory results from pile installations performed on a smaller scale (mainly centrifuge testing results) as well as ring shear and triaxial results representing the behaviour of soil subjected to high strains

2. Existing formulations in Finite Element Methods (FEM) to resolve the issues related with the finite deformation range

3. Approaches to numerical modelling of pile installation effects

4. Constitutive models proposed to represent soil behaviour at very high strains

2.1 Experimental results

2.1.1 Experimental pile installations

Laboratory-scale investigations into pile behaviour remain popular because of the high cost of field testing and the possibility of achieving specific soil characteristics in a laboratory environment [67]. Experimental test results applied on model piles are presented hereafter in chronological order.

Shakhirev et al. [102] performed *in situ* and laboratory studies of the effects of pile driving (pushed-in) in sand and clay for cylindrical and pyramidal piles. In terms of boundary conditions two types of tests were performed, namely, plane strain conditions and full three-dimensional conditions.

It is found that when the pile driving process begins a strong densification of the soil near the pile occurs whose form depends on the geometry of the pile. In the case of sands the form of the zone in compression is a peach-like form while for clays it is closer to a cylinder. The vertical displacements of the soil are considerably more relevant than the displacements in the horizontal direction. Some horizontal dilation is found at the top of the pile near the soil surface. The zones in compression involve a larger volume for the case of the pyramidal piles. This compression zone is found to vary between 3-4 pile diameters in the horizontal direction and up to 5 diameters in depth. The deformed area goes up to a distance of between 6-8 pile diameters in the horizontal direction. This compression becomes quite pronounced with the dynamic loading. During the whole process there is an increase in the vertical stress near the pile base but which dissipates quite rapidly in depth and in the radial direction.

Klotz and Coop [65] performed pile testing namely pile installation procedure (pushed-in) in the centrifuge. This work demonstrated that the foreknown initial state, which is defined by the combination of the void ratio (density) and stress level to the critical state line, is a crucial factor in pile capacity. However, the usual state parameter, which is defined in terms of volume is found unsuited (unless the critical state line is assumed to be straight) for an adequate description and therefore, a stress ratio also has to be incorporated in the initial state definition.

Two sands with very different mineralogic nature and particle strengths were tested, Dog's Bay (susceptible to particle breakage) and Leighton Buzzard. Measures were taken of the variation of the unit base resistance, unit shaft resistance and radial stresses during the pile penetration process. They were all found to increase with depth when considering Leighton Buzzard sand but showed an arching effect with the Dog's Bay sand. Figure 1 clearly shows the vertical arch effect present in the stresses of the soil considering the Dog's Bay sand.

Also relevant is the study that is performed considering the soil-pile interface mobilized friction angle which is obtained by the ratio between the mean unit shaft friction and the radial stress. They are found during the pile testing to be much lower than the ones measured during a standard shear test but similar to those determined in interface ring tests performed by Cavalieri [13]. Also, these angles are similar for both soils, which might

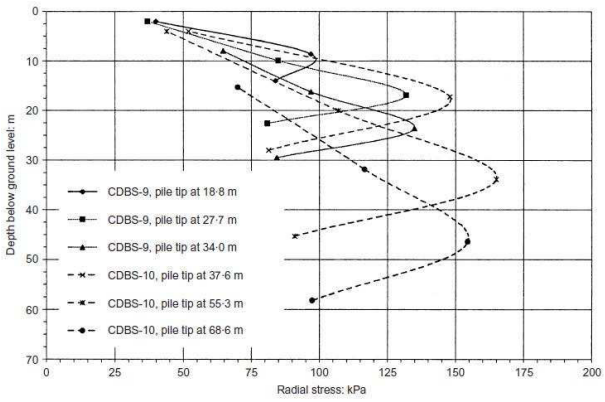

Figure 1: Distribution of radial stresses along the pile during installation of Dog's Bay sand [65]

suggest that there are other factors beyond the soil friction angle, which are quite different between the two materials. The paper also points out an important correlation between the interface mobilized friction angle and the particle dimension of the soil grains, the smaller the grains the higher the mobilized friction angle. The effect of particle breakage consists of a change in granulometry of the sample which might lead to differences in the mobilized friction angles. Considering the pile tests the surface roughness of the pile was not thought to be the major effect on the increase of the normalized roughness but that it arises from the particle size due to crushing during penetration beneath the pile tip. It was found that the variation in particle size of the soil immediately adjacent to the pile shaft, albeit difficult to measure, was of considerable magnitude. It was however noted by the authors that this variability in the interface friction angle might be due to the scale of the pile used in centrifuge testing and will not occur in prototype piles.

White and Bolton [116] performed calibration chamber testing combined with a new technique of displacement measurement using image analysis to study the penetration of a jacked pile. The sand used was the Dog's Bay carbonate sand which is known to suffer particle breakage. The study is focused on the known "friction fatigue" phenomena, more accurately, the behaviour of the soil adjacent to the pile is thoroughly analyzed.
It is found that the "friction fatigue", as a function of the radial stress acting on the pile-soil interface, appears to be somewhat of a combination of two factors: a contraction at the interface level due to continued shearing and unloading of the radial stresses of the zone next to the soil-pile interface layer. This framework is explained in the following figure 2.

The contraction at the soil-pile interface level is considered to be due to particle rearrangement and repacking as a consequence of the pile rough surface (this rearrangement is considered to be more important with increasing number of cycles) and to fine broken particles that move away from the interface. This particle breakage is thought to have an effect not only in the radial stress, and therefore in "friction fatigue", but also in the coefficient of pile-soil friction (also referred by Klotz and Coop [65]). For sands suscepti-

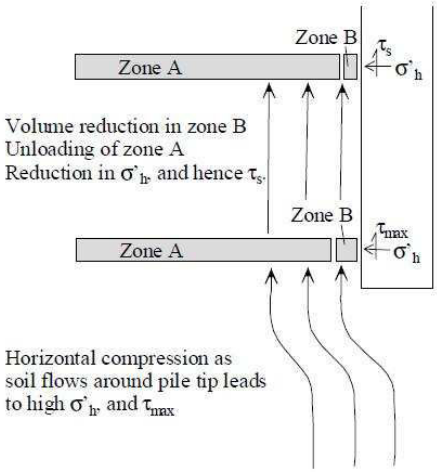

Figure 2: Friction fatigue mechanism [116]

ble to particle breakage (figure 3) this effect can be quite relevant for great granulometric changes.

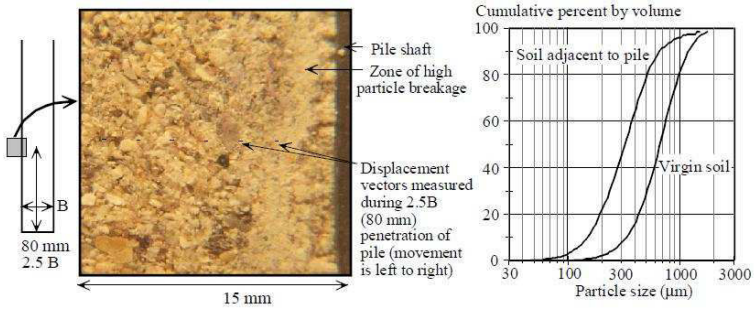

Figure 3: Post-mortem analysis of sand adjacent to pile shaft [116]

White and Bolton [117] present a series of plane strain calibration chamber tests to quantify both the pile base and shaft whilst installation of the pile (pushed-in) is performed.

Two types of sands are tested (same as in Klotz and Coop [65]), Dog's Bay sand (crushable) and Leighton Buzzard sand (uncrushable).The distinction between these two types of sand is very important in mechanical behaviour terms. Whereas crushable sands tend to be defined by very high peak angles of friction that decay with shear strain and stress level, uncrushable sands are characterized by smaller variations in the friction angle with stress level. In terms of volumetric behaviour crushable sands may experience significant volume change due to compression, offsetting the influence of dilation, while uncrushable sands show high dilation with shearing. The displacement field of the soil around the pile, during the installation process and afterwards, is described in detail in this study. No evidence of a bearing-like capacity mechanism, where the soil flows along

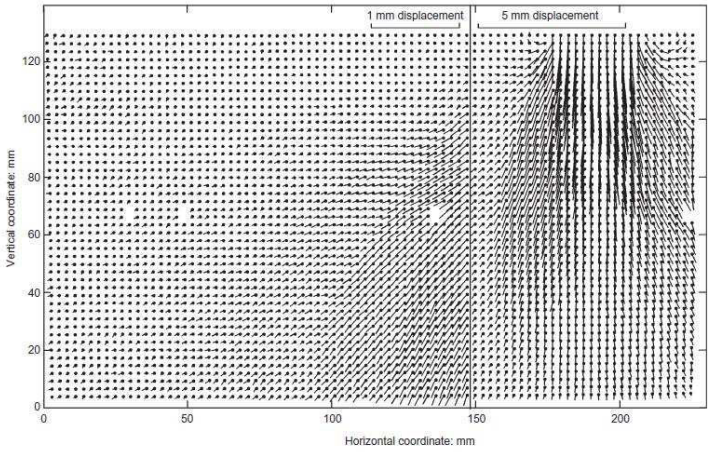

Figure 4: Displacement field around pile tip [117]

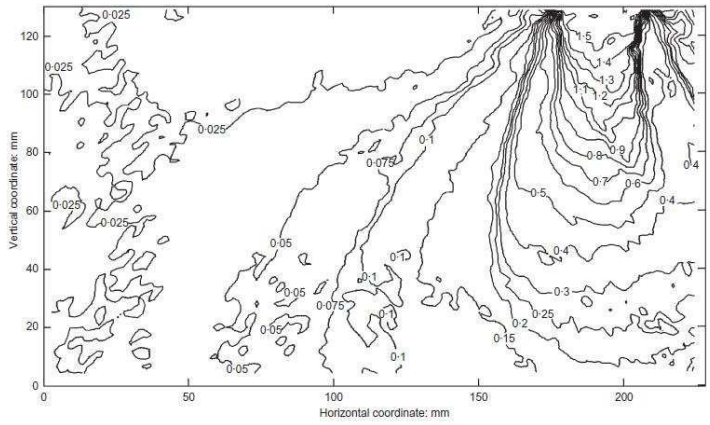

Figure 5: Contours of displacement field magnitude [117]

streamlines curving from below the pile base around to the upward direction on either side of the shaft, is found. Rather the observed mechanism is similar to cavity expansion theory despite the fact that contours of displacement follow a circumferential path immediately below the pile, but then return to the pile "shoulder", whereas, accordingly to the theory, should only vary with the radial coordinate. Figure 4 and figure 5 show the displacement field around the pile tip and the contours of displacement field magnitude and figure 6 shows the full trajectories for the two soil types during pile installation. This distribution of strain corresponds to the initial state of the soil media before the loading is applied to the pile having a considerable influence on its response. The authors conclude that this distribution of strains is of the utmost importance to, among other uses, correctly predict the stiffness of the soil prior to loading which has a strong influence the base reaction.

It is concluded by the authors that the displacement fields and strain paths during pile installation are mostly independent of the soil material except for differences in terms

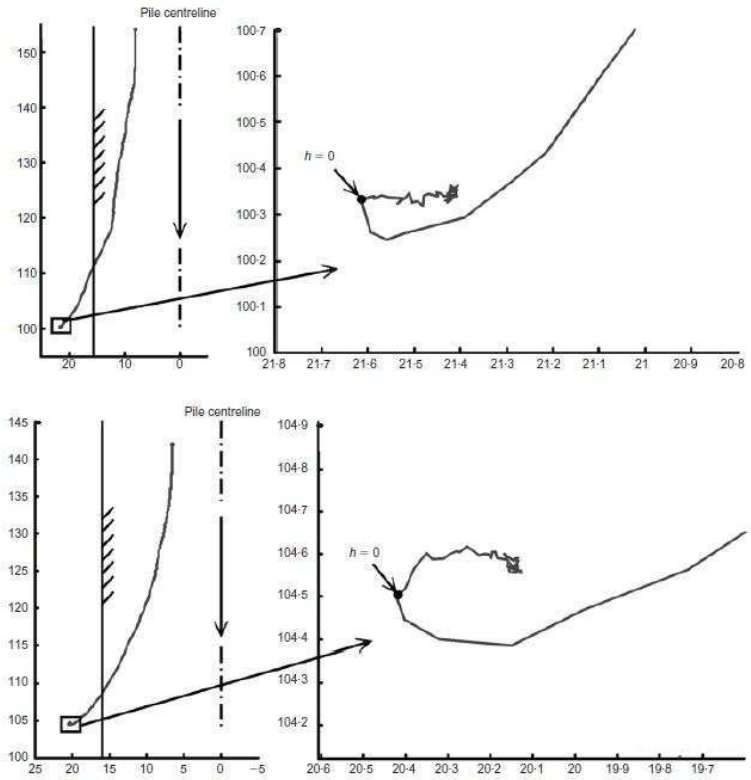

Figure 6: Soil element trajectories during pile installation [mm] [117] Top - Dog's Bay sand ; Bottom - Leighton Buzzard sand

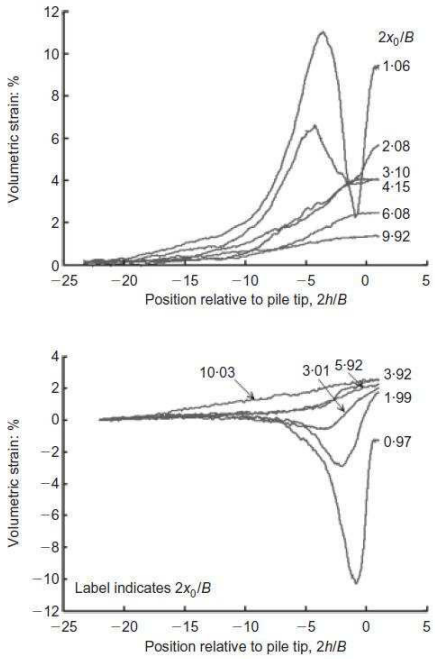

Figure 7: Volumetric strain paths Top - Dog's Bay sand ; Bottom - Leighton Buzzard sand [117]

of area of influence in stress distributions. The use of a finite strain calculation to take account for rotations is considered unavoidable by the authors. The study also incorporates the analysis of strain distribution during the installation process of which the volumetric behaviour of the soil after pile installation can be seen in figures 7 and 8.

The volumetric variation of the soil near the soil-pile interface during the pile installation process is of major importance for the mechanical behaviour of the interface. In fact it is found that the soil-interface is significantly denser than even the very near field. Some of this variation is an irrecoverable volume reduction ($\geq 10\%$) from grain crushing due to continued shearing, during and after the pile tip has passed [117] and high compression below the pile tip. As was found by Luzzani and Coop [74] soil that suffers particle damage does not reach a constant volume state, moreover, a new critical line must apply that lies "below" the critical state line for the uncrushed sand.

White and Lehane [118] performed a series of experiments considering the installation of displacement piles by three different methods, monotonic, jacked and "pseudo-dynamic", followed by load tests, monotonic compression, cyclic compression and cyclic compression-tension. The objective is the study of the "friction fatigue" phenomena and the conclusion is that this effect should be more related to the number, mode (one-way or two-way cycling) and amplitude of cycles than to the empirical h/R presented by Jardine and Chow [61]. The study does conclude that the friction fatigue effect is not observed in monotonic installation or loading phases since no decrease in radial stress is observed and that it is independent of the distance behind the pile tip. However, considering a

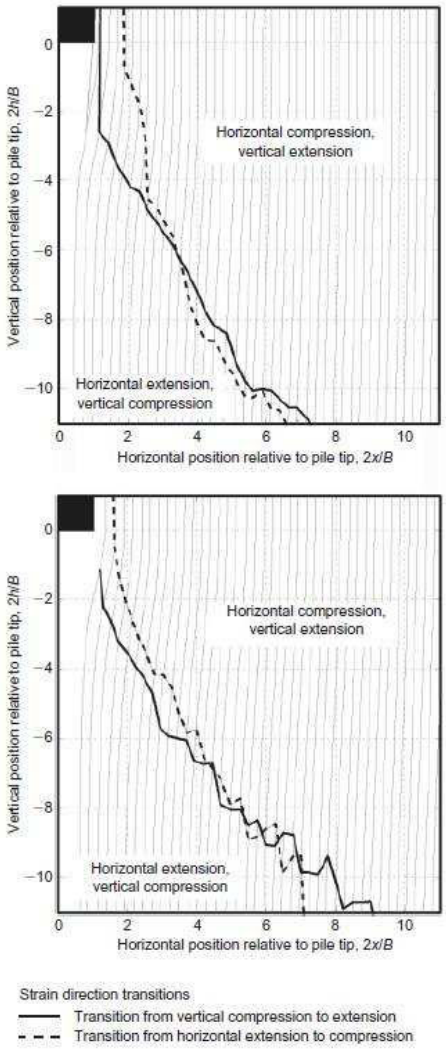

Figure 8: Streamlines of soil flow and strain rate reversal points Top - Dog's Bay sand ; Bottom - Leighton Buzzard sand [117]

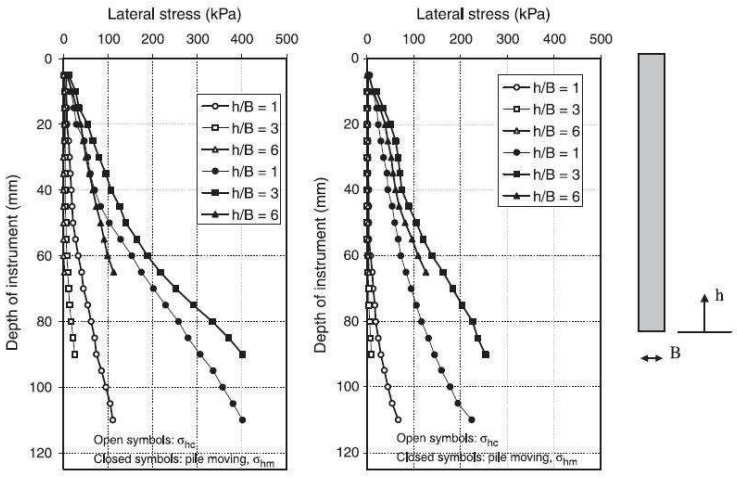

Figure 9: Lateral stress recorded during installation (average values) Left - jacked pile ; Right - pseudo-dynamic [67]

cyclic installation method, the number of cycles has a significant impact on the radial stresses despite the fact that the shaft friction resistance of the pile is never fully mobilized. Comparing the jacked and the cyclic cases the difference between radial stress distributions is smaller for a decreasing number of cycles. For a higher number of cycles it is found that for the cyclic case the radial stress decrease is more pronounced than for the jacked method. Each cycle, at the soil-pile interface level, is found to be composed of an initial contraction followed by a dilation that does not, however, fully recover the initial volume decrease since the net value of each cycle is a contraction. This in turns reflects in the radial stress evolution which decreases with each cycle. Therefore, the effect already observed by Kelly [64] is confirmed, for an increasing amplitude of each cycle the radial stress decrease is higher. Finally, the authors point out that the loss in radial stress during cyclic installation may not be recovered during subsequent shearing to failure.

Lehane and White [67] describe a series of centrifuge tests of pile installation and loading in NC sand. Also, a series of interface shear experiments considering constant normal load (CNL) and constant normal stiffness (CNS) are performed to verify the mechanism at the soil-pile interface level. The values of the radial stress are clearly dependent on the installation phase (figure 9). It is found that the residual radial stresses, after installation, are lower for the cases of the dynamic installation procedure (2-way cycling) than for the jacked case (1-way cycling). These results are in agreement to those presented by the same authors in [118]. Despite the net decrease in radial stress (due to strain path reversal [117]), these increase substantially during the increment often to more than 10 times the stationary values.

White [115] present a general framework for the pile shaft friction mechanism on displacement piles in sand. The framework is based on the loading history of a soil element at the pile-soil interface described in figure 10.

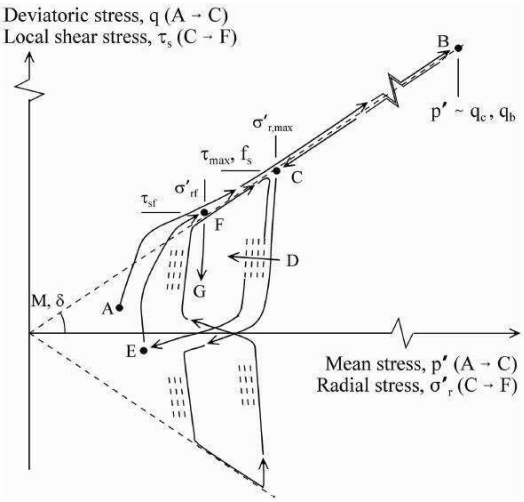

Figure 10: Loading history of a soil element adjacent to a displacement pile [115]

This element will start beneath the pile tip and will then be moved to be adjacent to the pile-soil interface once the pile base passes through that depth. In this representation points A to F (and G) represent respectively the *in situ* conditions, directly beneath the pile tip, point of maximum shaft friction, friction fatigue phenomena takes place, post-installation state and, finally, the application of working load. The increase from A to B is due to the proximity of the pile base and, therefore high compression with the pile movement in the downwards direction. The reduction between B-C is considered to be a result of the "passing" of the soil element from beneath the pile base to the pile shaft. The points from C to E represent the cycles of shearing when the pile is driven or jacked and, as other authors have shown, there is a substantial decrease in the radial stresses known as "friction fatigue" (net contraction of each cycle). Final stages from E to F where the loading phase, until pile failure, is represented and point G which represents a cyclic working load stage.

Yang et al. [125] studies the processes of particle crushing, shear banding and their influence on the behaviour of displacement piles. With that purpose in mind, centrifuge tests, to simulate the non-monotonic installation of piles, and ring shear tests, to replicate the soil-pile interface behaviour to high strains, were performed and observing the results noted that pile installation in pressurized and/or dense sand involves particle breakage and shear band formation. The shear bands are constituted of broken soil particles forming beneath the pile tip. It is found that considerable grain breakage takes place at the interface level starting beneath the pile tip during monotonic pile installation. The authors propose a schematic representation for the undergoing key processes (figure 11)

The crushed material is displaced radially and were the "zones" represent different levels of particle crushing. The first zone, adherent to the pile shaft, was found to contract more than 15% due to high compression and extreme shearing. A shear band zone is found to be formed near the tip and which scales with particle size [96]. Around 20% of zone 1

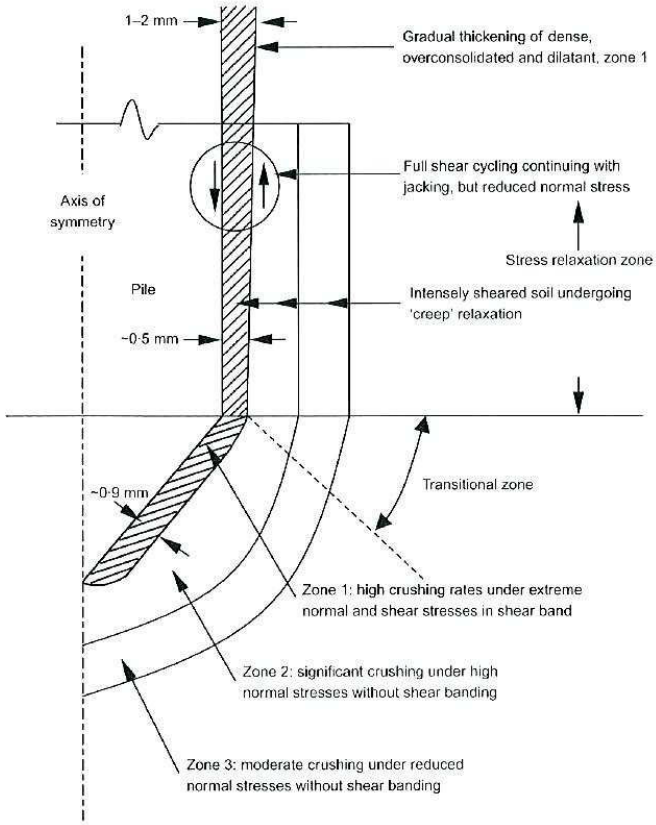

Figure 11: Schematic development of zones 1 to 3 and their relationship to stress regime [125]

material was crushed (final void ratio well below the minimum void ratio of the uncrushed material) while only 6-8% for zone 3 and none discernable for zone 3. Evolution of radial stresses is consistent with what was found by White and Bolton [117], sharp increase as the pile tip approaches followed by sharp decrease due to strain path reversal. Continued shearing at the pile, for even far from the pile tip, produced continued contraction of zone 1. This process is thought to be true also for large-displacement cyclic loading.

The authors also performed monotonic ring shear tests. The monotonic ring shear tests generated an interface layer that is comparable to the one obtained for the soil-pile interface layer during centrifuge testing as well as broadly similar patterns of interface roughness, in spite of leading to thinner shear zones and lower proportions of fractured sand. Non-monotonic ring shear tests are thought to produced even higher particle damage albeit not being able to replicate the high-pressure particle crushing and shear band development taking place ahead of the pile tip during installation.

2.1.2 Experimental results of triaxial and ring shear tests

Ring shear testing (RS) is a practical and valid tool to simulate soil behaviour under very large shear displacements. This test is, therefore, very useful to explore the behaviour that would occur at soil-pile interface during the installation process [125] such as shear and normal stresses application, initiation of bifurcation and shear band development among others.

Coop et al. [17] performed ring shear tests where the sand used was Dog's Bay carbonate sand which is known to suffer particle breakage. The results showed that a stable grading could be reached when breakage ceased but only at very high shear strain levels and which depended on both the normal stress and initial grading. The definition of the critical state from small strain tests is brought into question. The results from the study support the claim by Baharom and Stallebrass [4] that the critical state found at small strain test is the result of a balance between volumetric compression arising from particle breakage and volumetric dilation from particle rearrangement. Considerable particle damage, mainly where localization was observed, during the ring shear tests resulted in the net contraction of the specimen. The phase transformation from dilative to contractive behaviour occurs at high strains and volume contraction is found to be very slow. The evolution of volumetric contraction decreases with decreasing normal stress which means that the strains required to reach a stable gradation increase rapidly as vertical stress is reduced. Finally, the critical state friction angle was found to remain constant.

Okada et al. [89] performed ring shear and triaxial tests, under drained and undrained conditions, on fine silica sand and Osaka-group coarse sandy soils. It is found that steady-state conditions (deformation at constant volume, constant normal effective stress, constant shear stress and constant velocity) cannot be attained with standard triaxial or ring shear testing. The results are similar to those found by Sadrekarimi and Olson [99] despite the fact that liquefaction is the main aspect in study. However, the authors study the effects on contraction as a result of grain crushing (trigger to sliding-surface lique-

faction) due to continue shearing to very high strains and find that it can occur at any initial void ratio. Two phase transformation points are found for dilative specimens and it is interpreted from the undrained tests that the decrease in shear resistance is related to an increase in pore pressure (contraction) as a result of considerable grain crushing in the specimen. This behaviour can be observed in figure 12 in the ring shear tests for silica sand but the same behaviour, qualitatively, is also found in medium-dense and dense Osaka-group coarse sandy soils.

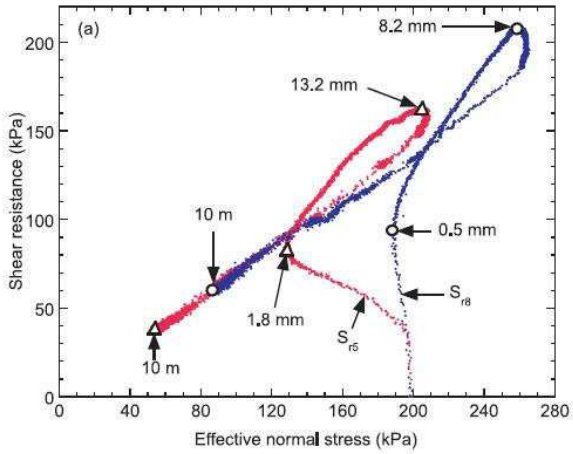

Figure 12: Effective-stress paths of medium-dense and dense silica sand (S_{r5}: $e_0 = 0.98$; S_{r8}: $e_0 = 0.86$) [89]

Both triaxial and ring shear tests are carried out and considerably different results are found. Lower shear resistances are obtained in RS tests than in triaxial tests which undoubtedly depended on the two different shearing modes of the tests. Shear deformation may have become concentrated along the shear surfaces where grain crushing was occurring which in turn lowered the deviator stress in the specimen along the critical state line in the stress plane. Finally a comparison between drained and undrained ring shear tests are performed to study the relationship between volumetric change and pore pressure variation. In order of magnitude, in the case of drained tests, the variation of the height of the specimen is more substantial than the pore pressure variation in the undrained tests. This is due, as interpreted by the authors, to the fact that the pore pressure can never surpass the total normal stress whereas, in the drained tests, variation in specimen height can continue as long as grain crushing does not cease.

Sadrekarimi and Olson [96] performed ring shear tests on three sands Ottawa (OT), Illinois River (IR) and Mississippi River (MR) sand reaching very high displacements.

The ring shear test device can shear specimens to virtually unlimited displacements, allowing the observation of the shear band evolution at very large shear displacements.

It is shown that the specimen shears uniformly over its entire height prior to shear localization. Bifurcation, under constant volume and drained conditions, occurs as the soil fully mobilizes its effective peak friction angle, and subsequent shear displacements

Sand	*Specific gravity* (G_s)	e_{max}	e_{min}	*Mineralogy*
OT sand	2.63	0.679	0.391	Quartz
IR sand	2.63	0.757	0.464	Quartz with traces of muscovite, chlorite and hematite
MR sand	2.65	1.038	0.563	70% albite, 21% calcite, 4% other

Table 2.1: Soil properties ([96] [97])

occur within the shear band. Substantial particle damage occurred within the shear band after large displacements especially for dilative sands at moderate consolidation normal stresses. No particle damage was observed outside the shear band however(figure 13).

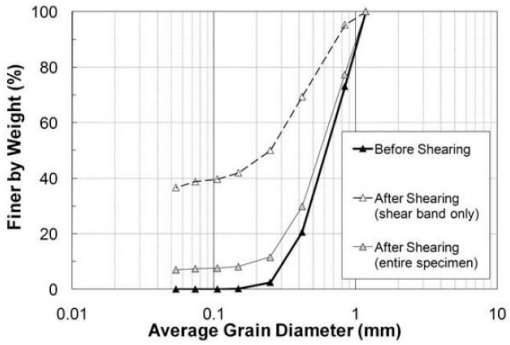

Figure 13: Grain-size distributions of IR sand before and after RS testing [96]

The shear band thickness evolution can be seen from schematic in figure 14.

The specimen is responding to competing shear mechanisms, namely, dilation and particle damage which lead to, respectively, increased shear resistance (dilation of the original grain structure) and decrease in shear resistance (local contraction). The shear band evolution starts with grain dilation dominating the behaviour and therefore increasing the shear resistance (points a-c) whilst from point (c) onward there is net contraction as a result of particle damage. The tests were terminated when the specimens reached their critical state with a stabilization of the shear band thickness.

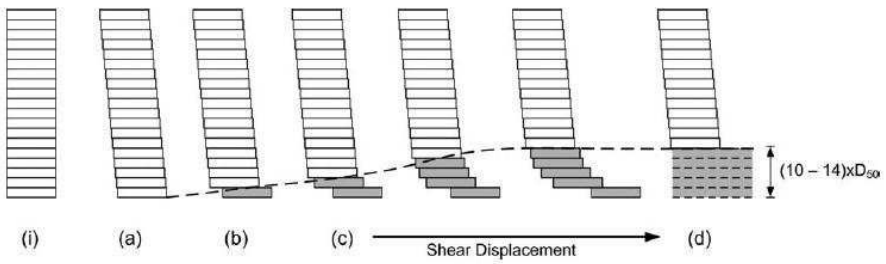

Figure 14: Shear band evolution [96]

Reference	Shear band thickness/D_{50}	Description
Sadrekarimi and Olson (2010)	10	OT sand
	10	IR sand
	14	MR sand
Roscoe (1970)	10	Sands and clays
Vardoulakis and Graf (1985)	15	Fine-grained Karlsruhe sand
Vardoulakis and Aifantis (1991)	20	Theoretical considerations
Yoshida (1994)	7-20	Ratio varied with mean effect stress and particle shape
Bardet and Proubet (1991; Iwashita and Oda (1998)	15-18	DEM simulation
Oda et al. (1997); Iwashita and Oda (1998)	10	DEM simulation with rotational resistance
Finno et al. (1997)	10-25	Clean masonry sand
Alshibli and Sture (1999)	10-11	Coarse-grained sand in PSC
	11-12	Medium-grained sand in PSC
	13-14	Fine-grained sand in PSC

Table 2.2: Comparison of Ratios of Shear Band Thickness to D_{50} [96]

The shear band thickness increased with shear displacement until reaching a constant thickness. After the stabilization in thickness of the shear band all the subsequent deformations were localized within the shear band (the rest of the specimen remained stationary). Therefore, strain and strain rate normal to the shear band orientation became practically zero at the inception of shear banding, in other words, the shear band corresponds to a zero-extension line. The thickness of the shear band at the final stage ranged from 10 to 14 times the median particle diameter.

Table 2.1.2 presents some of the results of shear band thickness from previous studies.

Sadrekarimi and Olson [97] focused on particle damage during ring shear testing, for Ottawa sand (OT), Illinois River sand (IR) and Mississippi River sand (MR), were it is found that stress concentration at particle asperities and moments applied to individual particles due to large internal shear stresses are the main mechanisms for particle damage. This results that particle damage can occur even at low confining stresses. Both drained and undrained ring shear tests were performed. More particle damage is found to occur in drained RS tests than in constant volume tests. The particle damage effects on stress-strain response found in drained conditions are that it causes contraction in the shear band, even for initially dilative specimens, while for undrained conditions it increases potential compressibility of the specimen. Similar to previous tests [96], as particle damage increases it overcomes dilation and produces net contraction (2nd phase transformation) which continues until normal stresses are small enough to cease particle damage and the critical state is reached.

Figure 15 and figure 16 presented by Sadrekarimi and Olson [97] show the evolution of the shear band and the stress paths for RS tests in OT sand (similar results are found for IR sand that had the same preparation method). The different steps identified by letters, (a) to (d), in the plots are explained by Sadrekarimi and Olson [97] where (a) is the first transformation point, (b) is the initiation of bifurcation, (c) is the second transformation point (in constant volume tests) and (d) is the end of the tests.

Sadrekarimi and Olson [99] and Sadrekarimi and Olson [98] considered the effect of large shear displacements, where grain crushing occurs, on the critical state friction angle,

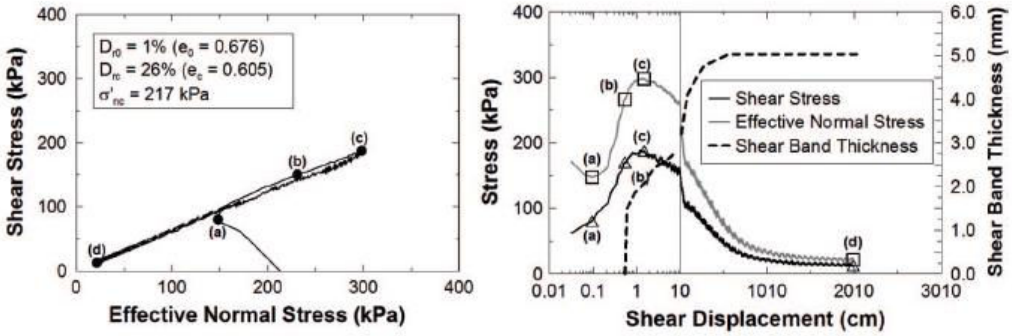

Figure 15: Shear band evolution and corresponding stress paths and stress-displacements plots in constant volume RS tests on OT sand [97]

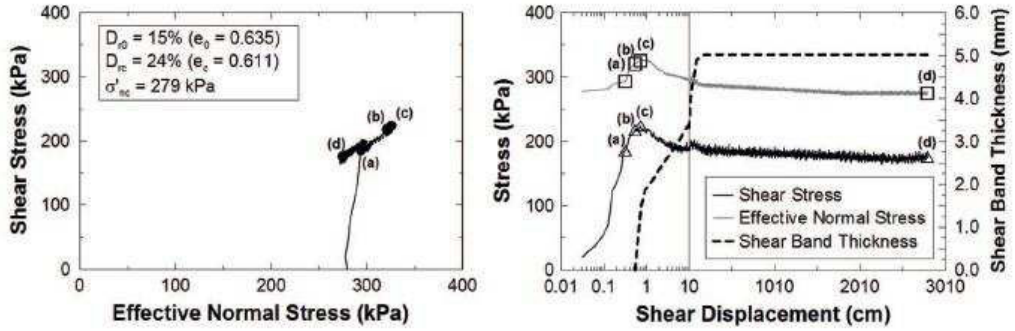

Figure 16: Shear band evolution and corresponding stress paths and stress-displacements plots in drained stress paths RS tests on OT sand [97]

normal consolidation line (NCL) and the critical state line (CSL) for Ottawa sand (OT), Illinois River sand (IR) and Mississippi River sand (MR) in ring shear and triaxial tests.

Regarding the friction angle, it was found to be independent of stress path, initial fabric, initial void ratio and consolidation stress while dependent on particle mineralogy, shape and the intermediate principal stress. The values of the friction angle were therefore influenced by particle damage of the specimen since it produces a wider particle size distribution and more angular particles. The friction angle was found to remain mostly constant until the first phase transformation point but, as shearing continued, sand particles became more angular and started filling void spaces which lead to an increase in the friction angle for both low and high consolidation stresses (Figure 17). The variation of the friction angle with particle damage is an open question with different authors finding contradictory results [95].

Considering the NCL and CSL in the volumetric space, both lines, for IR and OT sands, "start" and remain mostly parallel even at large shear displacements, for IR and OT sands both lines become much steeper with shearing and finally that for MR only the CSL becomes steeper and the NCL does not change significantly. This result has

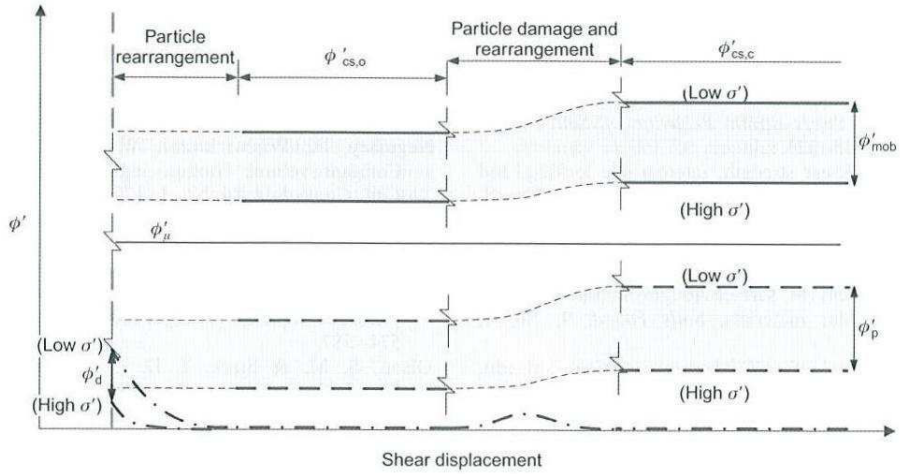

Figure 17: Evolution of friction angle mobilized in sand [99]

profound implications on the definition and position of the critical state of specimens. The traditional position of the CSL is clearly not applicable when particle damage occurs for no constant volume state is reached at the levels of deformation usually considered as limiting values. Figures 18 and 19 shows the results for OT and IR sands

From the works summarized here it can be seen that, despite the fact that both shear and normal stresses are relatively low during the tests performed, high levels of particle crushing are found which brings into question the notion that crushing only occurs at elevated levels of stress in the soil. It may be assumed that high levels of shear strain will produce high stresses at the asperities of particles which can result in considerable particle damage.

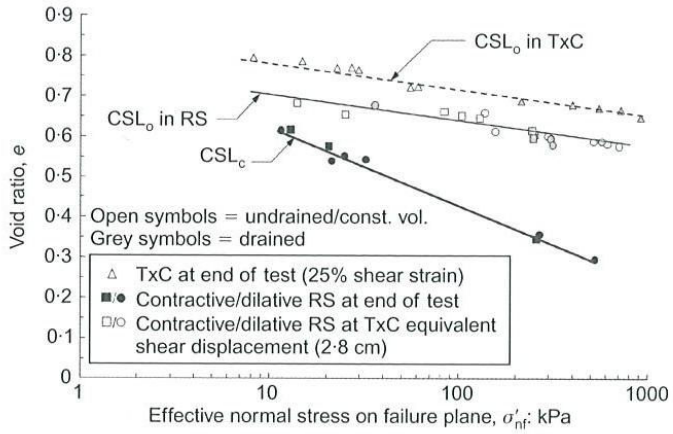

Figure 18: Critical state lines of original (CSL_0) and crushed (CSL_c) OT sand from triaxial and ring shear tests [99]

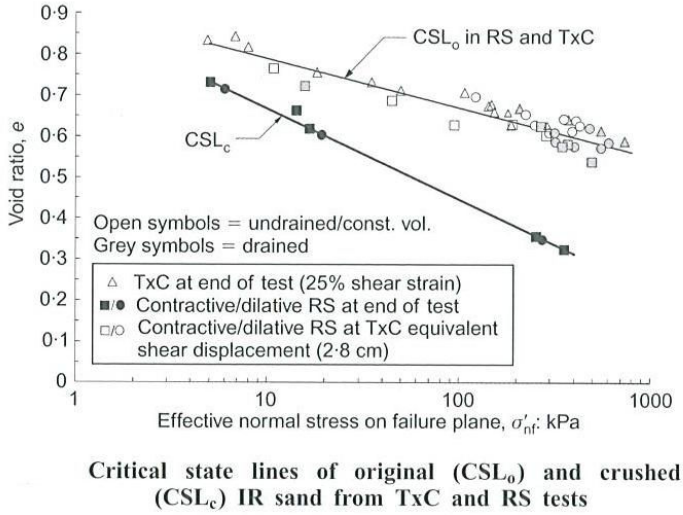

Figure 19: Critical state lines of original (CSL_0) and crushed (CSL_c) IR sand from triaxial and ring shear tests [99]

2.2 Constitutive models

Numerous authors have proposed constitutive models to tackle the behaviour of soil specimens subjected to grain crushing and large shear displacements, namely at the interface level ([24] [83] [38] [71] [101] [8]), in order to simulate geotechnical structures. A brief summary of some of the models is presented henceforth.

Cecconi et al. [14] formulated a model developed for a pyroclastic soil - coarse-grained soft rock. The central assumption is that the frictional properties of the material change with the development plastic strains and proposes three variables to model that influence. The properties that are considered to change include the friction angle, the elastic domain and the slope of the NCL, and finally a parameter that controls the yield locus shape. The change of the friction angle implies a change in the classical stress-dilatancy formulation. The model focuses on grain crushing effects despite borrowing heavily from the effects of debonding in terms of mathematical formulation. Three internal variables are added to simulate the behaviour of the specimen whence particle damage occurs. The plastic yield locus is dependent on the evolution of two variables, the first of which describes mechanical degradation of interparticle bounding in structured granular soils and a second due to variation in grain size distribution (the authors however point out to the lack of physical evidence if grain size distribution affects the yield locus overall shape). Also, a variable describes the decrease in the friction angle with decreasing grain diameter.

Russell and Khalili [95] propose a model where the critical state line (CSL) in the volumetric space steepens when grain crushing occurs and then flattens at some point afterwards. The critical state line takes the form of 3 linear segments dependent on the stress level interval. The phases are: particle rearrangement in sliding and rotation, particle crushing (substantially more contraction) and finally particle crushing is no longer the main factor (contraction reduces considerably which results in an almost flat CSL). The model considers the Roscoe dilatancy rule and friction angle is considered to be a constant which is validated by triaxial testing. This model considers particle damage only due to high levels of compression based on experimental results from Hagerty et al. [45].

Salim and Indraratna [100] proposed a model for coarse granular aggregates that considers particle damage based on an extra internal variable dependent on the back-calculation of triaxial test results. This internal variable is the breakage index from Marsal [75] which requires laboratory testing to be defined and hence adds 5 additional parameters that are required for the definition of the breakage mechanism. The plastic flow rule, based on Roscoe dilatancy rule, incorporates the breakage variable and a Mohr-Coulomb yield locus is considered. The model does not appear to show much difference considering the breakage parameters than without despite both fitting the laboratory results presented.

Hu et al. [55] propose a model with two yield surfaces: shear sliding (Roscoe dilatancy rule) and isotropic compression (associated flow rule). A breakage function is proposed connecting the evolution of the CSL to the energy consumed which then results that

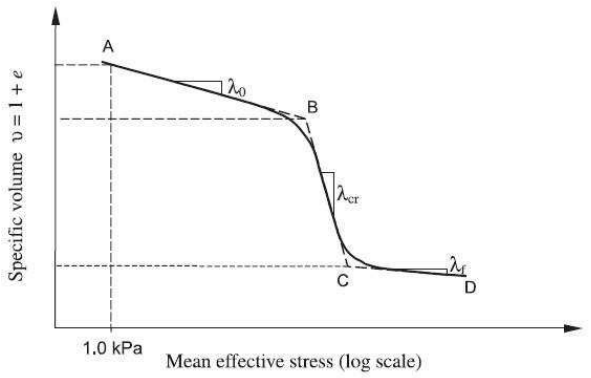

Figure 20: General critical state line for sands [95]

the position of the CSL is dependent on gradation. The position of the CSL is defined by Biarez's correlation between peak friction angle and intrinsic friction angle using the present void ratio and the critical void ratio. Void ratio depends on breakage index therefore correlating breakage index with the CSL while considering the gradation of the specimen.

From the models presented here none attempts to model the second transformation phase seen in some of the laboratory tests. A great deal of attention is given to the determination of the evolution of gradation by some of the models but the furthest that these models consider is to limit or annul dilation but not in reversing the volumetric behaviour.

2.3 Formulations in the Finite Element Method

There have been successful applications of the finite element method to non-linear problems even when considering large strain plasticity in the material constitutive structure. There are however some problems that arise with finite element analysis when extending it to the finite deformation range, such as a correct formulation of the problem, mesh elements distortion, modeling of the contact boundary conditions, incorporation of the plastic incompressibility condition and accounting for plastic anisotropy [114].

The existing approaches in finite element analysis for solid mechanics may be divided, in general terms, in Lagrangian-type formulations, total Lagrangian and Updated Lagrangian formulations, Eulerian formulation and, more recently, an Arbitrary Lagrangian-Eulerian formulation. Some of the characteristics, advantages and drawbacks, of these formulations will be analyzed hereafter.

Lagrangian-type formulations are very efficient and suited for nonlinear problems where only small strains are considered. Boundary condition nonlinearities do not change with deformation and mesh distortion is not a factor in the analysis. The movement of

the continuum is specified as a function of the material coordinates and time. The particle description is often applied in solid mechanics and the nodes of the Lagrangian mesh move together with the material.

These necessary conditions reveal some of the drawbacks of this kind of formulation for the analysis of finite deformation problems.The volume incompressibility constraint is usually violated as well as load fluctuations together with mesh distortions and element entanglements. On the other hand, some automatic mesh rezoning methods exist for Lagrangian formulations but these methods are not so robust and efficient to remedy the mesh distortions. These methods are based on rediscretizing the mesh configuration after certain "special" deformations. Their use for complex constitutive models, involving state variables, is an open problem.

The problems of contact and friction boundary are a serious issue with this type of formulation. Even though the interface between two parts is precisely tracked and defined problems arise with convergence, specification of stiffness parameters as well as accuracy of element formulation and assumptions. They undergo anomalous response behaviour when employed in situations where large strain kinematics are considered which is reflected in invalid stiffness characterizations, i.e., poorly conditioned Jacobians. Situations requiring friction effects require a considerable amount of iterations to converge the calculation. Lastly, the contact elements parameters have to be chosen by the user.

Two main Lagrangian methods have been defined in previous studies for problems considering finite deformations: Total-Lagrangian and the Updated-Lagrangian method. The main difference between the two methods is the configuration with respect to which the kinematics and state variables of motion are measured. Despite being two different methods their solutions do not coincide due to the fact that different stress and strain measures, therefore different constitutive laws, are used.

In the Total-Lagrangian formulation the second Piola-Kirchoff stress tensor and the Green-Lagrange strain tensor, which are work-conjugate, are used. However, constitutive laws are rarely expressed in terms of the this pair of stress strain measures. It is also notable that the yield function should always be checked with the Cauchy stresses during the stress integration. This is due to the fact that most existing constitutive models for soil are expressed in terms of the Cauchy stress this transformation would be the greatest difficulty in their extension to the finite deformation range. If a substepping technique is used, one has to transfer the 2^{nd} Piola-Kirchhoff stresses to the Cauchy stresses and, therefore, within each sub-increment or each iteration. Despite that, it may be fully justified from a mathematical standpoint though, the direct pertinence to the physical reality may not be guaranteed. Therefore, the resultant mathematically equivalent constitutive formulation might be not only physically irrelevant but also rather complex in mathematical form. Finally, the additive decomposition of the strain tensor in elastic and plastic parts is not trivial and will be described in a later section.

The Updated-Lagrangian method has been used by many investigators in recent years.

Simpler integration of the constitutive equations than in the Total-Lagrangian method and a direct extension from infinitesimal elastoplastic theory are some of the reasons. In this method the mesh is modified after each incremental step calculation. There is, therefore, the ability to re-mesh or re-zone areas with important geometrical changing and where the stresses and strains are taken from the old mesh and introduced in the new one. Despite this, large element distortions are still possible if not "small" enough increments are considered specially in cases of localized deformation where very frequent re-meshing is required.

Two important methods of this formulation are presented by Nazem [86], the first by Bathe and Ozdemir [6], latter improved by Bathe [5], and a second one based on the objective stress rates. The method by Bathe and Ozdemir [6], Bathe [5] requires, however, that all constitutive laws are written in terms of the second Piola-Kirchhoff stress tensor which is rarely possible in practice. Also, the latest version of the method uses the strain increment considering the Green-Lagrange strain tensor which poses, once more, the problem of additive decomposition. The second method considers a constitutive structure based on linear strain increments and an objective stress rate (in this case the Jaumann stress rate). The extension from infinitesimal strain constitutive laws to the finite strain range can be easily obtained but the stress integration scheme must be modified to include rigid-body rotation. This stress transformation may be performed before or after the integration of the stress-strain equation without much difference or additional hardships. In any case this transformation is done separately from the stress integration procedure.

In an Eulerian approach the motion of the continuum is specified as a function of the spatial coordinate and time. In the finite element analysis based on Eulerian formulation the finite element mesh is fixed in space and does not move with material points. Therefore, the Eulerian reference mesh which remains undistorted is needed to trace the motion of the material in the Eulerian domain. Also, if displacements are the main unknowns, the state of the material "state" (strain, stress, etc.) momentarily the integration points occupying must be determined at the beginning of each numerical step. However, the method of updating the material properties is not perfectly defined ([111] [114]).

An Eulerian formulation is mostly used where the domain of interest is a fixed region in space and which has to be known *a priori* suitable for the study of flow-like problems. Also, one main advantage of this kind of approach is that no element distortions can ever occur. However, numerical diffusion may happen in case of two or more materials in the Eulerian domain. Therefore, since it introduces complexities such as the appropriate representation of the free body it is less suited for domains whose boundaries or interfaces move substantially. To successfully simulate non-steady static or dynamic behaviour within the framework of this formulation is not a trivial endeavour.

The Arbitrary Lagrangian-Eulerian (ALE) formulation is an attempt to join the main advantages of the previous approaches and also to eliminate some of their more important drawbacks. This approach has been subject to various studies from researches recently ([113], [36], [35]). This method consists on uncoupling nodal point displacements and

velocities from material displacements and velocities therefore eliminating the mesh distortion present in the Lagrangian formulation. Due to the uncoupling, convection must be taken into account to update the state at the nodal points (between material and mesh displacements and velocities). In an ALE formulation the finite element mesh need not adhere to the material or be fixed in space but may be moved arbitrarily relative to the material. Combining the merits from both Eulerian and Lagrangian formulation, ALE is more suitable to handle mesh distortion and special boundary condition changes.

Despite the fact that ALE does not have a formal definition as of yet most authors agree that a proper ALE formulation should reduce to a Lagrangian formulation and to an Eulerian formulation when choosing the same motion for the the computational mesh and materials meshes or if the computational mesh is fixed, respectively.

The number of unknowns in a purely ALE formulation surpasses the number of equations since there is a new set of unknowns due to unknown mesh displacements in addition to the already existent material displacements, which means that a mesh motion must be specified. Therefore, multiple mesh motion procedures, also known as mesh refinements, have been proposed in the literature to deal with this issue where most consider an arbitrary mesh motion as to not interfere with the results.

From a theoretical point of view, a fully coupled ALE approach represents a true kinematic description in which material deformation is described relative to a moving reference configuration. In a coupled ALE the two sets of unknown displacements (mesh and material) are solved simultaneously. The majority of ALE analyses, however, whether quasi-static or dynamic, are based on a computationally convenient operation known as operator split-technique (decoupled ALE). In this approach material deformation and convective terms are treated separately which means each time step is subdivided in a Lagrangian followed by an Eulerian step. The reason for this are the advantages of this method over a fully coupled approach. Not only a reduction in the cost of the implementation of ALE to current Lagrangian codes, as the Lagrangian step is unchanged and only the Eulerian step needs to be added, but also the equations to be solved are much simpler.

Now lets consider the different steps of this formulation. In the Lagrangian step the "usual" operations are taken into account such as solving incremental displacements and by integrating the constitutive equations to obtain the stresses and verify equilibrium at the end of each iteration based in an error tolerance interval. In this step state variables satisfy both the global equilibrium and local consistency requirements but the mesh may become distorted since it accompanies the material. In the Eulerian step a mesh refinement must be prescribed to eradicate the possible existing distortions form the Lagrangian step and then all kinematic and state variables are transferred to the new mesh by considering the relationship between the material derivative and reference time derivative of a physical quantity [56]. Nazem [86] proposed a mesh refinement where the arbitrary principle of mesh motion is considered but adds two additional requirements to be fulfilled by this motion which are, roughly, to maintain boundaries of the domain and materials and that the new mesh's topology and connectivity should remain the same as in the original mesh.

Some authors, however, have found that the Eulerian step encounters problems in fulfilling the objectivity requirement making it necessary to take into consideration addition corrections (in general, more iterations) to confirm objectivity of the remapped variables in the new mesh.

2.4 Numerical modelling of pile installation

Numerical tools have become common use in recent years of which the finite element method is now considered the main tool for geotechnical design and research. Most analyses are performed considering the small strain hypothesis in the constitutive framework of the numerical tools due to simplicity. However, as has been shown from the experimental studies performed by various authors, pile installation and special loading cases have to consider large strains in the finite element structure. Moreover, for a complete analysis of the effects in surrounding structures, stress distribution, volumetric effects, etc. empirical methods are clearly insufficient and inaccurate.

Thus arises the issue of choosing a numerical tool to deal with these aspects. It can be acknowledged that the most promising candidates are the finite element methods, discrete element methods and/or meshless methods. Discrete elements methods are still considered incapable of accurate modeling large scale analysis which, therefore, eliminates this possible numerical tool to date [12]. The finite element method has been object of various works, many for monotonic installations but fewer for dynamic installation procedures, of which some are presented henceforth. The meshfree method, to the author's knowledge has not known works concerning the installation of driven piles despite the fact that the method has been considered suitable for large deformation analysis [119] [34].

It is evident though that the finite element method has many disadvantages when solving geotechnical problems with large deformations, especially the ones, such as pile analysis, which involve frictional contact problems and large mesh distortions. Many authors have dedicated time for the resolution of this complex geotechnical engineering problem and various approaches have been researched and developed. One of the main challenges in this type of numerical analysis using the finite element method is the convergence to a stable solution. Some recent studies will now be object of a more detailed description and will be divided according to their numerical approach, namely, Updated Lagrangian, Eulerian or Arbitrary Lagrangian-Eulerian.

Sheng et al. [103] used ABAQUS to perform the installation (pushed-in) and loading of a pile in a 2D axisymmetric Updated Lagrangian formulation (which stress rate is used is not revealed). The pile is considered as a rigid body and the soil is described by a Modified Cam Clay constitutive model. No contact elements are considered (ABAQUS master-slave principle), and the contact problem is solved by using a Lagrangian multiplier method with the Mohr-Coulomb contact law.

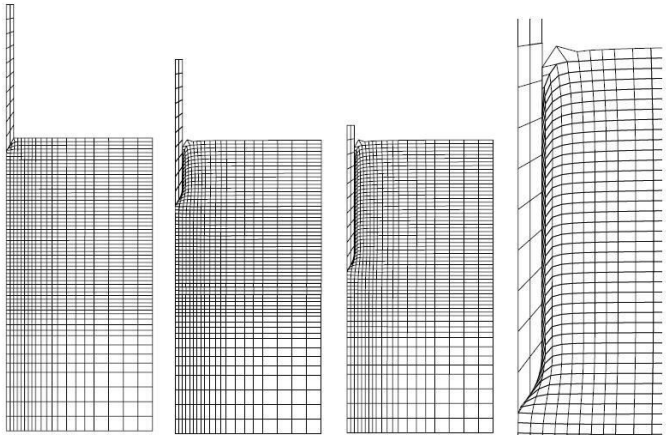

Figure 21: Deformed mesh at different penetration depths [103]

Numerically, this study presents valuable insight in the limitations of an Updated Lagrangian analysis to fully prevent mesh distortion. In case of the pile installation, the authors have found a limiting angle for the pile base (pile base angle must be taken as inferior to 90°) otherwise risking numerical non-convergence and, as mentioned beforehand, mesh distortion. Flat end piles cannot, therefore, be analyzed resorting to this procedure.

By comparing experimental centrifuge data and the results for the numerical analysis the authors conclude that, although the total resistance is similar, the shaft resistance is not well predicted. In terms of volumetric strain (void ratio) variation it is found that a thin layer from the pile-soil interface to approximately one pile radius, in radial distance, and from the ground surface to one radius of the pile base is expanding (dilation). Outside this zone, a U-shaped compression area is determined in the calculation. The initial OCR value is not found to affect the results in a significant manner.

Sheng et al. [104] performed an analysis of pile installation (pushed-in) in a 2D axisymmetric Updated Lagrangian formulation using the Jaumann stress rate. The pile is considered elastic and the soil follows a Modified Cam Clay constitutive model.

An analysis of the deformed mesh is performed by the authors. They find that, by observing the deformed meshes of multiple calculations, the most important deformations, radial and vertical, occur within the first column of soil elements adjacent to the pile-soil interface. This characteristic is of the utmost importance for approaches where the mesh has to be adapted to avoid mesh distortion issues. This kind of approach shows that modelers must find balance between accuracy, where elements should be as small as possible, and numerical stability and convergence, since the elements must be large enough to withstand deformation while maintaining a positive Jacobian, for the soil elements at pile-soil interface (also highly dependent of the friction interface coefficient) and pile base. The numerical formulation for frictional contact used in the study is the one

proposed in the same article based on the theory of plasticity. For the contact treatment the simple penalty method is used with the Mohr-Coulomb friction law. The authors find that the friction coefficient cannot be higher than 0.4 to prevent numerical breakdown. The authors observe, however, some overlap of soil elements around the transition point between the pile base and the pile-soil interface due to a smooth discretization of the pile surface.

The results of pile resistance have an oscillatory behaviour which begins whenever an element is moved from vertical compression, at the pile base, to radial compression and shearing, at the pile-soil interface. The authors declare that to completely remove the oscillations finer soil elements must be used but that would cause serious problems in an Updated Lagrangian formulation and could only possibly be achieved with an Arbitrary Lagrangian-Eulerian approach.

Gui [43] performed an analysis of pile installation (hydraulically-driven) in a 2D axisymmetric Updated Lagrangian formulation. The pile is considered rigid and the soil an empirical nonlinear plastic hardening stress-strain relation validated from triaxial compression tests.

The prevention of geometrical distortion was done by re-meshing the grid just before there was a numerical breakdown. The re-meshing would cause the same element to have the same stresses but at a slightly different geometrical center. However, successful analysis required multiple and successive mesh reformations, the elimination of the dilation induced peak in soil strength and, finally, that the soil near the mesh boundaries would never reach peak strength. Interface elements were characterized by the Mohr-Coulomb model.

Dijkstra et al. [25] performed in "Tochnog" (open source FE code) an analysis of pile installation (monotonic loading) in a 2D axisymmetric Eulerian formulation (the authors refer that the method is Eulerian although still a special version of ALE). No contact elements are considered but the elements at the pile-soil interface are reduced in shear strength to match shear box test results. The FE code "Tochnog" allows for the uncoupling of material and nodal displacements which defines an Eulerian approach in the finite element method. The pile is considered elastic and the soil is ruled by the Drucker-Prager behaviour law with tension cut. The analysis performed considered the phreatic level at the surface in order to simulate fully saturated conditions. The authors also performed a small strain analysis concluding that it was incapable of performing a correct analysis of the installation procedure where large strains are unmistakably relevant. The authors suggest that the combination of large strain and small strain to compute the installation and loading of pile might be the best solution (such as the implementation of the Material Point Method).

It is found that the vertical stress below the pile base highly increases with the pile installation. The shear strain exceeds 150% at its maximum but it is found that for shallow depths the soil is mainly undisturbed.

Dijkstra et al. [26] performed in "Tochnog" (open source package) an analysis of pile installation (jacked pile) in a 2D axisymmetric Eulerian formulation. The soil is ruled by the hypoplastic constitutive model proposed by von Wolffersdorff [112], Gudehus [42] with a Masuoka-Nakai yield surface. The analysis is performed considering that the pile is fixed and embedded 5m already from the start and the soil is displaced at constant speed in the upward direction.

Different void ratios were computed and it was found that for lower initial void ratio the magnitude of change in void ratio and vertical stress increases. The simulations show that densification occurs below the pile base and that near the pile-soil interface there is dilation of the soil (increase in volume).

Dijkstra et al. [28] performed in "FEAT"(2008) (commercial program) an analysis of pile installation (jacked pile) in a 2D axisymmetric Eulerian formulation. The pile is considered elastic and the soil follows a Mohr-Coulomb constitutive model. Two different simulations are considered where the first considers the pile fixed and the soil moving and the second the first's reverse, therefore simulating the real penetration process. It is found that the second approach is better suited for the modeling. Although the equilibrium equations have a negligible error the end bearing resistance curve deviates considerably from experimental centrifuge results.

Henke and Grabe [48] presented a numerical study in ABAQUS of two different installation methods, vibration and driving (jacked), in a 3D coupled ALE formulation. In the ABAQUS coupled ALE the Eulerian material is tracked as it flows through the mesh by computing its Eulerian volume fraction (EVF). Each Eulerian element is designated a percentage representing the quantity of that element filled with a material (EVF=1 is completely filled with a material and EVF=0 there is no material in the element). Contact between Eulerian and Lagrangian elements is enforced using a general contact law that does not enforce contact between the elements themselves. Therefore, a Lagrangian element can move through Eulerian elements until it encounters an Eulerian element with material (EVF $\neq$ 0).

The numerical model only considers a quarter of the total pile due to symmetry and numerical costs. The soil is ruled by the hypoplastic constitutive model proposed by von Wolffersdorff [112], Gudehus [42]. To cope with the accumulation effects and hysteretic material behaviour under cyclic loading the intergranular strain proposed by Niemunis and Herle [87] is used. The pile is considered rigid. When considering the dynamic pile installation (vibration) infinite elements are considered at the boundaries so that ground waves can disappear nearly hindered from the model.

It is found that the variation of the void ratio is much higher for the vibratory than for the jacked installation method. This densification is considered to be due to cyclic and dynamic effects. However, the jacked installation has a much wider influence area in both void ratio and radial stress variations. At the pile base both methods show high vertical stress and also high horizontal stress due to interlocking (these can go up to 4

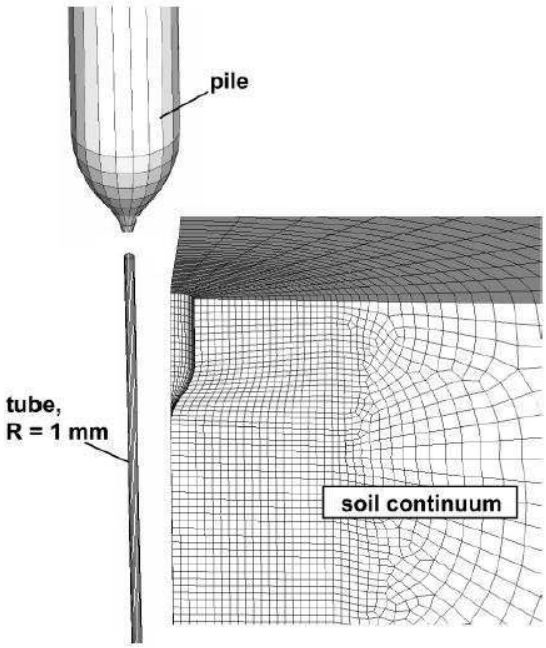

Figure 22: Modelling the pile penetration into the soil-continuum [48]

times higher for the jacked installation method).

Qiu et al. [90] performed in ABAQUS an analysis of pile installation (jacked pile) in a 3D mesh considering a coupled ALE formulation. The soil is ruled by the hypoplastic constitutive model proposed by von Wolffersdorff [112], Gudehus [42]. To cope with the accumulation effects and hysteretic material behaviour under cyclic loading the intergranular strain proposed by Niemunis and Herle [87] is used. The pile is considered rigid.

It is found that the coupled ALE is in good agreement with classical finite element codes when only a partial installation of the pile is considered to avoid mesh distortions. Void ratio and radial and vertical stress variations follow the usual trend.

Dijkstra et al. [29] performed in ABAQUS an analysis of pile installation (jacked pile) in an axisymmetric ALE formulation. The soil is ruled by the hypoplastic constitutive model proposed by von Wolffersdorff [112], Gudehus [42] also used by Qiu et al. [90]. The pile is considered rigid. No contact elements are considered but the elements at the pile-soil interface are reduced in shear strength to match shear box test results.

Evolution of the vertical stress is in reasonable agreement with centrifuge experimental data. The radial and vertical stress variations are found to go up to three diameters distance from the pile.

2.5 Summary

This Chapter consisted of a literature review of the main issues that must be addressed in order to properly study the installation process of displacement piles.

Firstly, laboratory results of simulations of pile installations were presented and the main physical phenomena that the soil material undergoes were identified and quantified by numerous authors. Their conclusions and remarks were selected and transcribed to provide a coherent and complete picture of the results.

The results showed that the soil specimens underwent extreme shearing as well as very high compression stresses in the vicinity of the moving pile. The behaviour of the soil near the pile shaft is of the utmost importance since it is where most changes are taking place.

To properly understand this behaviour a simpler test is required that allows the isolated study of this zone. Some authors noted that ring shear tests were ideal to represent the soil-pile interface behaviour and their ability to subject unlimited shear displacements to the soil was extremely convenient.

Ring shear test results are thereafter presented and important conclusions can be taken from them concerning the behaviour of the soil under such conditions. Particle damage is seen to have an increasingly important role in the stress-strain paths observed in these tests.

To model these results the finite element method is the obvious choice for this task and such has been the choice for numerous authors. The different most commonly used formulations of the finite element method are briefly described and approaches for numerical modelling of the pile installation behaviour are presented. These prove to be varied with different issues and characteristics to resolve the problems associated with the finite deformation range.

Finally, a short review of constitutive structures which attempt to described the behaviour of soil subjected to high strains is made. In order to model the behaviour of the soil specimens, as the laboratory testing results show, special features must be added to standard constitutive models. Despite interesting features of the models that were presented none attempts to model the second transformation phase seen in some of the laboratory tests. A great deal of attention is given to the determination of the evolution of gradation by some of the models but the furthest that these models consider is to limit or annul dilation but not in reversing the volumetric behaviour and determining a different critical state line as it is found in the laboratory tests.

Chapter 3

Finite Deformations

The classical theory of elastoplasticity presents fascinating findings already in the limited case of small deformation analysis. Over the years, multiple yield criterion for different materials have shown the potential of this approach, such as the Drucker's and Ilyushin's postulates (normality rule for plastic flow and the convexity of yield surface), and from them general results are derived such as extremum principles, uniqueness theorems, plastic collapse theorems, etc.

Infinitesimal theories can be adopted to model the behaviour of inelastic solids as long as the strains and rotations remain sufficiently small. However, the deformations of solids under loading or imposed displacements can also be large in cases such as ductile fracture, impact and damage analysis, metal forming processes, soil mechanics, etc. This evidence led to development of constitutive laws to model material behaviour beyond the infinitesimal deformation range, both in elastic and plastic domains. Impressed and inspired by the discoveries in the case of the small elastoplastic deformations, one may be attracted to explore the more complex phenomena beyond the range of small deformation. Since most theories of material behaviour (relationship between deformation and stress) are written considering the infinitesimal deformation hypothesis most of the effort concerning the finite deformation range has been the extension of these theories. This extension is not, however, straightforward and it has lead to different opinions, approaches and heated debates in the scientific community. The extension of these theories encounters issues with the stress and strain measures, decomposition of strain in elastic and plastic, the stress rate, observer independent yield function and rotation of material texture.

The expression finite deformations or large deformations is usually associated with problems where differences between the undeformed and deformed state, important geometrical changes, cannot be neglected when considering the behaviour law of the material under analysis. Finite deformation analysis must be considered even for infinitesimal strains if either displacements and rotations are not of that magnitude.

The formulation of elastoplastic constitutive models in the geometrically nonlinear range can be traced back to the late 1950s. Early references to this subject are provided by the pioneering works of Hill [51] and Green and Naghdi [40]. After several decades of

development of the subject including formulations, models and theories for finite elastoplasticity the relevant existing literature is now in abundance. Based upon distinct physical assumptions and starting points multiple constitutive structures exist to address the modeling of finite elastoplasticity.

Finite deformation analysis must take into consideration the complexity due to strong non-linearity in geometry. Such complexity lies not only in the definition of various strain measures but also in their conjugate stress measures (as well as their rates). Therefore, a key issue is then which configuration (reference state or current state) should be used to form the equations that will govern the material's behaviour.

In the case of geomaterials the existing constitutive structures (formulations) can, in general terms, be divided in the following groups: classical Eulerian rate formulations and Lagrangian formulations for the case of elastoplastic models and formulations with unstressed configurations for the case of hyperelastic-based formulations. These constitutive formulations have distinct starting points based on the basic and central concepts concerning a deforming material body including the deformation state, the strained state, the stressed state, the instantaneous changing of deformation state, strain rates, objective rates of Eulerian tensors, etc.

The physical pertinence and simplicity of the specific form of a constitutive function (yield function, flow rule, etc.) would suggest that the most appropriate constitutive variables should be those which can, in a natural and direct manner, characterize and represent the physical essence and feature of the deformation behaviour under consideration.

During early stages of development, hypoelastic-based solutions were subject to intense discussion and debate as was already mentioned. Many controversial issues have arisen ranging from the use of different objective stress rates in the formulation of the constitutive equations to fundamental drawbacks such as the possible lack of objectivity of incremental constitutive laws, the fact that dissipative behaviour may be predicted even within the "elastic domain" and also the observation of oscillatory stress response under monotonic loading [124].

The choice of "appropriate" objective stress rates for the definition of finite plasticity models is not trivial ([63], [70], [69]) and it was though that, no matter what objective rate was chosen, fundamental drawbacks would be present in models defined on a purely *ad hoc* basis. These limitations will be further explained in the next sections.

These drawbacks, mainly the dissipative behaviour within the "elastic domain", led to the development of hyperelastic-based formulations. The main hypothesis underlying the hyperelastic-based constitutive framework is the multiplicative decomposition of the deformation gradient into elastic and plastic contributions. In recent years this approach has become popular even though it is not derived from the direct extension of the small deformation case but motivated by physical considerations, namely in the slip theory of

crystals. Nevertheless, a number of issues have been pointed out and will be discussed further ahead.

3.1 Hypoelastic-based formulations

Truesdell [109] proposed the theory of hypoelasticity which establishes a linear relationship between an objective rate (increment) of the Cauchy (true) stress and the rate (increment) of deformation state via a fourth-order stress-dependent moduli tensor. The classical theory for infinitesimal deformation is established by introducing strain-like variables and their rates and additively separating them in elastic and plastic parts. The infinitesimal strain, $\underline{\underline{\epsilon}}$, and its rate, $\dot{\underline{\underline{\epsilon}}}$, can then be separated as

$$\underline{\underline{\epsilon}} = \underline{\underline{\epsilon}}^e + \underline{\underline{\epsilon}}^p, \quad \dot{\underline{\underline{\epsilon}}} = \dot{\underline{\underline{\epsilon}}}^e + \dot{\underline{\underline{\epsilon}}}^p \tag{3.1}$$

The linear relationship of Truesdell could then be written by considering the generalized Hooke's law of the infinitesimal elasticity in the rate form

$$\dot{\underline{\underline{\sigma}}} = 2\mu\dot{\underline{\underline{\epsilon}}} + \lambda tr(\dot{\underline{\underline{\epsilon}}})\underline{\underline{I}} \tag{3.2}$$

The inelastic response of finitely deformed solids can also be modelled by means of *hypoelastic-based* constitutive theories. The starting point of hypoelastic-based models is the formulation of the constitutive equations for stress in terms of objective stress rates. This formulation type became quite popular in solid mechanics for its ability to easily extend existing constitutive equations for small strains to finite strain analysis. However, hypoelastic-based plasticity models do not usually account for truly reversible behaviour even in the absence of plastic flow (dissipative behaviour may be predicted even within the "elastic domain") despite their simplicity. Also, the formulation of incremental constitutive equations that preserve objectivity (frame-invariance) of the rate (time-continuum) forms is not trivial.

Crucial to the formulation of hypoelastic-based models of plasticity is the definition of objective stress rates. This concept is naturally strongly related to the principle of material objectivity which requires that under a change in observer scalars, vectors and tensors change according to specific relations (see Appendix A).

In order to ensure material objectivity in the formulation of finite strain constitutive laws directly in terms of stress rates it is essential that the constitutive equation for the stress tensor be defined in terms of objective stress rates. Objective stress rates are defined so that the material time derivative of the stress tensor fulfills the principle of objectivity. This definition is, however, somewhat arbitrary which led to the existence of numerous objective stress rates for Eulerian formulations in hypoelasticity since, unlike a Lagrangian tensor quantity, the direct flux of an objective Eulerian tensor quantity is not objective (see Appendix A). The choice of the objective stress rate is not, therefore, unique. Although multiple objective stress rates exist most may be written in the form

$$\underline{\underline{\Lambda}}^{\triangledown} \equiv \dot{\underline{\underline{\Lambda}}} + \underline{\underline{\Lambda}} \cdot \underline{\underline{B}} + \underline{\underline{B}}^{T} \cdot \underline{\underline{\Lambda}} \tag{3.3}$$

where the second-order tensor $\underline{\underline{B}}$ may be supplied by a tensor-valued function of the deformation gradient $\underline{\underline{F}}$ and the velocity gradient $\underline{\underline{L}}$. Two different types of objective rates can be defined: corotational and non-corotational, which are defined by skew symmetric and non-skew symmetric $\underline{\underline{B}}$ ($\underline{\underline{B}}^{T} = -\underline{\underline{B}}$ and $\underline{\underline{B}}^{T} \neq -\underline{\underline{B}}$), respectively.

- Jaumann Stress Rate (corotational)

$$\underline{\underline{\sigma}}^{\triangledown} = \frac{\partial}{\partial t}(\underline{\underline{\sigma}}) - \underline{\underline{W}} \cdot \underline{\underline{\sigma}} + \underline{\underline{\sigma}} \cdot \underline{\underline{W}} \tag{3.4}$$

- Green-McInnis or Green-Naghdi Stress Rate (corotational)

$$\underline{\underline{\sigma}}^{\triangledown} = \frac{\partial}{\partial t}(\underline{\underline{\sigma}}) - \underline{\underline{\Omega}} \cdot \underline{\underline{\sigma}} + \underline{\underline{\sigma}} \cdot \underline{\underline{\Omega}} \tag{3.5}$$

where $\underline{\underline{\Omega}}$ is the angular velocity or rate of rotation tensor defined as

$$\underline{\underline{\Omega}} = \dot{\underline{\underline{R}}} \cdot \underline{\underline{R}}^{T} \tag{3.6}$$

- Cotler-Rivlin or convected Stress Rate (non-corotational)

$$\underline{\underline{\sigma}}^{\triangledown} = \frac{\partial}{\partial t}(\underline{\underline{\sigma}}) + \underline{\underline{L}}^{T} \cdot \underline{\underline{\sigma}} + \underline{\underline{\sigma}} \cdot \underline{\underline{L}} \tag{3.7}$$

- Oldroyd's Stress Rate (non-corotational)

$$\underline{\underline{\sigma}}^{\triangledown} = \frac{\partial}{\partial t}(\underline{\underline{\sigma}}) - \underline{\underline{L}} \cdot \underline{\underline{\sigma}} - \underline{\underline{\sigma}} \cdot \underline{\underline{L}}^{T} \tag{3.8}$$

- Truesdell Stress Rate (non-corotational)

$$\underline{\underline{\sigma}}^{\triangledown} = \frac{\partial}{\partial t}(\underline{\underline{\sigma}}) + \underline{\underline{\sigma}} \cdot tr\underline{\underline{D}} - \underline{\underline{L}} \cdot \underline{\underline{\sigma}} - \underline{\underline{\sigma}} \cdot \underline{\underline{L}}^{T} \tag{3.9}$$

There are substantial differences between between corotational and non-corotational rates. A corotational rate of an objective Eulerian tensor quantity is the conventional time rate of this tensor quantity observed in an associated spinning (rotating) frame and hence preserves the structure of classical Galilean space-time. Because of this property, a corotational rate obeys Leibniz's chain rule for derivatives. However, a non-corotational rate does not: The Galilean space-time structure is distorted and Leibniz's rule is violated. A significant consequence is as follows:

According to a non-corotational rate, the increment of a tensor quantity with changing principal values may vanish, and, in contrast, the vanishing of a corotational rate always renders the principal values of a tensor quantity stationary.

The issue of choice of "proper rates" in hypoelastic formulation has often been treated as a matter of numerical convenience alone rather than being considered that different stress rates define in fact different material models with different responses.

3.2 Hyperelastic-based formulations

The main hypothesis underlying the finite strain elastoplasticity constitutive framework is the multiplicative decomposition of the deformation gradient into elastic and plastic contributions. It is therefore assumed that the deformation gradient can be decomposed as follows

$$\underline{\underline{F}} = \underline{\underline{F}}^{e} \cdot \underline{\underline{F}}^{p} \tag{3.10}$$

where $\underline{\underline{F}}^{e}$ and $\underline{\underline{F}}^{p}$ are respectively named the elastic and plastic deformation gradients. This embodies the assumption of the existence of a local unstressed intermediate configuration defined by the plastic deformation gradient $\underline{\underline{F}}^{p}$. At each material point, the local intermediate configuration is obtained from the fully deformed configuration by a purely elastic unloading (associated with the inverse of $\underline{\underline{F}}^{e}$) of its neighborhood.

The central idea is the notion of local intermediate unstressed configurations at each particle defined by an imaginary destressing process. For now the question as to how the destressing procedure is achieved will be left unexplained.

Once the above separation could unambiguously be established via a destressing procedure, the elastic and plastic parts of the deformation gradient would be separated exactly

from the total elastoplastic deformation and hence endowed with the desired physical features. This would, therefore, allow for $\underline{\underline{F}}^e$ and $\underline{\underline{F}}^p$ to be used as variables which could perform physically pertinent formulations of elastic and plastic behaviour. However, a central issue with the separation is the non-uniqueness in the sense that, if $\underline{\underline{F}}^e$ and $\underline{\underline{F}}^p$ obey the multiplicative decomposition then it must also be true for $\underline{\underline{F}}^e \cdot \underline{\underline{Q}}^T$ and $\underline{\underline{Q}} \cdot \underline{\underline{F}}^p$ for any rotation $\underline{\underline{Q}}$. This means that the rotational parts of $\underline{\underline{F}}^e$ and $\underline{\underline{F}}^p$ and, therefore, $\underline{\underline{R}}^e$ and $\underline{\underline{R}}^p$, would be rendered indeterminate. This non-uniqueness fails to separate the elastic and plastic rotations from the total deformation achieving only a partial separation.

The multiplicative decomposition does, however, allow a very concise and direct formulation of elastic behaviour. The stress may be specified by the single variable $\underline{\underline{F}}^e$ noting the invariance property of elastic moduli in elastoplastic deformations. All the elastic domains correspond to the same elastic potential which means that the elastic behaviour for every elastic domain will be described by the initial elastic domain prior to the occurrence of yielding.

Some aspects and kinematic consequences of the multiplicative decomposition will now be addressed. Following the multiplicative split of $\underline{\underline{F}}$, stretches and rotations associated with the elastic and plastic parts of the deformation gradient can be obtained by polar decomposition.

$$\underline{\underline{F}}^e = \underline{\underline{R}}^e \cdot \underline{\underline{U}}^e = \underline{\underline{V}}^e \cdot \underline{\underline{R}}^e \tag{3.11}$$

as well as

$$\underline{\underline{F}}^p = \underline{\underline{R}}^p \cdot \underline{\underline{U}}^p = \underline{\underline{V}}^p \cdot \underline{\underline{R}}^p \tag{3.12}$$

The meaning of the above tensors is analogous to that of the tensors obtained from the polar decomposition of the total deformation gradient.

Considering now the consequences of the assumed multiplicative split of $\underline{\underline{\mathrm{F}}}$ on the velocity gradient $\underline{\underline{\mathrm{L}}}$, a straightforward differentiation using the product rule gives the following decomposition of $\underline{\underline{\mathrm{L}}}$

$$\underline{\underline{L}} = \underline{\underline{L}}^e + \underline{\underline{F}}^e \cdot \underline{\underline{L}}^p (\underline{\underline{F}}^e)^{-1} \tag{3.13}$$

where

$$\underline{\underline{L}}^e = \dot{\underline{\underline{F}}}^e \cdot (\underline{\underline{F}}^e)^{-1}, \qquad \underline{\underline{L}}^p = \dot{\underline{\underline{F}}}^p \cdot (\underline{\underline{F}}^p)^{-1} \tag{3.14}$$

are named the elastic and plastic velocity gradients. In order to have a physically pertinent formulation for the plastic behaviour (flow) the separation of the rate of deformation and vorticity tensors, $\underline{\underline{D}}$ and $\underline{\underline{W}}$, in elastic and plastic parts is considered. Despite it being obviously possible, this separation has been proved to be not so clear and simple.

$$\begin{aligned} \underline{\underline{D}} &= \underline{\underline{D}}^e + \underline{\underline{V}}^e \cdot \underline{\underline{D}}^p \cdot \underline{\underline{V}}^{e^{-1}}|_S + \underline{\underline{V}}^e \cdot \underline{\underline{W}}^p \cdot \underline{\underline{V}}^{e^{-1}}|_S \\ &= \dot{\underline{\underline{F}}}^e \cdot \underline{\underline{F}}^{e^{-1}}|_S + \underline{\underline{F}}^e \cdot \dot{\underline{\underline{F}}}^p \cdot \underline{\underline{F}}^{p^{-1}} \cdot \underline{\underline{F}}^{e^{-1}} \end{aligned} \tag{3.15}$$

$$\underline{\underline{W}} = \underline{\underline{W}}^e + \underline{\underline{V}}^e \cdot \underline{\underline{D}}^p \cdot \underline{\underline{V}}^{e^{-1}}|_A + \underline{\underline{V}}^e \cdot \underline{\underline{W}}^p \cdot \underline{\underline{V}}^{e^{-1}}|_A \tag{3.16}$$

where $\underline{\underline{D}}^e$, $\underline{\underline{W}}^e$, $\underline{\underline{D}}^p$ and $\underline{\underline{W}}^p$ are the symmetric and antisymmetric parts of $\dot{\underline{\underline{V}}}^e \cdot \underline{\underline{V}}^{e^{-1}}$ and $\underline{\underline{L}}^p$, respectively, and the subscripts S and A denote the symmetric and antisymmetric parts of a tensor. Considering the expression it indicates a very involved coupling of $\underline{\underline{V}}^e$, $\underline{\underline{D}}^p$ and $\underline{\underline{W}}^p$ to produce the total rate of deformation. Also, note that

$$\underline{\underline{D}} \neq \dot{\underline{\underline{F}}}^e \cdot \underline{\underline{F}}^{e^{-1}}|_S + \dot{\underline{\underline{F}}}^p \cdot \underline{\underline{F}}^{p^{-1}}|_S \tag{3.17}$$

Therefore, generally, $\underline{\underline{D}} \neq \underline{\underline{D}}^e + \underline{\underline{D}}^p$. The inequality shown and the non-uniqueness property of the multiplicative decomposition can be resolved to show

$$\dot{\underline{\underline{F}}}^e \cdot \underline{\underline{F}}^{e^{-1}} = \dot{\underline{\underline{V}}}^e \cdot \underline{\underline{V}}^{e^{-1}} + \underline{\underline{V}}^e \cdot \dot{\underline{\underline{R}}}^{e^T} \cdot \dot{\underline{\underline{R}}}^e \cdot \underline{\underline{V}}^{e^{-1}} \tag{3.18}$$

$$\dot{\underline{\underline{F}}}^p \cdot \underline{\underline{F}}^{p^{-1}} = \dot{\underline{\underline{R}}}^p \cdot \underline{\underline{R}}^{p^T} + \underline{\underline{R}}^p \cdot \dot{\underline{\underline{U}}}^p \cdot \underline{\underline{U}}^{p^{-1}} \cdot \underline{\underline{R}}^{p^T} \tag{3.19}$$

where each rate term in the equation of $\underline{\underline{D}}$ is essentially dependent on either the elastic rotation $\underline{\underline{R}}^e$, or the plastic rotation $\underline{\underline{R}}^p$, or both. This means that additional assumptions must be taken. One possible assumption is to consider that

$$\underline{\underline{F}}^{e^T} = \underline{\underline{F}}^e \tag{3.20}$$

where this extra condition when in addition to defining elastic and plastic deformation rates as

$$\underline{\underline{D}}^e = \underline{\underline{\Lambda}}^{-1} : (\dot{\underline{\underline{B}}}^e + \underline{\underline{B}}^e \cdot \underline{\underline{W}} - \underline{\underline{W}} \cdot \underline{\underline{B}}^e), \quad \underline{\underline{D}}^p = \underline{\underline{\Lambda}}^{-1} : (2\underline{\underline{V}}^e \cdot \dot{\underline{\underline{F}}}^p \cdot \underline{\underline{F}}^{p^{-1}}|_S \, \underline{\underline{V}}^e) \tag{3.21}$$

with $\underline{\underline{\Lambda}}$ a fourth order tensor given by

$$\Lambda_{ijkl} = B^e_{ik}\delta_{jl} + B^e_{jl}\delta_{ik} \tag{3.22}$$

and $\underline{\underline{B}}$ the left extension tensor of Cauchy-Green, allows the reestablishment of the separation of the rate of deformation tensor.

Partial conclusions

The multiplicative decomposition of the deformation gradient tensor is intended for physically pertinent formulations of elastoplasticity considering an imaginary unstressed configuration from an also imaginary process of destressing the deformed state at every instant. Having a well defined $\underline{\underline{F}}^e$ a decoupled formulation is available for dissipationless elastic behaviour derivable from a potential function.

The issue with the non-uniqueness property of the multiplicative decomposition of $\underline{\underline{F}}$ might mean that its not only indeterminate in a mathematical sense but also in a physical sense due to its inability to detach elastic from plastic deformations. This fact, as pointed out by Naghdi [85], represents the inability of a constitutive formulation based in this decomposition, without any further assumptions (usually of an ad hoc nature), to fulfill the objectivity requirement.

Finally, the separation of the rate of deformation tensor, in elastic and plastic parts, in terms of the deformation tensor is not trivial without the consideration of additional assumptions. These assumptions can be of various forms the one presented above being a single example of various existing possibilities (such as $\underline{\underline{F}}^{e^T} = \underline{\underline{F}}^e$ or $\underline{\underline{F}}^p = \dot{\underline{\underline{F}}}^p \cdot \underline{\underline{F}}^{p^{-1}}|_S = \underline{\underline{0}}$ or even simply $\underline{\underline{V}}^e = \underline{\underline{I}}$) which would, in turn, give different kinematic formulations for $\underline{\underline{D}}$. This means that even the elastic strain rate cannot be defined in a unique manner. In addition to those already indicated, there are many other possibilities for modifying variables at the constitutive formulations such as the yield function, flow rule, hardening rule, etc. To sum up, whether $\underline{\underline{F}}^e$ and $\underline{\underline{F}}^p$ can be well defined is of fundamental importance.

3.3 Elastoplastic Eulerian formulation for finite strains

The first effort of elastoplastic behaviour at finite deformations led to an Eulerian rate type (hypoelastic) theory based on the true stress and the natural deformation rate (stretching) representing a simple and direct extension of the Prandtl-Reuβ theory. In finite deformation, the natural deformation rate with flow-like characteristics is $\underline{\underline{D}}$ leading to a direct extension of the separation in infinitesimal strain. The rate of deformation $\underline{\underline{\mathrm{D}}}$ tensor can then be separated in two parts because of its linear expression with the velocity gradient.

$$\underline{\underline{D}} = \underline{\underline{D}}^e + \underline{\underline{D}}^p \tag{3.23}$$

In the previous expression $\underline{\underline{D}}^e$ and $\underline{\underline{D}}^p$ are called elastic and plastic stretching respectively and represent the instantaneous elastic and plastic deformation increments over an infinitesimal time interval, each being referred to the current configuration. The pair $\underline{\underline{D}}^e$ and $\underline{\underline{D}}^p$ may be regarded to represent the recoverable and irrecoverable parts of the total stress work increment.

Note that in this connection no attempt is made to separate the deformation gradient $\underline{\underline{F}}$ into the elastic and plastic parts. $\underline{\underline{F}}$ does not play a role at all in this formulation. This separation is an independent starting point of the rate-type formulation for finite strains

as well as for infinitesimal strains.

As a fundamental kinematic quantity, the stretching $\underline{\underline{D}}$ offers a direct natural measure of the rate of length change in any line element and the rate of change of the angle between any two intersecting line elements in the deforming body [33].

An essential difference emerges when extending the linear relationship of Truesdell from infinitesimal strains to finite strains. As was already mentioned, the direct flux of an objective Eulerian tensor quantity is not objective and therefore an objective rate (increment) will be required, more specifically there is a need to define an objective rate of the Cauchy (true) stress. The general form of the simplest of hypoelastic relations, a direct objective extension of infinitesimal strain theory, can be defined as

$$\underline{\underline{\sigma}}^{\nabla} = f(\underline{\underline{D}}^{e}) \tag{3.24}$$

While the previous equation would at first appear to be rather general in form it is noted that the behaviour of $\underline{\underline{\sigma}}^{\nabla}$ and $\underline{\underline{D}}$ under superposed rigid-body motion restricts the constitutive equation f to be an isotropic tensor function in $\underline{\underline{D}}$ due to the objectivity requirement.

The simplest hypoelastic equation (grade zero) to finite deformation can be defined as

$$\underline{\underline{\sigma}}^{\nabla} = 2\mu\underline{\underline{D}}^{e} + \lambda tr(\underline{\underline{D}}^{e})\underline{\underline{I}} \tag{3.25}$$

Yield function and flow rule [23]

As a starting point in this formulation it is postulated that the evolution of the stress tensor is governed by a constitutive law of the form

$$\underline{\underline{\sigma}}^{\nabla} = \underline{\underline{\underline{\underline{E}}}}^{e} : (\underline{\underline{D}} - \underline{\underline{D}}^{p}) \tag{3.26}$$

where $\underline{\underline{\sigma}}^{\nabla}$ denotes some objective stress rate and $\underline{\underline{\underline{\underline{E}}}}^{e}$ is some suitable defined tangential elasticity operator. The above equation is complemented by a constitutive law for $\underline{\underline{D}}^{p}$ known as a flow rule normally stated as

$$\underline{\underline{D}}^{p} = \dot{\gamma} \cdot \frac{\partial \Psi}{\partial \underline{\underline{\sigma}}} \tag{3.27}$$

where $\dot{\gamma}$ is the plastic multiplier and $\Psi(\underline{\underline{\sigma}}, \underline{\underline{\alpha}})$ is a flow potential, with $\underline{\underline{\alpha}}$ denoting a set of internal variables whose evolution is governed by

$$\dot{\underline{\underline{\alpha}}} = \dot{\gamma} \cdot \underline{\underline{\underline{\underline{H}}}}(\underline{\underline{\sigma}}, \underline{\underline{\alpha}}) \tag{3.28}$$

where $\underline{\underline{\underline{\underline{H}}}}$ is a given evolution function. Lastly, the plastic multiplier $\dot{\gamma}$ defines the load/unloading criteria through the usual complementarity condition

$$f \leq 0, \quad \dot{\gamma} \geq 0, \quad f \cdot \dot{\gamma} = 0 \tag{3.29}$$

with $f(\underline{\underline{\sigma}}, \underline{\underline{\alpha}})$ denoting a yield function.

Finally the consistency condition is defined

$$\dot{f} = 0 \tag{3.30}$$

Finite deformation elastoplasticity based on the Jaumann stress rate

(valid for all corotational stress rates)

This model has been widely used to extend conventional isotropic infinitesimal plasticity models to the finite strain range. Its basic rate evolution law for stress is the following

$$\underline{\underline{\sigma}}^{\nabla} = \underline{\underline{\underline{\underline{E}}}}^{e} : (\underline{\underline{D}} - \underline{\underline{D}}^{p}) \tag{3.31}$$

where

$$\underline{\underline{\underline{\underline{E}}}}^{e} \equiv 2\,G\,\underline{\underline{\underline{\underline{I_S}}}} + (K - \frac{2}{3}\,G)\,\underline{\underline{I}} \otimes \underline{\underline{I}} \tag{3.32}$$

where $\underline{\underline{\underline{\underline{I}}}}$ the fourth-order identity tensor with $\underline{\underline{\underline{\underline{I_S}}}}$ being its symmetric part and G and K constant coefficients.

1. The "Elastic" range ($\underline{\underline{D}}^{p} = \underline{\underline{0}}$)

$$\underline{\underline{\sigma}}^{\nabla} = \underline{\underline{\underline{\underline{E}}}}^{e} : \underline{\underline{D}} \tag{3.33}$$

2. The "Plastic" range

Analogously to the rate form of infinitesimal plasticity, the stress rate equation is reduced under plastic flow to

$$\underline{\underline{\sigma}}^{\nabla} = \underline{\underline{\underline{\underline{E}}}}^{ep} : \underline{\underline{D}} \tag{3.34}$$

where $\underline{\underline{\underline{\underline{E}}}}^{ep}$ is the elastoplastic tangent operator which, when considering a corotational stress rate, has exactly the same format as the elastoplastic (continuum) tangent operator

for the infinitesimal plasticity model.

Considering the consistency equation this deduction starts by taking the time derivative of the yield function f

$$\begin{aligned}
\dot{f} &= \frac{\partial f}{\partial \underline{\underline{\sigma}}} : \dot{\underline{\underline{\sigma}}} + \frac{\partial f}{\partial \underline{\underline{\alpha}}} \cdot \dot{\underline{\underline{\alpha}}} \\
&= \frac{\partial f}{\partial \underline{\underline{\sigma}}} : (\underline{\underline{\sigma}}^{\nabla} + \underline{\underline{W}} \cdot \underline{\underline{\sigma}} - \underline{\underline{\sigma}} \cdot \underline{\underline{W}}) + \frac{\partial f}{\partial \underline{\underline{\alpha}}} \cdot \dot{\underline{\underline{\alpha}}} \\
&= \frac{\partial f}{\partial \underline{\underline{\sigma}}} : [\underline{\underline{\underline{\underline{E}}}}^e : (\underline{\underline{D}} - \dot{\gamma} \cdot \frac{\partial \Psi}{\partial \underline{\underline{\sigma}}}) + \underline{\underline{W}} \cdot \underline{\underline{\sigma}} - \underline{\underline{\sigma}} \cdot \underline{\underline{W}}] + \dot{\gamma} \cdot \frac{\partial f}{\partial \underline{\underline{\alpha}}} \cdot \underline{\underline{\underline{\underline{H}}}}(\underline{\underline{\sigma}}, \underline{\underline{\alpha}})
\end{aligned} \tag{3.35}$$

The above equation can be simplified by considering the symmetry of $\underline{\underline{\sigma}}$ and $\frac{\partial f}{\partial \underline{\underline{\sigma}}}$ and the skew symmetry of $\underline{\underline{W}}$ (and $\underline{\underline{\Omega}}$)

$$\begin{aligned}
\frac{\partial f}{\partial \underline{\underline{\sigma}}} : (\underline{\underline{W}} \cdot \underline{\underline{\sigma}} - \underline{\underline{\sigma}} \cdot \underline{\underline{W}}) &= \frac{\partial f}{\partial \underline{\underline{\sigma}}} : [(\underline{\underline{W}} \cdot \underline{\underline{\sigma}})^T - \underline{\underline{\sigma}} \cdot \underline{\underline{W}}] \\
&= -2 \frac{\partial f}{\partial \underline{\underline{\sigma}}} : (\underline{\underline{\sigma}} \cdot \underline{\underline{W}}) \\
&= -2 \quad (\underline{\underline{\sigma}} \cdot \frac{\partial f}{\partial \underline{\underline{\sigma}}}) : (\underline{\underline{W}})
\end{aligned} \tag{3.36}$$

Also, due to the isotropy of the model $\underline{\underline{\sigma}}$ and $\frac{\partial f}{\partial \underline{\underline{\sigma}}}$ commute and their product remains symmetric leading to

$$\frac{\partial f}{\partial \underline{\underline{\sigma}}} : (\underline{\underline{W}} \cdot \underline{\underline{\sigma}} - \underline{\underline{\sigma}} \cdot \underline{\underline{W}}) = 0 \tag{3.37}$$

which replaced in the original equation results in the following formula for f

$$\dot{f} = \frac{\partial f}{\partial \underline{\underline{\sigma}}} : \underline{\underline{\underline{\underline{E}}}}^e : (\underline{\underline{D}} - \dot{\gamma} \cdot \frac{\partial \Psi}{\partial \underline{\underline{\sigma}}}) + \dot{\gamma} \cdot \frac{\partial f}{\partial \underline{\underline{\alpha}}} : \underline{\underline{\underline{\underline{H}}}}(\underline{\underline{\sigma}}, \underline{\underline{\alpha}}) \tag{3.38}$$

The above equation has an identical format to that of the infinitesimal deformation theory. By equating the expression to zero (consistency condition) the general expression for the plastic multiplier $\dot{\gamma}$ is obtained

$$\dot{\gamma} = \frac{\partial f / \partial \underline{\underline{\sigma}} \; : \; \underline{\underline{\underline{\underline{E}}}}^e : \underline{\underline{D}}}{\partial f / \partial \underline{\underline{\sigma}} \; : \; \underline{\underline{\underline{\underline{E}}}}^e : \partial \Psi / \partial \underline{\underline{\sigma}} - \partial f / \partial \underline{\underline{\alpha}} : \underline{\underline{\underline{\underline{H}}}}} \tag{3.39}$$

Replacing in the original equation leads to

$$\underline{\underline{\underline{\underline{E}}}}^{ep} = \underline{\underline{\underline{\underline{E}}}}^{e} - \frac{(\underline{\underline{\underline{\underline{E}}}}^{e} : \partial\Psi/\partial\underline{\underline{\sigma}}) \otimes (\underline{\underline{\underline{\underline{E}}}}^{e} : \partial f/\partial\underline{\underline{\sigma}})}{\partial f/\partial\underline{\underline{\sigma}} : \underline{\underline{\underline{\underline{E}}}}^{e} : \partial\Psi/\partial\underline{\underline{\sigma}} - \partial f/\partial\underline{\underline{\alpha}} \cdot \underline{\underline{\underline{\underline{H}}}}} \tag{3.40}$$

which has the format of its small strain counterpart. Note that the small strain format is a direct consequence of the identity $\frac{\partial f}{\partial \underline{\underline{\sigma}}} : (\underline{\underline{W}} \cdot \underline{\underline{\sigma}} - \underline{\underline{\sigma}} \cdot \underline{\underline{W}}) = 0$. It will hold whenever the difference between the material derivative of the stress and the corresponding objective rate comprises only of terms with products between the stress and a skew symmetric tensor (corotational rates).

Partial conclusions

An Eulerian formulation has a direct physical pertinence, conceptual clarity and structural simplicity. These advantages may lead to an efficient numerical treatment with finite element codes. However, the issue of how to select suitable rates for the hypoelastic formulation arises since the objectivity requirement becomes far from being trivial. Multiple studies have been done specially dedicated to this purpose considering the five "classical" stress rates: Jaumann, Green-McInnis or Green-Naghdi, Cotler-Rivlin, Oldroyd's and Truesdell stress rates. Also, troublesome non-uniqueness and multiplicity of the separation of $\underline{\underline{D}}$ would persist in the presence of infinitely many possible objective rates implying too many different characterizations of the elastic stretching $\underline{\underline{D}}^e$ for the recoverable energy part (elastic).

The former problems/conditions have to be fulfilled so that the composite structure of the constitutive formulations of $\underline{\underline{D}}^e$ and $\underline{\underline{D}}^p$ as well as the evolution of the stress and the back stress are free of possible inconsistency and contradiction. For the latter, Prager's criterion must be satisfied as well. The yielding stationarity which was first pointed out by Prager which can be defined by the corollary: "The simultaneous vanishing of the stress rate, back stress and hardening parameters should render the yield function stationary". This requirement has been accepted to be basic by many researchers that if violated inconsistency or contradiction would be incurred as an unavoidable consequence. Prager's criterion in a general sense implies that "the definitions of the stress rate and the back stress should be the same and corotational". Prager latter demonstrated that of the "classical" stress rates only the Zaremba-Jaumann rate would be admissible. However, the most popular named Jaumann stress rate has been dismissed in recent years due to showing spurious phenomena known as shear oscillations even when considering elastic simple shear. Since the inappropriateness of the Jaumann stress rate to rate-form constitutive models was recognized, considerable efforts were made to deal with the problem with choosing an appropriate objective stress rate. However, most other stress rates were simply introduced to replace the Jaumann stress rate and, although instructive and instrumental in some cases, conclusions in this respect were drawn merely from non-oscillatory shear stress responses to the simple shearing.

The above discoveries may suggest that the foundation of this formulation might not be so secure and sound in spite of the fact that the composite structure of classical Eulerian elastoplasticity is composed of many basic constituents and that it does not appear easy to identify its deficiencies. Also, yet another unexpected finding was made by Simo and Pister [107] who demonstrated that the hypoelastic rate equation fails to be exactly integrable and, therefore, self-inconsistent since a non-integrable hypoelastic formulation is path-dependent and dissipative, deviating from the notion of recoverable elastic-like behaviour. It should be noted, however, that such inconsistencies remain negligible where elastic strains are small but pose serious limitations where elastic deformations become considerable. Finally there is also a restriction to initial isotropic behaviour.

Due to the non-uniqueness and multiplicity of the separation of $\underline{\underline{D}}$, the shear oscillation phenomena and the non-integrability issue, the *ad hoc* nature of the separation for finite deformations was questionable on the fundamental ground for the inherent consistency of the composite structure of the constitutive formulation. Considering "small" elastic deformations with this formulation and notwithstanding the deficiencies already pointed out, using the "most common" stress rates would be adequate and reasonable as long as the elastic deformation, strain and rotation, remain small. However, whenever the yielding sets in, therefore, presence of plastic flow, non linear effects can play an important role even at small strains. Also, recent studies show that there is a monotone accumulation effect of residual stresses (errors) with a simple deformation cycle. In spite the fact that this error might be acceptable for the first cycle it rapidly magnifies itself with the increasing of cycle number to unacceptable values.

The present pessimistic description might discourage further developments on the classical Eulerian rate theory. Nonetheless, its direct physical pertinence, conceptual clarity and simplicity in structure are impressive. The following section will address this issue.

3.3.1 Logarithmic stress rate

As was pointed out before, with the use of Truesdell's hypoelastic relation arises the integrability issue. A consistent Eulerian formulation by Xiao et al. [122] has been proposed based upon two consistency criteria, yielding stationarity and elastic integrability, which avoid the serious problems of inconsistency accompanied by arbitrariness, uncertainty and limitations of the previous stress rate attempts ([123], [11], [78], [84]).

The first consistency criteria has already been discussed in the form of Prager's criterion. It should be noted, despite the issues with the Jaumann stress rate ,that the applicability of this criterion to Eulerian rate formulations of finite plasticity is universal.

The second consistency criteria consists in the complete integrability of elastic behaviour. This means the establishment of a self-consistent elastic rate formulation where $\underline{\underline{D}}^e$ can characterize recoverable elastic behaviour. It has been shown by Simo and Pister [107] that the Eulerian rate equation of hypoelastic type yields the integrability issue which relies on the definition of the stress rate. This means that the criterion of elastic integra-

bility, introduced by Bruhns et al. [10], namely "For every process of elastic deformations with $\underline{\underline{D}} = \underline{\underline{D}}^e$, the rate equation should be exactly integrable to deliver a dissipationless elastic relation and hence really characterize recoverable elastic behaviour", is not verified.

Finally, the uniqueness property of the logarithmic rate in the above solutions. Recently it has been demonstrated that there is one and only one choice for the stress rate such that the elastic equation satisfies the integrability criterion. Obviously, from the definition of objective corotational stress rates, if the definition of the stress rate is unique so is the spin tensor by which it is defined. These are respectively the logarithmic stress rate and logarithmic spin tensor [124].

The separation of $\underline{\underline{D}}$ is now taken as an independent starting-point. Considering that, as said before, $\underline{\underline{D}}$ is solely related to the ever-changing current configuration, $\underline{\underline{D}}^e$ and $\underline{\underline{D}}^p$ need not be related to any "elastic" or "plastic" deformation quantities relative to either a fixed referential or a changing intermediate configuration. To sum up, consistent constitutive formulations should be established where $\underline{\underline{D}}^e$ is indeed elastic (recoverable) while $\underline{\underline{D}}^p$ is is definitely plastic-like (dissipative).
The elastic rate equation of grade zero will be written as

$$\underline{\underline{\sigma}}^{log} = 2\mu\underline{\underline{D}}^e + \lambda tr(\underline{\underline{D}}^e)\underline{\underline{I}} \tag{3.41}$$

where $\underline{\underline{\sigma}}^{log}$ is the logarithmic stress rate defined as

$$\underline{\underline{\sigma}}^{log} = \frac{\partial}{\partial t}(\underline{\underline{\sigma}}) - \underline{\underline{\Omega}}^{log} \cdot \underline{\underline{\sigma}} + \underline{\underline{\sigma}} \cdot \underline{\underline{\Omega}}^{log} \tag{3.42}$$

where $\underline{\underline{\Omega}}^{log}$ is the logarithmic spin tensor.
Its defining equation is such that

$$\underline{\underline{D}} = (ln\underline{\underline{V}})^{\cdot} - \underline{\underline{\Omega}}^{log} \cdot ln\underline{\underline{V}} + (ln\underline{\underline{V}}) \cdot \underline{\underline{\Omega}}^{log} = (ln\underline{\underline{V}})^{log} \tag{3.43}$$

Thus it is remarkable that, by considering the logarithmic stress rate, it can be rewritten as

$$(ln\underline{\underline{V}})^{log} = \underline{\underline{D}}, \tag{3.44}$$

and moreover it is found that the solution for the hypoelastic equation considering the logarithmic stress rate considering the initial condition $\underline{\underline{\sigma}} = \underline{\underline{0}}$

$$\underline{\underline{\sigma}}^{log} = 2\mu\underline{\underline{D}}^e + \lambda tr(\underline{\underline{D}}^e)\underline{\underline{I}} \tag{3.45}$$

can be written as

$$\underline{\underline{\sigma}} = 2\mu\, ln\underline{\underline{V}} + \lambda tr(ln\underline{\underline{V}})\underline{\underline{I}} \tag{3.46}$$

In this equation, and as it has been demonstrated by Xiao et al. [122], the Cauchy stress and the logarithmic strain can form a conjugate pair of stress and strain.

Now returning to the definition of the logarithmic stress tensor, an explicit basis-free expression of the "log-spin" $\underline{\underline{\Omega}}^{log}$ in terms of $\underline{\underline{D}}$, $\underline{\underline{W}}$ and $\underline{\underline{B}}$ is as follows

$$\underline{\underline{\Omega}}^{log} = \underline{\underline{W}} + \underline{\underline{N}}^{log} \tag{3.47}$$

where $\underline{\underline{N}}^{log} = \begin{cases} 0 & \text{if } b_1 = b_2 = b_3 \\ v\,[\underline{\underline{B}} \cdot \underline{\underline{D}}] & \text{if } b_1 \neq b_2 = b_3 \\ v_1\,[\underline{\underline{B}} \cdot \underline{\underline{D}}] + v_2\,[\underline{\underline{B}}^2 \cdot \underline{\underline{D}}] + v_3\,[\underline{\underline{B}}^2 \cdot \underline{\underline{D}} \cdot \underline{\underline{B}}] & \text{if } b_1 \neq b_2 \neq b_3 \end{cases}$

in which $\underline{\underline{B}} = \underline{\underline{V}}^2$ is the left Cauchy-Green tensor and $b_i = \lambda_i^2$, i=1,2,3 are its eigenvalues. The bracket is defined here by

$$[\underline{\underline{B}}^r \cdot \underline{\underline{D}} \cdot \underline{\underline{B}}^s] = \underline{\underline{B}}^r \cdot \underline{\underline{D}} \cdot \underline{\underline{B}}^s - \underline{\underline{B}}^s \cdot \underline{\underline{D}} \cdot \underline{\underline{B}}^r \tag{3.48}$$

The other parameters in the equation are here defined as

$$v = \frac{1}{b_1 - b_2}\left(\frac{1 + b_1/b_2}{1 - b_1/b_2} + \frac{2}{lnb_1/b_2}\right), \tag{3.49}$$

$$v_k = -\frac{1}{\Delta}\sum_{i=1}^{3}(-b_i)^{3-k}\left(\frac{1+\epsilon_i}{1-\epsilon_i} + \frac{2}{ln\epsilon_i}\right), k = 1, 2, 3 \tag{3.50}$$

$$\Delta = (b_1 - b_2)(b_2 - b_3)(b_3 - b_1), \tag{3.51}$$

$$\epsilon_1 = \frac{b_2}{b_3}, \quad \epsilon_2 = \frac{b_3}{b_1}, \quad \epsilon_3 = \frac{b_1}{b_2} \tag{3.52}$$

It should be pointed out that the antisymmetric tensor $\underline{\underline{N}}^{log}$ is a particular form of the general skewsymmetric tensor derived by Dafalias [18] in the investigation of the plastic spin. Also, from the above one can notice that the explicit basis-free expressions presented enable us to determine the log-spin $\underline{\underline{\Omega}}^{log}$ directly using the deformation gradient $\underline{\underline{F}}$ given under any coordinate system.

It can be shown that not only the simple shear response but all possible responses of the hypoelastic model based on the log-rate agree with those of the finite deformation isotropic elastic model by the grade zero elastic rate equation. Also, the phenomenon known as hypoelastic yield at the simple shear deformation can be predicted using the hypoelastic model considering the log-rate.

The approach considering the logarithmic stress rate never attempts to separate the total elastoplastic deformation $\underline{\underline{F}}$ and therefore returning to the basic idea of the earlier Eulerian rate formulation employing physical pertinent quantities. The resultant constitutive formulation might not only be physically pertinent but also endowed with a simple structure.

Thus arises a possible solution for the dilemma. The existing dilemma being how to attain a consistent, physically pertinent formulation of finite elastoplasticity considering the inherent inseparability of the total elastoplastic deformation as a physical entity since a proper definition of elastic behaviour is unavoidably linked with an elastic or plastic deformation-like variable. However, the introduction of an additional variable associated with an unstressed state can not be separated out of the total elastoplastic deformation in principle for it would force it to be considered only as a formal parametric variable. This might, however, lead to a formal mathematical formulation not so close to physical reality but also might not meet the basic requirement for a complete, testable physical theory.

The essence behind the uniqueness of choice for the stress rate and back stress rate to be the logarithmic rate is a also unique, intrinsic relationship between Hencky's natural strain and the natural deformation rate. The kinematical relationship can be expressed as

$$\underline{\underline{D}} = \underline{\underline{h}}^{log} = \dot{\underline{\underline{h}}} + \underline{\underline{h}} \cdot \underline{\underline{\Omega}}^{log} - \underline{\underline{\Omega}}^{log} \cdot \underline{\underline{h}} \tag{3.53}$$

It is the above unique, intrinsic relationship between the natural strain $\underline{\underline{\mathrm{h}}}$ and the natural deformation rate $\underline{\underline{\mathrm{D}}}$ that ensures the foregoing natural, consistent combination of hypoelasticity and hyperelasticity and thus endows the traditional Eulerian rate theory of finite elastoplasticity with a self-consistent composite structure, both in a unique, intrinsic sense.

3.4 Elastoplastic Lagrangian formulation for finite strains

As has been said the rate-type formulation is a direct generalization of the incremental small-strain elastoplasticity to large strains. In a Lagrangian formulation the classical conjugate pair of stress and strain are the 2^{nd} Piola-Kirchhoff stress tensor and the Green-Lagrange strain tensor. One of the practical characteristics of these tensors is their frame indifference, i.e., their invariability when considering rigid-body motion.

Towards an extension of classical small deformation theory to finite deformations, a perhaps more direct and simpler idea is to use a finite strain measure and its conjugate stress. However, the decomposition of the deformation tensor or that of its rate is unfortunately not possible in finite deformations unless for very particular cases

$$\underline{\underline{E}} \neq \underline{\underline{E}}^e + \underline{\underline{E}}^p, \quad \dot{\underline{\underline{E}}} \neq \dot{\underline{\underline{E}}}^e + \dot{\underline{\underline{E}}}^p \tag{3.54}$$

This can easily be seen by considering the strain-displacement relation

$$\underline{\underline{E}} = \frac{1}{2}(\underline{\underline{C}} - \underline{\underline{I}}) = \frac{1}{2}(\nabla \underline{u} + \nabla \underline{u}^T + \nabla \underline{u}^T \cdot \nabla \underline{u}) \tag{3.55}$$

which cannot be separated into the sum of two parts due to the nonlinear terms in the displacement gradient.

On account to the complexity, ambiguity and difficulties involved in defining the notion of plastic strain, Green and Naghdi [41] introduced a strain-like variable of Lagrangian type, called plastic strain and denoted $\underline{\underline{E}}^p$. Well understanding the limited applicability of the additive separation of $\underline{\underline{E}}$ the difference $\underline{\underline{E}} - \underline{\underline{E}}^p$ was not interpreted as an elastic strain but as an alternative convenient variable used for well-motivated purposes.

Partial conclusions

In a Lagrangian formulation the basic idea is to use the Green-Lagrange strain tensor and an additional plastic strain (metric) to formulate elastic and plastic behaviour. Since it is expressed in terms of Lagrangian constitutive variables the objectivity principle is automatically fulfilled. However, the 2^{nd} Piola-Kirchoff stress tensor does not have so clear physical meaning as the Cauchy (true) stress tensor. The use the total strain $\underline{\underline{E}}$ and the plastic strain $\underline{\underline{E}}^p$ as primitive variables results that the constitutive formulation will tend to assume a general mathematical form which might deviate somewhat from the physical pertinence to the incremental essence of the flow-like characteristic of elastoplastic behaviour. This is because the finite deformation referred to any fixed "preferred" state should not play a basic role in the physical mechanisms. There is then a lack of the directly physical pertinence which might not tend towards formulation physical facts in a simple manner.

There is not, however, a restriction on the type of initial material symmetry and also the integrability issue involved in Eulerian formulations is irrelevant for the elastic formulation is already dissipationless. Although Lagrangian formulation cannot be considered incorrect, since it is fully justified from a mathematical point of view whereas only the direct pertinence to the physical reality is being criticized.

3.5 Numerical Integration

In finite deformation analysis, due to important geometrical changes in the material's configuration, the constitutive equation is normally expressed as a relation between some

objective stress rate and the rate of deformation tensor. Another aspect of the integration of rate constitutive equations is verifying the material constitutive laws and incremental plastic consistency conditions. For large deformation analysis, the return mapping algorithm schemes should be applied consistently with the integration algorithm to correct the stress for rigid body motion.

The standard integration schemes ([108] [107]) used in small deformation analysis can be used in the finite deformation if additional corrections and parameters are made or added to it. This section will address the issues of stress transformation for large strain analysis, to ensure objectivity of the respective rate and the "location" of this transformation respective of the return mapping algorithm.

The stress transformation for rigid body motion considering stress rates is done in a rather simple fashion. Generally it can be written that, for any objective stress rate, the stress transformation is done by performing the following steps.

1. Enter with current stresses $\underline{\underline{\sigma}}$, stress rate $\dot{\underline{\underline{\sigma}}}$, the deformation gradient $\underline{\underline{F}}$ and the velocity gradient tensor $\underline{\underline{L}}$ as initial values

2. Compute $\underline{\underline{\sigma}}^{\nabla}$ by

$$\underline{\underline{\sigma}}^{\nabla} = \dot{\underline{\underline{\sigma}}} + \underline{\underline{\sigma}} \cdot \underline{\underline{\Omega}} + \underline{\underline{\Omega}}^{T} \cdot \underline{\underline{\sigma}} \tag{3.56}$$

   where the second-order tensor $\underline{\underline{\Omega}}$ may be supplied by a tensor-valued function of the deformation gradient $\underline{\underline{F}}$ and the velocity gradient $\underline{\underline{L}}$ according to different equations depending on the stress rate to be considered.

3. Exit with the corrected stress increment $\underline{\underline{\sigma}}^{\nabla}$

The return mapping algorithm is a fairly common and well-known numerical tool used to satisfy material constitutive relations and incremental plastic consistency requirements. Generally it is composed of an elastic predictor which obtains the stresses at the end of the increment from the use of the elastic stress-strain relations, followed by a mapping of the obtained stresses onto a suitably updated yield surface and therefore restoring plastic consistency. In finite deformation the constitutive relation is not the same as for small strain analysis but the elastic predictor may still be determined, and used, assuming that the deformation in the current increment is completely elastic. The important issue in large deformation analysis is whether the return mapping should be performed before or after the stress transformation. The motion is, therefore, considered to be decomposed in two steps: a rigid body motion and a second one where only straining takes place. If the return mapping is performed before the stress transformation the plastic consistency is maintained after the transformation. However, performing it before results that the "elastic" stress increments include the incremental stress due to proper transformation, which means taking into account the change in configuration. If the return mapping is performed after the stress transformation an additional numerical step is required to keep the final stress plastically consistent, i.e., on the yield surface. These numerical procedures

are hereafter adapted from [37] and [86]

Transformation before return mapping

1. Enter with the current stresses $\underline{\underline{\sigma}}$, the deformation gradient $\underline{\underline{F}}$ and the velocity gradient tensor $\underline{\underline{L}}$ as initial values
2. Call the stress transformation (presented before in equation 3.56) and determine the corrected stress increment $\underline{\underline{\sigma}}^{\nabla}$ where $\underline{\underline{\dot{\sigma}}}$ is determined considering the increment totally elastic
3. Perform the stress integration resorting to the constitutive relations and the corresponding return mapping algorithm, if necessary
4. Exit with final stresses $\underline{\underline{\sigma}}$

Transformation after return mapping

1. Enter with the current stresses $\underline{\underline{\sigma}}$, the deformation gradient $\underline{\underline{F}}$ and the velocity gradient tensor $\underline{\underline{L}}$ as initial values
2. Perform the stress integration resorting to the constitutive relations and the corresponding return mapping algorithm, if necessary, and determine $\underline{\underline{\dot{\sigma}}}$
3. Call the stress transformation presented before in equation 3.56 and determine the corrected stress increment $\underline{\underline{\sigma}}^{\nabla}$
4. Exit with final stresses $\underline{\underline{\sigma}}$

[86] found that, in terms of accuracy, applying before or after the stress transformation leads more or less to the same results. However, in terms of computational efficiency, it is preferable to apply the correction before the integration.

Finally, the numerical treatment of $\underline{\underline{D}}$ is addressed. The tensor $\underline{\underline{D}}$ is objective if it transforms in a proper tensorial manner under a superimposed rigid body rotation. The objectivity of $\underline{\underline{D}}$ means that under finite incremental step, its components will be independent of any rigid body rotation. It is noted that an analytical calculation of $\underline{\underline{D}}$ will always produce null values for superimposed rigid body rotations. In numerical treatments, however, and since time discretization schemes are used, the analytical case is not necessarily verified and $\underline{\underline{D}}$ may no longer be objective. Therefore, the use of conventional forward difference methods in such analyses may only achieve objectivity when the time steps are very small and it may lead to excessive error accumulation in practice.
Gadala and Wang [37] then propose the inclusion of an additional modification term to be applied to the definition of $\underline{\underline{D}}$ in 2-dimensional problems in order to ensure the objectivity of the latter for arbitrary values of the time step. This would take the form of

$$D_{ij} = \frac{1}{2}\left(\frac{\partial v_i}{\partial x_j} + \frac{\partial v_j}{\partial x_i}\right) - \delta_{ij} m \tag{3.57}$$

where m is the modification term given by

$$m = \frac{\sqrt{1 - (W_{12}\Delta t)^2} - 1}{\Delta t} \tag{3.58}$$

The above modification, according to the authors, coupled with the forward difference scheme may be applied in explicit as well as implicit integration procedures. It can also be employed in various material models where the rate of deformation tensor is used for expressing the constitutive relation.

3.6 Summary

This Chapter was concerned with the mechanical formulation in finite deformations. Various formulations were presented each being described and detailed concerning its advantages and disadvantages as well as its range of validity.

In Appendix B results for the different stress rates are presented considering a simple shear test as well as deformation cycles in hypoelasticity. These serve to show the properties already described previously of the different stress rates, and their respective spin tensors, in both monotonic and cyclic loading scenarios.

The interested reader can find a more complete coverage of this topic in Truesdell [109], Green and Naghdi [41], Simo and Pister [107], Dafalias [18], Naghdi [85], Xiao et al. [122], Bruhns et al. [10], Xiao et al. [123], Fish and Shek [33], Bruhns et al. [11], Meyers et al. [78], Naghdabadi et al. [84], Wu [120], Xiao et al. [124] and Chakrabarty [16].

The Eulerian formulation for finite strains with logarithmic rate will be used henceforth in the mechanical formulation and constitutive model. This is considered since it is a consistent, physically pertinent formulation of finite elastoplasticity which considers the inherent inseparability of the total elastoplastic deformation as a physical entity since a proper definition of elastic behaviour is unavoidably linked with an elastic or plastic deformation-like variable.

Chapter 4

Constitutive Models

The numerical modelling in solid mechanics is invariably linked with constitutive models that represent the behaviour of materials subjected to loading. This chapter is concerned with the detailed presentation of one such constitutive model for granular cohesionless materials. The ECP's constitutive model (also known as 'Hujeux's model') is an elastoplastic multimechanism model ([2], [57], [79]). However, the most commonly used constitutive models, of which the ECP model is part, were developed under the framework of small strain analysis and therefore limited in their scope. Taking into account the laboratory results already presented, pile installation and ring shear tests, one cannot fail to notice the inability of the standard models, which consider a critical state at a relatively small strain, to replicate the behaviour of the specimens. Therefore, the constitutive model is altered for it to cope with the behaviour of the soil specimens when subjected to very high volumetric and shear strains where additive phenomena such as grain crushing may take place. This adaptation is validated by comparing the numerical results with the laboratory data.
Ziegler and Wehrli [127] considered that any " attempt to physically understand material response turns continuum mechanics into thermodynamics" meaning that "thermodynamics and continuum mechanics become inseparable, forming one single branch of science". In this chapter, the thermodynamic formulation, free energy and dissipation functions, for adapted versions of the original and revised ECP constitutive models are presented. These adaptations were made in accordance with the physical nature of the universal laws and the experimental results. Examples of triaxial shear tests considering both models are presented and analyzed in both stress and energetic terms.

4.1 ECP constitutive model

The ECP's constitutive model, commonly known as Hujeux model, is an elastoplastic multimechanism model (Aubry et al. [2] Hujeux [57] Modaressi [79] Daouadji et al. [22] and Sica et al. [105]) characterized by different yield surfaces, allowing for an anisotropic response. It also incorporates critical state soil mechanics and considers a Coulomb failure line. The model is defined with a very small elastic domain were the behaviour is non-linear elastic. Isotropic hardening with plastic strains represents the effect of compressive effective pressure in soil (barotropy) and the progressive mobilization of the friction. The

latter is also a result of isotropic hardening due to increasing plastic deviatoric strains. Cyclic behaviour is defined by kinematic hardening of the yield surfaces and the internal variables with discontinuous evolution laws. The flow rule is associated for the isotropic mechanism and deviatoric plastic strains while a Roscoe type dilatancy rule [94] governs the volumetric plastic deformations generated by the deviatoric mechanisms. The isotropic nonlinear elastic behaviour is represented in the model by an evolution of the elastic variables with the mean compressive effective stress. The bulk and shear modulus, K and G, are determined as

$$K(p') = K_{ref}(\frac{p'}{p'_{ref}})^{n_e} \tag{4.1}$$

$$G(p') = G_{ref}(\frac{p'}{p'_{ref}})^{n_e} \tag{4.2}$$

where K_{ref} and G_{ref} are the moduli measured at the reference pressure p'_{ref} and n_e is the degree of non-linearity ($n_e = 0$ corresponds to linear elasticity).

The model has one isotropic and three deviatoric mechanisms defined in orthogonal planes. For each deviatoric plastic mechanism "k" associated with a plastic plane strain, a projection matrix $\underline{\underline{O}}_k$ is defined in the base plane $(\underline{e}_i, \underline{e}_j)$ with $\underline{e}_k$ as the normal vector, such that:

$$\underline{\underline{\sigma}}_k = \underline{\underline{O}}_k \underline{\underline{\sigma}} \underline{\underline{O}}_k \tag{4.3}$$

where $\underline{\underline{O}}_k$ is

$$\underline{\underline{O}}_k = \underline{e}_{(1+mod(k,3))} \otimes \underline{e}_{(1+mod(k+1,2))} + \underline{e}_{(1+mod(k+1,3))} \otimes \underline{e}_{(1+mod(k,2))} \quad , \quad k \in [1,2,3] \tag{4.4}$$

and $mod(k, j)$ is the remainder of the division of k by j. Thus,

$$\underline{\underline{O}}_1 = \underline{e}_2 \otimes \underline{e}_3 + \underline{e}_3 \otimes \underline{e}_2 \tag{4.5}$$
$$\underline{\underline{O}}_2 = \underline{e}_1 \otimes \underline{e}_3 + \underline{e}_3 \otimes \underline{e}_1 \tag{4.6}$$
$$\underline{\underline{O}}_3 = \underline{e}_2 \otimes \underline{e}_1 + \underline{e}_1 \otimes \underline{e}_2 \tag{4.7}$$

This projection which results in the following form for the stress tensor associated to the "k" plane, verifies the plastic plane strain hypothesis in this plane

$$\underline{\underline{\sigma}}_k = \sigma_{ii}\underline{e}_i \otimes \underline{e}_i + \sigma_{jj}\underline{e}_j \otimes \underline{e}_j + \sigma_{ij}(\underline{e}_i \otimes \underline{e}_j + \underline{e}_j \otimes \underline{e}_i) \tag{4.8}$$

The variables considered per mechanism can therefore be defined

$$p'_k = \frac{tr(\underline{\underline{\sigma'}}_k)}{2} \tag{4.9}$$

$$\underline{\underline{s}}_k = \underline{\underline{\sigma'}}_k - p'_k \underline{\underline{I}}_k \tag{4.10}$$

$$q_k = ||\underline{\underline{s_k}}|| \tag{4.11}$$

$$D_{vk} = tr(\underline{\underline{D}}_k) \tag{4.12}$$

$$\underline{\underline{D}}_{Dk} = \underline{\underline{D}}_k - D_{vk}\underline{\underline{I}}_k \tag{4.13}$$

where

$$\underline{\underline{I}}_k = \underline{e}_i \otimes \underline{e}_i + \underline{e}_j \otimes \underline{e}_j \tag{4.14}$$

$\underline{\underline{D}}$ is the rate of deformation tensor (symmetric) that can be decomposed in $\underline{\underline{D}}^e$ and $\underline{\underline{D}}^p$ which are called elastic and plastic stretching respectively as presented in Section 2. Also, $\underline{\underline{D}}^p = \sum_{k=1,4} \underline{\underline{D}}^p_k$ where only active mechanisms contribute.

The yield criterion for a given deviatoric plane "k" is defined by

$$f_k(\underline{\underline{\sigma}}, p_c, r_k) = q_k - p_k \cdot sin\phi_{pp} \cdot r_k \cdot (1 - b \cdot \ln(\frac{p_k}{p_c})) \leq 0 \tag{4.15}$$

where

$$\dot{r_k} = \dot{\Lambda}\,\frac{(1-r_k)^2}{a} \quad , \quad \dot{p}_c = p_c \beta tr(\underline{\underline{D}}^p) \tag{4.16}$$

and $\dot{\Lambda}$ is the plastic multiplier. The expressions presented here introduce material properties. The parameter "β" is the plastic compressibility modulus which serves to represent the influence of the densification in the material behaviour and is taken into account in the state variable "p_c" (pycnotropy). This parameter defines the variation of "p_{c0}" which corresponds to the critical mean effective stress at the initial void ratio. Parameter "ϕ_{pp}" is the friction angle of the material representing the critical state line (state where deformation occurs at constant volume) in the stress plane and "b" is a parameter that defines the shape of the yield surface. A value of "$b = 1$" represents a Cam-Clay-type yield surface and "$b = 0$" a Mohr-Coulomb-type yield surface. The variable "r_k" represents the deviatoric hardening variable. This variable starts at an initial value "r_k^{el}", representing the size of the deviatoric elastic domain, and evolves until the value of unity at the perfect plasticity state. The parameter "a" has a great influence on

the evolution of the deviatoric hardening, a lower value of "a" leads to faster increase of the hardening parameter. This variable varies with the deviatoric deformations according to the relationship proposed by Hujeux [57]

$$a = a_1 + (a_2 - a_1)\alpha(r_k) \tag{4.17}$$

where $\alpha(r_k)$ evolves depending on the interval where the value of r_k is

$$\alpha(r_k) = \begin{cases} 0 & \text{if } r_k < r_{hys} \quad \text{pseudo-elastic domain} \\ (\frac{r_k - r_{hys}}{r_{mob} - r_{hys}})^m & \text{if } r_{hys} < r_k < r_{mob} \quad \text{hysteretic domain} \\ 1 & \text{if } r_{mob} < r_k < 1 \quad \text{mobilized domain} \end{cases}$$

The deviatoric mechanisms are subjected to a non-associated flow rule based on a Roscoe dilatancy rule [94]

$$\underline{\underline{D}}_k^p = \dot{\Lambda} \cdot \frac{1}{2} \cdot [\frac{(\underline{\underline{s}}_k)}{q_k} + (sin\psi - \frac{q_k}{p_k})\underline{\underline{I}}_k] \tag{4.18}$$

where ψ is the characteristic angle associated with a zero volume variation and divides the stress plane in contractive and dilative behaviour (first phase transformation / characteristic line). Data shows that usually $\phi = \psi$ and that relative density does not influence either of the two lines [66].

Figure 1 shows the graphical representation of the phase transformation and instability lines. The instability line is defined as the line in stress space where the plastic strain increment vector is perfectly vertical and indicates a point where sand may become unstable [51]. For the revised ECP constitutive model the definition of these lines is crucial.

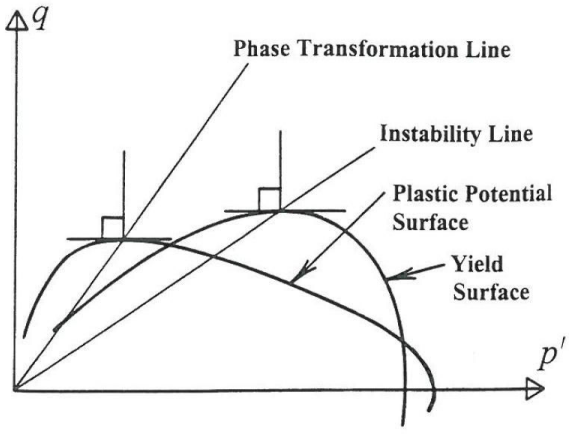

Figure 1: Comparison of phase transformation and instability lines [66]

In the ECP constitutive model the position of the instability line is dependent on a number of parameters. Figure 2 shows the influence of the initial normal stress while

Figure 3 shows the influence of parameter "b" on the position of the instability line for a certain initial normal stress in the model for an undrained shear loading path.

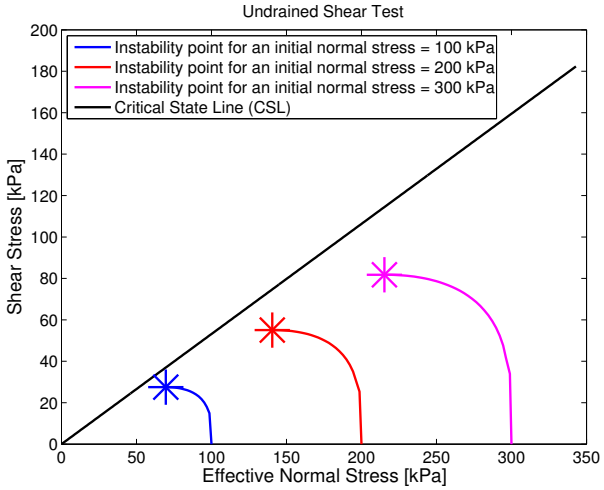

Figure 2: Influence of the initial normal stress on the position of the instability line

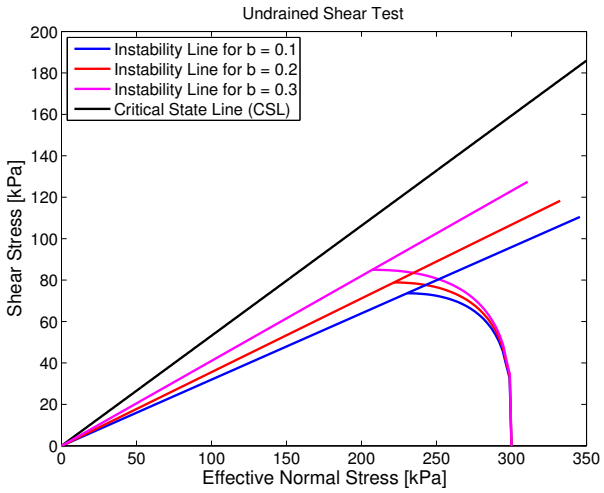

Figure 3: Influence of parameter b on the position of the instability line

The ECP multimechanism model also includes an isotropic mechanism which is governed by the spheric part of the stresses and produces only volumetric variations. The yield criterion of the forth mechanism, the isotropic mechanism, is given by

$$f_4 = f_{iso} = |p'| - dp_c r_{iso} \tag{4.19}$$

where

$$\dot{r}_{iso} = \dot{\Lambda} \frac{(1 - r_{iso})^2}{c} \frac{p_{ref}}{p_c} \tag{4.20}$$

The parameter "d" represents the distance between the normal consolidation line and the critical state line in the volumetric plane and the parameter "c", mirroring the parameter "a" in the deviatoric hardening, controls the isotropic hardening. It can be seen that as all four mechanisms "share" the volumetric strain variable they are coupled.

Cyclic yield function

The cyclic behaviour is considered in the ECP constitutive model in a rather complex manner. The cyclic deviatoric mechanism is "activated" when an unloading occurs and the elastic domain is surpassed in the monotonic mechanism. The cyclic yield function is therefore given by

$$f^c = 0 \tag{4.21}$$

where

$$\begin{aligned} f^c &= q_k^c - p_k \cdot M \cdot r_k^c \cdot (1 - b \cdot log(\frac{p_k}{p_c})) \\ &= \frac{q_k^c}{p_k \cdot M \cdot (1 - b \cdot log(\frac{p_k}{p_c}))} - r_k^c \end{aligned} \tag{4.22}$$

The variables are hereby defined as

$$q_k^c = ||\underline{\underline{s_k^c}}|| \quad , \quad \underline{\underline{s_k^c}} = \underline{\underline{s_k}} - p_k \cdot M \cdot (1 - b \cdot log(\frac{p_k}{p_c})) \cdot (\underline{\underline{X}}^H + r_k^c \cdot \underline{\underline{t}}^H) \tag{4.23}$$

$$\underline{\underline{X}}^H = \frac{\underline{\underline{s_k^H}}}{p_k^H \cdot M \cdot (1 - b \cdot log(\frac{p_k^H}{p_c^H}))} \quad , \quad \underline{\underline{t}}^H = \frac{(\underline{\underline{s_k^{cH}}})}{q_k^c} \tag{4.24}$$

The memory tensor $\underline{\underline{X}}^H$ defines the point of tangential contact between the monotonic loading yield surface and the cyclic loading yield surface. Also, the vector $\underline{\underline{t}}^H$ defines the direction of loading prior to the change in the loading direction. The full development of this integration can be found in Appendix C.

Finally, the cyclic yield function for the isotropic mechanism is given by

$$f_{iso}^c = |p'^c| - d\, p_c\, r_{iso}^c \tag{4.25}$$

where

$$X^H = \frac{p'^H}{d\, p_c^H} \tag{4.26}$$

$$p'^c = |p'| - d\, p_c\, X^H \tag{4.27}$$

and p^H and p_c represent the values of p and p_c at the unloading moment.

4.2 Revised ECP constitutive model

In order to consider the behaviour of soil when subjected to significant shear strains the constitutive model has to take into account the main physical phenomena taking place under such conditions. As the laboratory testing results show, special features must be introduced into the constitutive models and numerous authors have proposed different constitutive models to tackle this issue of which some were already presented in Section 3.

In this section a revised version of the ECP constitutive model valid to represent the behaviour of soil under large strains where the second phase transformation occurs is presented. The need for modifications in the constitutive model will be better demonstrated with the model application at the end of the chapter. Some could readily be observed in the results from RS testing where the second phase transformation occurs.

The results showed that the soil specimens underwent extreme shearing as well as high compression stresses in the vicinity of the moving pile which resulted in particle damage and influenced the volumetric behaviour and stiffness of the specimen. The shearing processes are addressed considering the results from ring shear tests while the isotropic compression mechanisms are not addressed directly (only indirectly from ring shear tests volumetric measurements) due to a lack of laboratory results concerning sands (since most existing results consider coarser granular materials) for a trend to be identified. This means that the behaviour of soil specimens under isotropic compression (such as the model from Hu et al. [55] and laboratory studies such as Hagerty et al. [45] and McDowell et al. [76]) was not considered in the formulation of the constitutive structure [14]. It is however considered indirectly by a variation of the parameter β which influences the slope of the critical state line in the volumetric plane which will be presented hereafter. Finally, the isotropic mechanism is not taken into account either due to the fact that the compression stresses are more relevant at providing the confinement of the soil at the interface level than being directly responsible for the particle breakage observed. This can be verified by comparing the compression stress required to produce particle breakage in an isotropic compression test [45] and the stresses found in pile experiments [60] with the possible exception of carbonate sands [116].

Finally, in this proposed model, no change is considered either to the dilatancy rule nor to the slope of the critical state line in the stress space (the critical friction angle in this model is constant [95]).

These assumptions are obviously related to the fact that not all the conditions that affect particle damage are taken into account in the existing constitutive models (a comprehensive list of these factors is presented by Sadrekarimi and Olson [97]). The attempt to take all of them into account is not pursued here. For this reason as well, the representation of the evolution of gradation of the specimen is not attempted either.

The proposed formulation attempts to address the issue concerning grain breakage and its effects on the mechanical behaviour, stress and strains, of the soil specimens at the interface level. In order to accomplish this two aspects must be considered, namely the choice of an internal variable able to reproduce the observed response in laboratory testing (reversal of the stress and volumetric trends) and the triggering mechanism for the evolution of this variable.

As it is mentioned by Sadrekarimi and Olson [96], as well as confirmed by other laboratory ring shear tests, particle damage is concentrated in the shear band while no particle damage is observed in the specimen outside the shear band and also that localization initiated before reaching peak shear resistance since the material was still strain-hardening. This leads to the conclusion that the particle breakage phenomena, in ring shear tests, is intrinsically linked with the formation of a shear band due to strain localization. Therefore, the search for the instability condition in geomechanics is of the essence for the formulation of a valid triggering mechanism. The shear band thickness evolution can be seen in Figure 4. The RS device used by Sadrekarimi and Olson [96] imposes shearing at the bottom of the specimen resulting in the formation of a shear band there as can be seen from this figure.

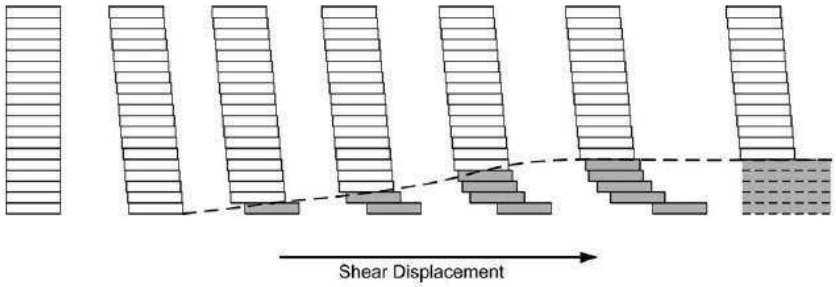

Figure 4: Shear band evolution in a RS test with shearing at the bottom of the specimen [96]

Instability conditions

This issue has been addressed by various authors in both experimental and theoretical works and will not be object of a detailed review here.

The localized failure mode is characterized by a shear band formation which represents a localization of strain ([92]). The first proposed instability criterion is considered for standard associated materials to be the failure criteria which represents the state at which a limit value of stress is reached and, therefore, unlimited deformation for a null variation in stress. This criteria is known as the Drucker's postulate ([31]). However, for non-associated materials this condition fails to detect instabilities which occur before reaching the plastic limit condition (in geomechanics the best example of this is the liquefaction phenomenon). The need for this analysis leads to the second criterion presented by [51] which can predict these failures which depend on the loading path as well as the initial state of the material. This criterion is related to the sign of the second-order work and allows a local follow-up of instabilities. This condition of stability considers that a stress-strain state is considered "stable" if for any incremental stress and strain connected by the constitutive model the second-order work is strictly positive

$$\forall(d\underline{\underline{\sigma}}, d\underline{\underline{\epsilon}}), \quad d^2W = d\underline{\underline{\sigma}} \cdot d\underline{\underline{\epsilon}} > 0 \tag{4.28}$$

which can be written in a totally analogous way in the case of finite deformation considering the Eulerian formulation

$$\forall(\underline{\underline{\sigma}}^{\nabla}, \underline{\underline{D}}), \quad d^2W = \underline{\underline{\sigma}}^{\nabla} \cdot \underline{\underline{D}} > 0 \tag{4.29}$$

where $\underline{\underline{D}}$ is the rate of deformation tensor (symmetric).

In the case of an incrementally linear constitutive law, the positiveness of the second-order work is a sufficient condition for the uniqueness of the solution. However, when considering that the stress−strain relationship is incrementally non-linear, as in the case of elastoplasticity or fully non-linear, such as hypoplastic models, the proof is not trivial. Nevertheless, various authors have proved the positive definiteness of the elastoplastic tensor, and therefore the positivity of the second-order work is a sufficient condition for the "uniqueness of the solution" or "no loss of the stability" of the boundary problem ([88]). This result is true for a large class of constitutive laws, including elastoplasticity, either with an associated, or non-associated flow rule, or hypoplasticity ([46]). Considering the present constitutive structure, [46] present a general overview of the existing approaches in this domain and show the potential of the elastoplastic ECP's constitutive model to predict these failures in triaxial and biaxial loading paths for drained and undrained conditions. Finally it can be shown that bifurcation cannot occur prior to a negative second-order work as proposed by [51]. For associated materials Hill's condition coincides with the bifurcation. The Hill's criterion is therefore a lower bound condition for instability states.

Hill's criterion will henceforth be taken as the triggering mechanism for the evolution of the internal variable representing the grain breakage phenomena in the constitutive model.

The internal variable to represent the mechanical behaviour of the soil under extremely high shear strains is now presented.
The monotonic deviatoric yield surface of the "k" plane is given by

$$f = q_k - p_k \cdot sin\phi_{pp} \cdot r_k \cdot r_{br_k} \cdot (1 - b \cdot \ln(\frac{p_k}{p_c})) = 0 \tag{4.30}$$

The proposed internal variable, r_{br_k}, is a hardening parameter of the same form as the shear hardening parameter r_k and will evolve, once the triggering mechanism is verified, according to

$$\dot{r}_{br_k} = -\dot{\Lambda}(a^{br} \cdot r_{br_k}) \tag{4.31}$$

The variable r_{br_k} will evolve from its initial value which is unity (=1) and decrease asymptotically to zero with the increase of deviatoric plastic strain. This progression was chosen for it works best in representing the behaviour of the soil specimen as was observed

from laboratory test results. The key parameter for the evolution of this variable is the parameter a^{br}. The evolution for the parameter a^{br} is here considered as

$$a^{br} = a_0^{br} - [(1 - r_{br_k}) \cdot a_0^{br}]^{m_a^{br}} \tag{4.32}$$

The parameter m_a^{br} allows the user an extra control over the rate of the evolution of parameter a^{br} to account for variability of different soil types with respect to breakage. Both the magnitude and the evolution of the breakage mechanism are "controlled" by these parameters in the stress space and, moreover, influence the volumetric plane indirectly. These parameters represent, therefore, a general approach to simulate the various factors in soils that influence breakage [97].

The evolution of these parameters is shown graphically in Figure 5 and the influence of the internal variable r_{br_k} on the yield surface can be seen in Figure 6.

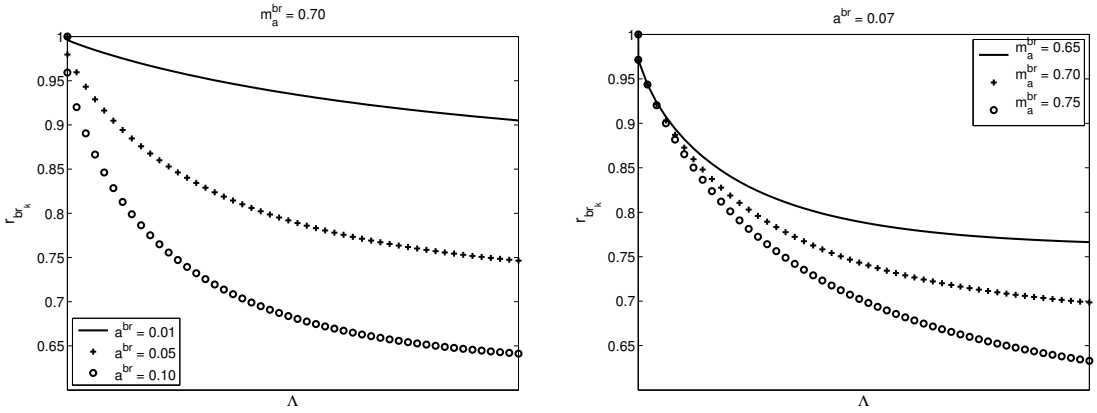

Figure 5: Evolution of r_{br_k}

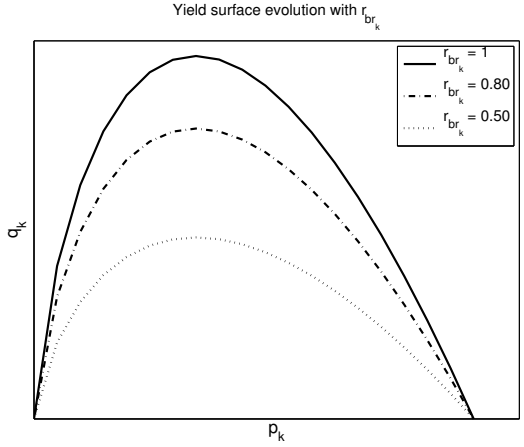

Figure 6: Yield function variation with the evolution of r_{br_k}

Figure 7 shows the magnitude and direction of plastic deformation increments in the revised ECP model for an undrained shear test. The vectors of plastic volumetric deformation reverse direction at both phase transformation points while the deviatoric plastic deformation vector never changes direction.

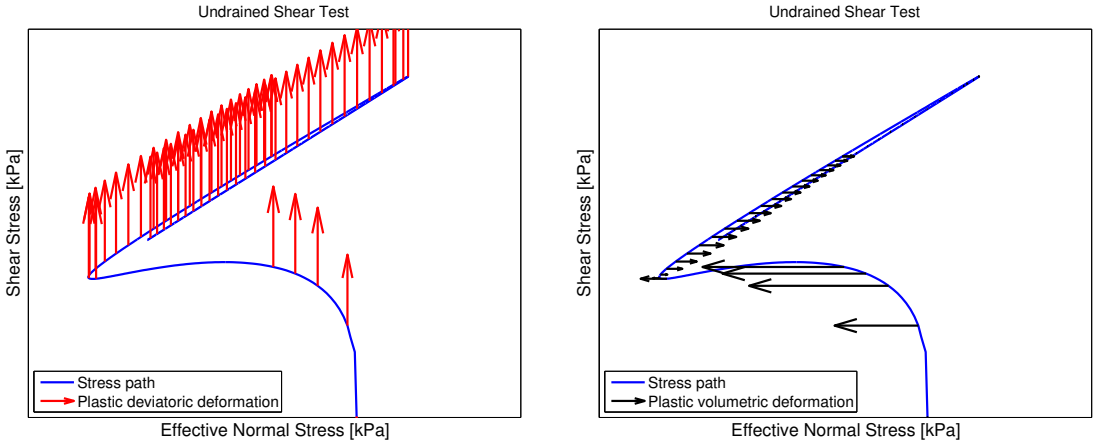

Figure 7: Vectors of plastic deformation during loading representing the non-associated flow rule for the revised model

Concerning the compressibility of the specimen, it was shown from results in ring shear tests and from pile installation tests that the critical state line in the volumetric plane for specimens subjected to particle damage was not properly defined. In fact, Sadrekarimi and Olson [99] among others showed the different CSL's for "uncrushed" and "crushed" sands and how they differed. One cannot fail to notice the different angle of the slope of the CSL (results from Sadrekarimi and Olson [99] show 62% and 38% variation in the angle for OT and IR sand, respectively) as well as its global position. While its position has been somewhat addressed by the introduction of the variable r_{br_k}, its slope concerns the variable β in the ECP constitutive model. To properly represent this phenomena the variable β is made to have an evolution law related with plastic work W^p which results in

$$\beta = \beta_0 \frac{b_{W_p}}{(b_{W_p} + W_p)} \tag{4.33}$$

where β_0 is the initial value of β which represents the slope of the "uncrushed" CSL. The parameter "b_{W_p}" is given by the user and represents the plastic work the soil has to undergo before significant change in the CS locus happens. The validity of this evolution relationship, however, cannot be demonstrated due to lack of laboratory evidence to properly define its evolution since only the initial and final values of β are known.

The ECP constitutive model is therefore enhanced to better represent the behaviour of sand specimens subjected to extreme shearing. This constitutive model allows for the simulation of the second phase transformation that has been observed in laboratory testing by some authors in large displacement shear resistance tests and to accurately represent the stress-strain relationship even at very high deformations. Also, the determination of a

critical state line at a different position in the volumetric space is possible considering this constitutive structure. Without loss of generality, the proposed constitutive structure can be applied to interface models such as Aubry et al. [3], D'Aguiar et al. [21] and D'Aguiar et al. [19].

Cyclic yield function

The cyclic yield function can now be written as

$$f^c = q_k^c - p_k \cdot M \cdot r_k^c \cdot r_{br_k} \cdot (1 - b \cdot log(\frac{p_k}{p_c})) \tag{4.34}$$

Note that the breakage internal variable r_{br_k} does not evolved according to a kinematic hardening function but rather an isotropic hardening function. The evolution of the breakage parameter is intrinsically and exclusively linked with the evolution of plastic deviatoric deformation. The evolution of the internal variable r_{br_k} will follow the hardening law presented before. The full development of this integration can be found in Appendix C.

4.3 Constitutive relations from free energy and dissipation functions

Ziegler and Wehrli [127] considered that any " attempt to physically understand material response turns continuum mechanics into thermodynamics" meaning that "thermodynamics and continuum mechanics become inseparable, forming one single branch of science". The purely mechanical behaviour of deformable solids must abide certain universal laws. These are the frame-indifference principle, the laws of conservation (momentum and mass) and the three thermodynamical laws which must be fulfilled. Ziegler and Wehrli [127] went on to propose a methodology for determining both the free energy and dissipation functions from existing constitutive structures for a range of materials which would fulfill the thermodynamical requirements. The formulation was, however, limited to infinitesimal strains and where the specific weight (ρ) would suffer no variation. The state function which characterizes the energy in the system corresponds to the free energy function (ψ) depending on state parameters (internal variables, $\underline{\epsilon}$, and state variables, $\underline{\underline{\alpha}}$ for the anisotropic or kinematic hardening behaviour usually known as back-stress and k which corresponds to the isotropic hardening). However, for the irreversible behaviour in the case of plastic dissipation (as is the case in soil mechanics) the thermodynamical equations require some complementary laws to be added to take this into account therefore, an extension of the classical concept of entropy is necessary when no reversible process exists between two configurations of the specimen that have different plastic strains [9]. The material indifference principle, and the positivity of the dissipation function must be verified when formulating these laws. Finally the second law of thermodynamics also restricts the proposed constitutive structures [93]. The second principle of thermodynamics postulates the existence of a function of state, called entropy. The entropy of a system is an extensive property (total is equal to the sum of the parts) and its change can be split into two parts, interactions with the exterior (flow of entropy) and changes inside the system. The part of entropy due to changes inside the system is never negative, it has the value of zero for reversible processes and superior to zero for irreversible processes. Therefore, similarly, the formulation by Ziegler and Wehrli [127] postulates the separation of the stress tensor into two distinct parts representing different states, reversible and irreversible stresses.

$$\underline{\underline{\sigma}} = \underline{\underline{\sigma}}^R + \underline{\underline{\sigma}}^I \tag{4.35}$$

The reversible part can be determined by the derivation of the free energy function by the strain tensor, $\underline{\epsilon}$ for infinitesimal strains, through the relationship

$$\underline{\underline{\sigma}}^R = \rho\, \delta_\epsilon \psi \tag{4.36}$$

while the irreversible processes are associated with the rate of the strain tensor $\underline{\dot{\epsilon}}$ derived from a convex, continuous and non-negative dissipation function and can be written by means of a new function ϕ

$$\underline{\underline{\sigma}}^I = \rho\, \delta_{\dot{\epsilon}} \phi \tag{4.37}$$

The free energy function can be therefore written as a function of the state parameters, for the case of initial isotropy, as

$$\rho\dot{\psi} = \delta_\sigma\psi : \dot{\underline{\underline{\sigma}}} + \delta_\alpha\psi : \dot{\underline{\underline{\alpha}}} + \delta_k\psi : \dot{k} \tag{4.38}$$

The dissipation function ϕ, which characterizes the irreversible processes ($\underline{\underline{\sigma}}^I$ as the irreversible stresses and $\underline{q}$ the thermal flux), can be described by the renowned Clausius-Duhem inequality (or second law of thermodynamics) as

$$\rho\dot{\phi} = \underline{\underline{\sigma}}^I : \dot{\underline{\underline{\epsilon}}} - \rho\delta_\alpha\psi : \dot{\underline{\underline{\alpha}}} - \frac{\underline{q}}{T}\nabla T = \rho\delta_{\dot{\epsilon}}\phi : \dot{\underline{\underline{\epsilon}}} + \rho\delta_{\dot{\alpha}}\phi : \dot{\underline{\underline{\alpha}}} + \rho\delta_{\dot{q}}\phi \cdot \underline{\dot{q}} \geq 0 \tag{4.39}$$

with ∇ the gradient operator. This expresses the entropy principle, namely, the irreversibility of macroscopic physical occurrences in deformable solids. The sum of the two terms in the first equation is known as plastic dissipation. It consists of the plastic work subtracted of the rate of stored energy in the material due to, e.g., hardening [68]. Note that no coupling is considered between the velocity terms and the thermal flux which results in that the orthogonality condition is separately considered for the two processes, plastic and thermal dissipation. Also, note that since the sum of the generalized thermodynamical forces related to the internal variables is zero it follows that

$$\underline{\underline{\beta}} = \underline{\underline{\beta}}^R + \underline{\underline{\beta}}^I = \rho\delta_\alpha\psi + \rho\delta_{\dot{\alpha}}\phi = 0 \tag{4.40}$$

This assumption is considered due to the absence of these forces in the first fundamental law of thermodynamics

$$\rho\dot{e} = \underline{\underline{\sigma}} : \dot{\underline{\underline{\epsilon}}} - div\,\underline{q} \tag{4.41}$$

where e is the specific internal energy. This law states that the changing rate of internal energy is composed by the sum of the internal power (due to stress) and the non-mechanical power (due to heat flux and heat supply).
These equations allow for the full definition of a dissipative deformable medium from defined free energy (function of kinematic variables) and dissipation (function of kinematic variables and their rates) functions.
When considering soil mechanics, Ziegler and Wehrli [127] mentions soil constitutive models when addressing the issue of non-associated flow rules and the thermodynamical consequences of such behaviour. It is demonstrated by Ziegler and Wehrli [127] that the orthogonality condition does not imply yield conditions and flow rules that are associated. Ziegler and Wehrli [127] mention that orthogonality in velocity space is apt to explain the actual behaviour of soils where the theory of the plastic potential and its justification by Drucker [30] are no longer valid. Later this consideration was used to construct the dissipation functions for models of geotechnical materials by Houlsby [53], Houlsby [54] and Houlsby [52] (Houlsby [52] derived the known Modified Cam-Clay model from defined functions of free energy and dissipation).

4.3.1 ECP constitutive model

The thermodynamical formulation of the ECP constitutive model will now be presented. The formulation presented in this chapter will not consider thermal effects (isothermal) in the constitutive model (purely mechanical behaviour) and will consider the infinitesimal strains and rotations hypotheses. The continuum mechanics sign convention is taken. The meaning of the variables presented in the equations here is the same as when the ECP constitutive model was introduced in this chapter. However, for simplicity purposes, isotropic linear elasticity is imposed. As presented before a constitutive model may be derived from the free energy and dissipation functions, if the latter is convex and non-negative, then the constitutive model derived would belong to the space of admissible thermodynamical processes. Finally the definitions of the invariants for isotropic and deviatoric stresses taken in the thermodynamical formulation are presented here.

$$p = (\lambda + \frac{2}{3}\mu)(\epsilon_v - \epsilon_v^p) = K(\epsilon_v - \epsilon_v^p) \tag{4.42}$$

$$\underline{\underline{\overline{\sigma}}} = 2\mu(\underline{\underline{\overline{\epsilon}}} - \underline{\underline{\overline{\epsilon}}}^p)\,, \qquad q = ||\underline{\underline{\overline{\sigma}}}|| \tag{4.43}$$

The free energy and dissipation functions for the ECP constitutive model are here postulated whose development was done by Modaressi et al. [81] and Modaressi and Modaressi [80].

Free energy function

$$\rho\psi = \frac{1}{2}(\lambda + \frac{2}{3}\mu)(\epsilon_v - \epsilon_v^p)^2 + \mu(||(\underline{\underline{\overline{\epsilon}}} - \underline{\underline{\overline{\epsilon}}}^p)||)^2 - \frac{p_{c0}}{\beta}\, exp[-\beta(\epsilon_v^p + \varpi(r))] \tag{4.44}$$

where,

$$r = \frac{M \int_0^t ||\underline{\underline{\dot{\overline{\epsilon}}}}^p||\, dt}{a + M \int_0^t ||\underline{\underline{\dot{\overline{\epsilon}}}}^p||\, dt} \tag{4.45}$$

$$\varpi(r) = \int_r \frac{a\,\alpha(r)}{1-r}\, dr\,, \quad 0 < r < 1 \tag{4.46}$$

$$\alpha(r) = M\,\eta\, r\,(1-r)^m\,, \quad 1 \geq m \geq 0; \quad \eta \geq 0 \tag{4.47}$$

The first and second terms in the free energy function correspond respectively to the isotropic and deviatoric elastic stored energy while the last term is the thermoplastic stored energy related to the isotropic hardening.

Dissipation function

$$\rho\phi = -[\, M\, ||\dot{\underline{\underline{\epsilon}}}^p||\, b\, \alpha\, r\, exp[-\frac{1}{b\, M\, r}(\frac{\dot{\epsilon}_v^p}{||\dot{\underline{\underline{\epsilon}}}^p||\, \alpha} + M\,(1-r)\,)\,] + \dot{\epsilon}_v^p + \Theta(r)\,\dot{r}\,] \tag{4.48}$$
$$p_{c0}\, exp[-\beta(\epsilon_v^p + \varpi(r))\,] + [\, 2\, G\, ||(\underline{\underline{\epsilon}} - \underline{\underline{\epsilon}}^p)||\,(1-\alpha) - \alpha\, M\,(1 - r\, b)\, K\,(\epsilon_v - \epsilon_v^p)\,]\, ||\dot{\underline{\underline{\epsilon}}}^p||$$

where

$$\Theta(r) = \frac{a\, \eta\, r\, M}{(1-r)^{1-m}} \tag{4.49}$$

The dissipation function introduces the non-associated flow rule by being a function of the mean pressure and the norm of the deviatoric tensor. The dissipation function must be positive, convex and zero (with respect to its variables) at the origin so that the loading surface and the flow rule respect the thermodynamical restrictions and whose resulting strain is dissipative. It is possible to verify that ϕ is positive and convex. For it to be zero at the origin the following condition must be verified

$$M - \frac{q}{p} < M\, r\, b \tag{4.50}$$

which can be simplified to $p \leq p_c exp(\frac{1}{b})$ and $r\, b \leq 1$. Note that the second term of the dissipation function could also be written as a function of stress instead of strain but rigorously ϕ should be expressed solely as a function of state variables. Moreover, this term is responsible for the non-associativity of the flow rule. The postulated evolution law for the variable "r" was obtained from the evaluation of experimental results (it cannot be determined directly from the thermodynamical formulation) while verifying the conditions for the free energy and dissipation functions. Hujeux [57], using experimental results, proposed a variation of "r" considering the variable "α" as a quadratic function tending to unity with "r". However, the proposed variation by Hujeux [57] is not a derivable function and has therefore been adapted by the one here presented formulated originally by Modaressi and Modaressi [80]. The parameter "η" is here introduced for that purpose. Finally, the thermodynamical formulation presented here does not consider the multi-mechanism approach of the original constitutive model proposed by Hujeux [57].
The consistency relationship gives that

$$\rho(\delta_{\epsilon_v^p}\psi + \delta_{\dot{\epsilon}_v^p}\phi + \delta_r\psi + \delta_{\dot{r}}\phi)\underline{\underline{I}} + \rho(\delta_{\underline{\underline{\epsilon}}^p}\psi + \delta_{\dot{\underline{\underline{\epsilon}}}^p}\phi) = 0 \tag{4.51}$$

which results in the non-associated flow rule being defined as

$$-\alpha\,(M - \frac{q}{p}) = \frac{-\dot{\epsilon}_v^p}{||\dot{\underline{\underline{\epsilon}}}^p||} \tag{4.52}$$

and finally the yield function which depends on the internal variables "r" and "ϵ_v^p"

$$q + M\ p\, r(1 - b\, ln\frac{p}{p_c}) = 0 \tag{4.53}$$

where $p_c = p_{c0}\, exp[-\beta(\epsilon_v^p + \varpi(r))]$. Therefore, the yield surface will now vary with two isotropic hardening parameters in isothermal conditions (not included in the original model proposed by Hujeux [57]).
The full development of these derivations can be found in Appendix D.

4.3.2 Revised ECP constitutive model

The revised ECP constitutive model is here presented in terms of its free energy and dissipation functions. The same concepts as for the original model are valid here concerning the functions.

Free energy function

$$\rho\psi = \frac{1}{2}(\lambda + \frac{2}{3}\mu)(\epsilon_v - \epsilon_v^p)^2 + \mu(||(\underline{\underline{\epsilon}} - \underline{\underline{\epsilon}}^p)||)^2 - \frac{p_{c0}}{\beta}\, exp[-\beta(\epsilon_v^p + \varpi(r) + \varpi(r_{br}))] \tag{4.54}$$

where,

$$r = \frac{M \int_0^t ||\dot{\underline{\underline{\epsilon}}}^p||\, dt}{a + M \int_0^t ||\dot{\underline{\underline{\epsilon}}}^p||\, dt} \tag{4.55}$$

$$\varpi(r) = \int_r \frac{a\,\alpha(r)}{1-r}\, dr\,, \quad 0 < r < 1 \tag{4.56}$$

$$\alpha(r) = M\,\eta\, r\,(1-r)^m\,, \quad 1 \geq m \geq 0; \quad \eta \geq 0 \tag{4.57}$$

$$r_{br} = r_{br_0} - exp[\,a^{br} \cdot \int_0^t ||\dot{\underline{\underline{\epsilon}}}^p||\, dt\,], \quad 1 \geq r_{br_0} \geq 0 \tag{4.58}$$

$$\varpi(r_{br}) = \int_{r_{br}} a^{br}(r_{br})\,(\,r_{br_0} - r_{br}\,)\, dr_{br}\,, \quad 0 < r_{br} \leq 1 \tag{4.59}$$

$$a^{br}(r_{br}) = a_0^{br} - [(1 - r_{br}) \cdot a_0^{br}]^{m_a^{br}}\,, \quad a_0^{br} \geq 0; \quad 1 \geq m_a^{br} \geq 0 \tag{4.60}$$

As before, the first and second terms in the free energy function correspond respectively to the isotropic and deviatoric elastic stored energy while the last term is the thermoplastic stored energy related to the isotropic hardening. The isotropic hardening now also depends on the evolution breakage interval variable.

Dissipation function

$$\begin{aligned}\rho\phi &= -[\,M\,||\dot{\underline{\underline{\epsilon}}}^p||\,b\,\alpha\,r\,r_{br}\,exp[-\frac{1}{b\,M\,r\,r_{br}}(\frac{\dot{\epsilon}_v^p}{||\dot{\underline{\underline{\epsilon}}}^p||\,\alpha}+M\,(1-r\,r_{br})\,)\,]+\dot{\epsilon}_v^p \\ &+ \Theta(r)\,\dot{r}\,+\Theta(r_{br})\,\dot{r_{br}}\,]\,p_{c0}\,exp[-\beta(\epsilon_v^p+\varpi(r)+\varpi(r_{br}))\,] \\ &+ [\,2\,G\,||(\underline{\underline{\epsilon}}-\underline{\underline{\epsilon}}^p)||\,(1-\alpha)-\alpha\,M\,(1-r\,r_{br}\,b)\,K\,(\epsilon_v-\epsilon_v^p)\,]\,||\dot{\underline{\underline{\epsilon}}}^p||\end{aligned} \tag{4.61}$$

where

$$\Theta(r)=\frac{a\,\eta\,r\,M}{(1-r)^{1-m}} \tag{4.62}$$

$$\Theta(r_{br})=(a_0^{br}-[(1-r_{br})\,a_0^{br}]^{m_a^{br}}\,)\,(\,r_{br_0}-r_{br}\,) \tag{4.63}$$

The consistency relationship gives that

$$\rho(\delta_{\epsilon_v^p}\psi+\delta_{\dot{\epsilon}_v^p}\phi+\delta_r\psi+\delta_{\dot{r}}\phi+\delta_{r_{br}}\psi+\delta_{\dot{r_{br}}}\phi)\underline{\underline{I}}+\rho(\delta_{\underline{\underline{\epsilon}}^p}\psi+\delta_{\dot{\underline{\underline{\epsilon}}}^p}\phi)=0 \tag{4.64}$$

which results in the non-associated flow rule being defined as

$$-\,\alpha\,(M-\frac{q}{p})=\frac{-\,\dot{\epsilon}_v^p}{||\dot{\underline{\underline{\epsilon}}}^p||} \tag{4.65}$$

and finally the yield function which depends on the internal variables "r", "r_{br}" and "$\dot{\epsilon}_v^p$"

$$q+M\;p\,r\,r_{br}\,(1-b\,ln\frac{p}{p_c})=0 \tag{4.66}$$

where $p_c = p_{c0}\,exp[-\beta(\epsilon_v^p+\varpi(r)+\varpi(r_{br}))\,]$. Therefore, the yield surface will now vary with three isotropic hardening parameters in isothermal conditions. Note that the breakage internal variable represents a negative hardening mechanism (as defined before) and that the influence of this mechanism is properly taken into account by the function $\varpi(r_{br})$ in the evolution law of p_c as well as with the interval variable r_{br}. Finally, the trigger criterion which was considered before for the breakage mechanism (Hill's criterion) is not compatible with a thermodynamically admissible formulation. Therefore, as can be seen, the evolution of the breakage internal variable is always active.
The full development of these derivations can be found in Appendix D.

4.3.3 Triaxial shear test

A numerical simulation of triaxial shear tests is performed here in order to demonstrate the validity of the thermodynamically admissible constitutive formulation. Three different triaxial tests are performed:

Case I: Constant radial stress test (" drained " test),

Case II: Constant volume test (" undrained " test - drained constant volume test),

Case III: Constant mean stress (" constant p' " test).

The objective of these tests is to demonstrate that the main characteristics of soil behaviour, which were captured by the ECP constitutive model, are still present in the current structure. The parameters were chosen for the material to exhibit initial contractive behaviour (similar to Ottawa sand) while verifying the conditions of thermodynamic admissibility. The flow rule and the evolution laws for the internal variables considered are those presented during the description of the model from the free energy and dissipation functions.

Original model

The results are presented here (figures 8 and 9) now considering the evolution of the stress invariants and internal variables during loading. An initial isotropic stress state was considered for all tests. The breakage mechanism is not considered in the following simulations.

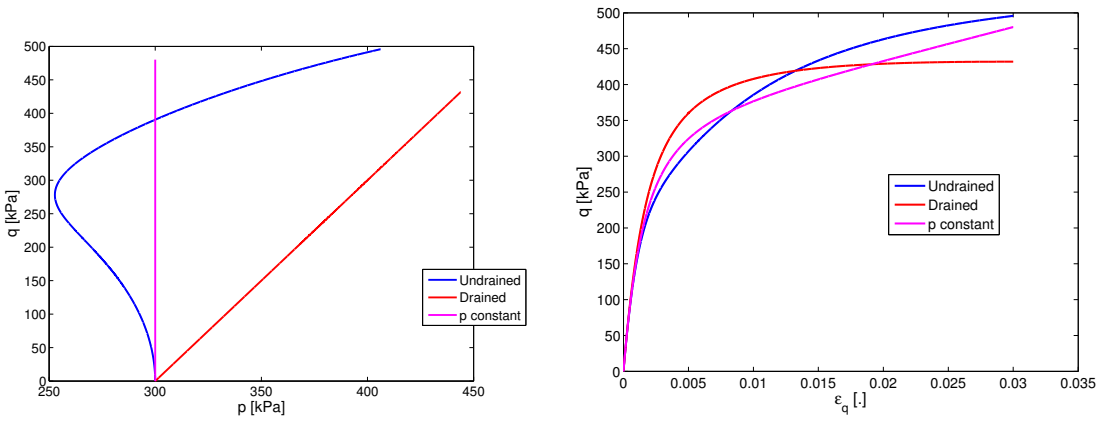

Figure 8: p' - q and ϵ_q - q

The curves show the common behaviour of a normally consolidated soil during a triaxial compression test for the different cases studied. Initial contractive behaviour is observed and a rapid evolution of the internal variable r as a result of the increase in deviatoric strain. Due to the different boundary conditions impose, the cases II ("undrained" test)

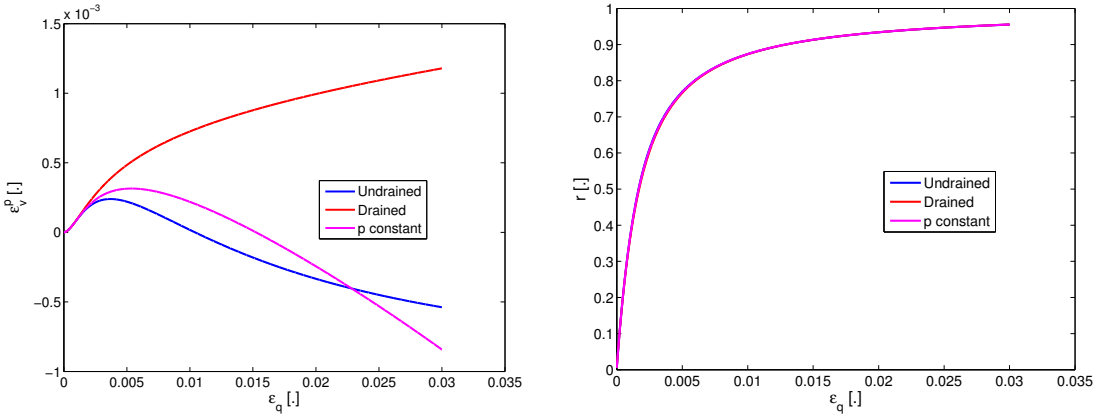

Figure 9: ϵ_q - ϵ_v^p and ϵ_q - r

and III (" constant p' " test) exhibit a phase transformation from contractive to dilative behaviour.

Now lets consider the energy dissipation due to friction and the stored energy as a result of the different hardening mechanisms. Taking the constant volume test as a reference the rate of the dissipation function $\dot{\phi}$ and the dissipation function ϕ have the generic forms (normalized by ρ) as presented in figure 10.

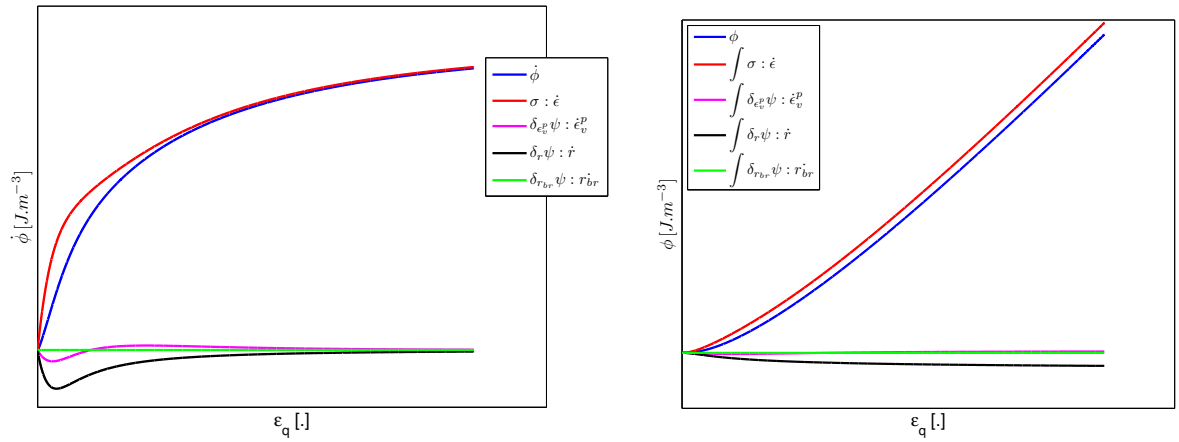

Figure 10: ϵ_q - $\dot{\phi}$ and ϵ_q - ϕ

In figure 10 the different terms that compose $\rho\dot{\phi} = \underline{\underline{\sigma}}^I : \underline{\underline{\dot{\epsilon}}} - \rho\delta_\alpha\psi : \dot{\underline{\underline{\alpha}}}$ from the Clausius-Duhem inequality (or second law of thermodynamics) are plotted. Note that the sign for the stored energy from hardening has been reversed in the figure and hence in accordance with the equation. The positivity requirement of the rate of the dissipation function is verified. The contribution of the breakage mechanism is zero since it is not considered in this simulation. Both hardening internal variables "r" and "ϵ_v^p" store reversible energy in the initial phase of the test. However, after the phase transformation, the mechanism

represented by the internal variable "ϵ_v^p" (volumetric hardening) dissipates energy as a result of the dilative behaviour exhibited by the material.

Revised model

The same tests were simulated considering the revised ECP constitutive model whose formulation was derived from the free energy and dissipation functions presented before. Only the "undrained" condition test will be analyzed in detail for the sake of clarity of the influence of the breakage mechanism and since all the phenomena are present all the same in their fundamental effects.

The "undrained" condition test simulation is now analyzed (figures 11 and 12).

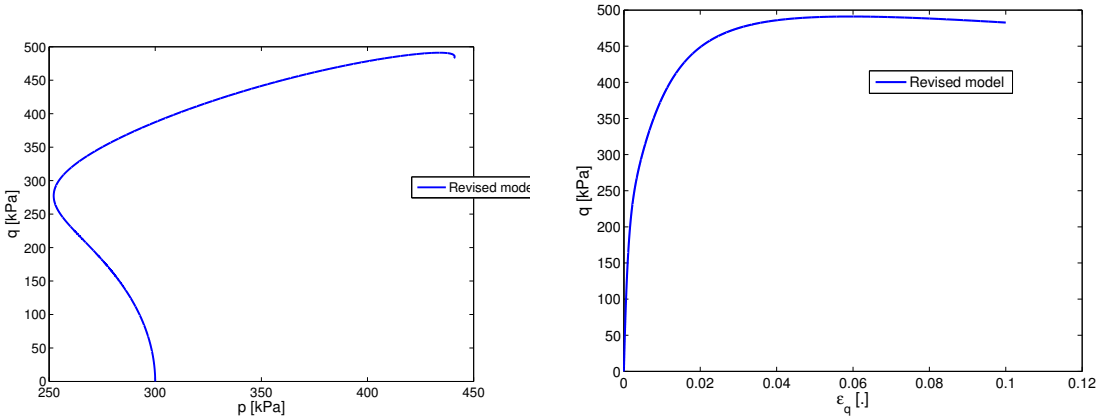

Figure 11: p' - q and ϵ_q - q

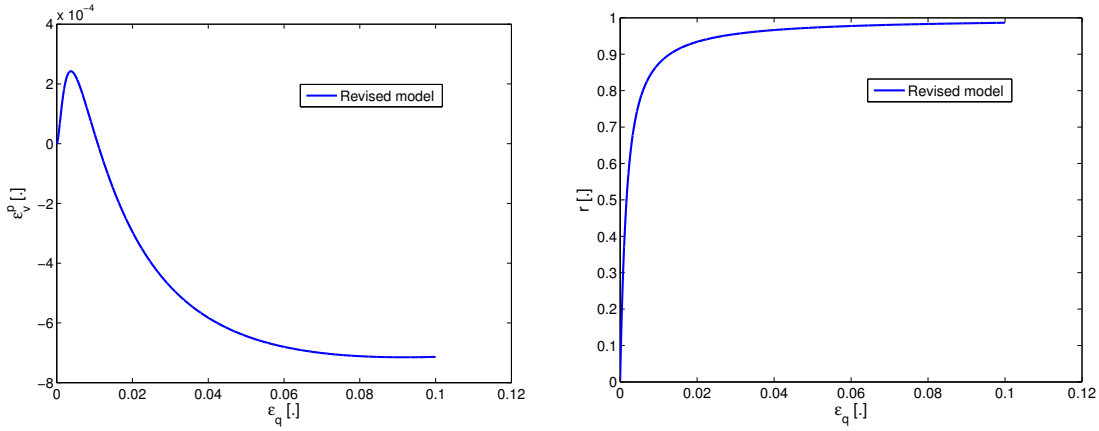

Figure 12: ϵ_q - ϵ_v^p and ϵ_q - r

Since the breakage mechanism is now active ($a_0^{br} > 0$) there is a negative hardening of the material as can be seen in figure 13.

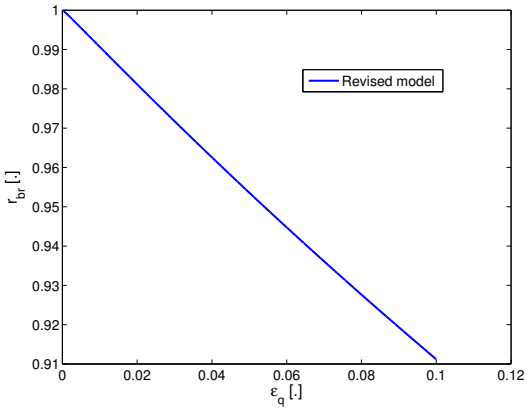

Figure 13: ϵ_q - r_{br}

As a result of this negative hardening there is a reversal of the volumetric strain which in turn results in a decrease of the mean stress in a constant volume condition (isochoric process) test. Finally, after the second phase transformation, the ratio between the deviatoric and mean stress is maintained (at the critical state angle in stress space) and therefore the deviatoric stress also decreases.

In terms of the rate of dissipation function $\dot{\phi}$ and the dissipation function ϕ there is now an extra term due to breakage. This term has the opposite sign of the other hardening variables due to its physical nature. Therefore, the breakage mechanism increases the energy which is dissipated during test. This can be seen in figure 14.

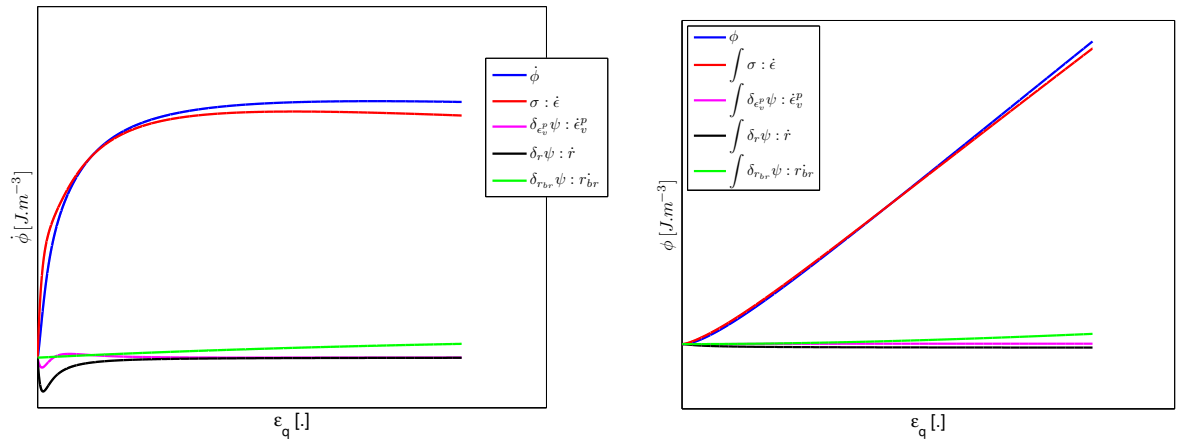

Figure 14: ϵ_q - $\dot{\phi}$ and ϵ_q - ϕ

The evolution of the breakage parameter follows an inverse hyperbola relationship with the deviatoric strain. This results, in terms of energy dissipated by this phenomenon, that it increases rapidly and then stabilizes (the stabilization point depending on the parameters chosen for the evolution of r_{br}). Depending on the values of the parameters

chosen for the breakage mechanism (indeed the amount of breakage of the material) it is possible that the dissipation as a result of breakage will be greater that the stored energy due to hardening. This would result in a reversal of the curves of ϕ and $\int \sigma : \dot{\epsilon}$ as occurs in figure 14.

The influence of the breakage mechanism on the yield surface also occurs by means of the function $\varpi(r_{br})$ in the evolution law of p_c. Once more the evolution of $\varpi(r_{br})$ has the opposite effect in the evolution of p_c when compared with $\varpi(r)$ and ϵ_v^p. This has physical pertinence as the breakage mechanism provokes irreversible contraction in the material. The development of $\varpi(r_{br})$ and $\varpi(r)$ can be seen in figure 15.

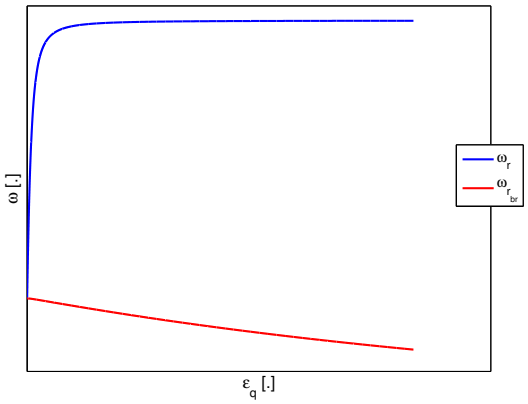

Figure 15: ϵ_q - ϖ

It should be noted that the influence of both $\varpi(r)$ and $\varpi(r_{br})$ is very minute when compared to ϵ_v^p in the evolution of p_c. This can be seen in figure 16. This fact justifies the standard version of the ECP constitutive model where only ϵ_v^p is considered in the evolution law of p_c.

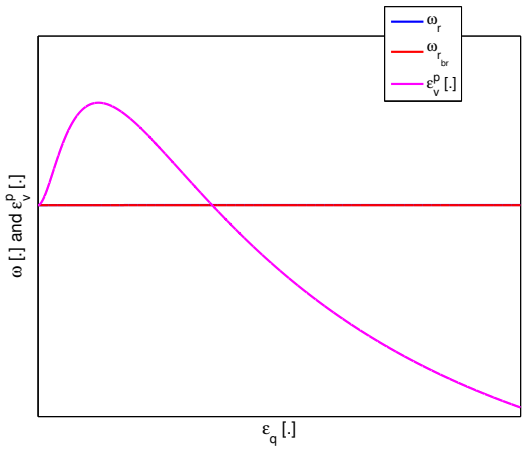

Figure 16: ϵ_q - ϖ and ϵ_v^p

4.4 Summary

This Chapter was concerned with the theoretical definition of the ECP constitutive model and its main features. This model has been used to simulate the behaviour of soil successfully due to its great versatility and realistic assumptions in the behaviour of the material. Its complexity is nonetheless a hindrance since it demands a considerably high number of parameters for its complete definition.

In spite of its versatility some of the aspects of soil behaviour, when very high shear is considered as loading, cannot be captured by the model as it stands. Therefore some adaptations to the yield function and evolution of certain variables were considered to allow for such characteristics of the material to be replicated numerically. The concepts of shear banding and instability conditions are considered and included in the model description due to its fundamental relevance in its definition. The adaptations to the constitutive model were described in detail in this Chapter. The critical state concept and dilatancy rule have been conserved. However, thanks to the modification of the yield function and the introduction of an additional internal variable which characterizes the irreversibility due to grain crushing, the second transformation phase is obtained resulting in the modification of the critical state line in the void ratio-stress plane.

The thermodynamical formulations of both the original and the revised constitutive model are presented. Idealization in terms of isotropic and linear elasticity were made as well as some changes in the evolution laws of some internal variables in order to have a thermodynamically admissible formulation. The free energy and dissipation functions are given and the full mathematical integration can be found in Appendix D to this chapter. Finally, triaxial shear test simulation results were analyzed and the validity of the models is tested in both physical pertinence, in that fundamental thermodynamic laws are respected, and experimental relevance, for the results are consistent with textbook soil behaviour.

Chapter 5

Numerical analysis and validation of the soil behaviour model

The previous chapters presented the framework of both the mechanical formulation and the constitutive model which will be used in the numerical simulation of soil behaviour. The numerical simulation of soil behaviour at very high shear strains will now be described in detail.

This chapter consists in the numerical modeling of undrained (constant volume) RS tests, a constant normal stiffness test and a constant normal load test. The numerical model results of the undrained tests are then compared to the laboratory test results in order to validate it both quantitatively and qualitatively. The constant normal stiffness test and its relevance to the soil-pile interface behaviour is also discussed. The most relevant trends of soil behaviour during a shear test performed to very large strains are shown to be represented by the proposed constitutive relationship. Also, the response of the original constitutive model is represented in order to show the influence of the new internal variable on the behaviour. Finally, cyclic shear tests are performed considering the numerical model used in the monotonic case. The influence of the breakage parameter on the behaviour of the model is discussed as well as its relevance in the observed friction fatigue phenomenon [118]. The influence of different boundary conditions in the cyclic tests is considered as well.

5.1 Numerical simulation of ring shear tests

The geometrical and mechanical configuration of the hollow cylinder shear test simulated numerically is given in figure 1. Assuming no radial soil displacement due to rigid lateral rings a double (radial and angular) plane strain simple shear condition is obtained. Moreover, one should not forget the radial non-uniformity of the stresses and shear strain which is however reduced due to the radial thickness of the apparatus (the ratio of outer to inner ring diameter is 1.33, resulting in an error of less than 2% at the peak shear stress due to strain nonuniformity [96]). Though, a precise analysis of the test results implies a 3D model, thanks to the double plane strain assumption, the resultant vertical load and torque can be computed as the sum of the resultant forces and moments on a series of

radial slices in which the normal and shear stresses can be considered constant.

The enhanced model was implemented in the GEFDyn finite element code and the boundary value problem considering a radial slice of one radian was modelled. As no specific method of regularization is used to circumvent the mesh dependence when shear strain localizes, the size of the elements is chosen to be equal to the shear band thickness observed in the specimen during the laboratory testing. The height of the shear band must, therefore, be considered as a known parameter.

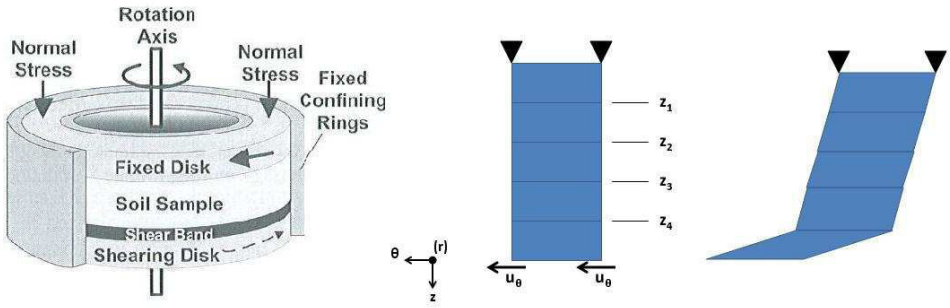

Figure 1: RS test device ([96]) and the finite element mesh for the numerical simulation

The results are analyzed at different heights presented in the figure as z_i. The mesh cannot deform in the vertical direction due to the boundary conditions imposed to replicate the no-volume-change condition of the tests. An imposed displacement (shear in the θ axis) is applied on the bottom element of the mesh which will result in the localization of deformation in that element. This is consistent with the laboratory results. The shear band is always located where shear is imposed [99].

The model is axisymmetric and, therefore, the cylindrical coordinate system (r, θ, z) is considered. The velocity vector and rate of deformation tensor can therefore be defined for this problem as such:

$$\underline{v} = v_\theta(z)\, r\, \underline{e}_\theta + v_z(z)\, \underline{e}_z \tag{5.1}$$

$$\underline{\underline{D}} = r\, \frac{\partial v_\theta}{\partial z}\, \underline{e}_\theta \otimes \underline{e}_z + \frac{1}{2}\, \frac{\partial v_z}{\partial z}\, \underline{e}_z \otimes \underline{e}_z \tag{5.2}$$

According to the vertical boundary conditions RS tests can be divided in three different types corresponding to a system represented by $d\sigma_n = \frac{K}{t}\, du_n$ where t is the thickness of the interface and K represents its stiffness:

Case I: Constant normal load test (CNL test) in which $K = 0$, $d\sigma_n = 0$, $du_n \neq 0$ (similar to "drained conditions"),

Case II: Constant volume test (CV test) in which $K = \infty$, $d\sigma_n \neq 0$, $du_n = 0$ (similar to "undrained conditions"),

Case III: Constant normal stiffness test (CNS test) in which $K = cst$, $d\sigma_n \neq 0$, $du_n \neq 0$.

The simulated tests are described in Table 5.1.

The model parameters identification has been the subject of several papers using different strategies such as constrained optimization procedure [15] or the definition of correlations [49]. We have used the strategy developed at ECP ([72] [73] [50]) and already applied to several materials ([19] [39]). The presentation of this strategy is out of the scope of this work and we will recall only the important points. The model parameters can be classified differently depending on ones objective. As the model is a plastic one, a preliminary classification of evident parameters is:

- Elasticity parameters K, G, n_e, p_{ref}
- Plasticity and critical state parameters ϕ_{pp}, β, b, d
- Hardening parameters

  Shear mobilization a_1, a_2, m

  Volumetric strain ψ, a_ψ, c_1, c_2

  Breakage parameters a^{br}, m_a^{br}, b_{W_p}
- Initial state parameter p_{c0}

Among the above parameters there are those which are directly measured from the quantitative analysis of observed results, such as parameters of elasticity and perfect plasticity. There are also the parameters which are not directly measurable and which must be obtained through calibration. For the breakage mechanism only parameters which cannot be directly measured are introduced in the model and therefore should be identified by calibration. Given the nonlinear character of the model and the high number of parameters, there is a risk not to obtain a single set of parameters after calibration, especially if only one type of stress path is considered. Using correlations and understanding the physical model and its parameters is the only way to ensure proper calibration. To do this, we must add that the mechanisms are directly related to the loading path experienced by the soil. In practice, different types of tests are performed in the laboratory to characterize soils. They concern essentially triaxial compression or extension or shear tests under drained or undrained conditions. Resonant column tests are performed for geotechnical earthquake engineering applications where small strains prevail. For the application in which the present model is developed, drained or undrained triaxial and shear tests can be used to calibrate most of the parameters. However, some large strain shear tests are necessary for the calibration of the breakage mechanism parameters. The model parameters are summarized in Appendix F.

In this section the performance of the model and the influence of the grain crushing mechanism are studied by modeling ring shear tests as a boundary value problem where a

Laboratory tests (Undrained RS tests)			Void ratios	
Sand	Effective consolidation stress [kPa]	Relative Density [%]	e_{min}	e_{max}
OT sand	217	26		
OT sand	279	24	0.391	0.679
OT sand	29	23		
IR sand	646	28		
IR sand	541	29	0.464	0.757
IR sand	553	35		

Table 5.1: Laboratory tests details from [99]

localized shear band is generated. On one hand, real tests are simulated numerically and the obtained results are compared to those measured during the experiment to validate qualitatively and quantitatively the model. On the other hand, different boundary conditions, similar to those encountered in the soil surrounding a pile are simulated to study the effect of this mechanism on the shear stresses and therefore the shaft resistance of the pile.

Model validation

We will first model the undrained RS tests (CV test) performed on Ottawa (OT) and Illinois River (IR) sands by Sadrekarimi and Olson [97]. Unfortunately, their drained (CNL) tests cannot be used as some incoherences are observed due to rotation of the lever arm.

The results from the RS tests are analyzed considering two different final strain levels at the shear band. In terms of volumetric variation the results are validated considering the two critical state lines, "crushed and uncrushed", at very high shear strains (see Sadrekarimi and Olson [99]). The measurements in the stress space and shear strains to stress are analyzed considering lower ranges of strain (in the order of 20 cm of displacement at the bottom). This simulation (Figures 2 and 3) shows the ability of the proposed constitutive model to replicate both the "critical state line" at usual shear strain levels known in geotechnical testing and at an extreme shear strain value where the breakage mechanism has a predominant role. These results imply that the critical state (deformation at constant volume) is much further away in terms of strain than the model predicts. This formulation allows for the capture of the observed behaviour of the soil specimen at high shear strains. The change in the slope of the critical state line from the "uncrushed" to the "crushed" state is also taken into account by means of the evolution in the parameter β.

Note though that the proposed model is indeed capable of reproducing the stress-strain relation at very high strains which follows and inversed hyperbola-shaped curve. Figure 4 shows the evolution of normal and shear stresses during an undrained RS test of IR sand for a vertical stress of 334 kPa with tangential displacement represented in a logarithmic scale.

The stress planes are now analyzed with results from undrained RS tests on Ottawa sand. Figures 5 and 6 show the evolution of stresses and plastic volumetric variation (at different heights of the mesh) during the simulated undrained shear test. Note that $\dot{J}^p$

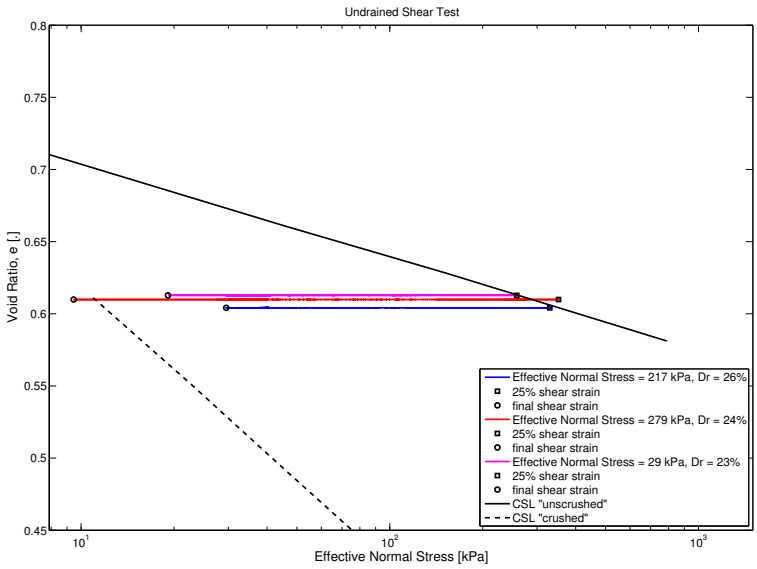

Figure 2: σ'_n - e (void ratio) with critical state lines from Sadrekarimi and Olson [99] for Ottawa sand

is the plastic variation of the Jacobian where $J = det\underline{\underline{F}}$. Three lines are present in the figures which correspond to the laboratory results found by Sadrekarimi and Olson [97] the results from the original model and those of the proposed model. When considering an undrained RS test, the variation of the normal stress is "controlled" by the elastic volumetric deformation of the specimen which will in turn determine the increase or decrease of the effective normal stress. The plastic volumetric variation of the specimen can be seen in figure 6. This figure clearly shows that the proposed constitutive formulation successfully reproduces the second phase transformation point in the shear band when the behaviour switches, from dilation to contraction, that was observed in laboratory tests while the original formulation does not. Note that despite continuity of stresses there is discontinuity of strains in the specimen as a result of localization. The different volumetric behaviours found are consistent with the laboratory data where the second phase transformation is only seen in the shear band where particle breakage is found to occur. The discontinuity in displacements can be seen also in figure 7 where the tangential and normal displacements for each section of the specimen are shown (the shear band is left out due to reasons of scale). Note that once localization occurs no tangential displacement is observed since shear strains are only developing at the shear band just as the experimental data show. The dilation at these levels is a result of the constant volume condition of the test imposed by the boundary conditions since the shear band is contracting.

The second phase transformation can be seen also clearly in the stress plane in figure 5. Sadrekarimi and Olson [96] describes this as competing shearing mechanisms which are found to be at play: dilation and particle damage (contractive behaviour) usually starting with dilation in a more important role leading to a shear resistance increase until the second phase transformation and finally ending with net contraction due to particle damage

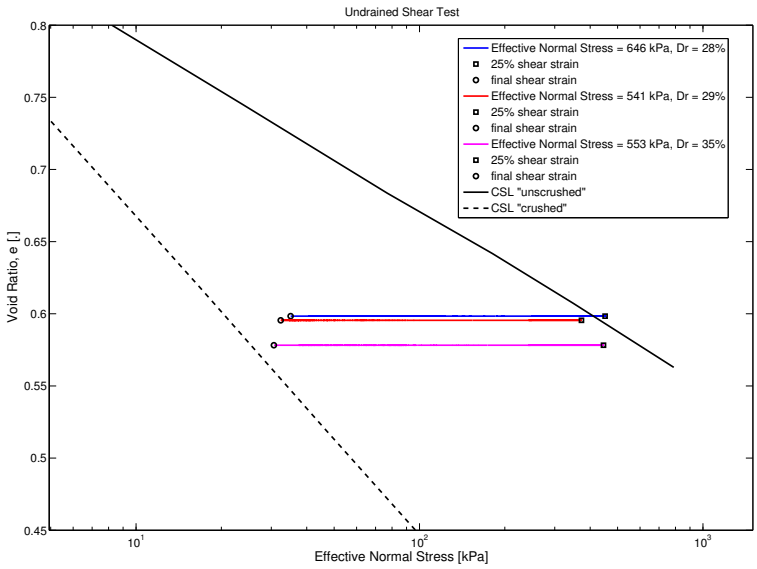

Figure 3: σ'_n - e (void ratio) with critical state lines from Sadrekarimi and Olson [99] for Illinois River sand

and decrease in shear resistance until reaching the critical state. Laboratory tests show that once in the stress space, the loading path reaches the critical state line (CSL) the ratio between the shear and normal stress does not change, thus, the stress path does not deviate from the CSL. The proposed constitutive relation is accurate in simulating this behaviour. Similar trends are found for Illinois River (IR) sand in undrained shear and the results are presented in Appendix G of this work.

In the figures presented the caption of the figures show u_t and not the shear strain as it is usually the norm in presenting these curves. This is due to the fact that the definition of strain in finite deformation is not straightforward and the sum of the increments of the vector $\underline{\underline{D}}$ has no direct physical meaning as total strain.

Finally, note that the criteria for the activation of the evolution of the breakage parameter is verified in the stress paths for both sands. However, results from other RS tests and for tests with different stress paths have been found to show particle breakage (results from Okada et al. [89] are an example of that). To consider the triggering mechanism proposed herein would be erroneous to simulate those findings. The need and choice of the triggering mechanism is brought into question. A possible solution is to consider the mechanism active from the start of loading (as the constitutive models presented by Cecconi et al. [14], Salim and Indraratna [100] and Hu et al. [55], among others, consider) meaning that an evolution of the gradation curve exists even at relatively small strains.

Role of stress path

The constant volume condition is the equivalent of considering an infinite constant

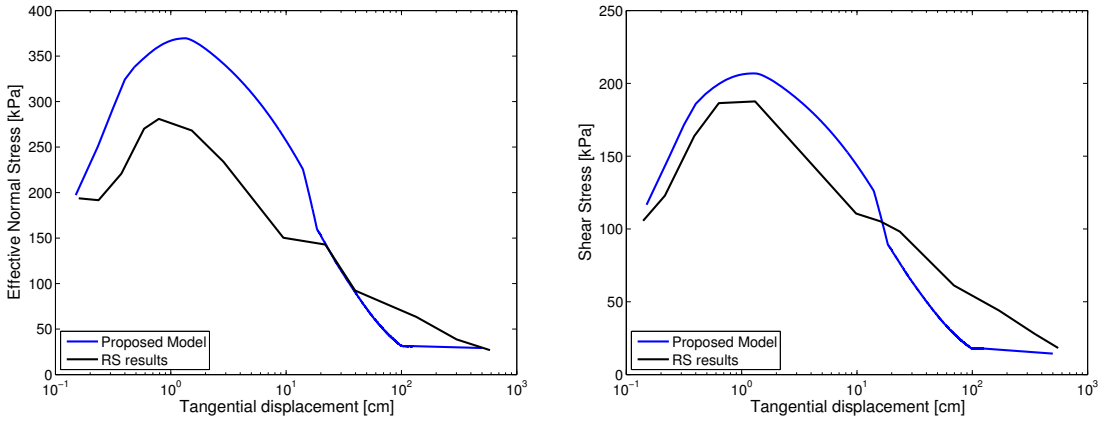

Figure 4: Illinois River sand : u_T - σ'_n and u_T - τ

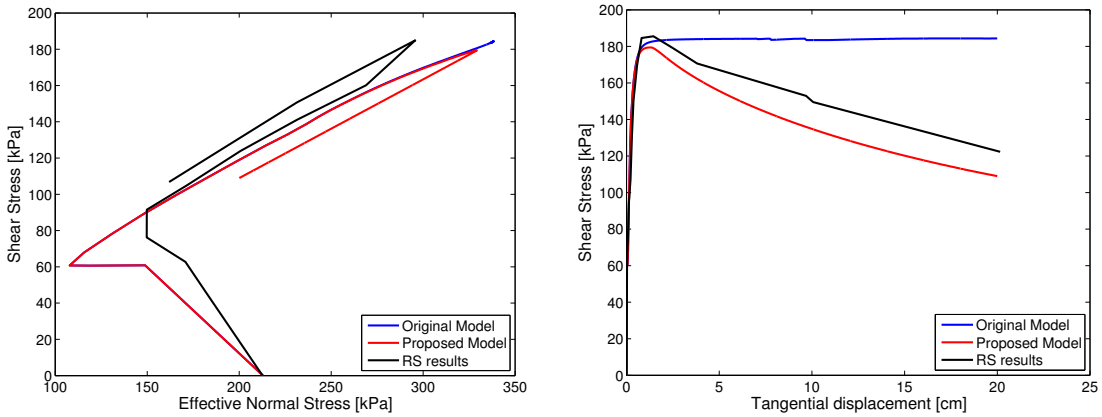

Figure 5: Ottawa sand : σ'_n - τ and u_T - τ

normal stiffness (CNS) condition. This is not, however, the case at the soil-pile interface. The stiffness imposed by the soil at the interface of the pile is finite (albeit very high) and the results will differ due to this. A RS test with a CNS condition might, therefore, be a better representation of the loads applied to the soil at the pile interface level. The CNS condition is achieved in finite element modelling by placing an elastic element with a given stiffness on the bottom of the model. The stiffness considered is of 2.96 MPa (bulk modulus) and the constitutive model of the specimen is that of OT sand. The constant normal load boundary condition (CNL) is also here considered in order to define both limit boundary conditions for a simple shear test - constant volume and constant normal load. The CNL test consists of shearing without any displacement condition in the bottom of the specimen while maintaining a constant normal load. The results for a CNS condition type RS test are presented here comparing the results with those found for the constant volume and constant normal load simulations.

The stress and strain paths shown are typical of a shearing test for each respective

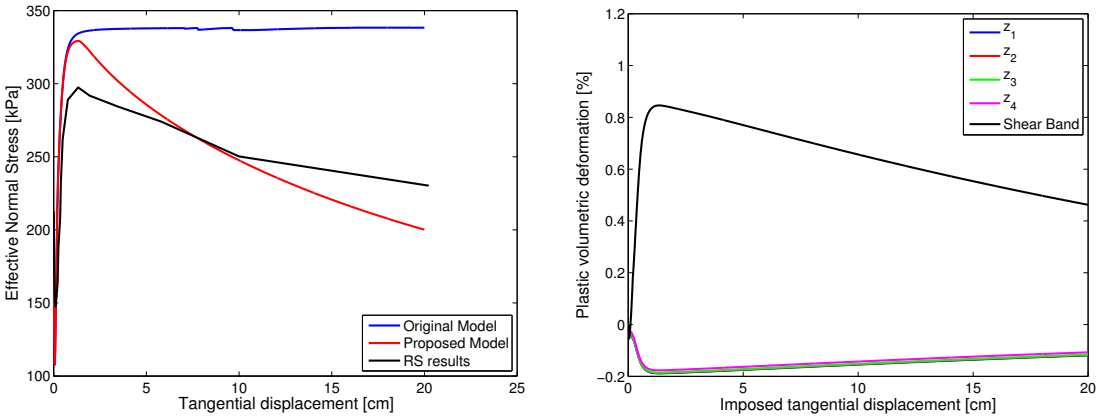

Figure 6: Ottawa sand : u_T - σ'_n and u_T - J^p

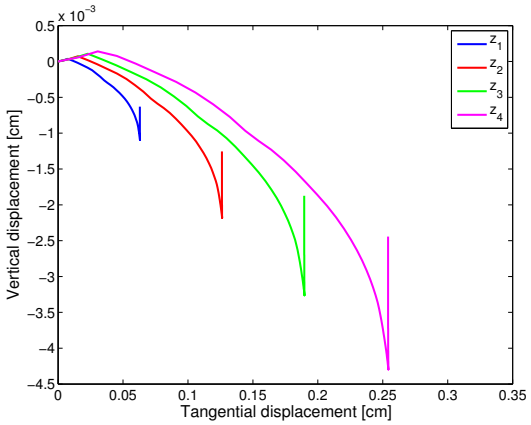

Figure 7: u_t - u_n

boundary condition (figures 8 and 9). Note that the critical state line in stress space is verified by all tests and that the second phase transformation is found to occur at the same level of tangential displacement as well. However, in terms of stress the second phase transformations occurs at different intervals as a result of the different boundary conditions. In the CNS and CNL cases, because dilation is not restricted by a rigid boundary condition, it allows for higher volumetric expansion of the specimen (figure 9). Also, the evolution of crushing is shown to vary in magnitude for each test. The degradation of the specimen, represented by the plastic volumetric variation, has a higher gradient in relation to the imposed tangential displacement for both the CNS and CNL tests than at the constant volume test. Not only the gradient but also the total contraction of plastic volumetric deformation is found to be higher in the CNL and CNS cases than the constant volume case. Similar results were found in laboratory testing (Okada et al. [89] and Sadrekarimi and Olson [97]) when comparing undrained and drained tests. It was found that there was considerably more contractive volume change in drained tests than in undrained tests due to grain breakage. This trend is also observed in the simulation per-

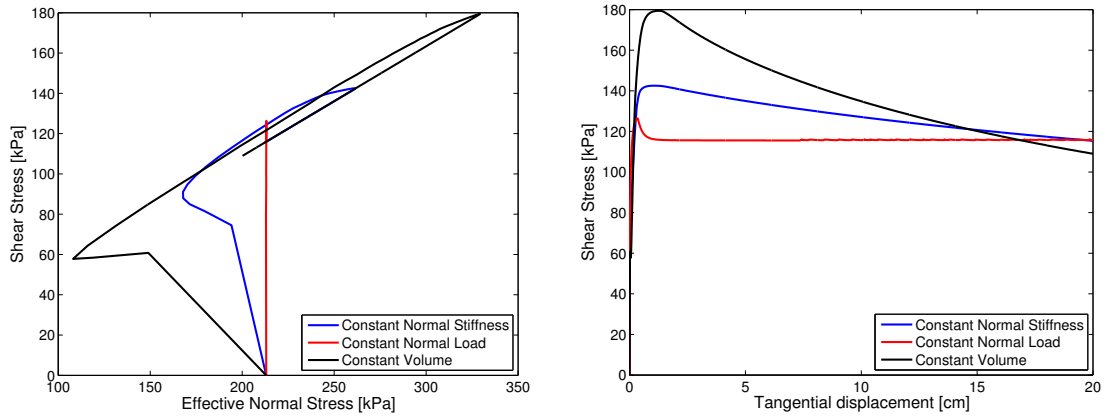

Figure 8: Ottawa sand : σ'_n - τ and u_T - τ

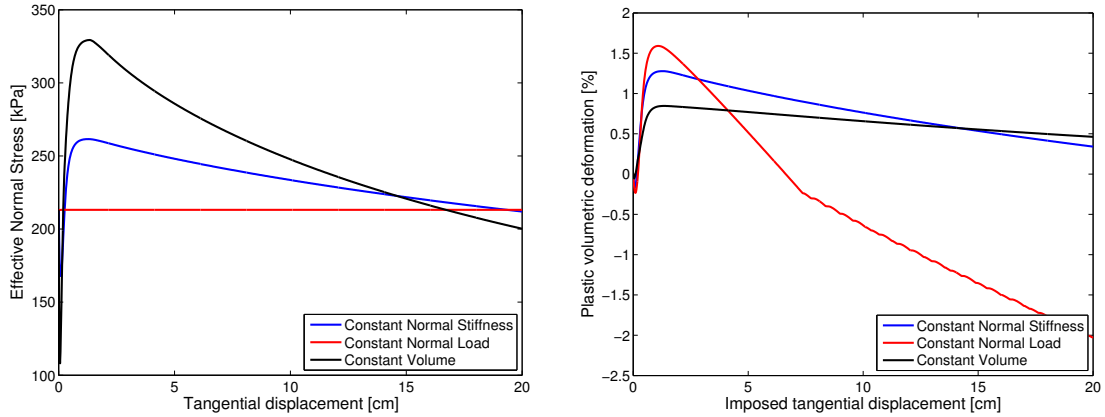

Figure 9: Ottawa sand : u_T - σ'_n and u_T - J^p

formed here. Since the CNS condition is an intermediate case between perfectly drained and undrained conditions it is only logical that more crushing is found in CNS test than constant volume tests.

5.2 Numerical simulation of cyclic shear tests

The cyclic behaviour of soil (granular materials) subjected to shear strains and stresses has been the focus of various studies, both experimental and numerical. In this section, numerical studies considering the soil column finite element model subjected to cyclic shear loading are analyzed. The purpose of this study is the simulation of the layer at the soil-pile interface level during cyclic installation or loading paths which involve cyclic motion. These include jacked (one-way cyclic) or two-way cyclic installation procedures as well as cyclic loadings after installation. The tests presented henceforth were defined to study the effect of test type, cycle amplitude effects, influence of the initial stress state

and relative density of the soil and the consideration of the breakage mechanism in the constitutive model.

The cyclic test presented in the following figures considers a two-way cycling shear motion which has a first amplitude of 2cm and then amplitudes of 3cm in alternating directions considering CV, CNL and CNS boundary conditions.

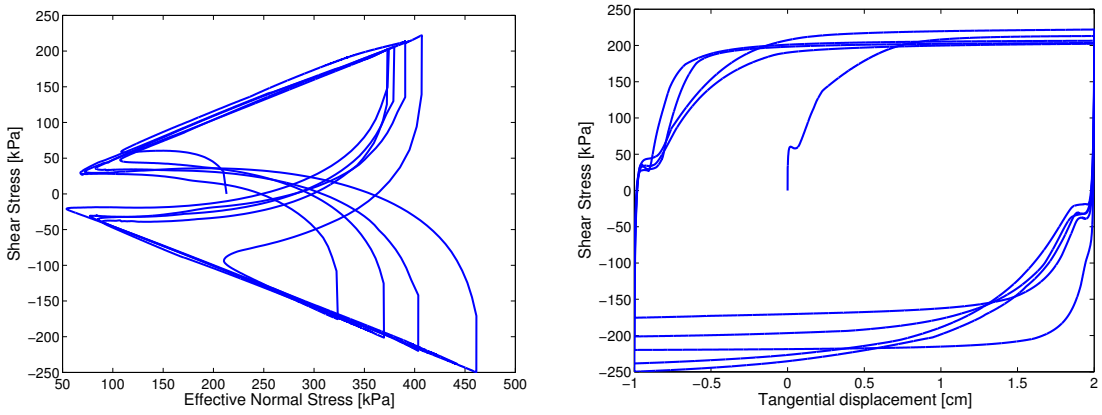

Figure 10: Ottawa sand - CV : σ'_n - τ and u_T - τ (breakage inactive)

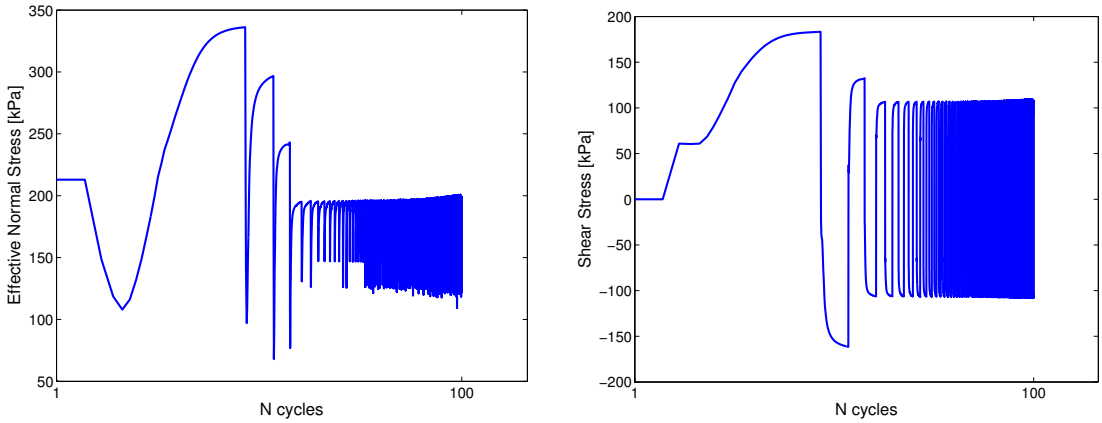

Figure 11: Ottawa sand - CV : N *cycles* - σ'_n and N *cycles* - τ (breakage inactive)

Firstly the simulations considering a CV boundary condition are presented. Figure 1 is the reference picture for the different heights of the specimen studied. Marked contraction is observed before the first phase transformation and is then followed by dilation. The stress paths climb the failure line in both directions of shear displacement with intermediate "collapses" in the shape of butterfly wings. Some small oscillations in the curves occur due to the proximity to the zero normal stress state as a result of the low initial relative density of the soil which influences the stress path. However, a stabilization can clearly be noted in the results after a small number of cycles.

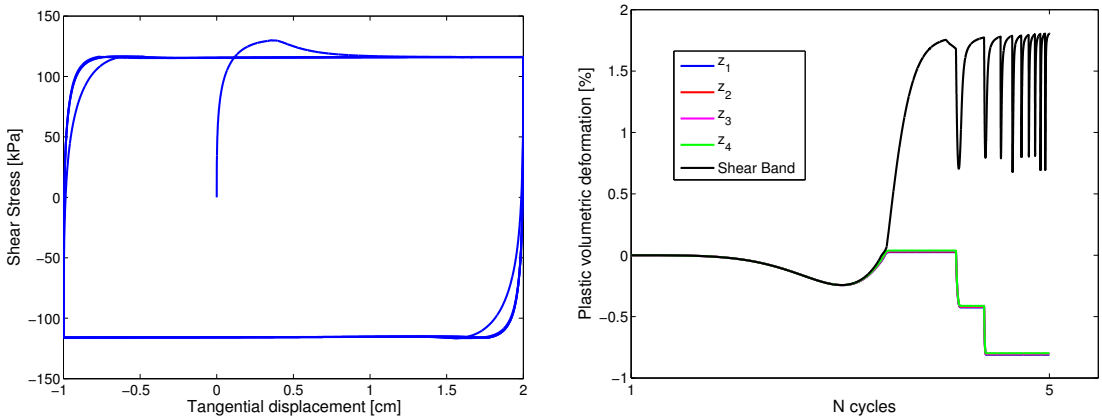

Figure 12: Ottawa sand - CNL : u_T - τ and N *cycles* - J^p (breakage inactive)

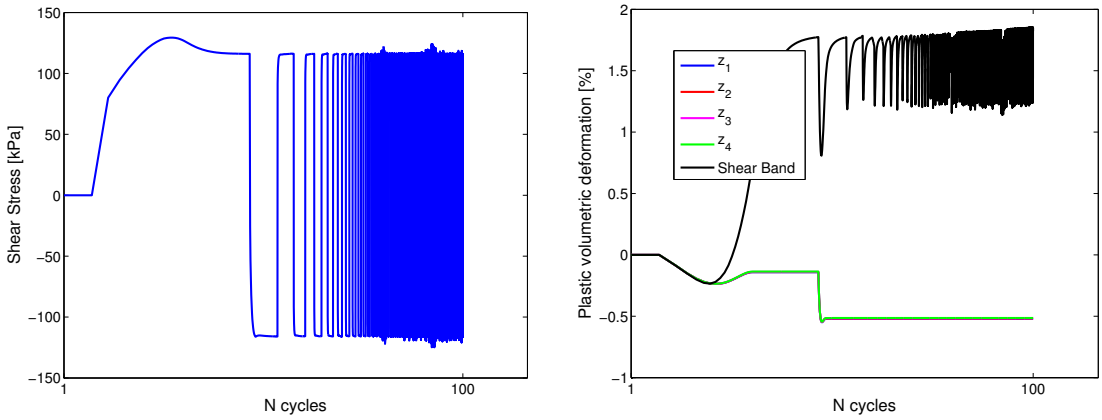

Figure 13: Ottawa sand - CNL : N *cycles* - τ and N *cycles* - J^p (breakage inactive)

Secondly the simulations considering a CNL boundary condition are presented. The normal stress is never shown in the figures since no variation is observed with the assumed boundary condition of CNL. Once more shear stress stabilization is observed as well as plastic volumetric deformation after a small number of cycles. The failure line is consistently reached in both directions of loading.

Finally the simulations considering a CNS boundary condition are presented. The results found in the CNS case can be interpreted in much the same way as the CV case.

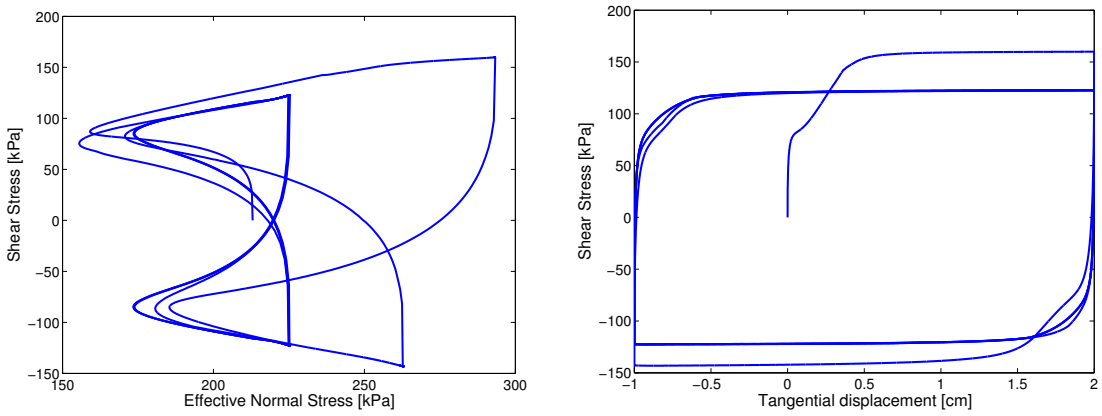

Figure 14: Ottawa sand - CNS : σ'_n - τ and u_T - τ (breakage inactive)

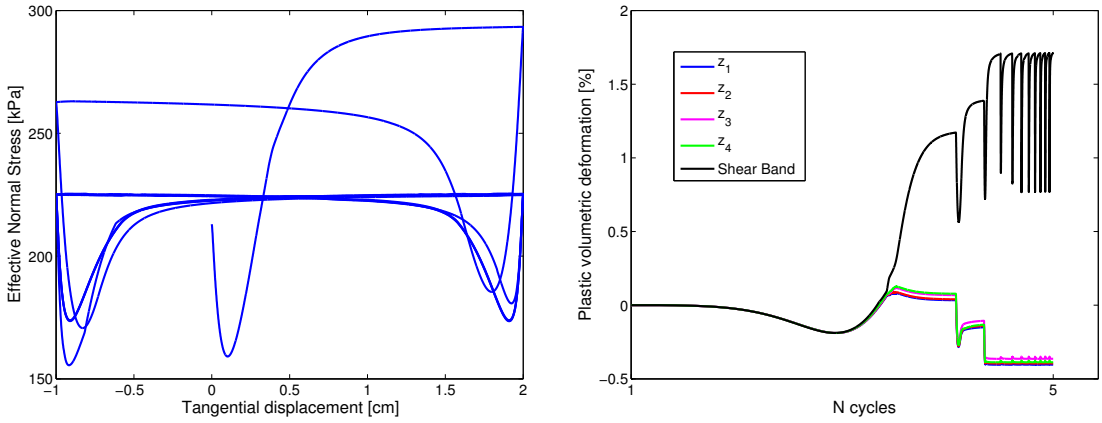

Figure 15: Ottawa sand - CNS : u_T - σ'_n and N *cycles* - J^p (breakage inactive)

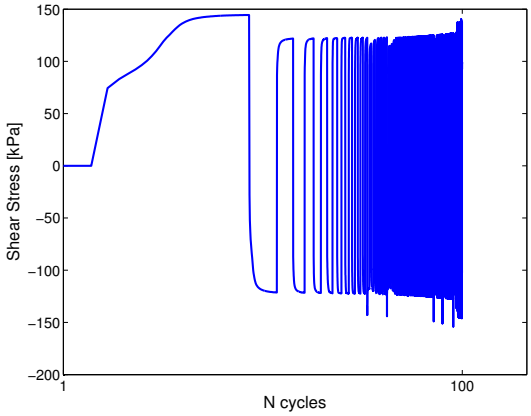

Figure 16: Ottawa sand - CNS : N *cycles* - τ (breakage inactive)

The previous stress paths followed describe the typical behaviour of soil specimens when subjected to cyclic loading with relatively high displacements for different boundary conditions. For the initial state considered, the contraction-dilation transition is seen to occur repeatedly with the cycles and a limit state of volume change can be seen after only a small number of cycles. This limit state is characterized by the mobilization of the same contraction and dilation in each cycle as well as the same shear and normal stress values. This behaviour, in qualitative terms, is independent of number of cycles and of the magnitude of the displacements. No breakage was considered in these simulations and one can notice the absence of any "fatigue" in terms of shear and normal stress mobilization even for the simulations with a higher number of cycles. In fact, the only way to observe the known phenomenon of "friction fatigue" considering the ECP constitutive model, without the breakage mechanism, is to consider very small cycle amplitudes. In that case, very little or no dilation is observed since the strain necessary for the phase transformation from contraction to dilation is either not reached or not large enough to produce net volume increase in the cycle [21]. Since net contraction will be the result of such loading, an increasing number of cycles will produce more pronounced decreases in the normal stress in CV and CNS conditions (cyclic mobility). The net contraction per cycle depends on the amplitude of the first cycle since it determines the position of the stress state in relation to the critical state line. This is undoubtedly one of the mechanisms which can produce "friction fatigue" as can be shown from figures 17 and 18 where low amplitude cycling of Toyoura sand was simulated after an initial higher shear displacement in order to maximize the fatigue observed. The soil considered (Toyoura sand with a relative density of 93%) is the same as the one used by D'Aguiar et al. [21] in the study of friction fatigue due to low level cycling in non-displacement piles. The model parameters can be found in Appendix F.

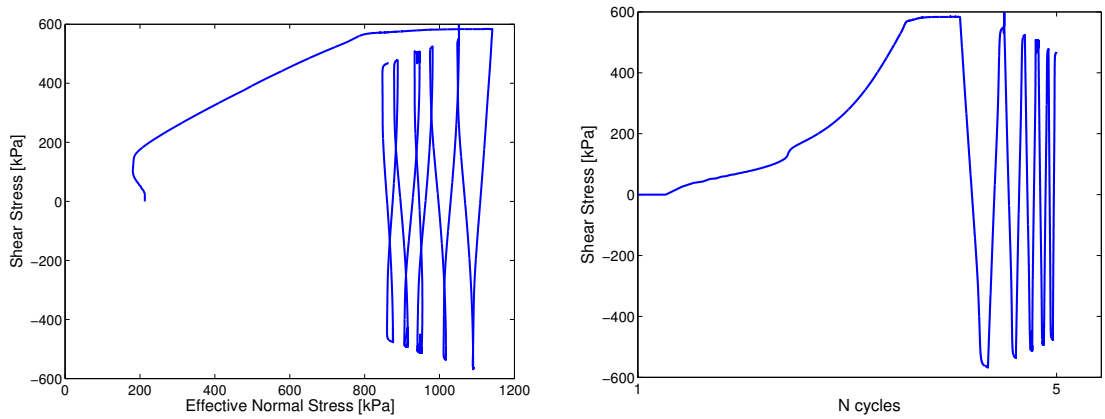

Figure 17: Toyoura sand - CNS : σ'_n - τ and N *cycles* - τ (breakage inactive)

Marked decreases in both normal and shear stresses can be observed as a result of contraction at the interface level. This conclusion must be considered with caution. Thermodynamic considerations come into play since this cumulation of contraction does not seem to have any imposed limit on the model which might then result in non-realistic

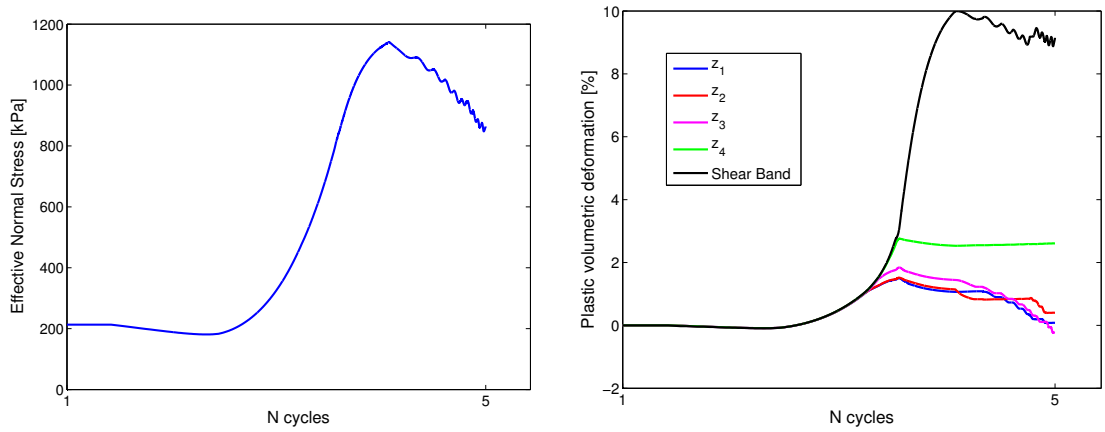

Figure 18: Toyoura sand - CNS : N *cycles* - σ'_n and N *cycles* - J^p (breakage inactive)

results concerning volumetric variations. This would be in disagreement with laboratory observed results where the rate of compression decreases with increasing cycles [32].

However, Fakharian and Evgin [32] and White and Lehane [118] showed that another mechanism exists which develops friction fatigue in piles and interfaces. It is found that the rate of degradation (decrease in normal stress at the pile shaft) depends not only on the number of cycles but also the amplitude of these cycles. Two-way cycling is found to lead to greater and faster degradation since it is more arduous than one-way cycling. Therefore, higher cycle amplitudes will result in higher degradation. This can be seen in figure 19 where a limiting value of normal stress is found in one-way cycling while it tends to zero in the two-way cycling loading at the soil-pile interface level.

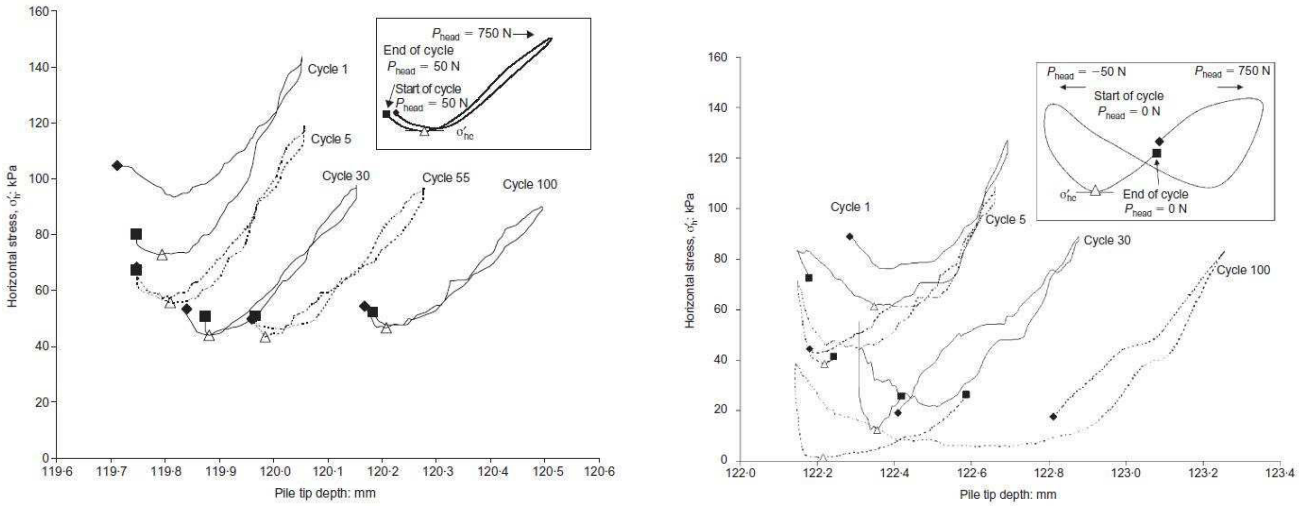

Figure 19: Horizontal stress degradation during one-way and two-way cyclic compression test in a jacked pile [118]

A comprehensive study of interface cyclic shear tests, between sand and steel, considering a CNS boundary condition was performed by Fakharian and Evgin [32]. The degradation which occurs at the pile shaft during two-way cycling loading is replicated by CNS shear tests. This degradation is shown by the reduction of shear stress. This is a consequence of decreasing effective normal stress due to compressibility (e.g. particle crushing) of the soil but also to the increased amount of mobilized sliding displacements at the interface with an increasing number of cycles. The boundary condition combined with the compressive behaviour of the soil forced the reduction of the normal stress in order to maintain the constant normal stiffness condition. Shear stress decrease follows (friction fatigue phenomenon) as a consequence. These results can be seen in figures 20 and 21 where each cycle has a duration of 200 seconds.

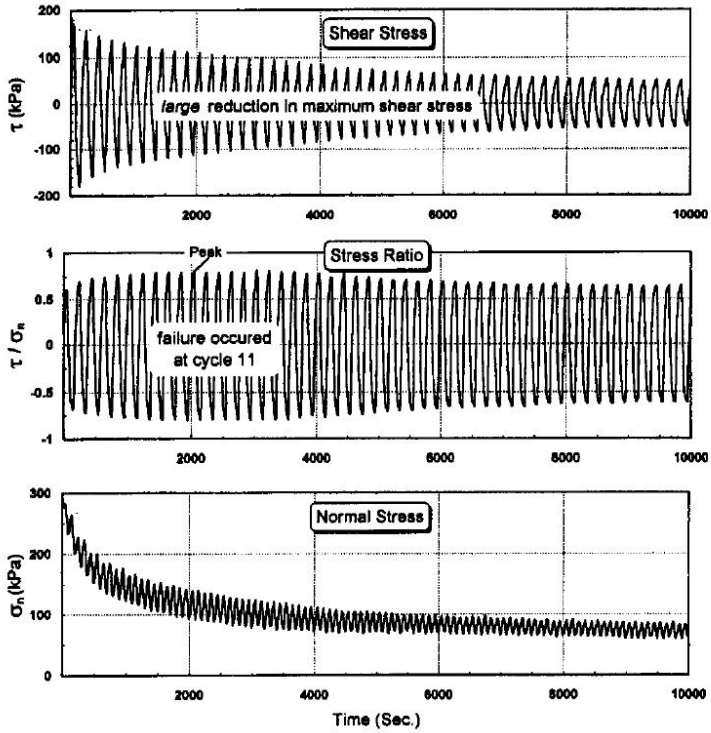

Figure 20: Variations of shear stress, stress ratio and normal stress [32]

A rapid and considerable reduction in both shear and normal stress can be seen in the results after which a residual value is reached. The maximum shear stress begins to decrease right after cycling starts and the rate of reduction is higher during the initial cycles. The rate of decrease in maximum stress is considerably affected by the magnitude of the tangential-displacement resulting in faster degradation after peak shear stress is reached. This is considered by Fakharian and Evgin [32] to explain the degradation of shaft resistance of axially loaded piles subjected to two-way cyclic axial displacements.

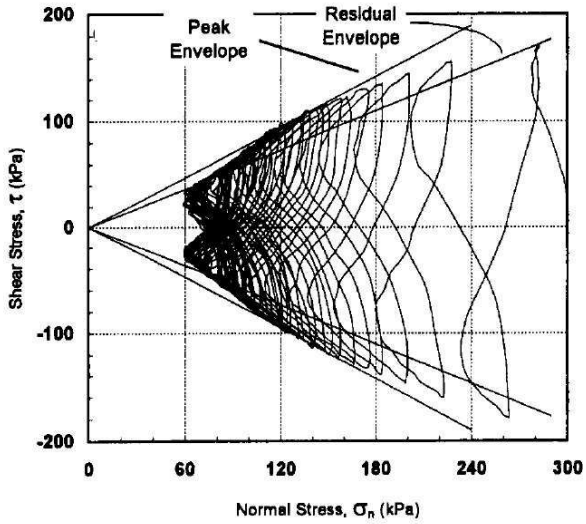

Figure 21: Stress path in τ - σ'_n space [32]

This cyclic degradation was also observed by Tsuha et al. [110] which considered it to be the result of a combined effect of plastic behavior in the soil mass and the gradually thickening and fracturing of interface shear zone (also observed by Yang et al. [125] in monotonic ring shear tests).
This degradation in shear and normal stresses observed in large amplitude cycles can only be simulated considering the breakage mechanism in the revised ECP constitutive model. Similarly to the results obtained from monotonic ring shear test simulations, the breakage mechanism will be able to correctly model the irrecoverable contraction at the interface level due to particle crushing. This degradation will in turn result in the decrease of normal and shear stresses with increasing number of cycles and of cycle amplitude as observed in laboratory tests.

The following results consider Ottawa sand subjected to high level shear cycling (same amplitude as before) for 5 (figures 22 and 23) and 100 cycles (figures 24 and 25). The results now show the decrease in an inverse-hyperbola form for both normal and shear stresses. Also, net contraction with cycling can now be simulated at the interface level for high amplitude cycles. Such as for monotonic loading, the magnitude and gradient of variation on the degradation of the stresses can be controlled by the parameters in the breakage mechanism proportional with the evolution of plastic volumetric deformation.

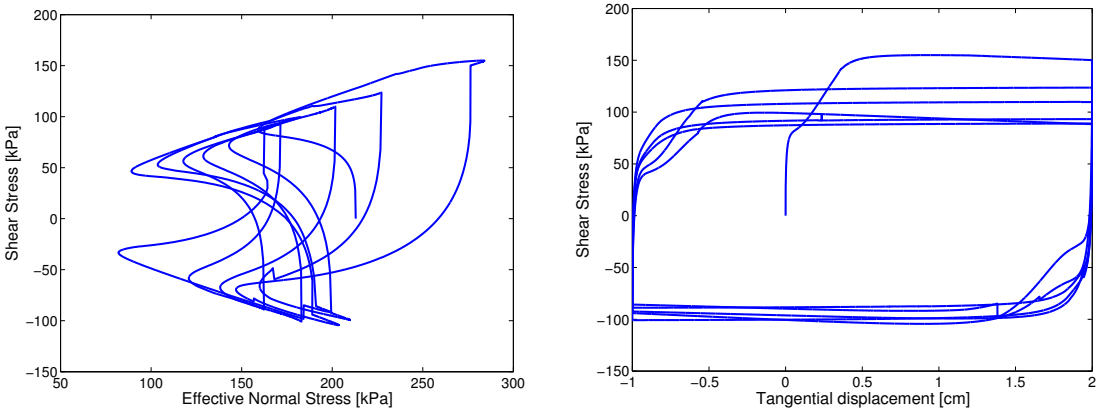

Figure 22: Ottawa sand - CNS : σ'_n - τ and u_T - τ (breakage active)

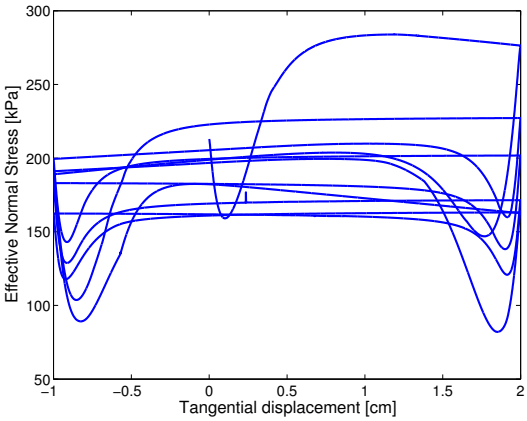

Figure 23: Ottawa sand - CNS : u_T - σ'_n (breakage active)

These results show a remarkable resemblance to those found by Fakharian and Evgin [32]. Since the breakage internal variable r_{br_k} evolves according to an isotropic hardening law, the "degradation" which is observed in the previous results is irreversible. This is taken to be physically coherent because particle breakage causes an irrecoverable volume decrease in the soil which must in turn, for CV and CNL boundary conditions, result in a decrease in both mobilized normal and shear stresses. Moreover, shaft resistance mobilization results from cyclic loading of piles show an irrecoverable shaft resistance decrease when performing constant amplitude cycles as well [110].

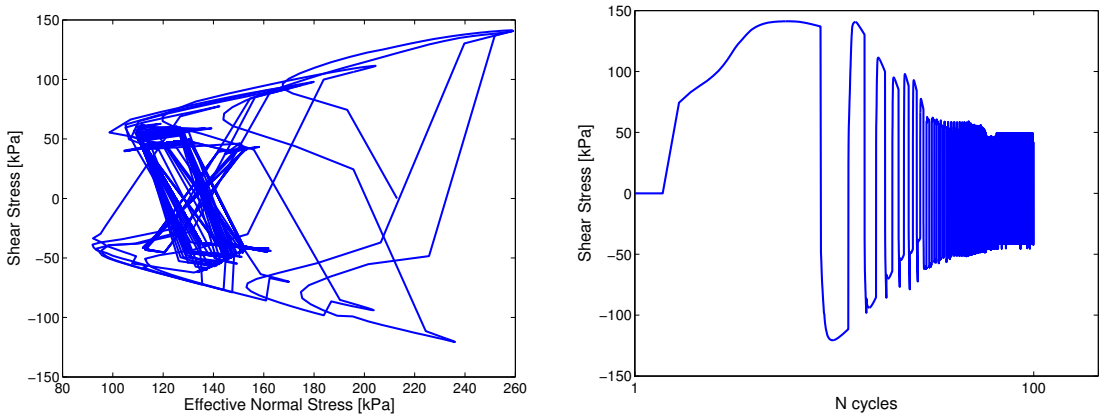

Figure 24: Ottawa sand - CNS : σ'_n - τ and N *cycles* - τ (breakage active)

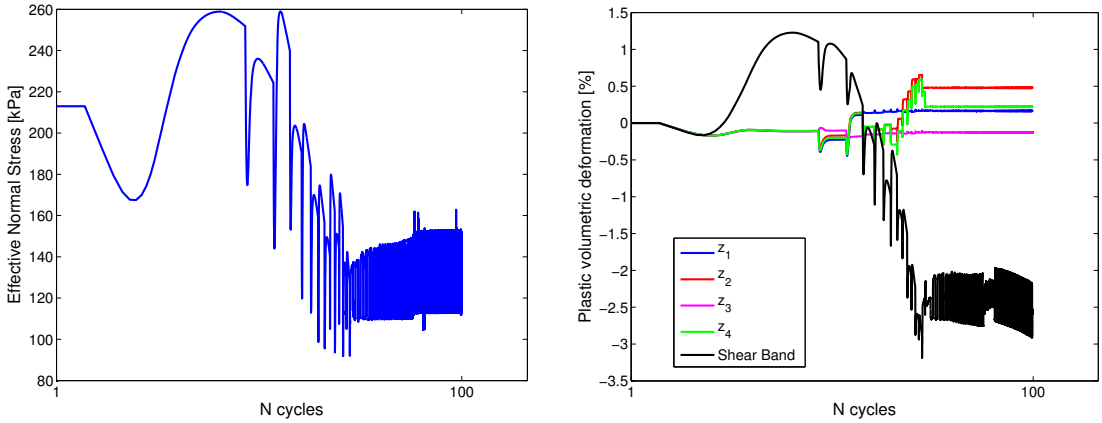

Figure 25: Ottawa sand - CNS : N *cycles* - σ'_n and N *cycles* - J^p (breakage active)

Influence of the initial state

The initial state can be considered to depend mainly on the relation between the initial normal stress and pre-consolidation stress. These two effects will studied separately.

In order to study the influence of the initial stress in the response of soil when subjected to cyclic shear loading CNS tests, different normal stresses were simulated. This simulation seeks to study the influence of depth in the case of the pile-soil interface. The results presented here are for an initial normal stress of 50kPa subjected to the same cycles as before. As can be seen from figures 26, 27 and 28 no major changes in behaviour are present concerning the degradation of shear stress with an initial mean pressure of 50kPa. However, due to the initial high dilative behaviour as a result of the low initial mean pressure state, the net contraction due to particle breakage considering only 100 cycles does not result in global contraction. Therefore, no decrease in normal stress when compared to the initial value is observed. This results in a decrease in the ratio of normal stress and shear stress as seen in figure 29 as a consequence of the degradation of the soil

at the interface level.

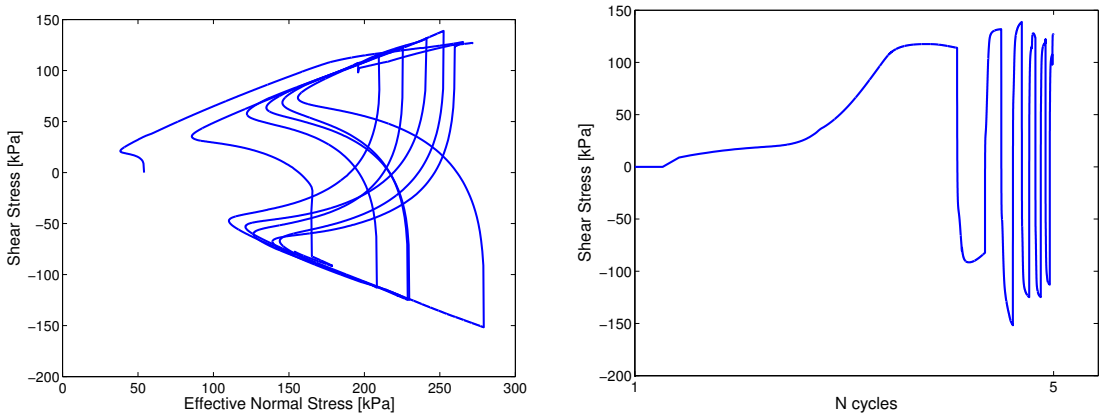

Figure 26: Ottawa sand - CNS : σ'_n - τ and N *cycles* - τ (breakage active)

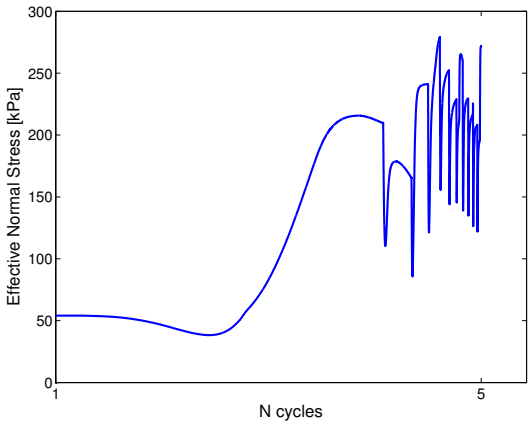

Figure 27: Ottawa sand - CNS : N *cycles* - σ'_n (breakage active)

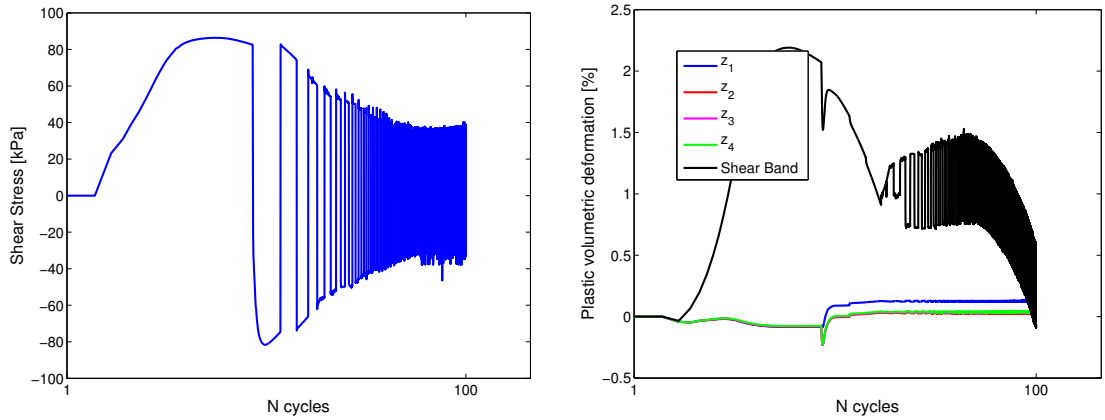

Figure 28: Ottawa sand - CNS : N *cycles* - τ and N *cycles* - J^p (breakage active)

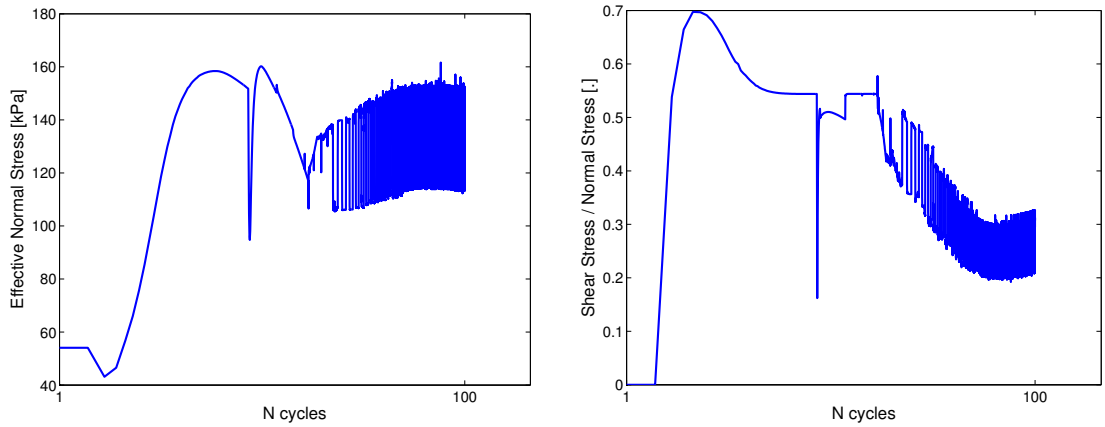

Figure 29: Ottawa sand - CNS : N *cycles* - σ'_n and N *cycles* - $|\tau|/\sigma'_n$ (breakage active)

In the volumetric deformation stress space, the slope between the normal stress and volume change is kept constant since no significant variation of the parameter β occurs. This can be seen in figure 30 where, for different initial normal stresses, the slope is shown to be the same even after severe degradation is observed.

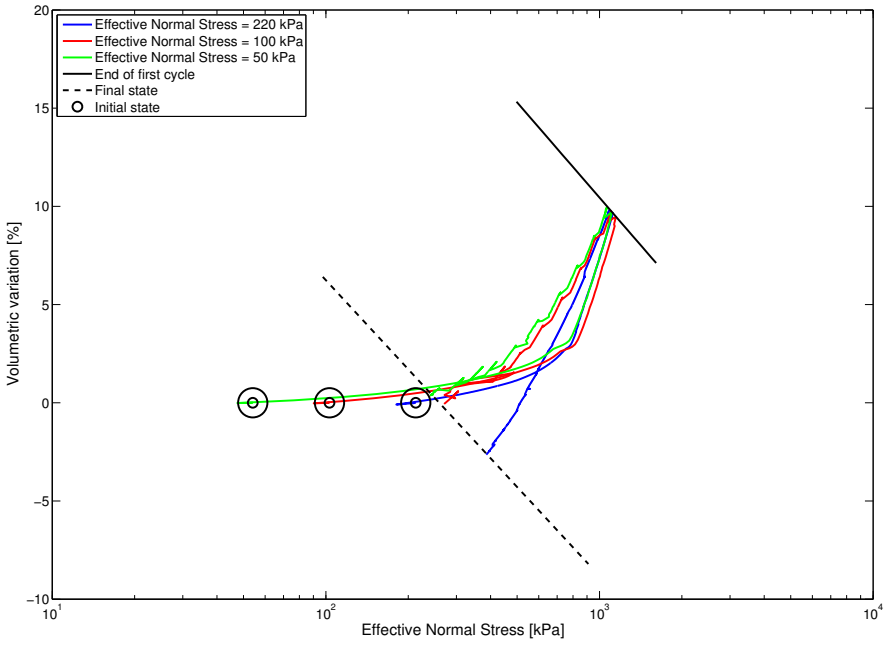

Figure 30: σ'_n - $\dot{J}$

The effect of the relative density of the soil on its cyclic behaviour will be studied here.

Considering the ECP constitutive model, the initial relative density is taken into account mainly through the parameter p_{c0}. The model parameters for Ottawa sand with a higher initial relative density result in a very substantial increase in the p_{c0} which in turn affects considerably the increment of plastic volumetric deformation variation. This influence on the volumetric variation is verified for both the dilative as well as for the contractive behaviour as can be seen in Figure 31 where different relative densities are considered by changing the parameter p_{c0} (ratio of $3,5$ between the p_{c0} of the different tests). It can be seen that for the denser soil more dilation is observed during the initial loading but also more contraction is observed during the degradation with increased number of cycles [32] [97].

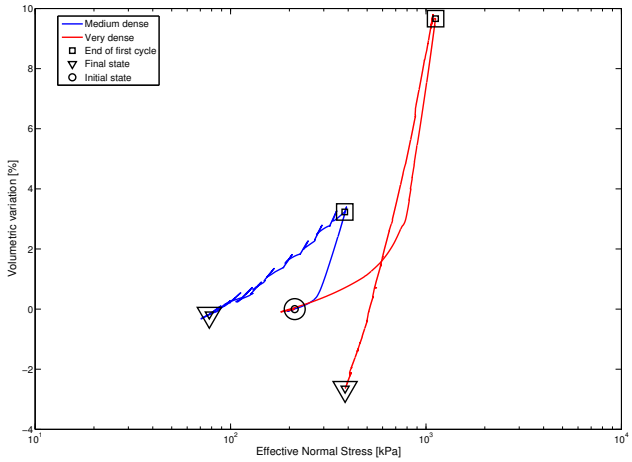

Figure 31: σ'_n - $\dot{J}$

The decrease observed in normal and shear stress is, therefore, quite substantial (Figures 32, 33 and 34). Some small oscillations in the curves occur due to the proximity to the zero normal stress state when nearing the final cycles. It must also noted that, due to the considerable increase in the parameter p_{c0}, the breakage mechanism has a strong influence on the stress path. This can be seen in figure 32 where the stress path shows that the ratio between normal and shear stress decreases.

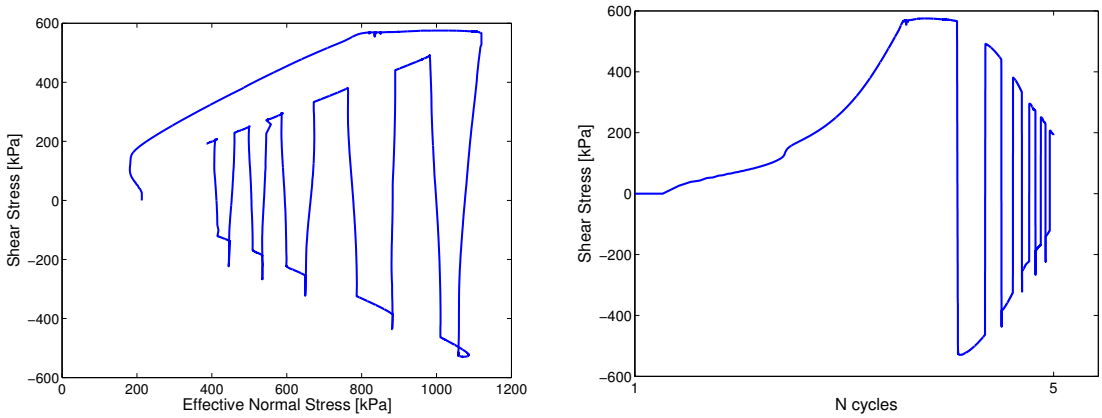

Figure 32: Very dense sand - CNS : σ'_n - τ and N *cycles* - τ (breakage active)

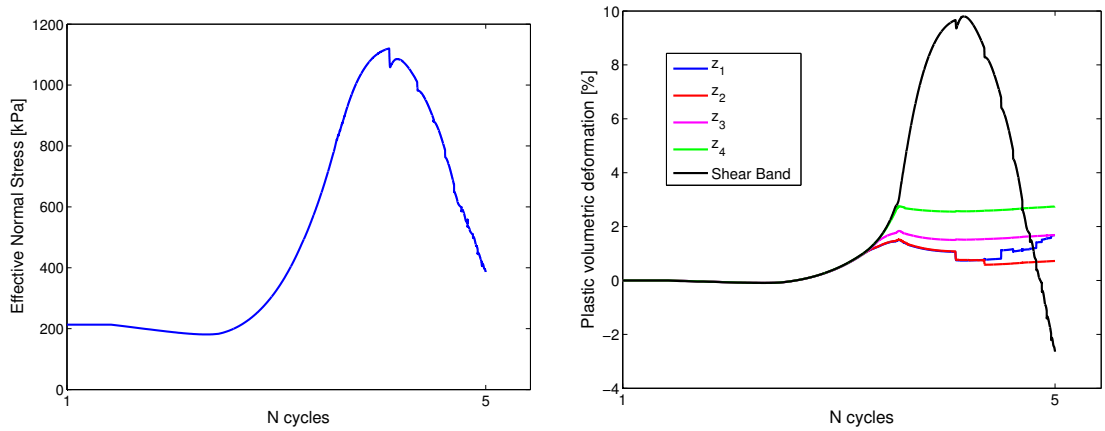

Figure 33: Very dense sand - CNS : N *cycles* - σ'_n and N *cycles* - J^p (breakage active)

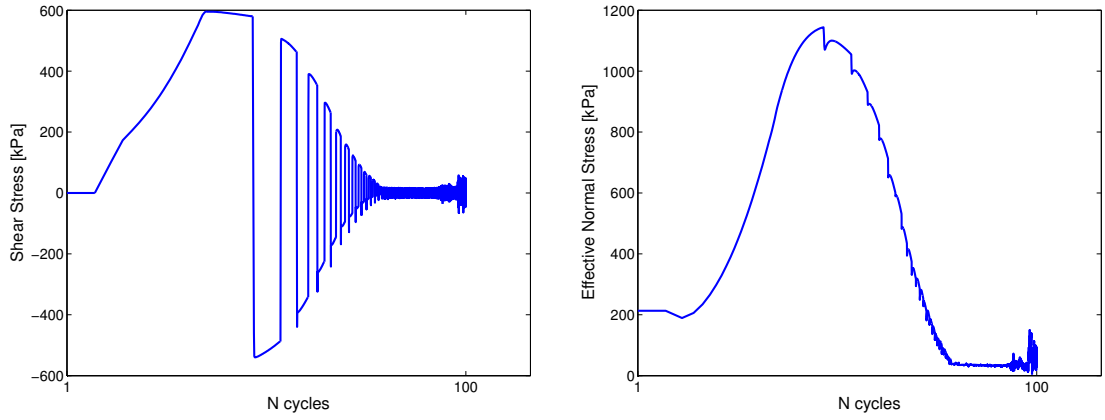

Figure 34: Very dense sand - CNS : N *cycles* - τ and N *cycles* - σ'_n (breakage active)

5.3 Summary

This Chapter was concerned with the simulation of monotonic and cyclic shear tests using the finite element code GEFDyn in which the enhanced constitutive model was implemented. The limitations of existing constitutive models in replicating the results from ring shear tests when considering high levels of shearing shown. The proposed internal variable and its evolution rule, as well as the triggering mechanism based on the detection of the beginning of instability, are shown to be successful in simulating the stress-strain relationship in ring shear tests. Constant volume, constant normal load and constant normal stiffness conditions were applied to highlight the capability of the model to capture interface non-linear behaviour for different stress paths.

Cyclic shear tests were also conducted in order to study the phenomenon of "friction fatigue" commonly observed in pile shaft mobilization under cyclic loading. A fundamental analysis of the issue is considered by simplification of the pile shaft problem with a soil column model. Considering high amplitude cycles, the ability of the revised constitutive model to replicate qualitatively the physical phenomenon of friction fatigue, which influences the degradation at the interface level due to cyclic shearing, is shown. The different stress paths by which normal and shear stress decrease can be observed in cyclic shearing were successfully captured by the numerical model in the simulations presented.

The mechanism introduced in the model can, without lack of generality, be applied to the other ECP elastoplastic constitutive models family based on the same theoretical and physical principles (e.g. interface elements).

Chapter 6

Numerical analysis of pile foundations

This chapter is concerned with the numerical simulation of different installation procedures as well as monotonic and cyclic axial loading of single isolated cylindrical piles. This numerical simulation will be performed using the finite element code GEFDyn. As shown before, some types of pile installation and other special loading cases have to tackle large strains in the finite element structure. An adaptation in the standard finite element method as well is considered and detailed here. Moreover, a new numerical integration was implemented in the behaviour law for the interface elements in order to obtain a converged solution for the installation, both the monotonic and cyclic loadings cases. This chapter will then serve to describe how the different materials and finite elements are modelled taking their respective constitutive laws and parameters. The importance of the soil-pile interface behaviour during installation is shown namely by the relevance of introducing the breakage mechanism in the constitutive model. Also, the model geometry and boundary conditions will be described as well as how the pile installation is modelled in a step by step method. The domain of validity and applicability of the model will be discussed along with the presentation of results from the numerical simulations and their interpretation. The installation effects will then be evaluated in terms of their order of magnitude (stress, strain and internal variables) and qualitatively compared with centrifuge test results. A parametric study is done where the geometry, installation type and interface constitutive law are analysed separately. The influence of the installation is also evaluated on pile behaviour when subsequently subjected to axial loading. Finally, the behaviour of a single isolated non-displacement pile subjected to different cyclic axial loading paths is modelled numerically and its results discussed in terms of the soil-pile interface behaviour and stress distributions. The pile shaft resistance degradation friction fatigue phenomenon is analysed in detail.

6.1 Numerical simulation of the installation procedure of displacement piles

This section will address the main components required for the complete description of the numerical model. Firstly the FEM formulation used is described followed by the main constituents of the model: numerical elements, materials and geometry of the mesh.

6.1.1 FEM - Updated Lagrangian formulation

The numerical analysis of the installation process of a displacement pile is a complex problem to solve using conventional tools. Extensions to the finite element method have already been the object of a comprehensive review in Chapter 2 of this work. The finite element code GEFDyn employs the standard Lagrangian formulation where, by definition, the reference mesh is always the one initially chosen. This approach is problematic for the convergence of problems where large deformations are present. Even more when frictional contact and nonlinear material behaviour is considered as well. In order to tackle this issue a similar procedure used by Gui [43] was employed which can be considered as an Updated Lagrangian approach (figure 1). The mesh must never deform excessively where the Jacobian would be zero or negative since that would violate the conservation of mass principle and cause a numerical breakdown. The desired calculation was then divided into several consecutive separate Lagrangian calculations and re-meshing was performed in between. This re-meshing consists of updating nodal coordinates from the displacements calculated in the previous simulation. The integration points' coordinates were, therefore, also updated along with the corresponding stresses and internal variables but the deformations were then taken as zero as an initial value. Unlike Gui [43] where FLAC was used and stresses/strains/variables are stored at the geometrical center of the element itself, GEFDyn stores stresses/strains/variables at the integration points. Therefore, no remapping of stresses/strains/variables is considered due to the lack of objectivity of this operation and the complexity associated with the interpolation of internal variables and the physical significance of such a procedure. This strategy allowed the calculation to be completed having converged to a given solution by the end of the installation procedure.

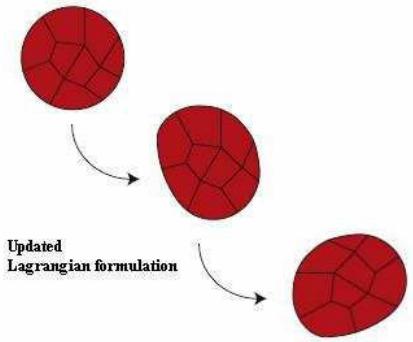

Figure 1: Updated Lagrangian formulation (adapted from [90])

As referred in Chapter 2 when citing Sheng et al. [103] and Sheng et al. [104], important limitations exist when considering an Updated Lagrangian formulation for the simulation of a displacement pile installation. The installation of flat end piles cannot be done without risking important numerical errors. Also, a balance must be found concerning the first column of soil elements adjacent to the pile-soil interface between accuracy, where elements should be as small as possible, and numerical stability and convergence, since the elements must be large enough to withstand deformation while maintaining a positive Jacobian. Finally, the consideration of interface elements becomes an absolute necessity in order to be able to have the important relative displacements between pile and soil which occur during installation. Despite these many precautions some oscillatory behaviour can be found which begins whenever an element is moved from vertical compression, at the pile base, to radial compression and shearing, at the pile-soil interface. The removal of these oscillations would require smaller elements but in order to avoid a numerical breakdown due to negative Jacobians a different formulation would have to be considered, e.g. arbitrary Lagrangian-Eulerian or a meshless approach.

Governing equations

During large deformation analysis the volume of the deformed body will not be constant. Assuming a body where all state variables verify equilibrium are known up to a time t. Considering the principle of virtual work where it states that equilibrium will be satisfied provided

$$\int_{V^{t+\delta t}} \underline{\underline{\sigma}}^{t+\delta t} \cdot \boldsymbol{\delta}^{t+\delta t} \underline{\underline{D}} \, dV = R^{t+\delta t} \tag{6.1}$$

for any virtual displacement field δu that satisfies the displacement boundary conditions is imposed. $\underline{\underline{D}}$ corresponds to the rate of deformation tensor consistent with the virtual displacements, V is the volume of the body and R represents the external power from external body forces.

The quantities in the previous equation are then transferred to a configuration in order to be solved. In the Updated-Lagrangian method all variables are transferred to the last equilibrium configuration at time t. Considering that

$$\underline{\underline{S}} = \underline{J} \cdot \underline{\underline{F}}^{-1} \cdot \underline{\underline{\sigma}} \cdot (\underline{\underline{F}}^{-1})^T \tag{6.2}$$

$$\underline{\underline{E}} = \frac{1}{2}(\underline{\underline{C}} - \underline{\underline{I}}) \quad , \quad \dot{\underline{\underline{E}}} = \underline{\underline{F}}^T \cdot \underline{\underline{D}} \cdot \underline{\underline{F}} \tag{6.3}$$

the equilibrium equation can be written as

$$\int_{V^t} {}^t\underline{\underline{S}}^{t+\delta t} \cdot {}^t\boldsymbol{\delta}\underline{\underline{E}}^{t+\delta t} \, dV^t = R^{t+\delta t} \tag{6.4}$$

where the left subscript represents the configuration in respect to which the quantities were measured. Since an objective co-rotational stress rate is considered in the constitutive model the global equilibrium for the Updated-Lagrangian method is expressed as

$$\int_{V^t} \underline{\underline{\underline{\underline{E}}}}^{ep} \cdot \underline{\underline{D}}\, \boldsymbol{\delta}(\underline{\underline{D}})\; dV^t + \int_{V^t} \underline{\underline{\sigma}}^t \cdot\; \boldsymbol{\delta}(\frac{1}{2}\,(\bigtriangledown \underline{u}^T \cdot \bigtriangledown \underline{u}))\; dV^t \tag{6.5}$$
$$+ \quad \int_{V^t} (\underline{\underline{\sigma}}^t \cdot \underline{\underline{B}} + \underline{\underline{B}}^T \cdot \underline{\underline{\sigma}}^t)\, \boldsymbol{\delta}(\underline{\underline{D}})\; dV^t = R^{t+\delta t} - \int_{V^t} \underline{\underline{\sigma}}^t\, \boldsymbol{\delta}(\underline{\underline{D}})\; dV^t$$

where the second-order tensor $\underline{\underline{B}}$ may be supplied by a tensor-valued function of the deformation gradient $\underline{\underline{F}}$ and the velocity gradient $\underline{\underline{L}}$.

6.1.2 Numerical elements, materials and geometry

In this section a description of the different types of elements, behaviour laws for the various materials and the geometry of the model is done in detail.

Numerical Elements

The simulation of the installation of a displacement pile in the finite element code GEFDyn is done resorting to 2 different types of elements: 2-dimensional solid 4-node isoparametric elements and linear 4-node interface elements. The volume elements are used to simulate the soil mass which constitutes most of the mesh of the model. These elements consider the Eulerian mechanical formulation with the logarithmic rate discussed in detail in Chapter 3 of this work. The integration order of these elements is 2 (4 integration points per element). Higher order elements were tested but the increased additional accuracy came at an elevated computational cost (calculation time).
The interface elements are considered at the boundary of the mesh representing the soil-pile contact zone. In geometrical terms these elements are linear and composed of two faces (parallel 2-node exhibiting relative displacement $\underline{u}$, where $\underline{u}$ is the relative displacement of the two faces of the interface) but numerically consider an interface thickness which defines the maximum normal displacement before a "gap" occurs and contact is lost. The mechanical formulation for the interface is written in terms of relative displacements and stress vector increments considering normal and tangential components. In terms of displacements it can be written that

$$u_n = \underline{u} \cdot \underline{n} \tag{6.6}$$
$$\tag{6.7}$$
$$u_t = \underline{u} \cdot \underline{t} \tag{6.8}$$

where $\underline{n}$ and $\underline{t}$ are unit vectors normal and tangential, respectively, to the interface element alignment. In terms of stress components and considering $\underline{T}$ the stress vector with respect to the interface

$$\underline{T} = \underline{\underline{\sigma}} \cdot \underline{n} \tag{6.9}$$

in can then be written

$$\sigma_n = \underline{T} \cdot \underline{n} = \underline{n} \cdot \underline{\underline{\sigma}} \cdot \underline{n} \tag{6.10}$$

$$\tag{6.11}$$

$$\tau = (\underline{T} - \sigma_n \cdot \underline{n}) \cdot \underline{t} \tag{6.12}$$

where σ_n and τ represent the normal and shear stresses respectively.

Materials

The soil is modelled considering either the original or the revised ECP constitutive model depending on the simulations. Both these models have been explained in detail in previous chapters of this work. The exception is the first row of elements near the surface where an elastic behaviour law is chosen in order to minimize numerical errors due to the singularity of a zero mean pressure in the ECP constitutive model (as in most soil constitutive models) during the extreme displacements imposed by the pile.
The interface elements follow the same constitutive behaviour law as the soil in the 2-dimensional volume elements. However, adaptations to the model have to apply to the interface case. Firstly, unlike for the volume elements case, only the shear mechanism is considered in the interface elements (isotropic mechanism is not introduced). Secondly, elasticity and plasticity are defined in terms of the normal and tangential direction and therefore all parameters are adapted accordingly. The monotonic yield function then becomes

$$f = \tau - \sigma_n \cdot tan\phi_{pp} \cdot r \cdot r_{br} \cdot (1 - b \cdot \ln(\frac{\sigma_n}{\sigma_c})) \leq 0 \tag{6.13}$$

A full description of the interface constitutive structure can be found in Appendix E. It should also be noted that to resolve the case of inter-penetration between the interface and volume elements the penalty method is considered in GEFDyn. As a solution of that contact problem an active constraint is added as a penalty term to the energy equation of the system. The penalty parameter can be interpreted as a spring stiffness since the energy of the penalty term has the same structure as the potential energy of a simple spring, in the contact interface between a point mass and a rigid support. Therefore, the penalty parameter is taken as the Young's modulus E of the interface. This is extremely important for the pile installation simulation since it will influence greatly the stress around the pile in the radial direction.
The properties for all the materials used in the reference simulation (Ottawa sand) can be found in table 6.1. A $K_0 = 1.0$ is taken for the soil mass to initialize the horizontal stresses.

Model parameters			
Materials / Elements	Ottawa sand	Elastic layer	Interface elements
Elasticity			
$K_{ref}/E_{ref}(MPa)$	285.0	28.50	2.850
$G_{ref}(MPa)$	215.0	21.50	2.150
n_e	0.00	0.00	0.00
$p_{ref}(MPa)$	1.0	1.0	1.0
Critical State and Plasticity			
$\phi'_{pp}(^\circ)$	33	n.a.	33
β	52	n.a.	520
d	2.00	n.a.	n.a.
b	0.22	n.a.	0.22
$p_{co}/\sigma_{co}(MPa)$	0.45	n.a.	0.45
Flow Rule and Isotropic Hardening			
$\psi(^\circ)$	33	n.a.	33
α_ψ	1.00	n.a.	1.00
a_1	0.0001	n.a.	0.0001
a_2	0.0100	n.a.	0.0150
c_1	0.0600	n.a.	n.a.
c_2	0.0300	n.a.	n.a.
m	1.00	n.a.	1.00
Threshold Domains			
r^{ela}	0.005	n.a.	0.005
r^{hys}	0.030	n.a.	0.030
r^{mob}	0.800	n.a.	0.800
r^{ela}_{iso}	0.0001	n.a.	n.a.
Breakage parameters			
a_0^{br}	0.0	n.a.	0.0
m_a^{br}	1.00	n.a.	1.00
$b_{W_p}(MPa)$	0.0	n.a.	0.0

Table 6.1: Model parameters

Note that the Young's modulus is considerably smaller at the interface element. This is due to numerical issues associated with high values for the penalty parameter in pile installation problems [104].

Geometry

The numerical analysis of a pile installation is performed considering an axisymmetric calculation. The pile is, therefore, always considered as having the form of a cylindrical prism with a conical tip with diameters of 400, 500 and 600 mm with a tip angle of 60 degrees (with the horizontal) and lengths of 5 and 8 meter. The reference configuration is a 5 meter long pile with a diameter of 500 mm which is represented in figure 2.

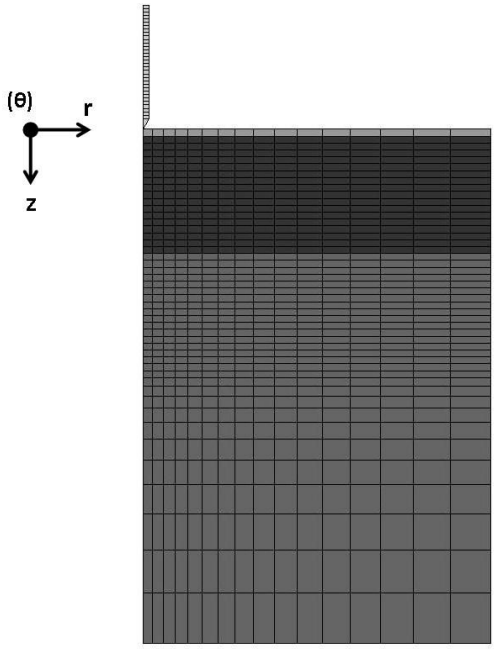

Figure 2: Finite element mesh

The different gray scales represent the separate groups of the simulation. These groups do not necessarily represent different materials (the 2 biggest layers of soil represent in fact the same material with the same parameters) but only separate analysis groups. The soil layer nearer the surface and the one adjacent to it have a combined height of the same value as the pile length representing, therefore, the main groups to be influenced by the pile in both radial and shear effects. The boundary conditions of the mesh are standard: nodes on the lateral edges of the mesh are constrained in the normal direction of movement to the boundary. For the lower boundary of the mesh (lowest z coordinate) also the tangential direction of movement is restrained. The total number of volume and

interface elements (and therefore the number of nodes) depends on the pile geometry: length and diameter. For the reference case the soil material is composed of 752 elements, the interface of 18 elements and the pile of 34 elements. Both the mesh width and length are always larger than 2.5 L, where L is the pile length. The radius of the elements adjacent to the interface elements depended heavily on both the pile diameter and the tip angle of the pile. However, an approximate square shape was always adopted for these elements in order to obtain better convergence and reduced oscillations.

6.1.3 Calculation procedure

The numerical steps considered in order to successfully and pertinently represent the pile installation are detailed here.
To simulate the penetration of the pile in the soil medium a 4-node interface element is considered. This element does not have a geometrical thickness which means that the 4 nodes of which it is composed have only two different sets of coordinates (the length of the interface is considered in the z-axis direction). In figure 3 this superposition of the points is not represented for illustrative purposes.
Figure 3 illustrates the numerical procedure. The arrows represent the prescribed displacement on all the interface nodes on the "side" of the pile. In contrast, the other nodes which compose the interface elements are connected to the soil elements.

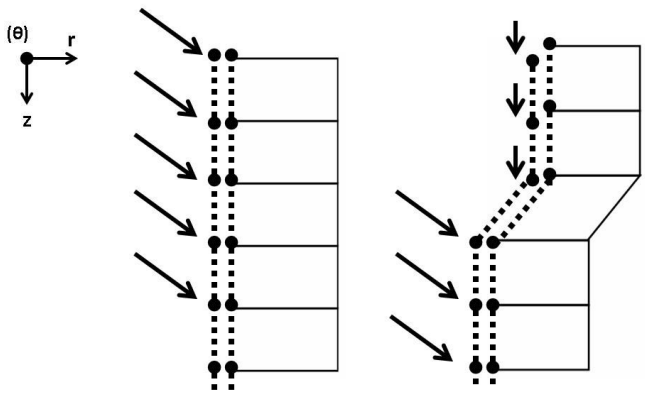

Figure 3: Installation procedure - prescribed displacements

Displacements are imposed based on the motion of entry of the pile. This implicitly implies that the pile is perfectly rigid. The sequence for prescribed displacements is determined automatically by a routine which depends on the geometry of the pile and the type of installation. No relative non-realistic displacements are allowed between the interface nodes below the pile tip in order to avoid friction at the mesh boundary. For the node positioned at the pile tip both horizontal and vertical displacements are imposed until the pile radius is reached. Once there, only vertical displacements are imposed on them and

the pile tip movement is imposed on another series of nodes. This process continued until the pile is completely installed, i.e. surface level (z = 0 coordinate). Subsequently, the pile is subjected to monotonic loading by imposing vertical displacements at the interface nodes. Once more this implies that the pile is perfectly rigid. Moreover, the elements which define the pile only serve as a visual aid having no numerical relevance.
The definition of the numerical procedure for the pile installation shows clearly the importance of the interface and the adjacent soil volume elements discretization. These will be the zones where most numerical issues will arise and, simultaneously, where the most relevant results will be obtained.

Types of installation

Two types of installation are simulated (inspired by White and Lehane [118]):

- Monotonic : Continuous prescribed displacement until the end of the installation
- "Pseudo-Dynamic" (will be referred to as cyclic) : Fixed displacement steps with an upward vertical displacement in between

The monotonic installation is self-evident. The pseudo-dynamic installation presumes the knowledge of the upward motion *a priori* of the calculation. This is due to the inability of numerical methods to "de-stress" a converged solution where displacements were prescribed. This value was assumed to be 3 centimetres. For simplicity, problems involving time-dependent behaviour are not considered, i.e. only quasi-static problems. These two different installation methods will be compared and the influence of the installation method analyzed.

6.2 Pile installation results

In this section the results obtained from the pile installation calculation will be presented. These will consist of the results designated as the reference case. The reference case considers a 5 meter long pile with a diameter of 500 millimeters and a tip angle of 60 degrees (with the horizontal) which is installed in Ottawa sand with the breakage mechanism deactivated.

6.2.1 Deformation and displacement patterns

The deformed mesh during different steps of the calculation can be seen in figures 4 and 5.

The first noticeable aspect of this simulation is how localized the effect of the installation is. Only negligible mesh deformation can be seen away from the immediate proximity of the soil-pile interface. Some minor surface effects near the pile can be seen which are also predicted by other numerical simulation results [104]. This behaviour of the elements near the surface pose a problem for standard geotechnical constitutive models to solve since the mean stress is near zero. As mentioned before, this simulation considers an elastic material at the top layer of the mesh in order to resolve this singularity.

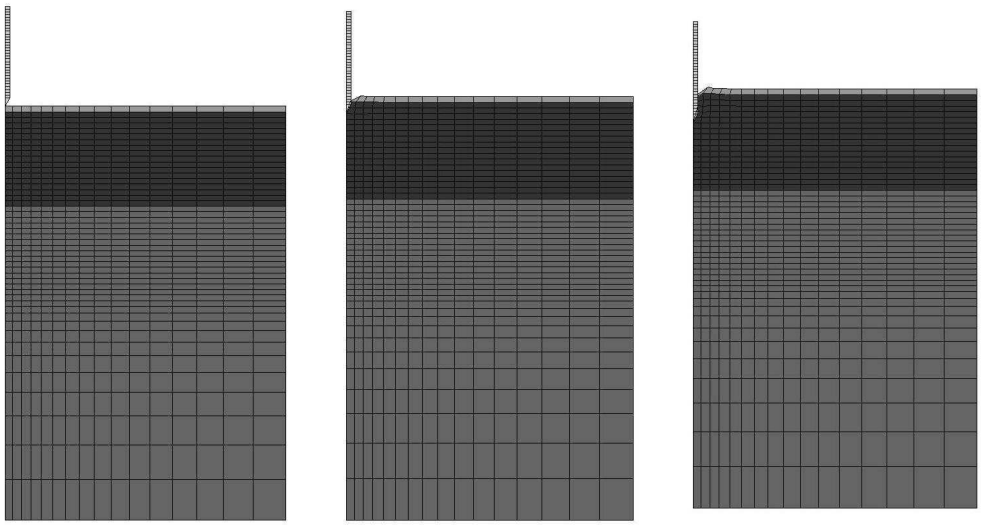

Figure 4: Deformed mesh: 1^{st} half of the installation procedure

This localized behaviour is the main reason for the numerical issues associated with this type of analysis. However, the completeness of information in numerical modelling is a great advantage when compared with empirical or even experimental data.

Except some elements near the surface, the thicknesses of most elements above the position of the tip of the pile remain mostly constant, even though the elements near the pile have been sheared downwards. The deformed shape of the mesh suggests therefore an unloading in the vertical direction once the pile tip has passed. Also, elements around the pile are not very severely distorted despite very large shear relative displacements between the pile and the soil at the interface level.

The evolution of the displacements in the radial direction can be seen in figures 7 and 8.

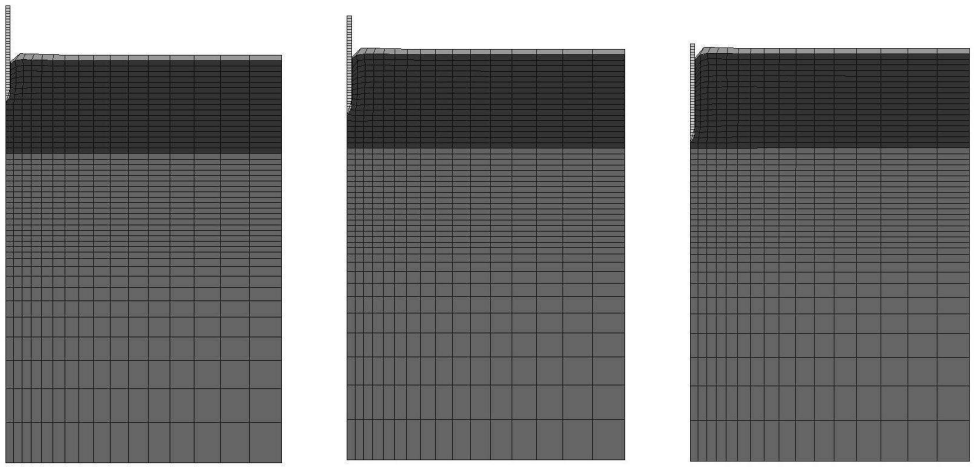

Figure 5: Deformed mesh: 2^{nd} half of the installation procedure

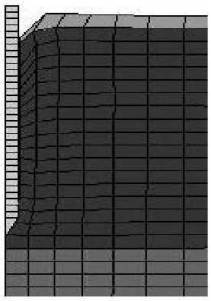

Figure 6: Zoom at the end of the installation procedure

The radial displacements show clearly the effect of the push by the pile penetration in the soil mass. The maximum radial displacement occurs at the interface level and has the value of the pile radius since the model is axisymmetric. The level of dissipation of the displacements with distance is high and becomes negligible after 2 to 3.5 times the pile radius.

The evolution of the displacements in the vertical direction can be seen in figures 9 and 10.

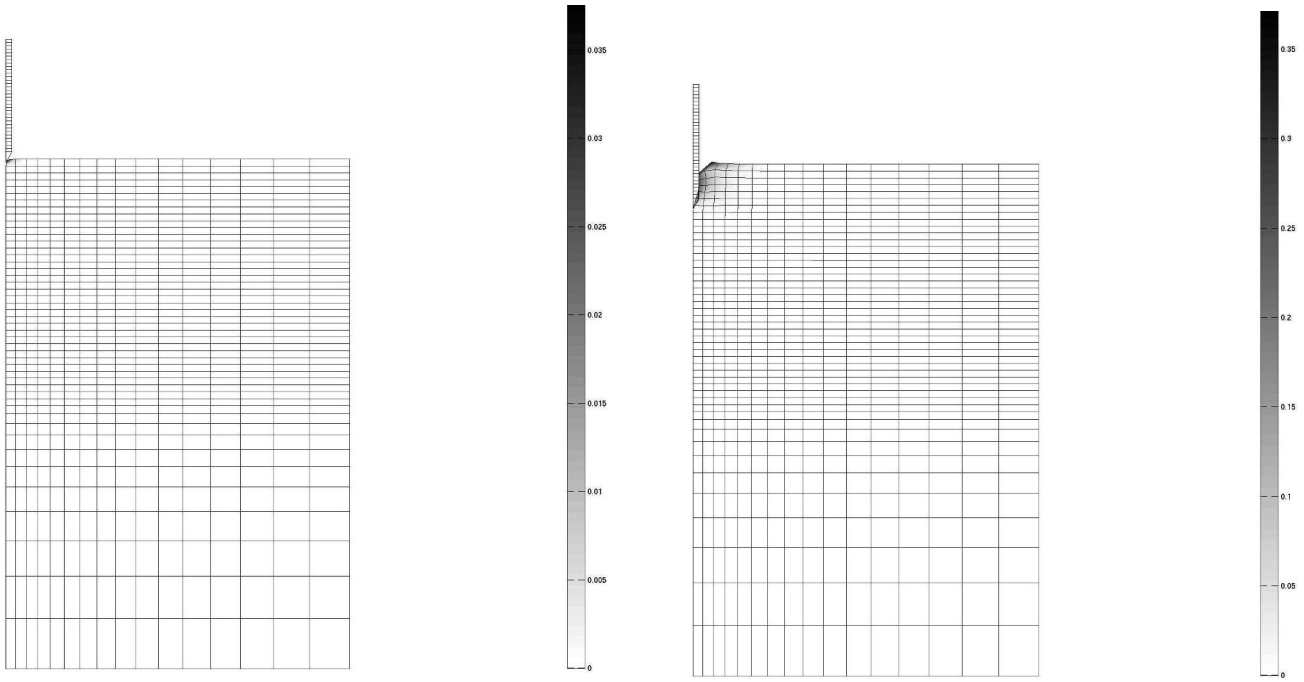

Figure 7: Radial displacements [m]: 1^{st} half of the installation procedure

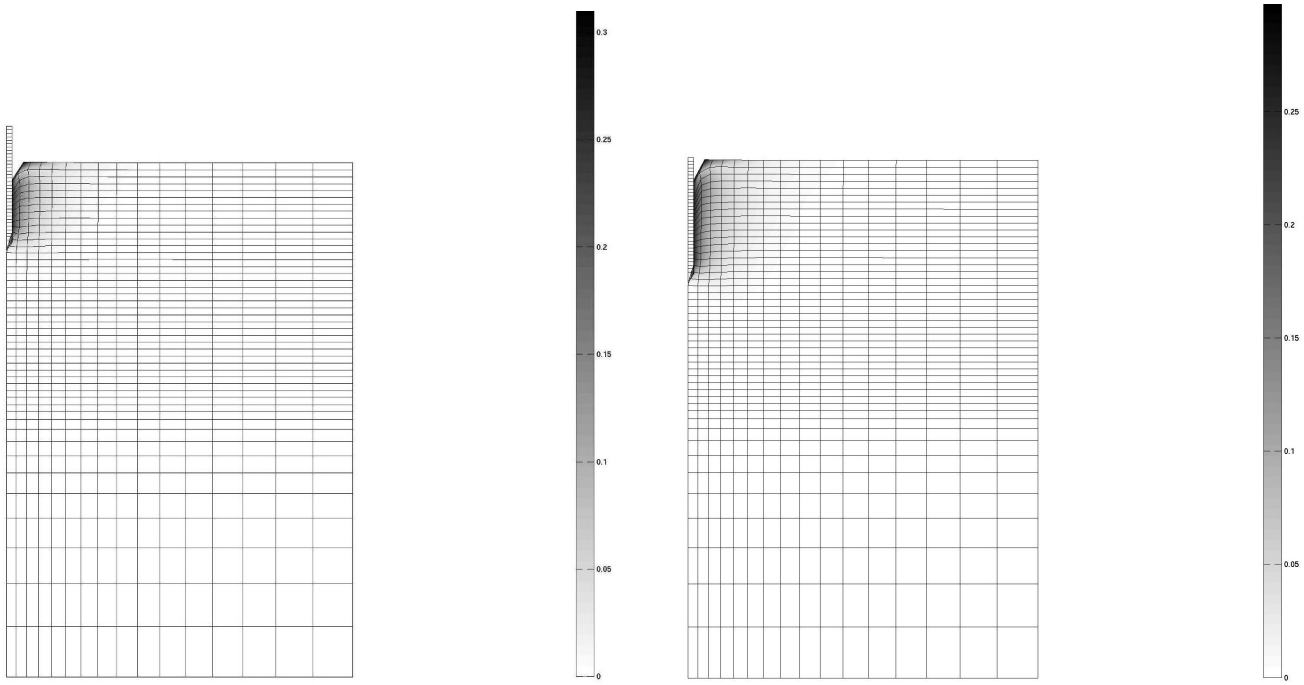

Figure 8: Radial displacements [m]: 2^{nd} half of the installation procedure

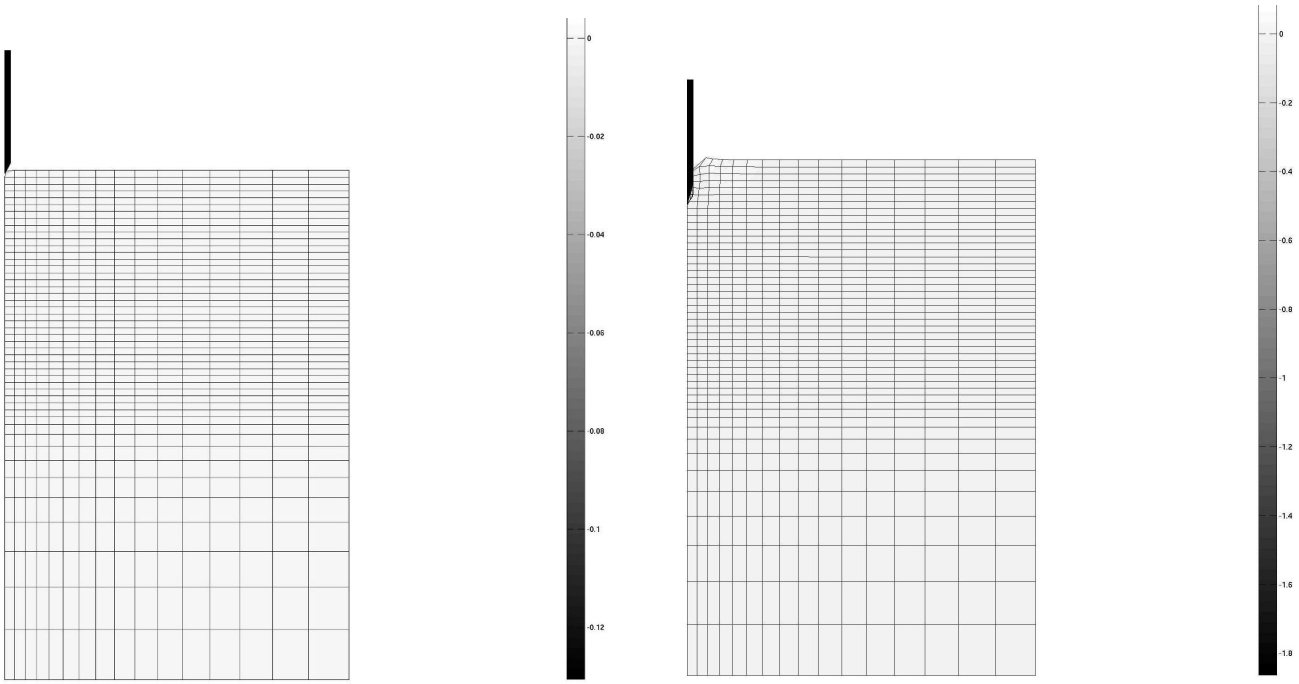

Figure 9: Vertical displacements [m]: 1^{st} half of the installation procedure

These figures show the degree of the relative displacements between the pile and the soil mass. This is possible as a result of the interface elements at the boundary of the mesh. Once more the installation effects are quite localized never surpassing 1.5 radius in radial distance before they become negligible.

The displacement paths for the volume element nodes in the vicinity of the pile all have a similar pattern as shown by White and Bolton [117] in figure 6 in Chapter 2. Figure 11 shows the paths of two points at different depths. While the point closest to the surface has already completed the radial displacement, due to the pile penetration, and shows important vertical displacement, the other does not. This shows that the critical state is almost reached during the passage of the cone since afterwards the soil and the pile show important relative displacements.

Unfortunately however, unlike the results from White and Bolton [117], no reversal is found in the displacement paths. This reversal occurs but only when considering a cyclic installation (and is more pronounced considering the breakage mechanism).

In figure 12 a qualitative validation of the contours below the pile tip is shown. These results show the contours of radial and vertical strain at the end of the pile installation. The dark line corresponds to the value zero. It is therefore the transition line from compression to extension. The line does not finish at the boundaries in the vertical direction due to numerical imprecisions near the value zero at such a distance from the pile (multiple points have a zero or close to zero value). These figures are quite similar to the results found by White and Bolton [117] and shown in figure 8 in Chapter 2 which; therefore,

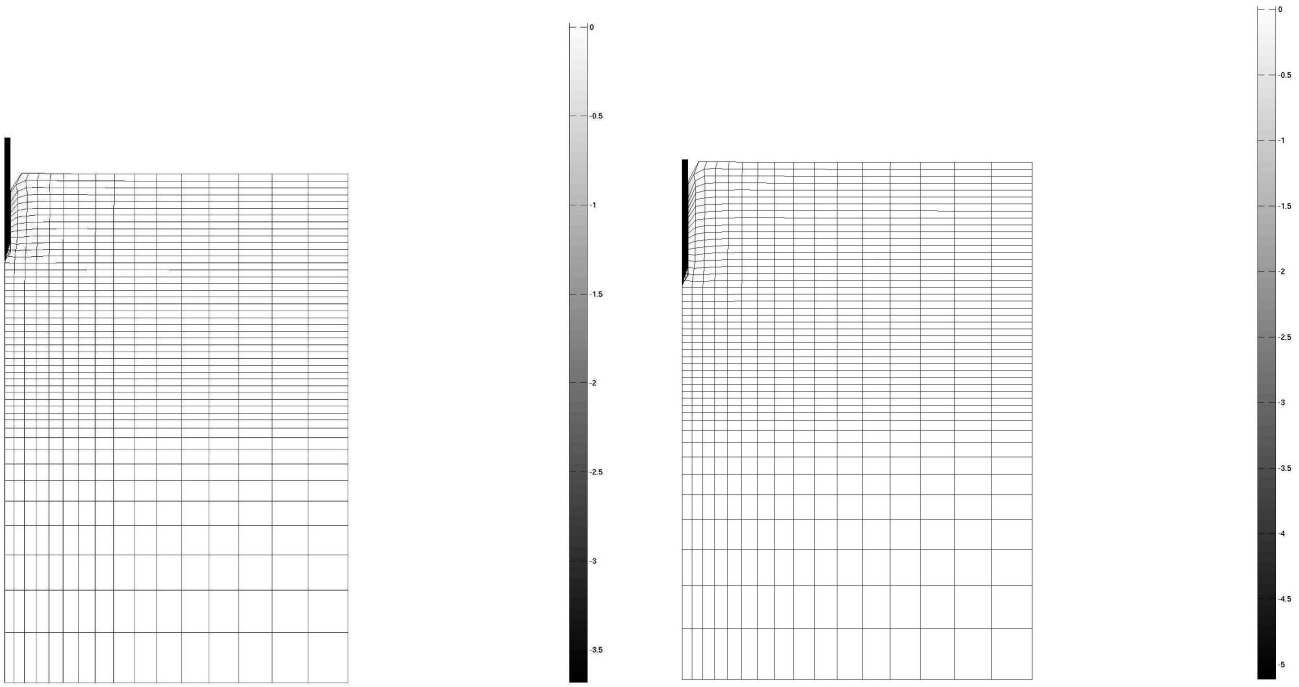

Figure 10: Vertical displacements [m]: 2^{nd} half of the installation procedure

validates qualitatively the results found here.

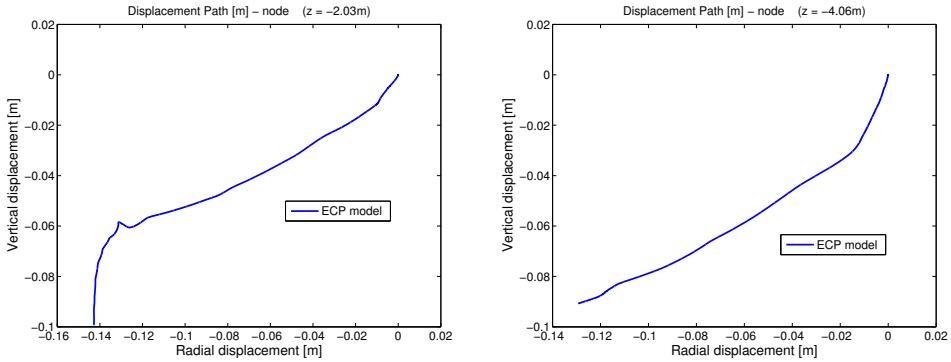

Figure 11: Vertical displacements [m]: 2^{nd} half of the installation procedure

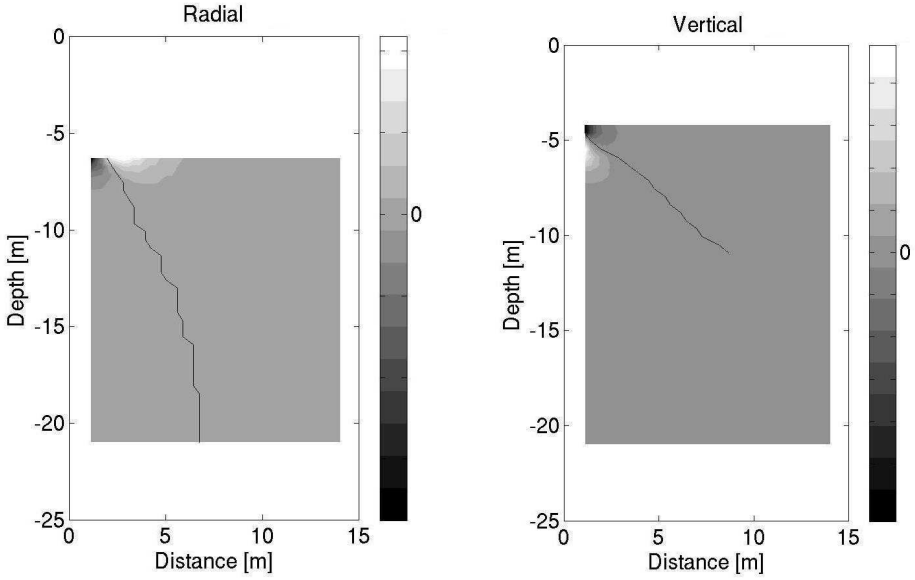

Figure 12: Radial and vertical strain [.]

6.2.2 Stresses in the soil mass

The radial, vertical and shear stress contours will be presented hereafter. Compression is positive. The representation of the contours is done resorting to a division in near and far field. This division is self-explanatory in figures 13 and 14. Due to high stress concentration at the pile tip and oscillations due to high levels of shear displacements, the interface zone will be treated separately to the global stress distributions in the mesh. This is also due to illustration issues using a gray scale for the representation of the contours.

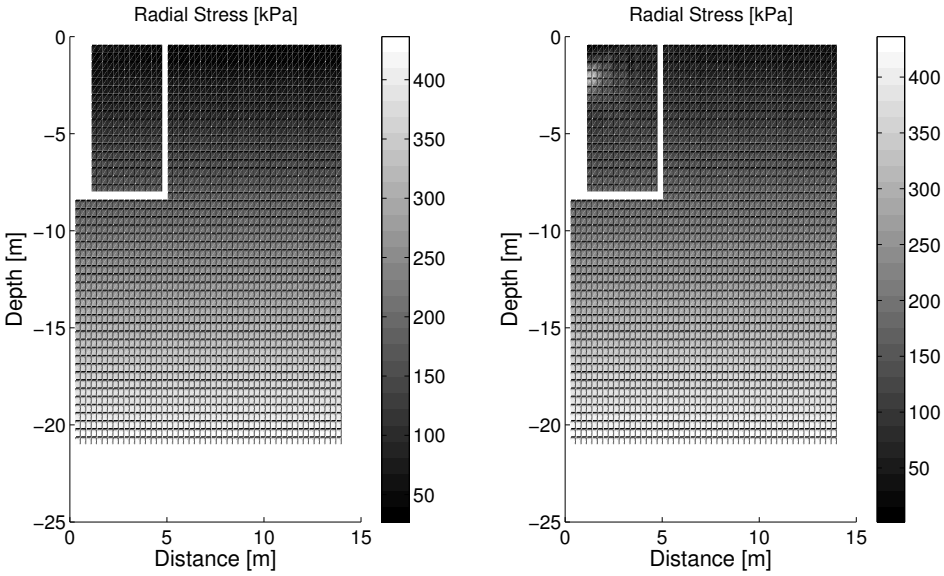

Figure 13: 1^{st} half of the installation procedure

The near field is clearly where most the stress variations occur [102]. Some oscillations are present in the results but the overall distribution is clear. The results from the radial stress show the de-stressing in the radial direction once the pile tip passes a certain depth after having increased substantially. This is noticeable since the stresses reduce sharply once the tip passes that certain depth. This increased confinement stress followed by its decrease effect, which is produced by the advancement of the pile tip, is also known as the h/R effect [7].

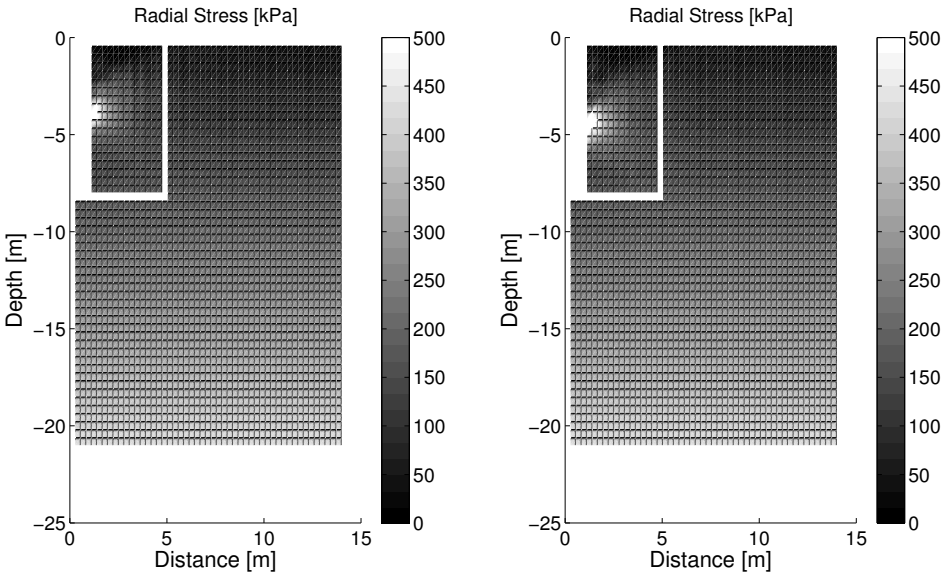

Figure 14: 2^{nd} half of the installation procedure

The h/R effect is also visible, albeit less clearly, in the vertical stress distributions in figures 15 and 16.

Most of the variation is found directly beneath the pile tip dissipating rapidly in the shaft once the tip has passed. Oscillations in the stress values in the vertical direction are more pronounced than those in the radial direction. This is due to the movement of the elements from the boundary to the shaft of the pile. The interface elements rotate from an initially perfectly vertical position to an intermediate diagonal configuration before becoming vertical once more at the pile shaft. This interface motion causes convergence issues at the elements right next to it during that brief passage. The problems are also associated with drastic reductions in the mean stress since vertical stresses are very near zero after the passing of the tip. Indeed, Sheng et al. [103] found a small zone above the cone where the vertical stress was negative (tension). A more detailed analysis of this is possible when the interface elements are analyzed directly.

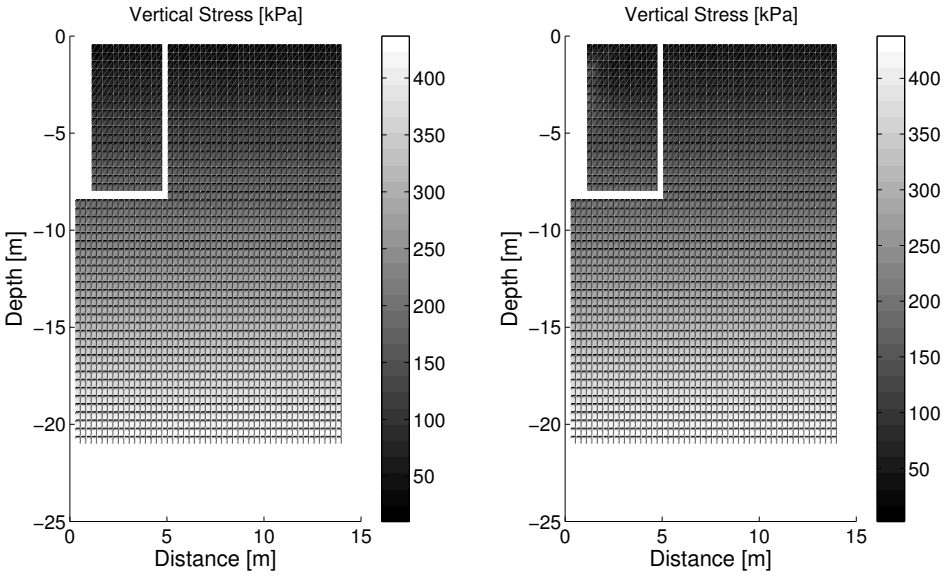

Figure 15: 1^{st} half of the installation procedure

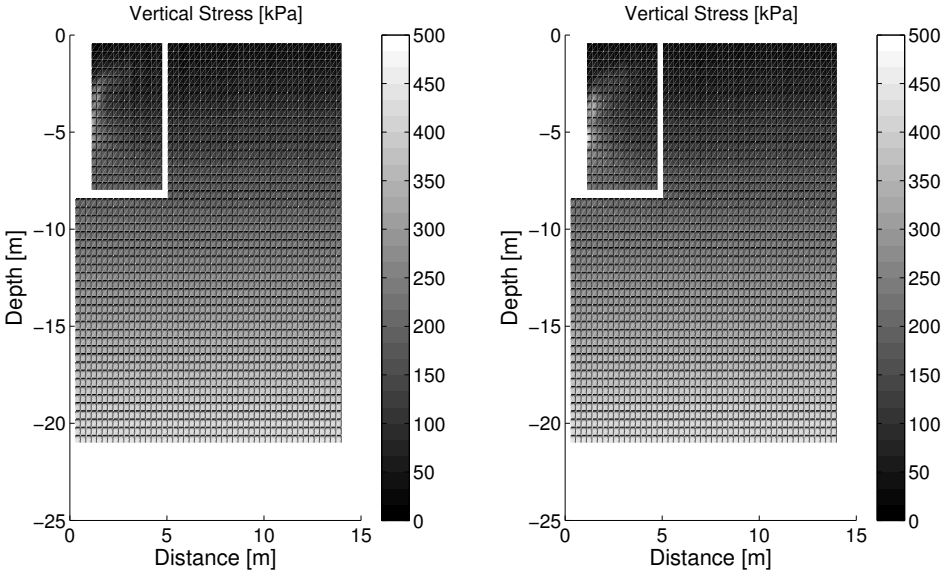

Figure 16: 2^{nd} half of the installation procedure

Finally, the contours of the evolution of shear stress are shown in figures 17 and 18.

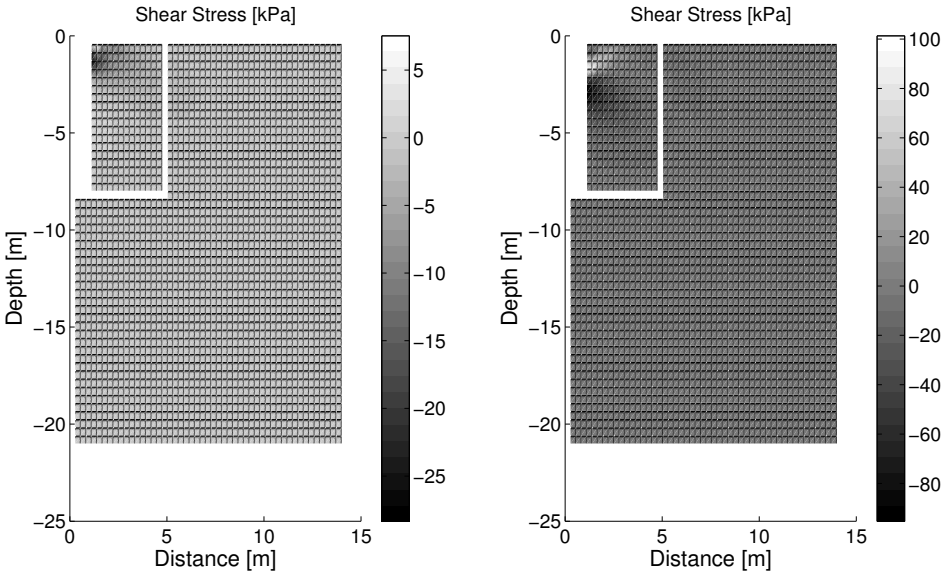

Figure 17: 1^{st} half of the installation procedure

The shear stress shows the common "X" shaped stress contours, with the center of the cross coinciding with the tip of the pile at each penetration depth is presented.

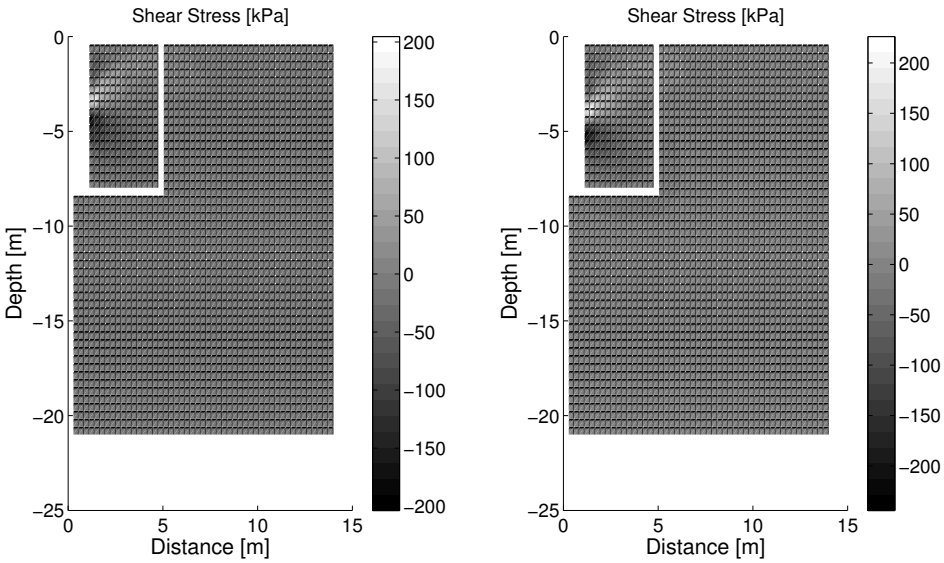

Figure 18: 2^{nd} half of the installation procedure

The results presented so far represent the effect of the pile installation on the soil mass in terms of distance and magnitude. However, the main effect is felt at soil-pile interface level and the first column of elements adjacent to it. The results from the column of elements will be presented henceforth. Compression is positive.
Firstly the variation in the mean stress in terms of the advancement of the penetration of the pile in depth.

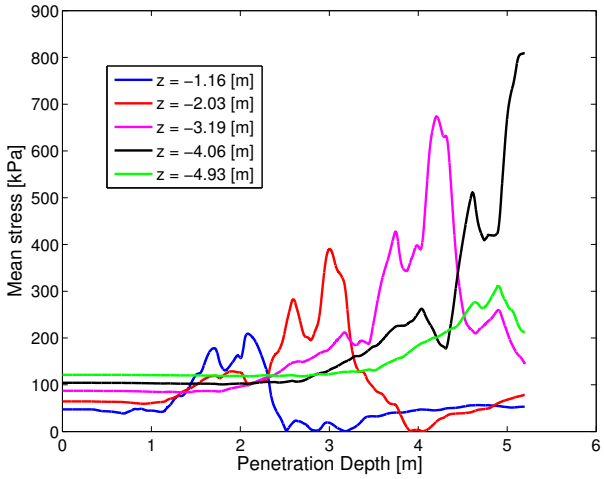

Figure 19: Mean Stress evolution during pile installation at different depths

Figure 19 is a very clear representation of the h/R effect [7] [67]. A sharp increase is found when the pile tip approaches followed by an equally fast decrease. This increase is divided into two distinct phases: the tip of the pile, due to its small contact surface, and

the dilative behaviour which follows the phase transformation in the soil. This volumetric behaviour is shown in figure 20. The volumetric "strain" shown here represents the infinitesimal volumetric strain quantity (engineering strain) which can also be seen as the gradient of the Jacobian of the transformation $\dot{J}$.

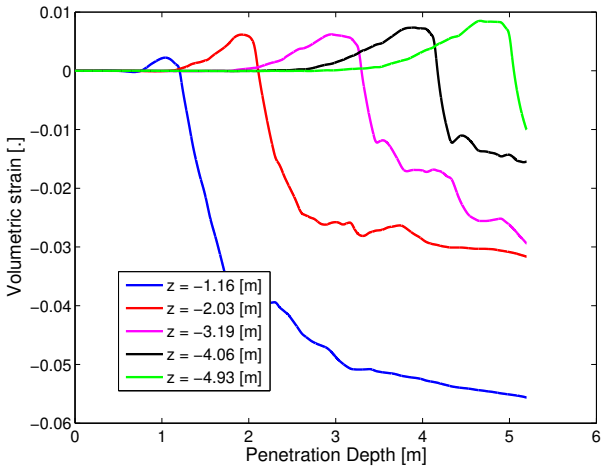

Figure 20: Volumetric Strain during pile installation at different depths

This behaviour is exactly the same as those shown by the ring shear tests (RS) considering CNS (constant normal stiffness) and CV (constant volume) boundary conditions. There is an initial compression followed by a reversal in the volume-stress path which results in dilative behaviour. Under the confinement of the soil mass, the elements near the soil-pile interface are sheared resulting in the same qualitative behaviour observed in RS tests.

Finally, the evolution of the deviatoric stress ($q = ||\underline{\underline{s}}||$) is shown in figure 21 with the same behaviour as the others before.

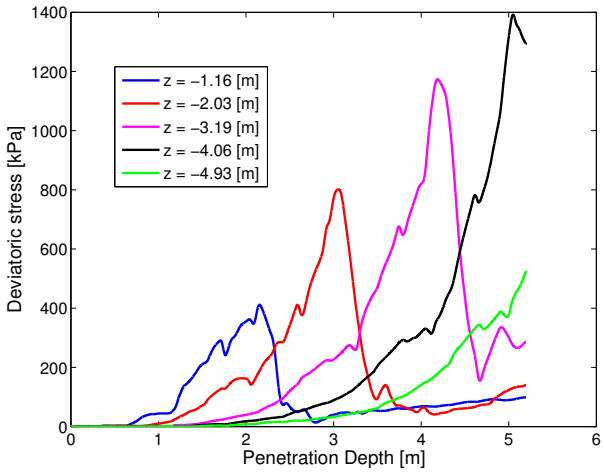

Figure 21: Deviatoric Stress during pile installation at different depths

The results presented here are qualitatively consistent with other numerical calculations [103] [104] [43] [25] [26] [90] [29] as well as with some experimental observations [102] [65] [117]. As a final note it should be mentioned that the results presented here are globally valid for most non-dynamic displacement pile installation procedures (with the exception of the path described by the nodal displacements). Cyclic or monotonic installation is not found to dramatically alter the shape of the stress or displacement fields. This is equally valid for the breakage mechanism whose influence is concentrated at the interface level.

6.2.3 Interface results analysis

The results presented so far concerned solely the soil volume elements adjacent, in the near and far fields in relation to the soil-pile interface. This section will present the results obtained for the interface elements at different depths and at different stages of the installation.

As described before, the interface is written in terms of relative displacements and stress vector increments considering only 2 directions, normal and tangential.

Firstly the normal and tangential relative displacements are shown in figure 22. The displacements shown here are relative between the two pairs of nodes which compose the interface element. It can be seen as the difference between the pile and the soil displacements.

The tangential (shear) displacements show the behaviour which would be expected. Important relative displacements are observed almost immediately with the approach of the pile tip. This is due to the extreme shearing present at the interface which results in the soil reaching the critical state very rapidly. The normal displacements are mainly due to the rotation of the interface element when the pile cone is passing. In general, no relative normal displacements occur between the interface and the soil volume elements due to the very high radial confinement (very similar to CNS conditions in RS tests).

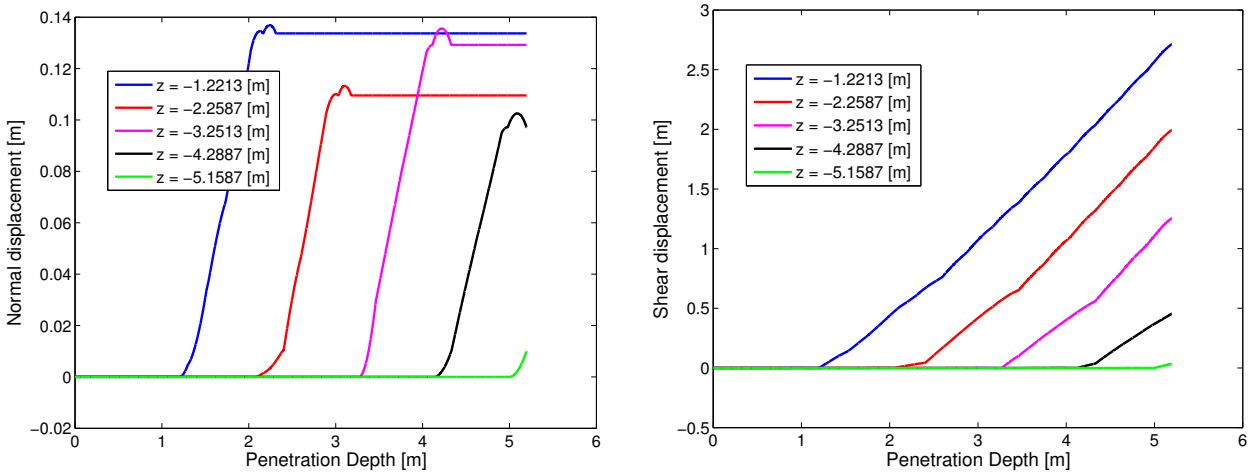

Figure 22: Evolution of normal and tangential interface relative displacements during installation at different depths

However, the normal direction of the interface element is pointing downwards during the rotation which means that the values measured actually correspond to vertical relative displacements.

In terms of stresses, figure 23 shows the evolution in relation to the penetration depth of the pile. The evolution of stresses show the same behaviour as the one observed in the adjacent volume elements to the interface. Due to contraction there is a small reduction in normal stress before the phase transformation after which it increases until the critical state is reached. Some arching effect can be seen where higher normal stress is found at the middle of the pile's length than below or above [65].

Figures 24 and 25 show the inter-related figures of the different variables. These results confirm the assumption of the similarities between a CNS boundary condition in RS tests subjected to shear and the soil-pile interface during installation or loading (similar to figure 10 in Chapter 2 from White [115]).

However, the volumetric behaviour shows some discrepancies between the RS and the pile installation interface case. Near the surface the volumetric behaviour follows the trend of initial contraction followed by a phase transformation to dilative behaviour. This is due to the low confining stress which is also related to the lower radial confinement by the soil mass around. This behaviour is not found for the higher depth interface element points. As seen before, the adjacent volume elements, even at higher depths, all show a phase transformation in their volumetric behaviour. It is therefore reasonable to assume that the dilative behaviour found in the adjacent elements "force" the higher depth interface elements into contraction. This can also be confirmed by the fact that no decrease is observed in normal stress at the interface level even though contractive behaviour is observed.

Finally the shaft and base resistances during installation are shown in figure 26. The

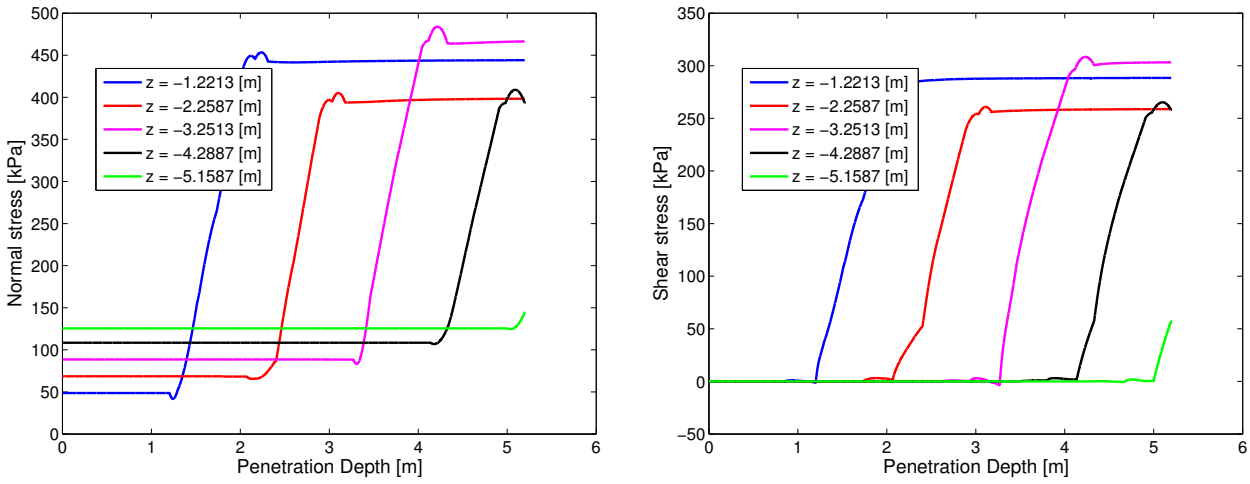

Figure 23: Normal and shear stresses evolution during installation at different depths

first meter is not considered in these results due to the elastic layer and the lack of representativity of soil behaviour laws at such low confining pressures. The base resistance shows considerable oscillations. These oscillations are due to the discretization of the mesh. The nodes which are considered for the base resistance are different for different penetration depths. If the discretization is not very high, oscillations will occur when nodal points pass from the base to the shaft of the pile and where the tip of the pile reaches the next nodal point. The discretization of the mesh faces the dilemma between convergence and numerical stability. Results from base resistance will not be studied in detail due to high oscillations in the calculated values.

Shaft resistance initially shows a negative value due to traction of the superficial elastic layer subjected to radial displacement (Poisson effect). Afterwards it increases to a peak followed by a decrease near the end of the installation. This decrease is followed by a plateau (it increases anew as will be seen with a longer pile). This plateau only occurs in the monotonic installation case as will be seen later when the cyclic installation results are shown. This is due to the dilative behaviour of the elements which adds to the anti-clockwise movement of the soil due to the entry of the pile. This effect might be exaggerated by numerical issues during the installation procedure using this finite element method and might be solely responsible for this effect. This rotation added with the dilation of the soil mass causes the soil to heave resulting in a reduction in shaft resistance before it stabilizes again due to its increase near the tip at higher depths. This is confirmed by the non existence of a plateau when considering the breakage mechanism even though less shaft resistance is calculated beforehand. The cyclic installation is found to allow for less cumulative dilation during the whole installation and therefore minimizing this effect.

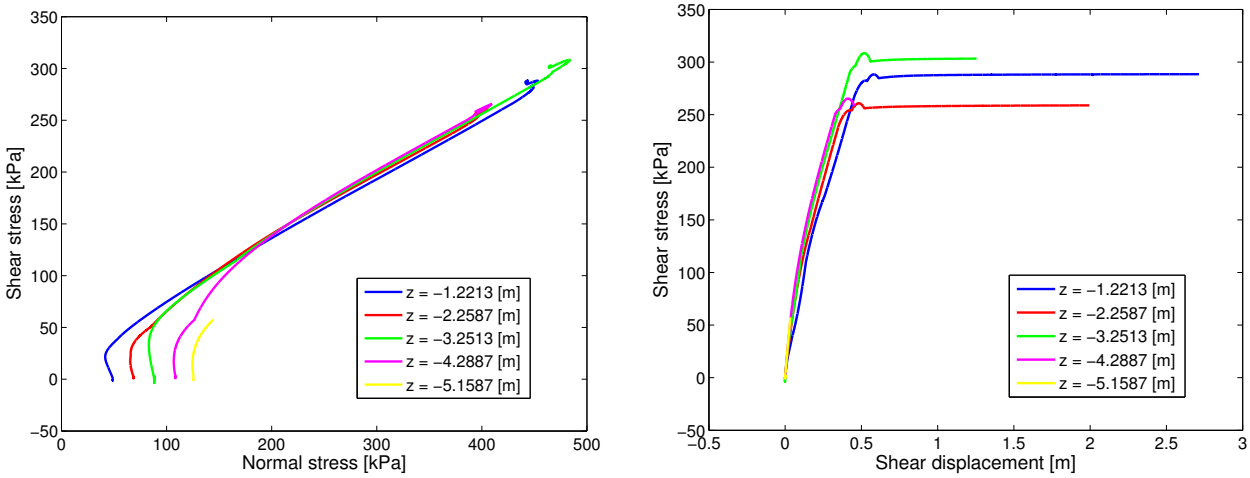

Figure 24: σ'_n - τ and u_T - τ evolution at the interface during installation at different depths

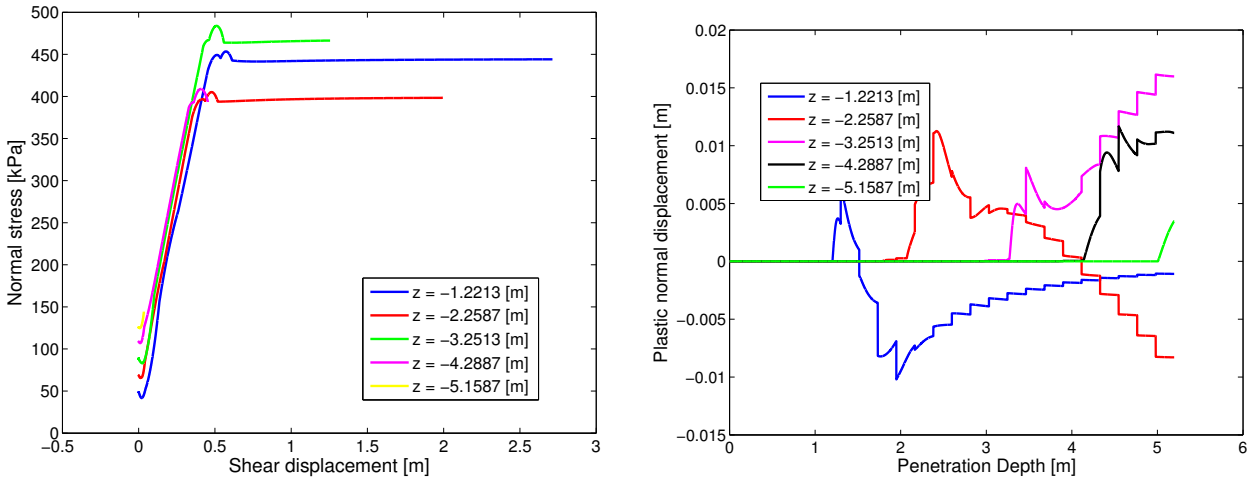

Figure 25: u_T - σ'_n and u_T - u_n^p evolution at the interface during installation at different depths

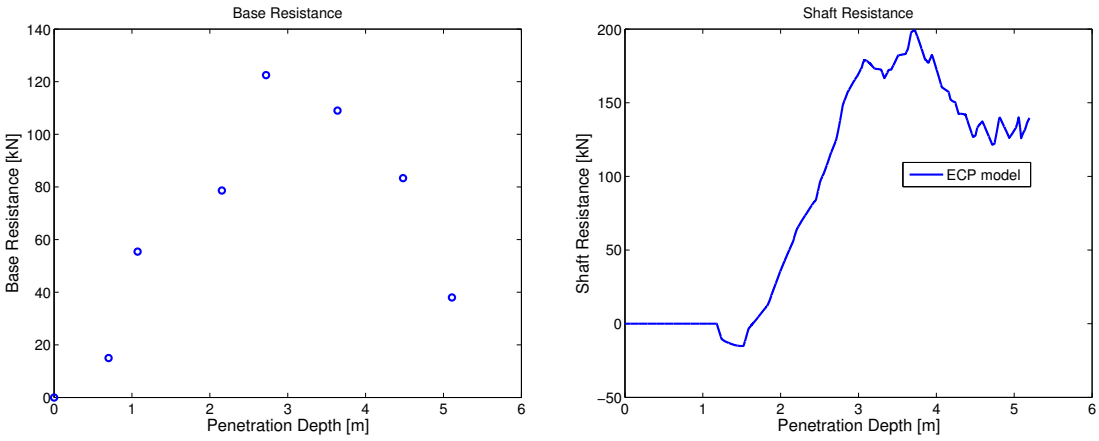

Figure 26: Base and Shaft resistances evolution during installation

6.3 Parametric studies

In this section a non-exhaustive parametric study will be performed to show the influence of different cases for the installation of a single pile foundation. These cases include geometrical variations (length and diameter), installation type, interface behaviour law and the consideration of the breakage mechanism. The reference calculation results give broadly the same results as the different cases presented here except at the interface level were most of the installation effects are concentrated. This section, therefore, is mainly concerned with interface results and shaft friction mobilization.

6.3.1 Pile diameter

Three different diameters are modelled. The reference configuration considers a 500 millimeter while here 400 and 600 millimeter diameter piles are additionally simulated. The installation type is monotonic such as the reference case. Note that, since the mesh is dependent on the geometry of the pile, the same exact depths are not found between the calculations. Nodes with approximately the same vertical and radial coordinates will be compared. The shape of distributions of stress and displacement fields are broadly the same as the reference case.

Firstly some obvious conclusions are given. Radial displacements are linearly and proportionately dependent on the diameter of the pile. Therefore, radial stresses on the soil mass increase and subsequently normal stress at the interface also increases as seen in figures 27 and 28 which compare the reference calculation with a 600 millimeter pile. Shear stress increases as well since the critical state is reached in both cases and the same critical state friction angle is considered.

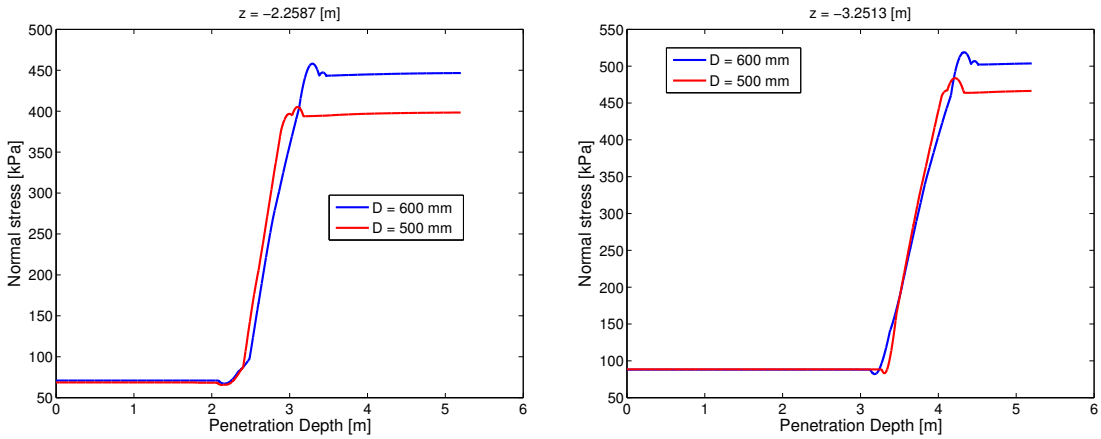

Figure 27: Interface normal stress evolution for two piles with different diameters

This increased radial confinement has an important influence on the volumetric behaviour of the interface. This effect, already present in the reference calculation, is augmented in the case of higher diameters. The dilative behaviour is limited even more as can be seen in figure 29.

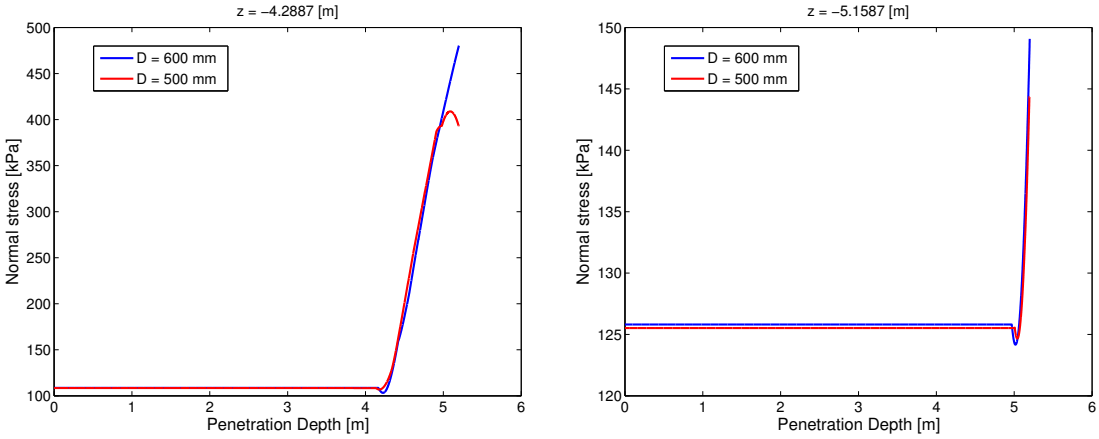

Figure 28: Interface normal stress evolution for two piles with different diameters

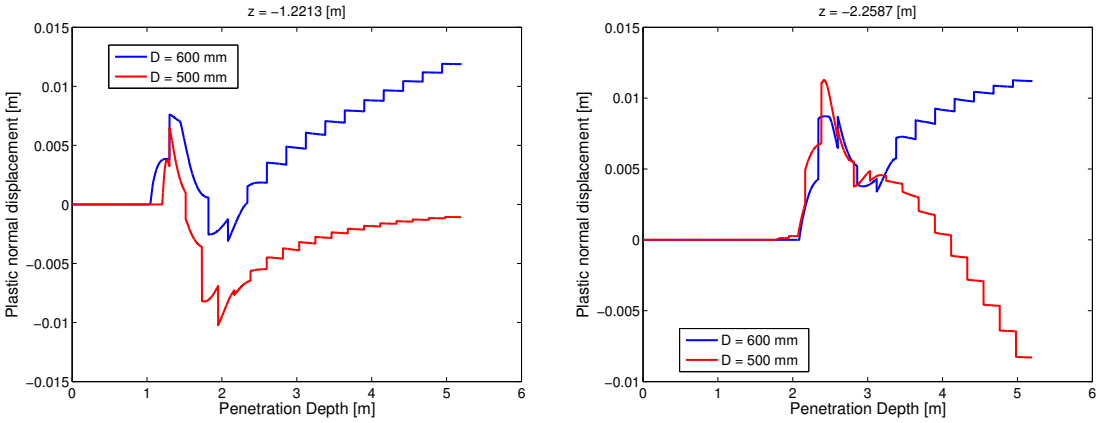

Figure 29: u_n^p evolution for two piles with different diameters

At a lower depth the dilative behaviour is no longer present (no phase transformation) in the higher diameter case due to the considerable radial stress imposed by the soil mass at the interface. All higher depths only show contraction for both diameters. Naturally the reverse is verified in the case of a 400 millimeter diameter pile.

Finally the development of shaft resistance is analyzed. The results for all three diameters are shown in figure 30.

As described before, there is a plateau in the development of shaft resistance. This plateau is offset by the diameter of the pile in terms of where it occurs during installation. Dilation is more restricted in the soil elements adjacent to the pile in the case of higher diameters as a result of higher radial stress. Since dilation is restricted there is less rotation, in relative terms, occurring in the soil and therefore shaft resistance increases continuously and the plateau is reached later in the installation.

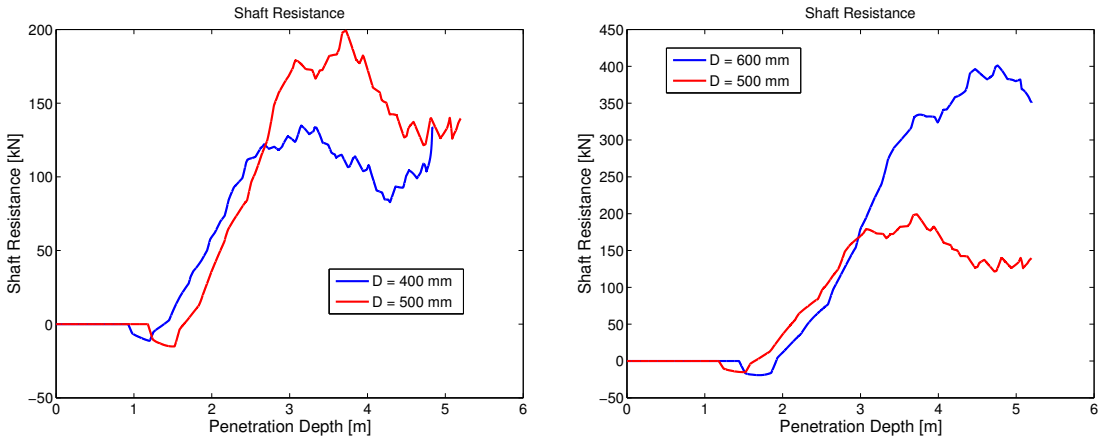

Figure 30: Shaft resistance during installation of piles with different diameters

6.3.2 Pile length

In this section the influence of pile length will be briefly discussed. The length of the pile influences installation at the interface level by mainly increasing the shear displacement imposed on the soil by the pile movement. The shape of distributions of stress and displacement fields are broadly the same as the reference case. The development of shaft resistance for an 8 meter long pile (with a diameter of 500 millimeter as well) can be seen in figure 31

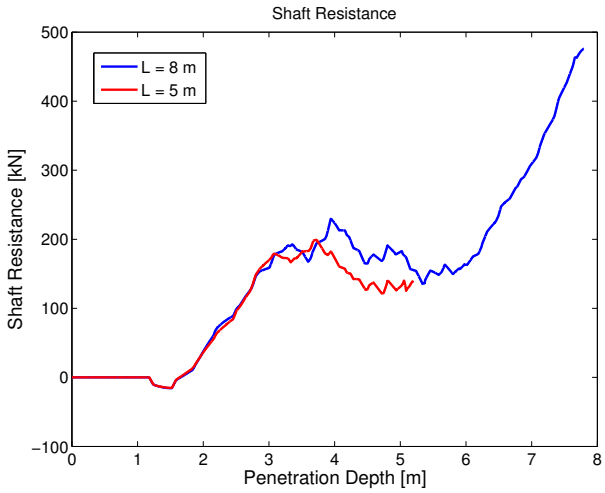

Figure 31: Shaft resistance during installation of two piles with different lengths

As predicted before the plateau is overcome and shaft resistance increases continuously during installation. It should be noted again that this plateau might be overstated by numerical issues with the finite element method and the behaviour law at very low confining stresses which results in the consideration of an elastic layer near the surface.

6.3.3 Installation type

Two different installation types are considered: monotonic and pseudo-dynamic. These have already being described in the beginning of this Chapter. Calculated interface normal stress results are compared with those of the reference case in figures 32 and 33.

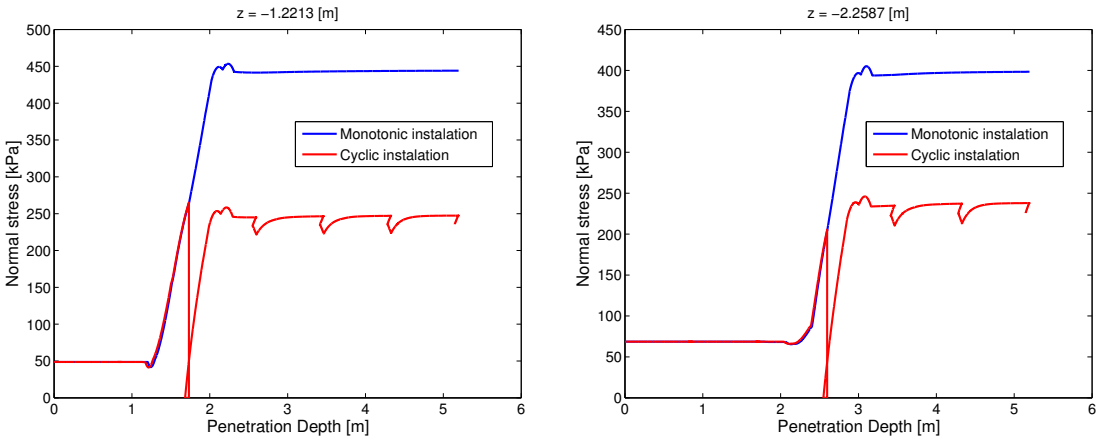

Figure 32: Interface normal stress for two different installation types

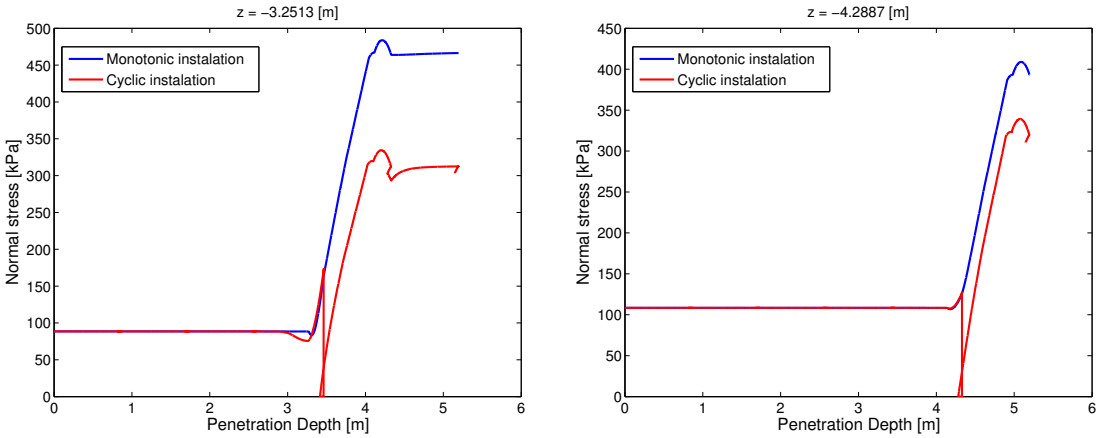

Figure 33: Interface normal stress for two different installation types

The effects of cycling are most significant at the interface level where the stress paths indicate constrained dilative behaviour with normal stresses increasing while, on the other hand, markedly contractive behaviour resulting in normal stress reductions are clear on unloading. This is consistent with what is observed by Jardine et al. [60]. The reduction during the first unloading is quite pronounced and can only be explained by a gap between

the soil and the pile. This occurs due to the position of the node near the cone edge which results in a detachment between the pile and the soil during unloading. This is possible since the unloading is done by applying a displacement on the "external" nodes in the upward vertical direction. This gap only occurs this one time for each depth since once the cone is passed no separation occurs between the soil and the pile. These results are analogous to the ones for the shear stress evolution.

The volumetric behaviour can be seen in figure 34.

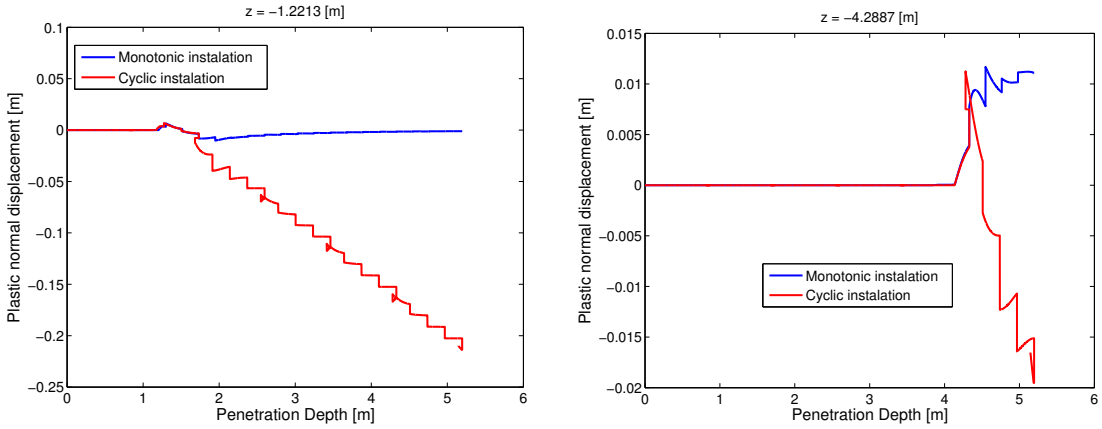

Figure 34: u_n^p for two different installation types

The cycling behaviour is shown to substantially increase the volume of the interface elements. In fact all depths show marked net increase of dilation with increasing number of cycles. Despite having an initial contraction there is a reversal in the volumetric response in which dilation clearly surpasses the initial volumetric decrease.

This behaviour at the interface level shows that the constraint on dilative volumetric behaviour at the interface level (very near field) is lower in the cyclic installation case. This has implications for the shaft friction mobilization as can be seen in figure 35.

Due to the lower confinement both normal and shear stress values are lower in the cyclic case than in the monotonic case. However, the dilative behaviour in the very near field (interface level) will result in the non-existence of a plateau in shaft resistance mobilization. Higher shaft resistance is determined as a result of this fact even though lower shear stresses are found at the interface. It is reinforced here that this effect of heave in the shaft resistance of the pile might be overestimated due to the elastic layer at the surface of the soil mass and the low confining stress of some elements near the pile.

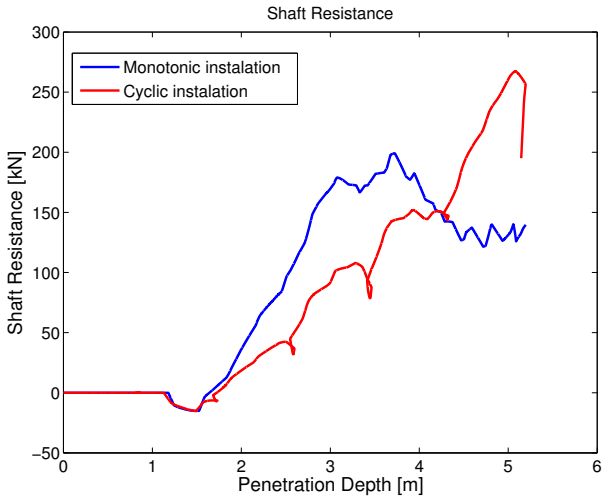

Figure 35: Shaft resistance for two different installation types

6.3.4 Interface constitutive law

In this section a comparison between the ECP or the Mohr-Coulomb (MC) constitutive model at the interface is made. The results will be focused once more at the interface level since that is where the changes in behaviour are relevant. The same critical state parameters are considered for the MC as for the ECP model. However, the MC model is considered as an elastic-perfectly plastic stress-strain constitutive law with a angle of dilatancy equal to zero. This, naturally, results in a zero plastic volumetric variation in the MC model case. The implications of this in the results can be better seen in the shaft resistance mobilization. The results for both types of installation are shown in figure 36.

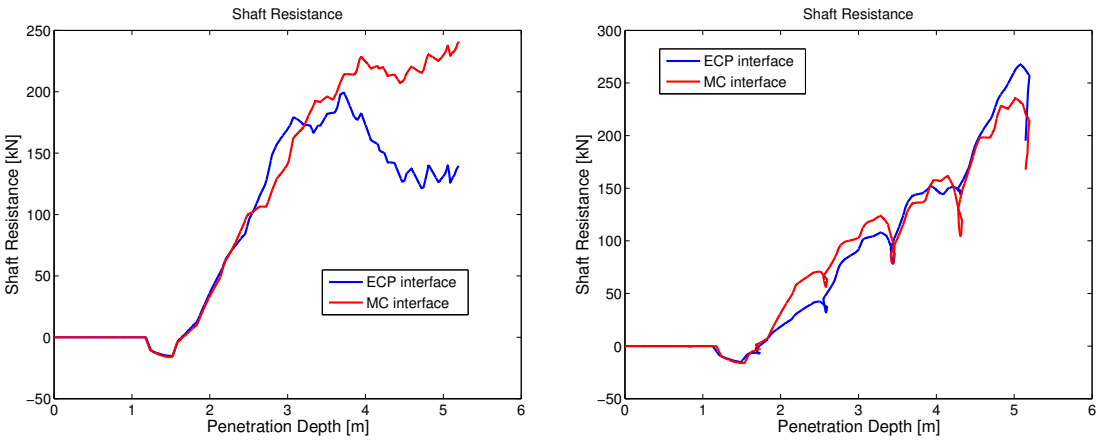

Figure 36: Shaft resistance evolution for two different interface models - Monotonic (left) and Cyclic (right))

The importance of the volumetric behaviour in the shaft friction mobilization is very

noticeable from these results. Note that where the volumetric variation influences less the behaviour of the soil mass (cyclic installation) the values calculated are very similar for both models. This is of course due to the fact that the critical state is defined equally for both models and simply the stress path is influenced. However, in the monotonic installation scenario the difference is clear and the plateau is not detectable in the MC model case.

6.3.5 Breakage mechanism

In this last section of the parametric studies the influence of the breakage mechanism is analyzed. The breakage is taken as "active" in both the interface and volume soil mass elements. The effects of considering the breakage mechanism "active" in the calculations has important influences in the stress path at the interface since it redefines the position of the critical state. This has important effects on the overall volumetric behaviour and shear stress development at the interface. In order to better illustrate the effects the breakage parameter a^{br} was considered to be 50% higher than the value given in Appendix F for Ottawa sand. The results are presented for both types of installation procedures.

Firstly the results from the monotonic type installation at the interface level are presented. The evolution of normal stress is shown in figures 37 and 38 for different depths. These results are analogous to those for the shear stress evolution.

The results show the exact same trend as in RS tests with CNS or CV boundary conditions [125]. Due to the first phase transformation there is an increase in both shear and normal stress as the soil switches from contractive to dilative behaviour. This is later followed by another phase transformation by the fact that the breakage mechanism overcomes the dilative tendency and there is volumetric decrease as the soil starts to contract [116] [118] [67] [125]. This causes normal and shear stresses to decrease until a residual value is eventually reached if shearing continued.

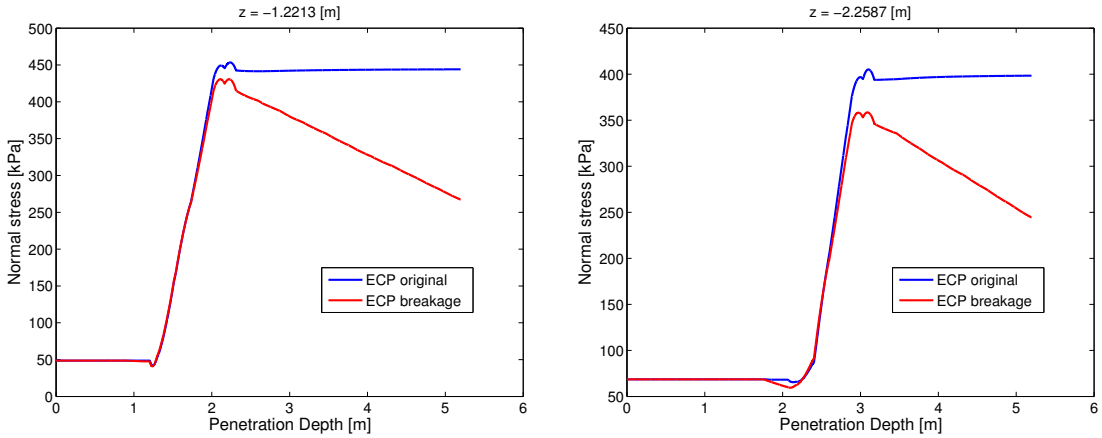

Figure 37: Interface normal stress evolution during installation considering or not the breakage mechanism

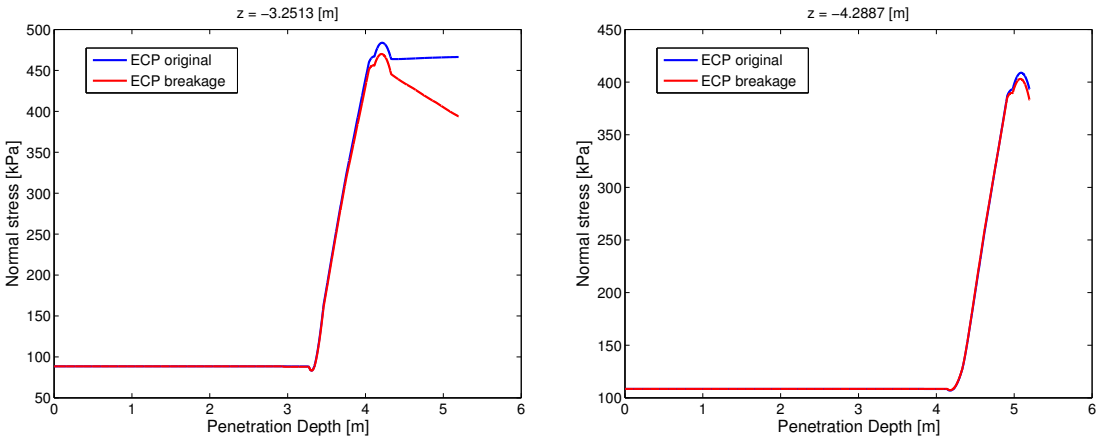

Figure 38: Interface normal stress evolution during installation considering or not the breakage mechanism

In terms of the volumetric behaviour the results are shown in figures 39 and 40. There is marked contraction after the second phase transformation which continues to develop until the end of the installation procedure. This results in an approximation of the nodal points to the shaft after the tip has passed [117]. As explained before the "real" critical state when considering the breakage mechanism depends heavily on the parameters a^{br} and m_a^{br}.

The transition from dilative to contractive behaviour occurs in a relatively rapid manner. There is a transition zone where the volumetric variation increment is zero (critical state assumed for most cases) before it starts decreasing due to crushing of the soil particles. This behaviour is found here to be quite similar to CNS conditions in RS test albeit hard to simulate exactly using a simplified model due to changing stiffness of the soil mass which corresponds to the boundary conditions in RS tests.

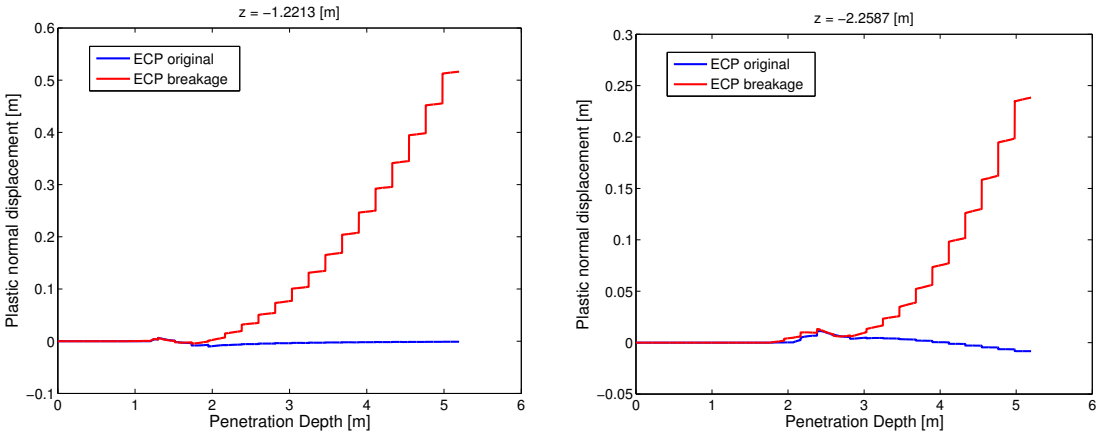

Figure 39: u_n^p evolution during installation considering or not the breakage mechanism

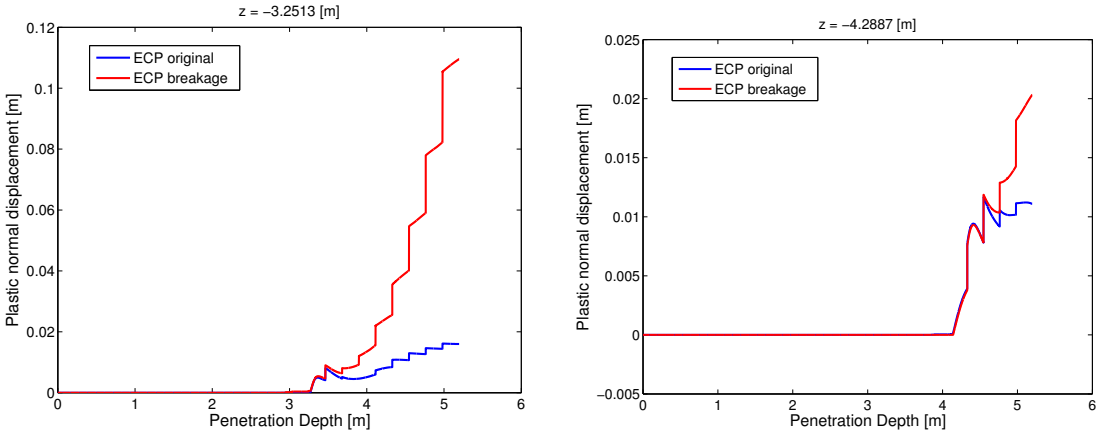

Figure 40: u_n^p evolution during installation considering or not the breakage mechanism

The results when considering the cyclic installation procedure will now be analyzed. The evolution of normal stress is shown in figures 41 and 42 for different depths. These results are analogous to the shear stress evolution. Due to the fact that during cyclic installation the total shear strain (cumulative shear strain) to which the soil is subjected is considerably higher than in the monotonic case, the importance of the breakage mechanism increases. This is seen as a more considerable decrease in both normal and shear stresses with increasing penetration depth.

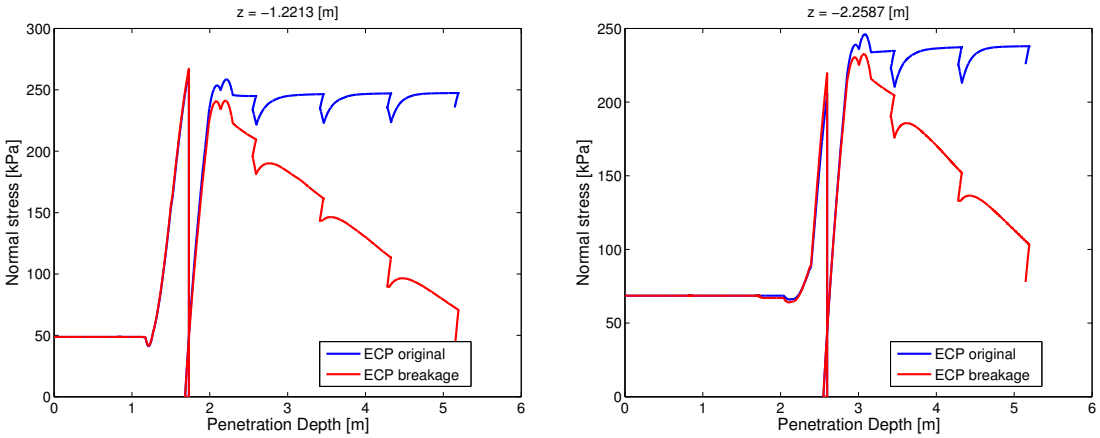

Figure 41: Interface normal stress evolution during installation considering or not the breakage mechanism

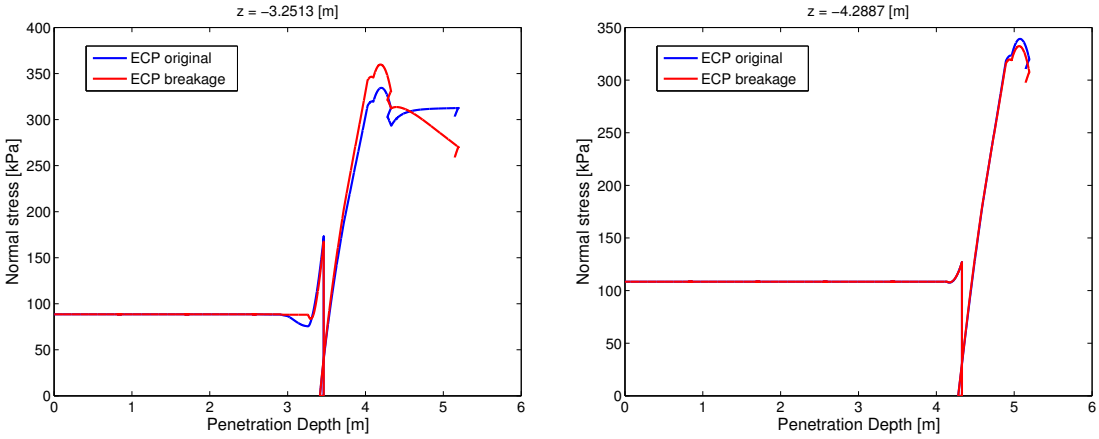

Figure 42: Interface normal stress evolution during installation considering or not the breakage mechanism

Due to the added relative shear displacement at the interface, as a result of cycling, there is a considerable cumulation of contraction as the calculation progresses. This is found to be valid for all depths with more relevant consequences near the surface since that is where the maximum shear strain imposed is located and, additionally, also where the initial mean stress is lower.

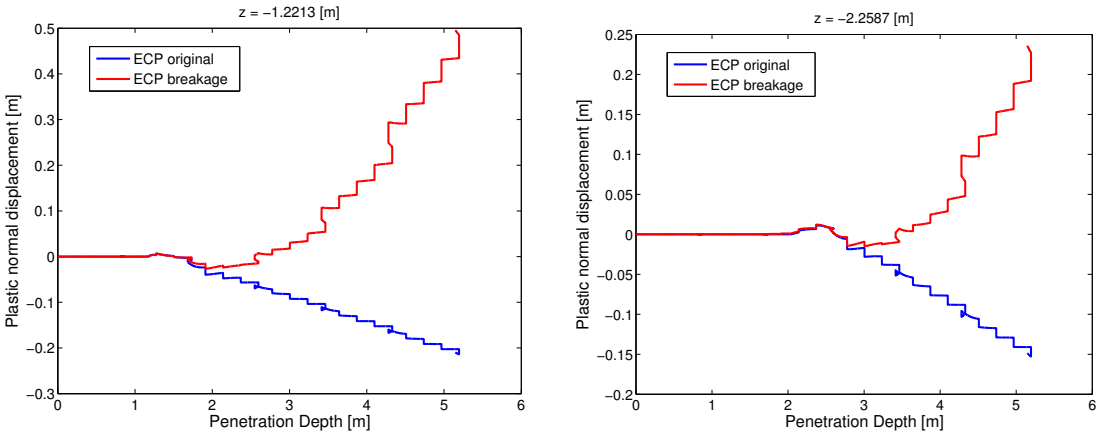

Figure 43: u_n^p evolution during installation considering or not the breakage mechanism

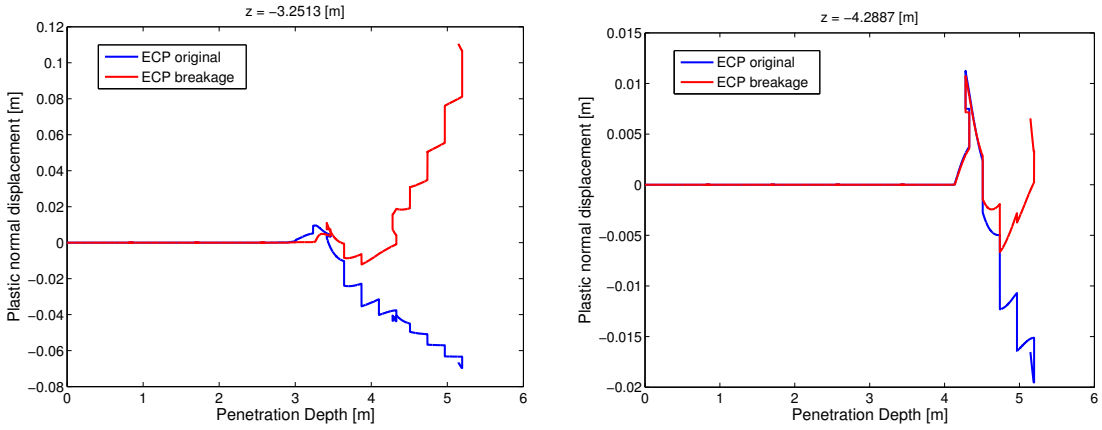

Figure 44: u_n^p evolution during installation considering or not the breakage mechanism

Finally, the shaft resistance evolution is analyzed. The breakage mechanism is considered for both the interface and volume elements which therefore influences considerably the shaft friction mobilization for both installation cases as can be seen in figure 45.

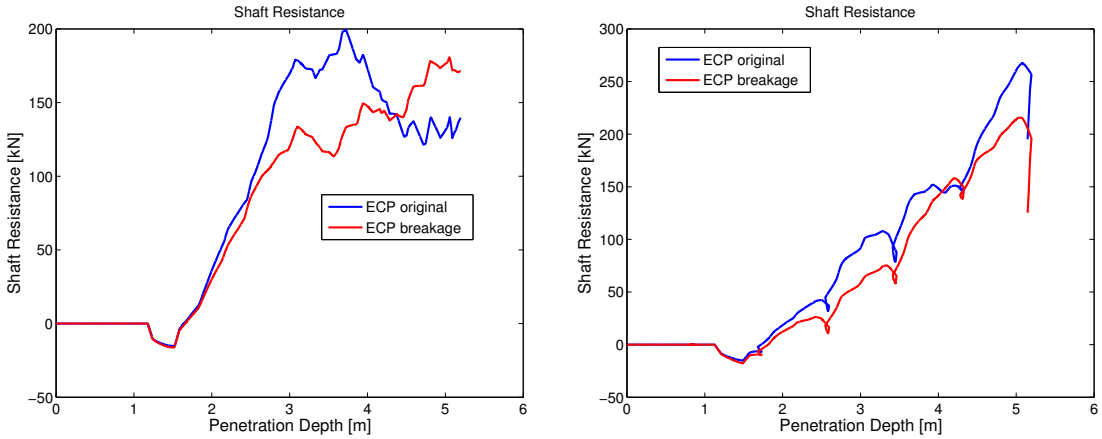

Figure 45: Shaft resistance - Monotonic (left) and Cyclic (right) installations

Due to the breakage mechanism, dilative behaviour is severely diminished mainly at the interface level but also, albeit less importantly, at the soil elements adjacent to the interface [117]. This effect, such as for the cyclic installation case, results in the absence of the plateau due to less dilation of the soil mass. This results in the contradictory result of finding higher shaft resistance in the monotonic case. This result should be considered with some reservations.

Immune to this issue, the cyclic installation case shows the expected result of lower shaft friction mobilization when considering breakage of soil particles. The figure shows an increasing divergence between the two curves which suggests that this effect would become more pronounced for longer piles. This would be a reasonable assumption since

it would result in higher levels of shearing along the shaft of the pile.

The importance of considering particle breakage in the constitutive model cannot be overstated. Significant changes in behaviour are observed as well as a redefinition of the location of the critical state line in volumetric-stress space. Notably, the fact that residual shear resistance does not remain constant with increasing shear strain is of the utmost relevance in terms of safety considerations.

6.4 Displacement vs Non-displacement piles

In this section a brief presentation is done of the results of shaft friction mobilization of a monotonic loading performed on displacement and non-displacements piles.

The effects of installation are usually seen by residual stresses present namely at the interface level and are noticed when shaft friction is mobilized during loading after installation. These residual stresses will strongly affect the stress path taken by the soil when subjected to loading since it changes its initial state. The installation cases are the monotonic and cyclic installation types already described before. After complete installation was attained, an unloading in order to obtain zero head load was performed and the pile was then subsequently reloaded. The no-installation case presumes the pile to be a non-displacement pile and, therefore, the soil is undisturbed before loading.

Two different interface behaviour laws are considered, the ECP model and a non-associated elastoplastic model with the Mohr-Coulomb (MC) yield function. Both the installation procedure and the loading phase are performed consistently with the same behaviour law.

Firstly the mobilization of shaft friction is shown in figure 46.

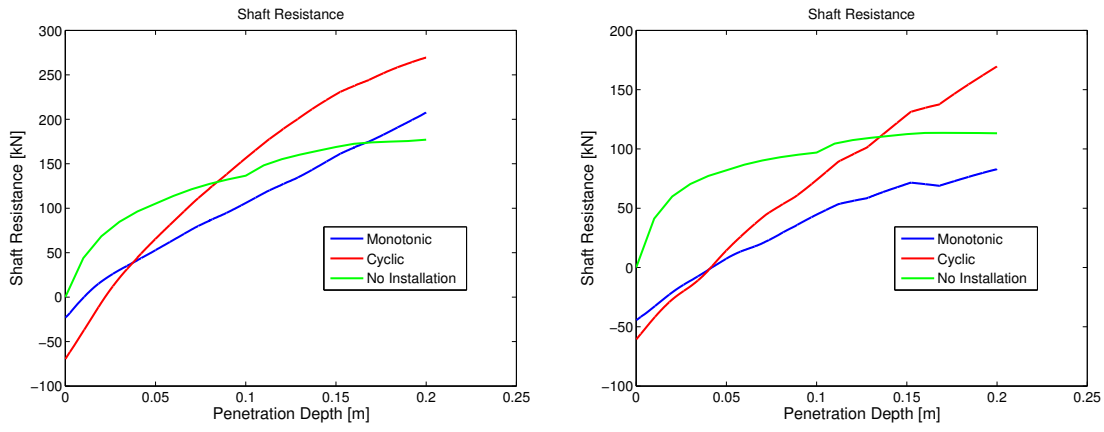

Figure 46: Shaft resistance - ECP model (left) - MC model (right)

Negative residual shear stress can be seen clearly in figure 46 as a result of the installation procedure. This results in different initial states for each case but the differences in

stress path are even more relevant. Although the hardening parameters have an influence on the results (different shaft resistances between the ECP and MC models) the different stress paths and final resistance values are mainly due to the considerable increase of normal stress at the interface. An increase in normal stress allows for higher shear stress to develop at the maximum friction mobilization. The influence of hardening results from both the volumetric and the deviatoric hardening parameters which, under the extreme radial confinement of the interface layer, allow for higher shaft resistances due to the smaller reduction in normal stress during unloading.

Results at the interface level will be presented hereafter. Figure 47 shows the evolution of normal stresses for two different depths for all three scenarios. For the installation cases, the variation of normal stress is barely noticeable due to the memory of the material during the previous actions. Net dilation occurs in the case of the non-displacement pile due to shearing at the interface resulting in higher normal stresses.

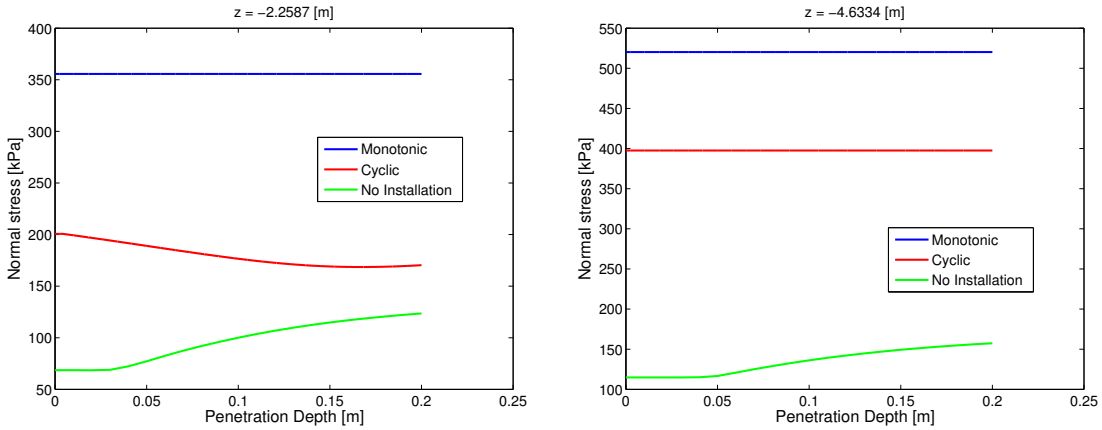

Figure 47: Interface normal stress (ECP)

The influence of the installation procedure results, in terms of plastic volumetric variation, in a higher contraction (mostly "elastic" behaviour) before dilation occurs. Due to the small amplitude of the loading compared to what the soil was subjected during the installation however, no phase transformation is observed for the installation cases. The no-installation case shows dilation in accordance with CNS RS monotonic tests which induced the increase in normal stress due to the similarities between the interface layer and a RS test.

Between the different installation types it can be seen that the monotonic installation consistently generates higher radial stress than the cyclic one at lower depths. This in turn results in higher shear stress developing at those depths despite that a lower total shaft resistance is determined. This difference in shaft resistance has already been discussed in the previous section in light of the observed heave of the soil elements near the interface.

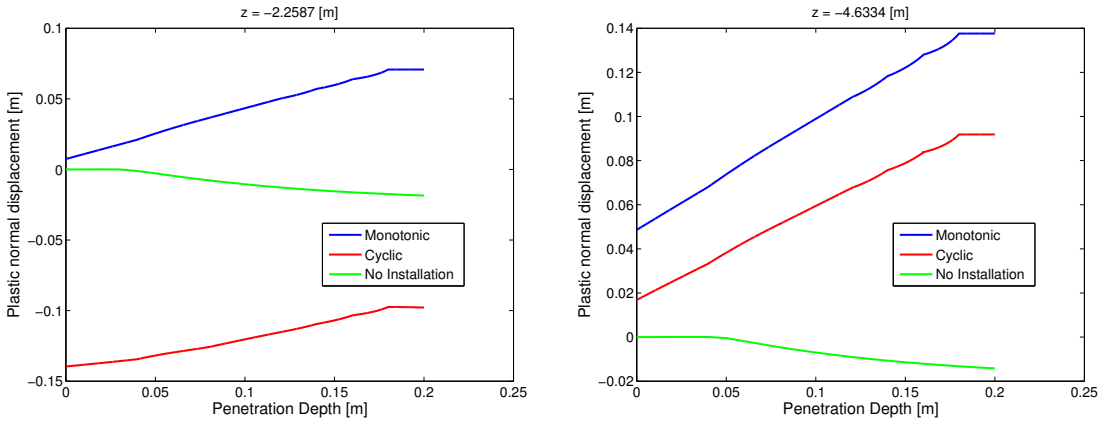

Figure 48: u_n^p (ECP)

Finally the shear stress evolution during loading is shown in figure 49.

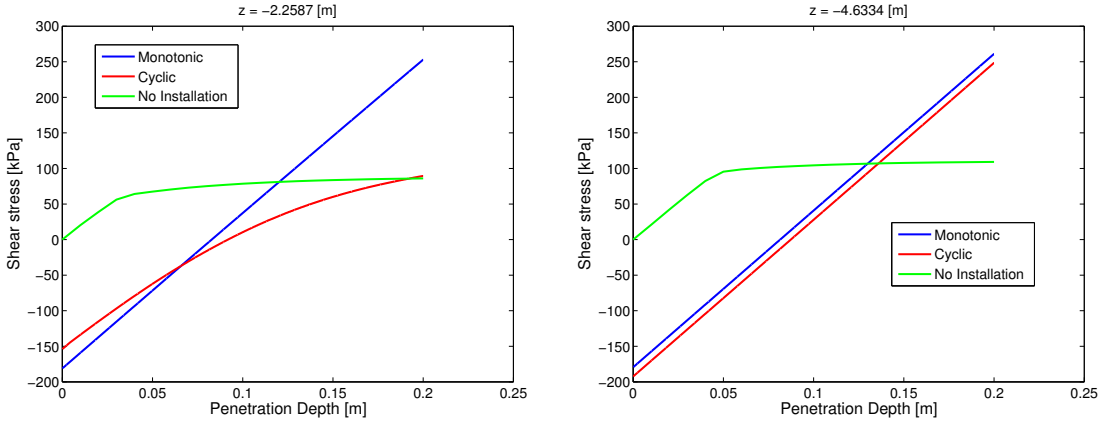

Figure 49: Interface shear stress (ECP)

A considerable stiffer response is found in the installation cases which was also observed in the shaft friction mobilization.

Similar results can be found with the MC behaviour law at the interface in figures 50 and 51.

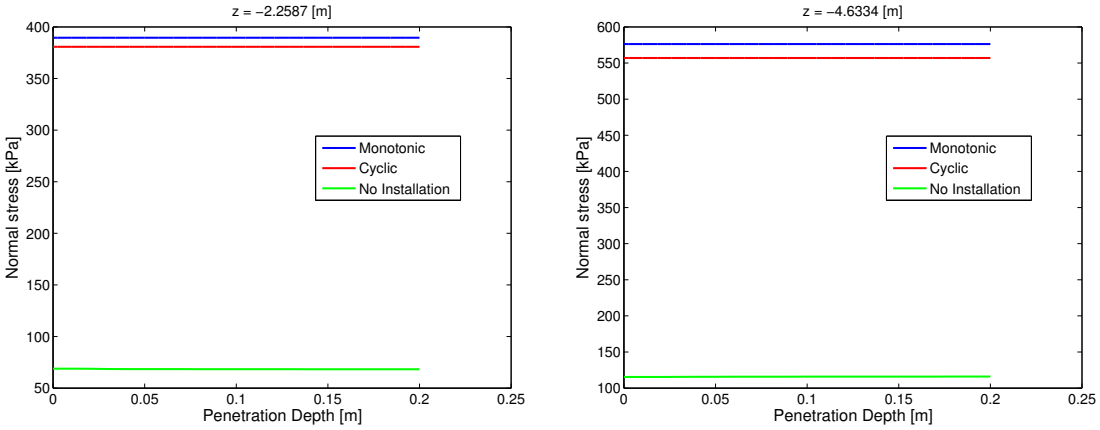

Figure 50: Interface normal stress (MC)

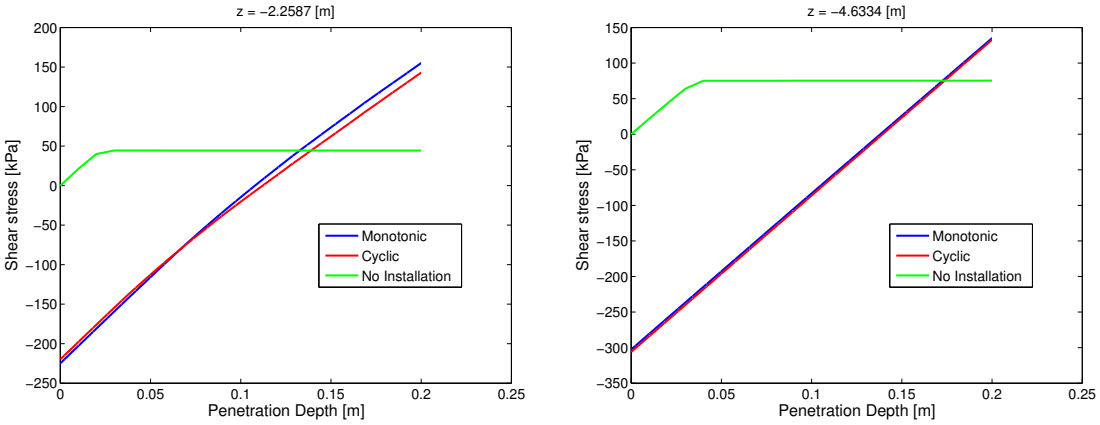

Figure 51: Interface shear stress (MC)

The importance of considering the installation procedure in determining the response of a pile during loading is highlighted here with these results. For both installation types, residual stresses are found to be present, dramatically shifting the point of origin in both normal and shear stresses at the interface level before loading occurs. The behaviour observed during loading is also different, higher stiffness is observed and contraction is found to occur when installation is considered while net dilation occurs in the non-displacement pile case. The initial state of the soil has been significantly modified altering its volumetric response to shearing during loading. The MC interface law fails to capture this difference in volumetric behaviour resulting in almost no variation in normal stress due to the fact that the behaviour is elastic. The shear stress (and therefore shaft resistance) increases in a linear progression with the same angle as the initial phase in the no installation case since the stiffness matrix is stress independent before the maximum shear mobilization is attained.

6.5 Cyclic axial loading of a single pile

This section will address the main components required for the complete description of the numerical model for the cyclic axial loading of a pile. The numerical elements, behaviour laws and model parameters will be defined followed by the calculation procedure and details of the simulations. Different cyclic paths, by varying the amplitudes of the cycles, are compared and studied in order to describe the soil-pile interface behaviour, namely, the degradation of shaft friction mobilization with increasing number of cycles.

6.5.1 Numerical elements, materials and geometry

In this section a description of the different types of elements, behaviour laws for the various materials and the geometry of the model is presented in detail.

Numerical Elements

The numerical elements used in the simulation of cyclic loading of a single pile are the same as the ones used before for the installation numerical calculation: volume elements and interface elements. However, in this calculation the pile is considered as a deformable solid being therefore modelled 4-node isoparametric elements. The pile is considered to be fully in place at the start of the calculation. The interface elements (linear) are used to transfer shear and normal stresses and displacements between the pile and the soil mass and vice-versa. They are obviously located at the nodes where the pile boundary is located both in the radial and vertical directions. The interface elements surround the pile shaft and base completely. This allows for the base of the pile the possibility to separate from the soil when an upward motion is considered.

Materials

The soil is modelled considering either the original or the revised ECP constitutive model depending on the simulations. In these calculations no elastic layer near the surface is considered unlike the pile installation case. The pile loading is not sufficiently severe to justify that simplification since no numerical instabilities occur during these calculations at this level of stress/strain. With the exception of the interface constitutive law only the characteristics of the loading cycles are varied during the calculations. Therefore the model parameters and geometry of the mesh remain unchanged. The properties for all the materials used in the reference simulation (Toyoura sand) can be found in Table 6.2. A $K_0 = 1.0$ is taken for the soil mass.

Model parameters			
Materials / Elements	Toyoura sand	Pile	Interface elements
Elasticity			
$K_{ref}/E_{ref}(MPa)$	296.0	$11.1 \cdot 10^3$	533.0
$G_{ref}(MPa)$	222.0	$8.33 \cdot 10^3$	222.0
n_e	0.40	0.00	0.40
$p_{ref}(MPa)$	1.0	1.0	1.0
Critical State and Plasticity			
$\phi'_{pp}(^\circ)$	30	n.a.	30
β	17	n.a.	43
d	3.50	n.a.	n.a.
b	0.22	n.a.	0.22
$p_{co}/\sigma_{co}(MPa)$	4.90	n.a.	0.30
Flow Rule and Isotropic Hardening			
$\psi(^\circ)$	30	n.a.	30
α_ψ	1.00	n.a.	1.00
a_1	0.0001	n.a.	0.0001
a_2	0.0150	n.a.	0.0150
c_1	0.0600	n.a.	n.a.
c_2	0.0300	n.a.	n.a.
m	1.00	n.a.	1.00
Threshold Domains			
r^{ela}	0.005	n.a.	0.005
r^{hys}	0.030	n.a.	0.030
r^{mob}	0.800	n.a.	0.800
r^{ela}_{iso}	0.0001	n.a.	n.a.
Breakage parameters			
a^{br}	0.0	n.a.	0.0
m^{br}_a	1.00	n.a.	1.00
$b_{W_p}(MPa)$	0.0	n.a.	0.0

Table 6.2: Model parameters

Geometry

The numerical calculation of the cyclic pile simulation is performed considering an axisymmetric condition. The pile is always considered as having the form of a cylindrical prism with a flat tip with a diameter of 500 mm and a length of 5 meters. This is represented in figure 52.

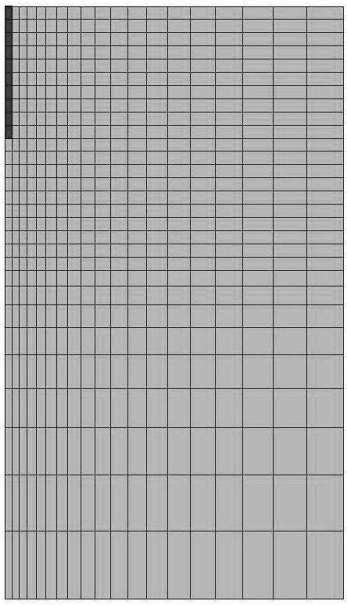

Figure 52: Finite element mesh

The boundary conditions of the mesh are standard: nodes on the edges of the mesh are constrained in the normal direction of movement. At the lower boundary of the mesh (lowest z coordinate) the tangential direction of movement is restrained. The total number of volume and interface elements (and therefore the number of nodes) depends on the pile geometry: length and diameter. The soil material is composed of 541 elements, the interface of 11 elements and the pile of 10 elements. The mesh width and length is always higher than $2.5\,L$, where L is the pile length.

The evolution of both base and shaft resistances considering a monotonic loading are shown in figure 53 where s/D is the settlement normalized by the pile diameter.

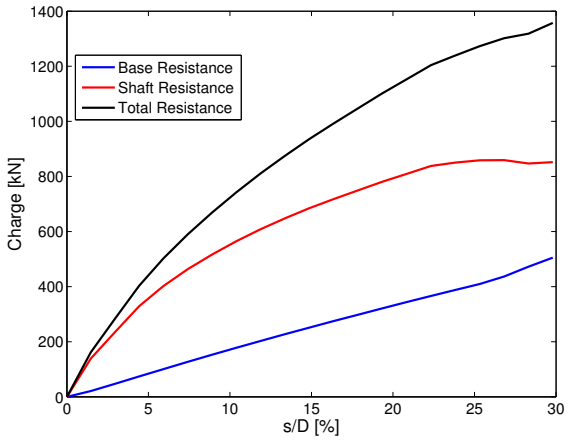

Figure 53: Base and Shaft resistances - Monotonic loading

6.5.2 Calculation procedure

The numerical definitions considered in order to simulate the axial cyclic loading are detailed here. A vertical pressure is imposed by means of a surface load element at the surface and at the top of the pile head.

Types of loading

Three different amplitude ranges with corresponding number of cycles are considered. Only 1-way cycling is performed. These different loading cycles are detailed in Table 6.3 (inspired from Tsuha et al. [110]).

Loading cycles					
Designation	Q_{max}	Q_{min}	Q_{mean}	Q_{cyclic}	Number of cycles
Stable	0.90	0.80	0.850	0.050	350
Meta-stable	0.65	0.10	0.375	0.275	100
Unstable	0.90	0.00	0.450	0.450	15

Table 6.3: Loading cycles

where,

$$Q_{cyclic} = \frac{(Q_{max} - Q_{min})}{2} \tag{6.14}$$

$$Q_{mean} = \frac{(Q_{max} + Q_{min})}{2} \tag{6.15}$$

The values of Q_{max} and Q_{min} are simply factors which must then be multiplied by the initial loading present at the pile shaft by means of friction mobilization. The values

of this initial loading in the following calculations are 80 kN, 215 kN and 440 kN. The 80kN is a low value in order to minimize the influence of the base resistance in the results. The main objective of this study in the degradation observed in shaft resistance with cycling and therefore the base influence must be studied separately. These three different loading values will henceforth be referred to as low, medium and high loadings respectively. Tsuha et al. [110] citing Jardine and Standing [62] divided these different loadings as being present in three different categories: Stable, Meta-Stable and Unstable (figure 54). The green, blue and red dots correspond to the Stable, Meta-Stable and Unstable loading cycles which will be simulated, respectively.

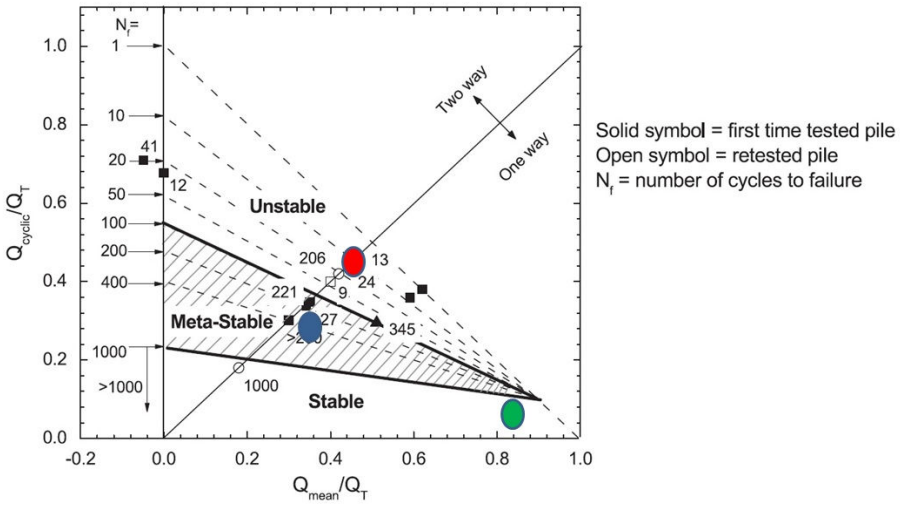

Figure 54: Loading cycles [110] [62]

These designations were assigned based on the cyclic loading by means of the abacus of figure 54 where the number of cycles is correlated with the characteristics of the cyclic loading.
This matrix of designations will be considered henceforth a reference to indicate the severity in terms of shear strain at the shaft of the cyclic loading imposed on the pile head.

6.5.3 Result analysis

In this section the results obtained from the cyclic axial loading of a single pile will be presented. The section is divided into three parts. Each part corresponds to one type of loading amplitude and number of cycles as defined in Table 6.3: Stable, Meta-stable and Unstable.

"Stable" - Loadings

This type of loading is defined as follows: after an initial loading, the pile is subjected to one-way cycling between 80% and 90% of this value.

Firstly the medium loading is analysed. Base and shaft resistances are shown in figure 55. No decrease in shaft resistance is observed during the cycles. Also, pile head displacement does not increase and is independent of the number of cycles. This is verified since the amplitude of the cycles is sufficiently low for the behaviour to remain in the elastic domain. No volumetric variations are determined at the interface level after the initial loading. There is a near zero net volume variation with the cycles.

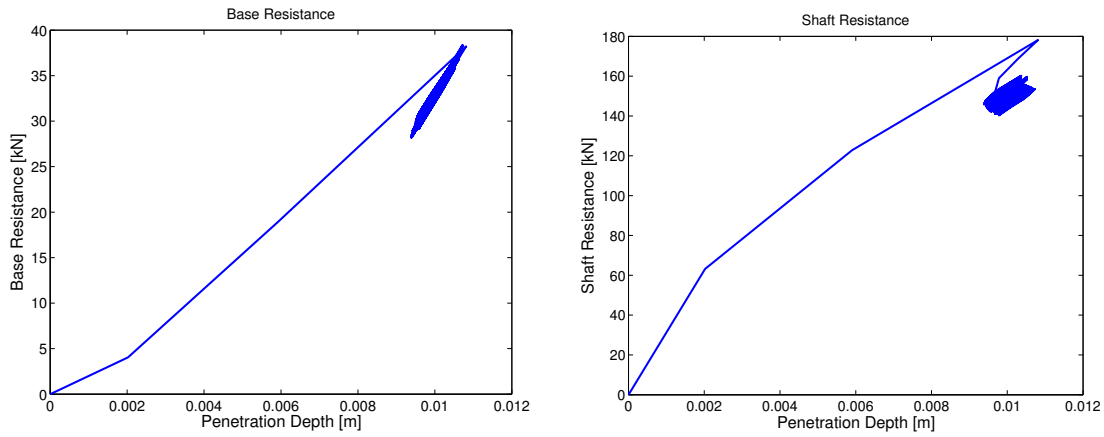

Figure 55: Base and Shaft resistances - Medium initial loading

Considering only the cyclic part of the loading, no significant differences can be seen between distinct behaviour laws. Calculations performed considering a Mohr-Coulomb behaviour law or where the breakage mechanism is active do not exhibit a different behaviour to the one presented here.

The base and shaft resistances for the high amplitude loading cycle are shown in figure 56. A marked decrease can be seen in shaft resistance mobilization which is compensated by the base. There is a net increase with the number of cycles of the pile head displacement as a result of the increase in relative tangential displacement at the interface level.

Figures 57 and 58 show the soil-pile interface behaviour for a depth of 3.4 meter. After the initial loading where very high dilation is determined, resulting in a considerable increase of both normal and shear stresses, there is net contraction with each cycle. This in turn results in a decrease of the normal stress at the interface which reduces the mobilized shear stress.

Similar results were observed in Chapter 5 when performing cyclic shear tests. Low amplitude cycling of dense sand, after an initial loading, might provoke contraction of the interface layer for a high number of cycles. As referred before this observation must be considered with caution in terms of modelling. Thermodynamic considerations come into play since this cumulation of contraction does not seem to have any imposed limit on the model which might then result in non-realistic results concerning volumetric variations.

Finally, the breakage mechanism does not have any significant influence on the results.

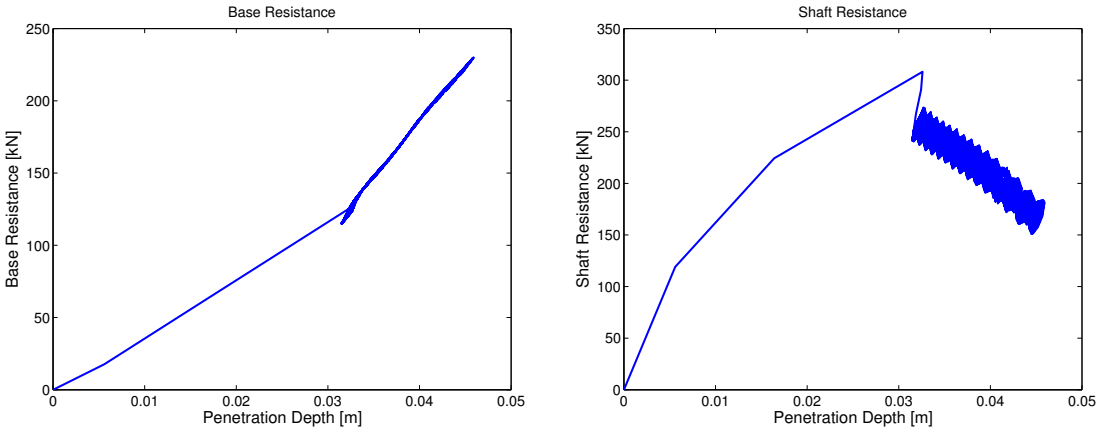

Figure 56: Base and Shaft resistances - High initial loading

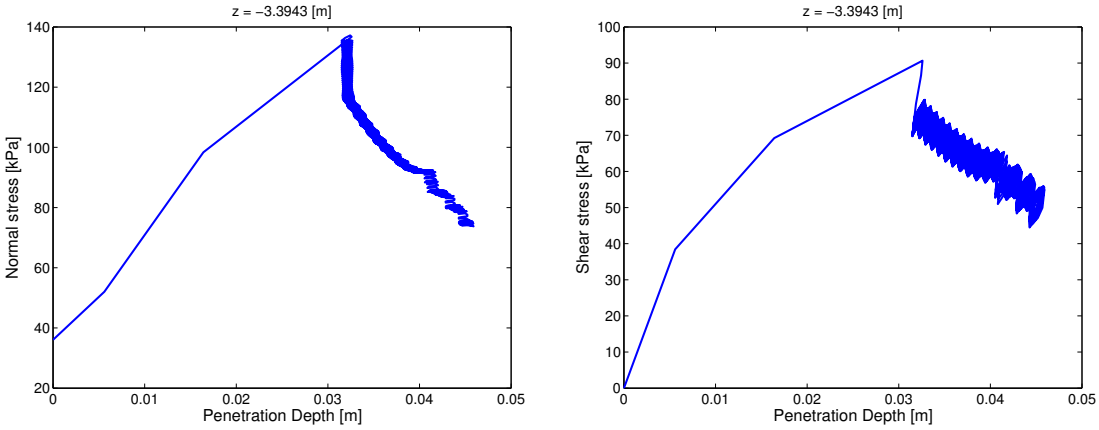

Figure 57: Normal and shear stresses

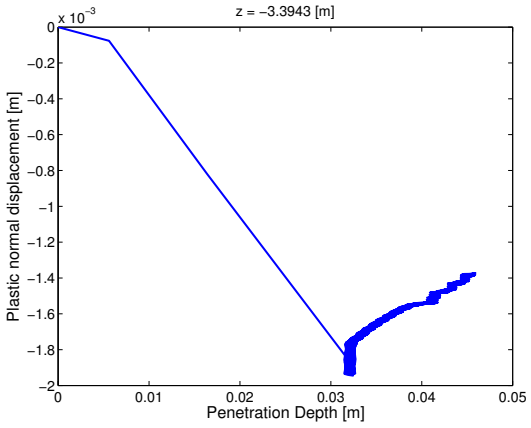

Figure 58: u_n^p

"Meta-Stable" - Loadings

This type of loading is defined as follows: after an initial loading the pile is subjected to one-way cycling between 10% and 65% of this loading.

Only the medium loading is analysed in this section. Base and shaft resistances are shown in figure 59. A continued decrease in shaft friction is determined from the simulations with the corresponding increase of base resistance and increased pile settlement. Similarly to the results from the "Stable" cyclic loading path the base resistance never decompresses completely after the initial cycles. This is due to a cumulation of relative tangential displacement at the interface level between the pile and the soil.

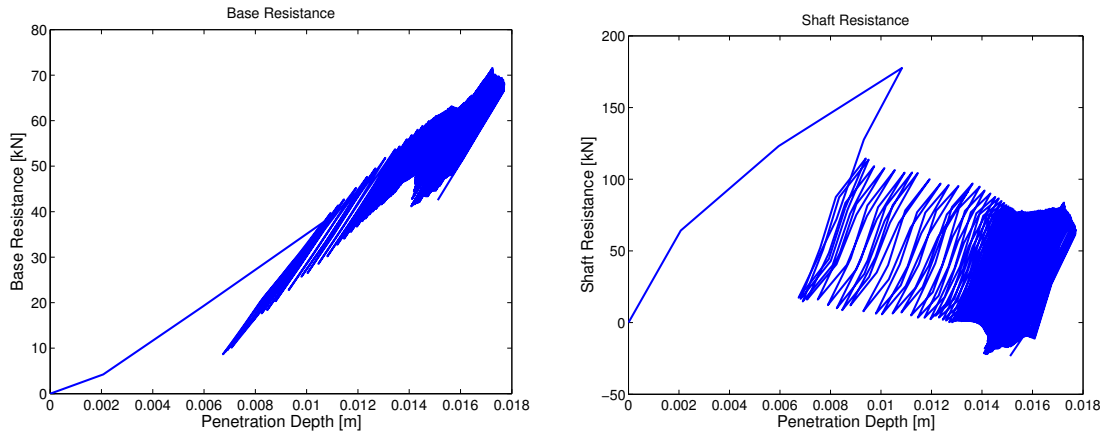

Figure 59: Base and Shaft resistances - Medium initial loading

Here the behaviour at the soil pile interface is analyzed. Figures 60 and 61 show the soil-pile interface behaviour for a depth of 3.4 meter. Marked contraction can be seen following the initial dilation and net contraction of the soil occurs after a relatively small number of cycles (figure 61). This contraction then results in a decrease of normal stress to a lower range than its initial value. Shear stress decreases as well since it is directly related to the normal stress at the interface.

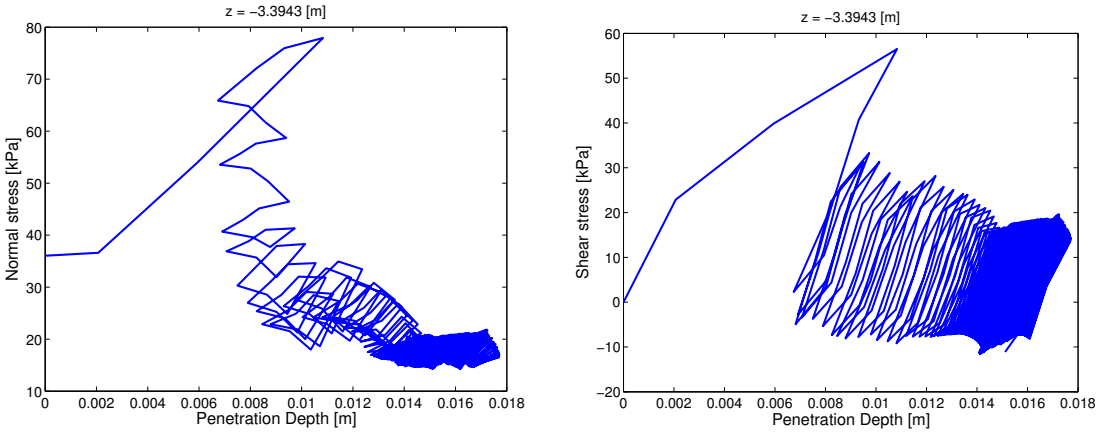

Figure 60: Normal and shear stresses

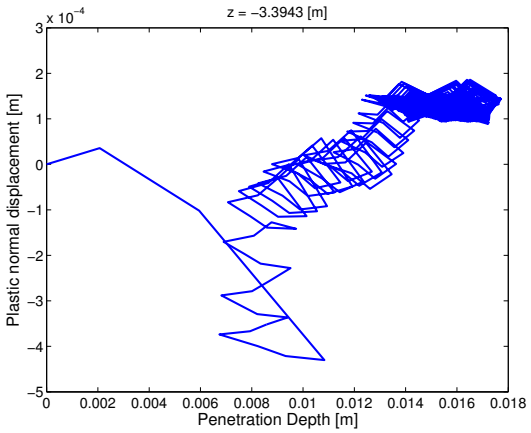

Figure 61: u_n^p - Plastic normal displacement

In the following results the breakage mechanism was considered active in the calculations.

In figure 62 the base and shaft resistances are shown. Qualitatively the same results are observed. However, a higher contraction of the interface layer is determined as a result of the evolution of the internal variable representing grain breakage (figure 64). In fact the contraction is found to double when the breakage mechanism is active. In spite of this, the residual value of horizontal stress is very similar to the previous case even if the stress reduction curve is different (figure 63). This is due to the very low stress which minimizes considerably the breakage's mechanism influence in the stress variation. Also, the pile shaft does not correspond exactly to shear tests with CNS or CV boundary conditions.

The results presented here show the pile shaft resistance degradation "friction fatigue" phenomenon. This degradation results from the contraction of the interface layer which causes decreases in both normal and shear stresses due to the boundary conditions of that element. However, other mechanisms can come into play during pile cyclic axial loading

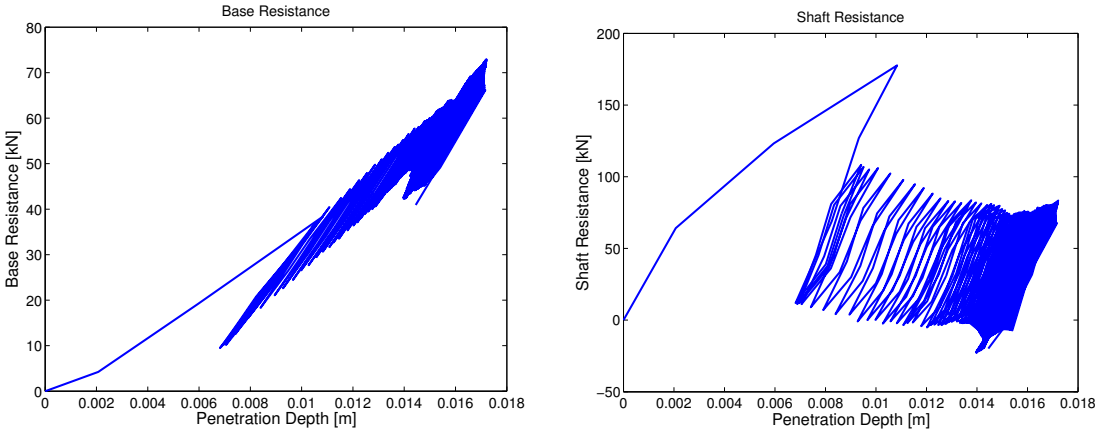

Figure 62: Base and Shaft resistances

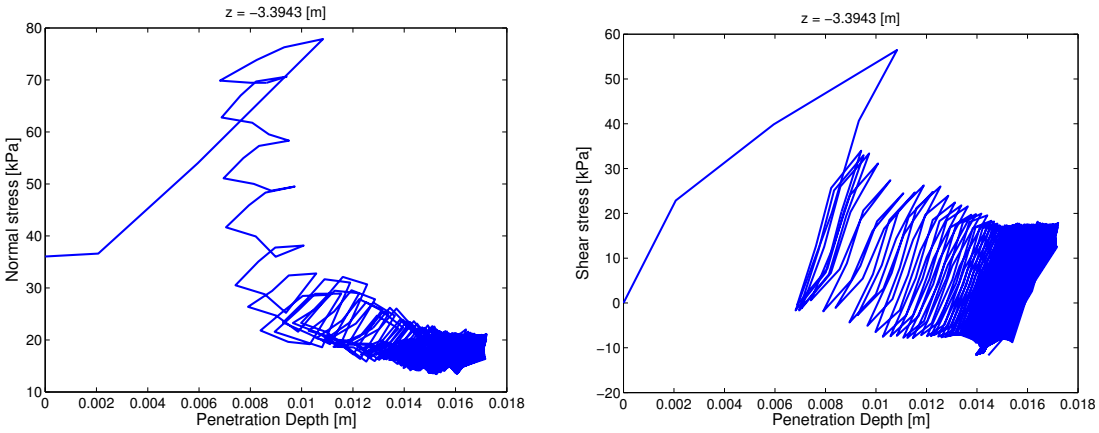

Figure 63: Normal and shear stresses

which can also cause friction degradation at the pile shaft as will be seen in the following section of "Unstable" tests.

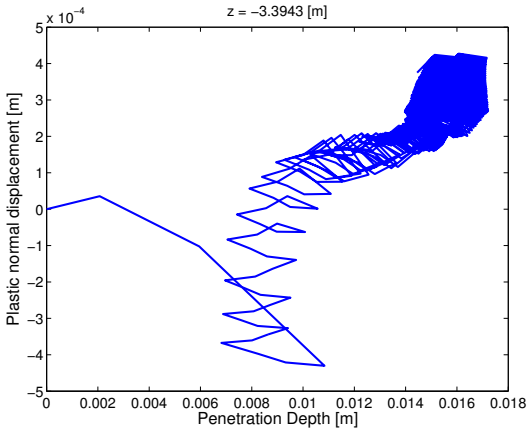

Figure 64: u_n^p - Plastic normal displacement

"Unstable" - Loadings

This type of loading is defined as follows: after an initial loading the pile is subjected to one-way cycling between 0% and 90% of this loading.

Firstly the low loading is analysed. Base and shaft resistances are shown in figure 65. The pile base resistance is barely mobilized (some small traction is determined as a result of numerical inaccuracies during interpolation since no traction is permitted in the model) and a very slight decrease in shaft resistance is determined during these calculations. Therefore, there is some degradation of shaft friction since although the total loading imposed is low the amplitude is high in relation to the loading path (100% variation).

Once more a contraction is observed at the interface layer (figure 67) which results in a considerable decrease in normal stress. This is due to the low loading value which is not high enough to trigger the phase transformation from contraction to dilation. As a result there is net contraction with each cycle (figure 66).

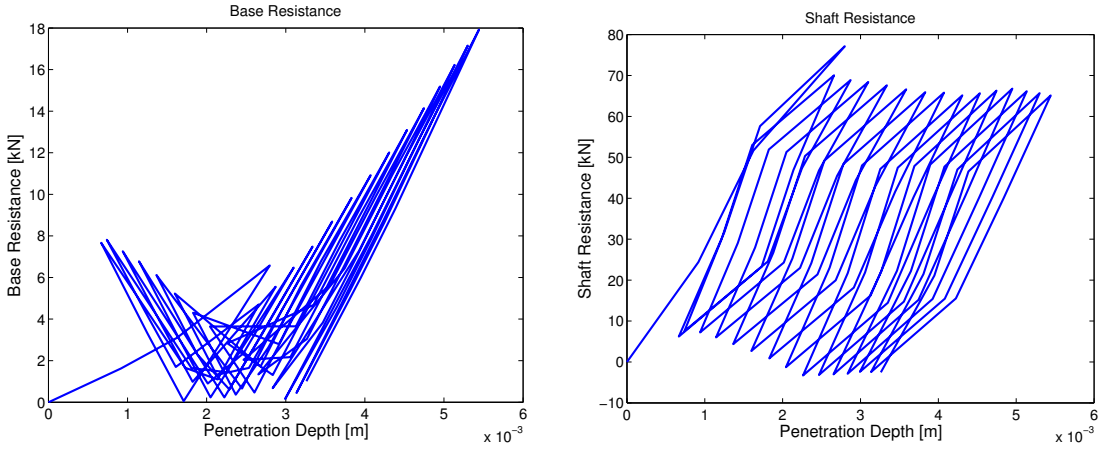

Figure 65: Base and Shaft resistances

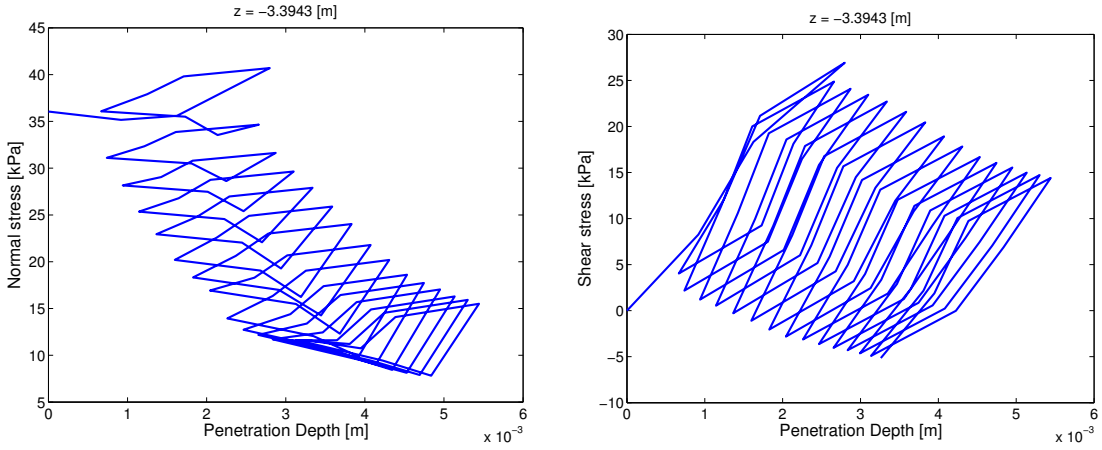

Figure 66: Normal and shear stresses

The base and shaft resistances for the high amplitude loading cycle are shown in figure 68. Once more shaft resistance degradation is observed but the base resistance has been considerably mobilized. This difference between the base resistance evolution is crucial since it is the cause for another mechanism for "friction fatigue".

When analysing the behaviour at the interface level (figures 69 and 70) it can be seen that, unlike previous results, no contraction is observed at the interface level. In fact the opposite is determined since there is net dilation with each cycle. Despite this, both normal and shear stresses are found to decrease. The reason for this apparent incoherent result is the fact that this simulation was carried out considering a pile and not a simple shear test with a CNS boundary condition. Stress redistribution from the shaft to the base is taking place during the loading. This results in a lower shear displacement being imposed at the interface which then causes the decrease in shear stress mobilization. This is then followed by a decrease in normal stress despite the dilation of the interface layer.

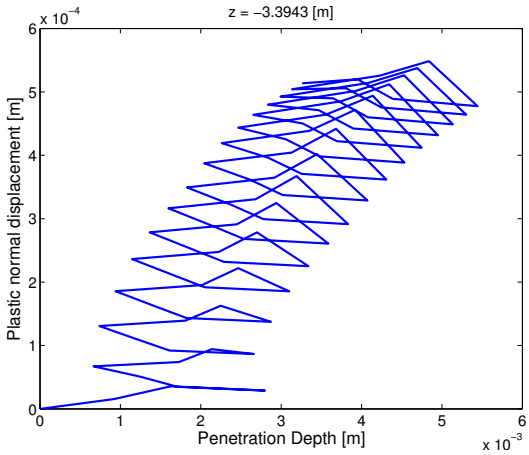

Figure 67: u_n^p - Plastic normal displacement

Similar results were found by D'Aguiar [20] where shaft resistance degradation is observed although there is dilation at the interface level.

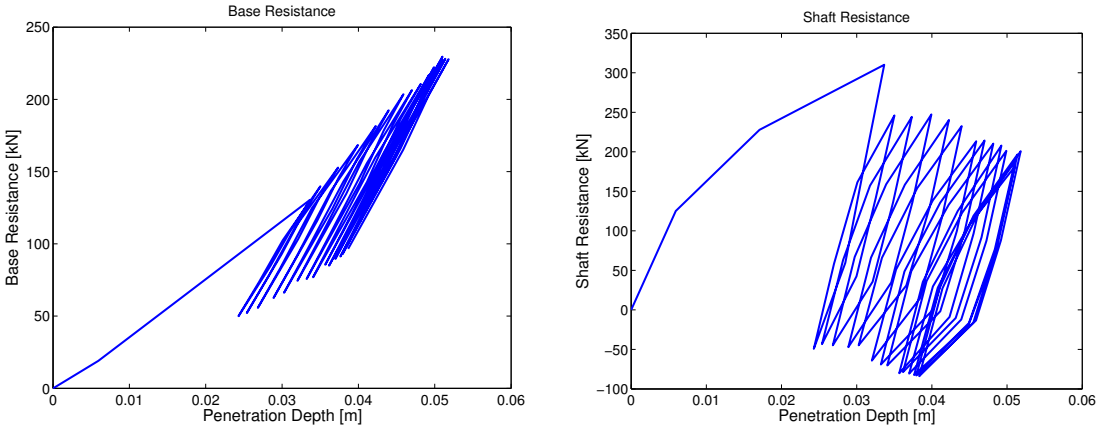

Figure 68: Base and Shaft resistances

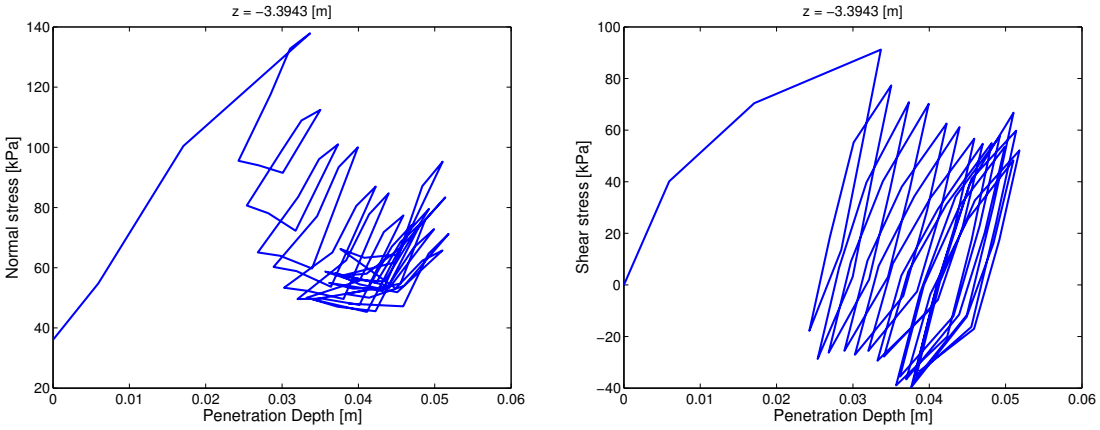

Figure 69: Normal and shear stresses

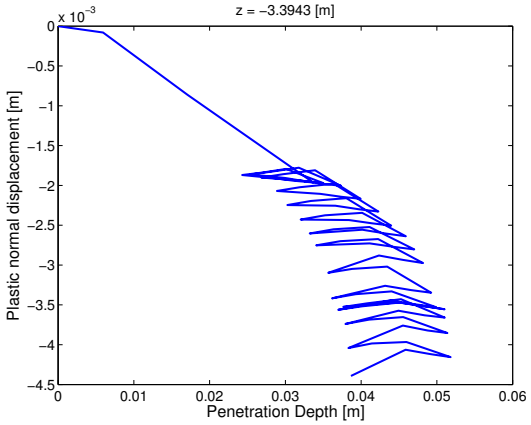

Figure 70: u_n^p - Plastic normal displacement

The results found here cannot be reproduced with a shear test since no redistribution occurs and all the shear displacement imposed is transmitted to the soil which aims to represent the interface behaviour.

The mechanisms by which "friction fatigue" can be observed seem to be twofold:

- contraction of the interface layer which causes normal stress reduction
- stress redistribution from the pile shaft to the pile base which reduces the shear displacement imposed at the interface

It is therefore clear that, for the pile case, "friction fatigue" can be observed in numerical results and is not necessarily associated with interface contraction.

6.6 Summary

This Chapter was concerned with the numerical simulation of different installation procedures as well as monotonic and cyclic axial loading of single isolated cylindrical piles using the finite element code GEFDyn.

A presentation of the numerical model was given in this Chapter with special focus on the calculation procedure, numerical elements and model parameters. Finally, results were thoroughly analyzed considering a reference configuration and parametric studies were performed in order to study the influence of pile geometry, installation type and the interface constitutive behaviour. Results were found to be in broad agreement with those found by other numerical simulation tools as well as having physical coherence with experimental observations. These validations were done in a qualitative manner which suggest that a parameter calibration procedure would allow for quantitative comparisons between results. The importance of the breakage mechanism was made clear when results from the parametric study comparing interface behaviour were performed. Experimental observations of a contracting thin layer of soil at the soil-pile interface (irrecoverable volume reduction as a result of particle crushing) were successfully replicated in the model. Numerical issues related with large deformations in the finite element method with the shaft resistance prediction were present albeit perfectly identified in the calculations [103]. Nonetheless, relevant conclusions were possible to extrapolate from the results.

Monotonic axial pile loading was simulated in order to study the influence of the installation procedure in the mobilization of pile resistance. Results for shaft resistance mobilization show the importance of explicitly considering the installation procedure and how different types of installation impact on shaft resistance evolution during loading as a result of the behaviour at the interface level.

The final part of this Chapter was concerned with shaft friction mobilization during cyclic axial loading of a single non-displacement pile. The installation procedure is not considered for these simulations. Amplitude controlled loadings were performed in order to study the different mechanisms at work at the soil-pile interface. Comparisons between different constitutive models at the interface level were made. This allowed the observation that complex phenomena at the interface level (e.g. volumetric behaviour, degradation) could not be replicated with elastic perfectly plastic models. The different mechanisms of shaft resistance degradation are replicated and the main physical phenomena identified. These seem to be twofold: contraction of the interface layer which causes normal stress reduction and/or stress redistribution from the pile shaft to the pile base which reduces the shear displacement imposed at the interface. The representativity of the results obtained in cyclic shear tests (Section 5.2) is determined as well as its limitations when attempting the simulation of pile shaft cyclic behaviour.

Chapter 7

Conclusions and further research

7.1 Conclusions

The use of displacement piles in foundation structures is a common occurrence. To analyse the behaviour of the pile foundation during loading, the installation phase is taken into account using empirical or analytical methods. These, however, fail to provide a complete description of stress and displacement distributions of the surrounding soil.

Numerical methods are used in order to determine the defining state parameters of the soil before loading. Problems involving frictional contact, particularly when large deformations and/or complex behaviour laws are present are notoriously difficult to solve. Several issues arise when attempting this numerical simulation, some of which this work addressed.

Finite deformation analysis must take into consideration the complexity due to strong non-linearity in geometry. Such complexity lies not only in the definition of various strain measures but also in their conjugate stress measures. After an extensive bibliographic research a consistent, physically pertinent formulation of finite elastoplasticity in finite deformations by considering the logarithmic strain rate [122] is presented. This Eulerian formulation with the logarithmic rate is based upon two consistency criteria, yielding stationarity and elastic integrability.

The main development in this work is the revision of the ECP constitutive model to include the behaviour of soil at high shear strain levels. This is achieved by considering a valid mechanical formulation for finite strains in the constitutive structure but mainly by integrating the grain breakage phenomenon due to continued shearing in the model. This change redefines the concept of critical state since it repositions it in the volumetric-stress space. Moreover, the critical state often considered is shown to be, for some materials following the stress path studied, not a stabilization of volume and stress evolution but a transition zone. This transition represents the increasing importance of particle breakage in the volumetric behaviour of the material and its effects on the stress path.

Both the ECP constitutive model and its revised form are shown to be thermodynamically coherent while being obtained from the free energy and dissipation functions [127]. These functions are then found to verify the fundamental laws of thermodynamics.

The numerical model is then validated and calibrated by means of ring shear tests under monotonic loading performed from 2 different materials. The numerical calculations show broad agreement with laboratory test results. During parametric studies different boundary conditions are tested. Namely, the CNS (constant normal stiffness) condition since it is considered to realistically represent soil-pile interface behaviour when subjected to continued shearing.

The physical relevance of the breakage mechanism (internal variable) in order to correctly model the laboratory results is made evident in this work. Moreover, the evolution laws proposed for the internal variable are shown to be adequate.

The comprehensive study of cyclic shear tests performed allows for an analysis, using a simplified numerical model, of the phenomenon of shear resistance degradation with increasing number of cycles (also known as "friction fatigue"). It is shown that friction degradation can only be observed, in this simplified model, as a result of a contraction of the shear band causing a decrease of normal stress which results in loss of shear mobilization.

The numerical modelling of 2 types of installation, monotonic and one-way cyclic, are carried out in the last Chapter of this work. The calculation procedure allows to simulate the pile installation using GEFDyn in a physically coherent manner by means of the interface elements, which can comply with the large relative displacements between the soil and the pile.

The qualitative validation of the results from the numerical simulations with pile calibration chamber tests shows the ability of the model to replicate the main effects of the installation in stress and displacement distributions.

The detailed analysis of the results, namely at the interface level, show the relevance of the constitutive model used along with the parameters chosen. The results at the interface level is where most of the effects are seen since they dissipate after a short distance in both the radial and vertical directions.

A parametric study of geometrical variations (length and diameter), installation type, interface behaviour law and the consideration of the breakage mechanism is performed to give a comprehensive view of the numerical modelling of the installation and physical phenomena present.

Considering the internal variable to reproduce particle breakage due to shearing in the simulations allowed for the interface to exhibit the behaviour seen in experimental tests when crushing occurs: irrecoverable contraction of the interface layer which leads to decreases in normal and, consequently, shear stress.

Cyclic loading of non-displacement piles is performed in order to study the phenomenon of shear resistance degradation with increasing number of cycles known as "'friction fatigue"'.

The need for a clear definition of the phenomenon is explained. The degradation of shear stresses mobilized with cycling at the soil-pile interface can be due to different factors. The decrease in shaft resistance can also be caused by a stiffening of the material at the pile base leading to stress re-distribution from the shaft to the base. This difference

is crucial since in this case the volumetric behaviour at the interface level is not contractive but dilative and the decrease is a result of less relative shear displacement between the pile and the soil.

The findings from the cyclic shear tests from Chapter 5 are confirmed here. The mechanisms by which contractive behaviour can be found at the interface are confirmed. The model is therefore adequate to represent the physical phenomena at the interface and relevance of the breakage mechanism in describing the interface behaviour during cyclic loading is shown.

The performance of the model is heavily dependent on the high number of parameters. These can be difficult to calibrate requiring a number of soil laboratory tests. Soil-structure shear tests performed to high level strains will be the most relevant ones for the calibration of the soil-pile interface behaviour law parameters.

7.2 Further research

Breakage due to isotropic compression

The constitutive model was revised in this work in order to include the effects of particle breakage due to continued shearing on the behaviour of soil. However, other stress and/or displacements paths can produce particle breakage of which isotropic compression is the most commonly studied. Some models have been proposed to consider this [95] but during this work no modification was performed to the isotropic mechanism of the constitutive model. The study of "crushable" sands, such as carbonate sands, will require this mechanism to be present in the constitutive structure of the model.

Water table

The presence of water in the medium was not considered during the numerical simulations performed during this work. This simplification should be tackled by future works since real conditions often include the presence of water. Moreover, the behaviour of the coupled medium will differ substantially from the one studied here and the flow of water will also to have be considered.

Interface contact algorithm

The pile installation simulations considered that the position of the interface was known at all times during the procedure. For a more complete analysis, the pile movement should be imposed by means of force at the head. This will not allow the installation to be controlled by displacements and will require an improvement on the interface algorithm namely on the detection and direction of contact.

Mesh motion implementation in the finite element code GEFDyn

The procedure for mesh updating known as the Updated-Lagrangian method was used during this work. However, other more powerful numerical tools exist which can prevent mesh distortion almost completely. These methods are usually associated with mesh refinement techniques which require interpolation between integration points for new locations. When complex constitutive models are considered the interpolation of state variables is an issue which should be addressed and implemented into the numerical code.

Dynamic installation

The installation procedures considered in this work neglected inertial effects which limited the analysis to either monotonic or "slow" cyclic installation types. A dynamic installation of piles is common practice and should be analysed numerically in order to assert the installation effects on the future behaviour of the pile in terms of resistance and deformability.

Appendix A

Concepts of basic mechanics

- Deformation gradient tensor

$$\underline{\underline{F}} = \frac{\partial}{\partial X}(\underline{x}), \quad J = det\underline{\underline{F}} > 0 \tag{A.1}$$

which can be decomposed recalling the polar decomposition theorem

$$\underline{\underline{F}} = \underline{\underline{R}} \cdot \underline{\underline{U}} = \underline{\underline{V}} \cdot \underline{\underline{R}} \tag{A.2}$$

where $\underline{\underline{U}}$ and $\underline{\underline{V}}$ are symmetric, positive definite tensors whose principal values are the stretch ratios of the deformation, right and left respectively, and $\underline{\underline{R}}$ is an orthogonal tensor called the local rotation tensor.
Directly from $\underline{\underline{F}}$ and related with $\underline{\underline{U}}$ and $\underline{\underline{V}}$ the right($\underline{\underline{C}}$) and left($\underline{\underline{B}}$) extension tensors of Cauchy-Green can be obtained

$$\underline{\underline{C}} = \underline{\underline{F}}^T \cdot \underline{\underline{F}} = \underline{\underline{U}}^2 = \underline{\underline{I}} + \bigtriangledown \underline{u} + \bigtriangledown \underline{u}^T + \bigtriangledown \underline{u}^T \cdot \bigtriangledown \underline{u} \tag{A.3}$$

$$\underline{\underline{B}} = \underline{\underline{F}} \cdot \underline{\underline{F}}^T = \underline{\underline{V}}^2 \tag{A.4}$$

- Displacement gradient

$$\bigtriangledown \underline{u} = \underline{\underline{F}} - \underline{\underline{I}} \tag{A.5}$$

The strained state is composed by relative length changes and relative changes of intersected angles for all line elements at each particle. It is required that a symmetric tensor quantity measuring the strained state should measure these changes. This quantity is known as a strain measure. A unified treatment was achieved by introducing the notion of scale function resulting in a general class of strain measures known as Hill strains. Two important examples are the Green-Lagrange and the Eulerian Hencky strain tensors

- Green-Lagrange and the Hencky Eulerian type, strain tensors

$$\underline{\underline{E}} = \frac{1}{2}(\underline{\underline{C}} - \underline{\underline{I}}) \tag{A.6}$$

$$\underline{\underline{h}} = \ln \underline{\underline{V}} = \frac{1}{2}(\underline{\underline{F}}\underline{\underline{F}}^T) \tag{A.7}$$

- Particle velocity

$$\underline{v} = \dot{\underline{x}} = \frac{\partial}{\partial t}(\underline{x}) \tag{A.8}$$

- Velocity gradient tensor

$$\underline{\underline{L}} = \frac{\partial}{\partial x}(\underline{v}) = \frac{\partial}{\partial X}(\underline{v}) \cdot \frac{\partial}{\partial x}(\underline{X}) = \dot{\underline{\underline{F}}} \cdot \underline{\underline{F}}^{-1} = -\underline{\underline{F}} \cdot \dot{\underline{\underline{F}}}^{-1} \tag{A.9}$$

$$\underline{\underline{L}} = \underline{\underline{D}} + \underline{\underline{W}} \tag{A.10}$$

$$\underline{\underline{D}} = \frac{1}{2}(\underline{\underline{L}} + \underline{\underline{L}}^T) \tag{A.11}$$

$$\underline{\underline{W}} = \frac{1}{2}(\underline{\underline{L}} - \underline{\underline{L}}^T) \tag{A.12}$$

These variables represent the decomposition of $\underline{\underline{\mathrm{L}}}$ where $\underline{\underline{\mathrm{D}}}$ is the rate of deformation tensor (symmetric) and $\underline{\underline{\mathrm{W}}}$ is the spin or vorticity tensor (skew symmetric). $\underline{\underline{\mathrm{D}}}$ and $\underline{\underline{\mathrm{W}}}$ can be written in terms of $\underline{\underline{\mathrm{F}}}$

$$\underline{\underline{D}} = \frac{1}{2} \cdot \underline{\underline{R}}(\dot{\underline{\underline{U}}} \cdot \underline{\underline{U}}^{-1} + \underline{\underline{U}}^{-1} \cdot \dot{\underline{\underline{U}}}) \cdot \underline{\underline{R}}^T \tag{A.13}$$

$$\underline{\underline{W}} = \frac{1}{2} \cdot \underline{\underline{R}}(\dot{\underline{\underline{U}}} \cdot \underline{\underline{U}}^{-1} - \underline{\underline{U}}^{-1} \cdot \dot{\underline{\underline{U}}}) \cdot \underline{\underline{R}}^T + \dot{\underline{\underline{R}}} \cdot \underline{\underline{R}}^T \tag{A.14}$$

or, similarly, by considering the left polar decomposition

$$\underline{\underline{D}} = \frac{1}{2}(\dot{\underline{\underline{V}}} \cdot \underline{\underline{V}}^{-1} + \underline{\underline{V}}^{-1} \cdot \dot{\underline{\underline{V}}} + \underline{\underline{V}} \cdot \dot{\underline{\underline{R}}} \cdot \underline{\underline{R}}^T \cdot \underline{\underline{V}}^{-1} - \underline{\underline{V}}^{-1}\dot{\underline{\underline{R}}} \cdot \underline{\underline{R}}^T \cdot \underline{\underline{V}}) \tag{A.15}$$

$$\underline{\underline{W}} = \frac{1}{2}(\dot{\underline{\underline{V}}} \cdot \underline{\underline{V}}^{-1} - \underline{\underline{V}}^{-1} \cdot \dot{\underline{\underline{V}}} + \underline{\underline{V}} \cdot \dot{\underline{\underline{R}}} \cdot \underline{\underline{R}}^T \cdot \underline{\underline{V}}^{-1} + \underline{\underline{V}}^{-1}\dot{\underline{\underline{R}}} \cdot \underline{\underline{R}}^T \cdot \underline{\underline{V}}) \tag{A.16}$$

- Unrotated rate of deformation tensor

$$\underline{\underline{d}} = \underline{\underline{R}}^T \cdot \underline{\underline{D}} \cdot \underline{\underline{R}} = \frac{1}{2}(\dot{\underline{\underline{U}}} \cdot \underline{\underline{U}}^{-1} + \underline{\underline{U}}^{-1} \cdot \dot{\underline{\underline{U}}}) \tag{A.17}$$

this represents the rate of deformation considering only $\underline{\underline{U}}$, therefore, it is "unrotated".

The rate of strain is related to the rates of deformation as

$$\dot{\underline{\underline{E}}} = \underline{\underline{F}}^T \cdot \underline{\underline{D}} \cdot \underline{\underline{F}} = \underline{\underline{U}} \cdot \underline{\underline{d}} \cdot \underline{\underline{U}} \tag{A.18}$$

- Rate of rotation tensor

$$\underline{\underline{\Omega}} = \dot{\underline{\underline{R}}} \cdot \underline{\underline{R}}^t \tag{A.19}$$

where $\underline{\underline{\Omega}}$ is skew symmetric since $\underline{\underline{R}} \cdot \underline{\underline{R}}^T = \underline{\underline{I}}$ and represents the angular velocity associated with the local rotation $\underline{\underline{R}}$

- Stress tensors

$$\underline{\underline{S}} = \underline{\underline{J}} \cdot \underline{\underline{F}}^{-1} \cdot \underline{\underline{\sigma}} \cdot (\underline{\underline{F}}^{-1})^T \tag{A.20}$$

$$\underline{\underline{\sigma}} = \underline{\underline{J}}^{-1} \cdot \underline{\underline{F}} \cdot \underline{\underline{S}} \cdot \underline{\underline{F}}^T \tag{A.21}$$

$$\underline{\underline{\sigma}}^U = \underline{\underline{J}}^{-1} \cdot \underline{\underline{U}} \cdot \underline{\underline{\tau}} \cdot \underline{\underline{U}} = \underline{\underline{R}}^T \cdot \underline{\underline{\sigma}} \cdot \underline{\underline{R}} \tag{A.22}$$

where $\underline{\underline{S}}$ is the symmetric Piola-Kirchhoff stress tensor (also known as 2^{nd} Piola-Kirchhoff stress tensor), $\underline{\underline{\sigma}}$ is the Cauchy (true) stress and $\underline{\underline{\sigma}}^U$ the unrotated Cauchy stress. As with the unrotated rate of deformation tensor the unrotated Cauchy stress is the "true" stress associated with the stretch $\underline{\underline{U}}$ alone.
With various strain measures, various stress measures may be introduced via a unified concept called work-conjugacy.

A.1 Conditions to verify objectivity

Note that a rotation of the body is equivalent to the rotation of the reference frame of the same magnitude but in opposite direction.

- Scalar

$$\overline{f} = f \tag{A.23}$$

- Vector

$$\overline{\underline{v}} = \underline{\underline{Q}} \cdot \underline{v} \tag{A.24}$$

$$\overline{\underline{v}} = \underline{\underline{Q}}^T \cdot \underline{v} \tag{A.25}$$

- Second order tensor

$$\overline{\underline{\underline{T}}} = \underline{\underline{Q}} \cdot \underline{\underline{T}} \cdot \underline{\underline{Q}}^T \tag{A.26}$$

$$\overline{\underline{\underline{T}}} = \underline{\underline{Q}}^T \cdot \underline{\underline{T}} \cdot \underline{\underline{Q}} \tag{A.27}$$

Either set of equations may be used to define objectivity.

Warning: An objective tensor does not always result in an objective rate tensor

$$\overline{\underline{\underline{T}}} = \underline{\underline{Q}} \cdot \underline{\underline{T}} \cdot \underline{\underline{Q}}^T \not\Longrightarrow \dot{\overline{\underline{\underline{T}}}} = \underline{\underline{Q}} \cdot \dot{\underline{\underline{T}}} \cdot \underline{\underline{Q}}^T \tag{A.28}$$

A.2 Verification of reference frame transformation independence (objectivity)

Considering a motion which differs from the given motion only by a superposed rigid body motion

$$\overline{\underline{x}} = \underline{a}(t) + \underline{\underline{Q}}(t) \cdot \underline{x} \tag{A.29}$$

where $\underline{a}(t)$ represents a rigid-body translation and $\underline{\underline{Q}}(t)$ is an orthogonal tensor representing a rigid-body rotation of the deformed state. For the quantities associated with the described motion the same symbol is used but "overlined"

- Basic kinematic variables

$$\overline{\underline{\underline{F}}} = \underline{\underline{Q}} \cdot \underline{\underline{F}}, \qquad \overline{\underline{\underline{R}}} = \underline{\underline{Q}} \cdot \underline{\underline{R}}, \qquad \overline{\underline{\underline{U}}} = \underline{\underline{U}}, \qquad \overline{\underline{\underline{C}}} = \underline{\underline{C}}, \qquad \overline{\underline{\underline{E}}} = \underline{\underline{E}} \tag{A.30}$$

- Rate relations

$$\overline{\underline{\underline{L}}} = \dot{\underline{\underline{Q}}} \cdot \underline{\underline{Q}}^T + \underline{\underline{Q}} \cdot \underline{\underline{L}} \cdot \underline{\underline{Q}}^T \qquad \overline{\underline{\underline{D}}} = \underline{\underline{Q}} \cdot \underline{\underline{D}} \cdot \underline{\underline{Q}}^T \qquad \overline{\underline{\underline{W}}} = \dot{\underline{\underline{Q}}} \cdot \underline{\underline{Q}}^T + \underline{\underline{Q}} \cdot \underline{\underline{W}} \cdot \underline{\underline{Q}}^T \tag{A.31}$$

$$\overline{\underline{\underline{\Omega}}} = \dot{\underline{\underline{Q}}} \cdot \underline{\underline{Q}}^T + \underline{\underline{Q}} \cdot \underline{\underline{\Omega}} \cdot \underline{\underline{Q}}^T \qquad \overline{\underline{\underline{d}}} = \underline{\underline{d}} \qquad \dot{\overline{\underline{\underline{E}}}} = \dot{\underline{\underline{E}}} \tag{A.32}$$

- Stress and stress rate tensors

$$\overline{\underline{\underline{\tau}}} = \underline{\underline{\tau}} \qquad \overline{\underline{\underline{\sigma}}}^U = \underline{\underline{\sigma}}^U \qquad \overline{\underline{\underline{\sigma}}} = \underline{\underline{Q}} \cdot \underline{\underline{\sigma}} \cdot \underline{\underline{Q}}^T \tag{A.33}$$

and

$$\dot{\overline{\underline{\underline{\tau}}}} = \dot{\underline{\underline{\tau}}} \qquad \dot{\overline{\underline{\underline{\sigma}}}}^U = \dot{\underline{\underline{\sigma}}}^U \qquad \dot{\overline{\underline{\underline{\sigma}}}} = \dot{\underline{\underline{Q}}} \cdot \underline{\underline{\sigma}} \cdot \underline{\underline{Q}}^T + \underline{\underline{Q}} \cdot \dot{\underline{\underline{\sigma}}} \cdot \underline{\underline{Q}}^T + \underline{\underline{Q}} \cdot \underline{\underline{\sigma}} \cdot \dot{\underline{\underline{Q}}}^T \tag{A.34}$$

We can now observe that certain of the rate variables are not objective such as $\underline{\underline{L}}$, $\underline{\underline{W}}$, $\underline{\underline{\Omega}}$, $\dot{\underline{\underline{\sigma}}}$

A.3 Velocity gradient tensor

- Equations of $\underline{\underline{D}}$ and $\underline{\underline{W}}$ in terms of $\underline{\underline{F}}$

$$\underline{\underline{L}} = -\underline{\underline{F}} \cdot \dot{\underline{\underline{F^{-1}}}} \tag{A.35}$$

using the polar decomposition of $\underline{\underline{F}}$ and considering that $\underline{\underline{R}}$ is an orthogonal tensor which means

$$\underline{\underline{R}}^{-1} = \underline{\underline{R}}^{T} \tag{A.36}$$

the previous equation becomes

$$\begin{aligned}
\underline{\underline{L}} &= -(\underline{\underline{R}} \cdot \underline{\underline{U}}) \cdot ((\underline{\underline{R}} \cdot \underline{\underline{U}})^{-1})^{\cdot} \\
&= -\underline{\underline{R}} \cdot \underline{\underline{U}} \cdot (\underline{\underline{U}}^{-1} \cdot \underline{\underline{R}}^{-1})^{\cdot} \\
&= -\underline{\underline{R}} \cdot \underline{\underline{U}} \cdot [(\underline{\underline{U}}^{-1})^{\cdot} \cdot \underline{\underline{R}}^{-1} + \underline{\underline{U}}^{-1} \cdot (\underline{\underline{R}}^{-1})^{\cdot}] \\
&= -\underline{\underline{R}} \cdot \underline{\underline{U}} \cdot (\underline{\underline{U}}^{-1})^{\cdot} \cdot \underline{\underline{R}}^{T} - \underline{\underline{R}} \cdot \dot{\underline{\underline{R}}}^{T} \\
&= \underline{\underline{R}} \cdot \dot{\underline{\underline{U}}} \cdot \underline{\underline{U}}^{-1} \cdot \underline{\underline{R}}^{T} + \dot{\underline{\underline{R}}} \cdot \underline{\underline{R}}^{T}
\end{aligned} \tag{A.37}$$

Taking the transpose of the equation gives

$$\underline{\underline{L}}^{T} = \underline{\underline{R}} \cdot (\underline{\underline{R}} \cdot \dot{\underline{\underline{U}}} \cdot \underline{\underline{U}}^{-1})^{T} + (\dot{\underline{\underline{R}}} \cdot \underline{\underline{R}}^{T})^{T} \tag{A.38}$$

From the decompostion in symmetric and antisymmetric of $\underline{\underline{L}}$

$$\begin{aligned}
\underline{\underline{D}} &= \frac{1}{2}(\underline{\underline{L}} + \underline{\underline{L}}^{T}) \\
&= \frac{1}{2} \cdot \underline{\underline{R}}(\dot{\underline{\underline{U}}} \cdot \underline{\underline{U}}^{-1} + \underline{\underline{U}}^{-1} \cdot \dot{\underline{\underline{U}}}) \cdot \underline{\underline{R}}^{T}
\end{aligned} \tag{A.39}$$

$$\begin{aligned}
\underline{\underline{W}} &= \frac{1}{2}(\underline{\underline{L}} - \underline{\underline{L}}^{T}) \\
&= \frac{1}{2} \cdot \underline{\underline{R}}(\dot{\underline{\underline{U}}} \cdot \underline{\underline{U}}^{-1} - \underline{\underline{U}}^{-1} \cdot \dot{\underline{\underline{U}}}) \cdot \underline{\underline{R}}^{T} + \dot{\underline{\underline{R}}} \cdot \underline{\underline{R}}^{T}
\end{aligned} \tag{A.40}$$

A.4 Objectivity of corotational stress rates

- Jaumann stress rate

$$\underline{\underline{\sigma}}^{*} = \frac{\partial}{\partial t}(\underline{\underline{\sigma}}) - \underline{\underline{W}} \cdot \underline{\underline{\sigma}} + \underline{\underline{\sigma}} \cdot \underline{\underline{W}} \tag{A.41}$$

To show that $\underline{\underline{\sigma}}^{*}$ is objective a reference frame transformation is applied to the stress rate

$$\overline{\underline{\underline{\sigma}}}^{\,*} = \underline{\underline{Q}} \cdot \dot{\underline{\underline{\sigma}}} \cdot \underline{\underline{Q}}^{T} - \underline{\underline{Q}} \cdot \underline{\underline{W}} \cdot \underline{\underline{\sigma}} \cdot \underline{\underline{Q}}^{T} + \underline{\underline{Q}} \cdot \underline{\underline{\sigma}} \cdot \underline{\underline{W}} \cdot \underline{\underline{Q}}^{T} \tag{A.42}$$

Recalling the reference frame transformations of $\underline{\underline{W}}$ and $\dot{\underline{\underline{\sigma}}}$

$$\overline{\underline{\underline{W}}} = \dot{\underline{\underline{Q}}} \cdot \underline{\underline{Q}}^{T} + \underline{\underline{Q}} \cdot \underline{\underline{W}} \cdot \underline{\underline{Q}}^{T} \qquad \dot{\overline{\underline{\underline{\sigma}}}} = \dot{\underline{\underline{Q}}} \cdot \underline{\underline{\sigma}} \cdot \underline{\underline{Q}}^{T} + \underline{\underline{Q}} \cdot \dot{\underline{\underline{\sigma}}} \cdot \underline{\underline{Q}}^{T} + \underline{\underline{Q}} \cdot \underline{\underline{\sigma}} \cdot \dot{\underline{\underline{Q}}}^{T} \tag{A.43}$$

Rewriting the reference frame transformations of $\underline{\underline{W}}$ and taking the transpose we obtain

$$\dot{\underline{\underline{Q}}}^{T} = \underline{\underline{Q}}^{T} \cdot \underline{\underline{W}}^{T} - \overline{\underline{\underline{W}}}^{T} \cdot \underline{\underline{Q}}^{T} \tag{A.44}$$

Replacing this equation in the reference frame transformations of $\dot{\underline{\underline{\sigma}}}$

$$\begin{aligned} \dot{\underline{\underline{\sigma}}} &= (\underline{\underline{Q}}^{T} \cdot \underline{\underline{W}}^{T} - \overline{\underline{\underline{W}}}^{T} \cdot \underline{\underline{Q}}^{T}) \cdot \underline{\underline{\sigma}} \cdot \underline{\underline{Q}} + \underline{\underline{Q}}^{T} \cdot \dot{\underline{\underline{\sigma}}} \cdot \underline{\underline{Q}} + \underline{\underline{Q}}^{T} \cdot \underline{\underline{\sigma}} \cdot (\underline{\underline{W}} \cdot \underline{\underline{Q}} - \underline{\underline{Q}} \cdot \overline{\underline{\underline{W}}}) \\ &= \underline{\underline{Q}}^{T} \cdot (\dot{\underline{\underline{\sigma}}} + \underline{\underline{W}}^{T} \cdot \underline{\underline{\sigma}} + \underline{\underline{\sigma}} \cdot \underline{\underline{W}}) \cdot \underline{\underline{Q}} - \overline{\underline{\underline{W}}}^{T} \cdot \overline{\underline{\underline{\sigma}}} - \overline{\underline{\underline{\sigma}}} \cdot \overline{\underline{\underline{W}}} \end{aligned} \tag{A.45}$$

which can be rewritten as

$$\dot{\underline{\underline{\sigma}}} + \overline{\underline{\underline{W}}}^{T} \cdot \overline{\underline{\underline{\sigma}}} + \overline{\underline{\underline{\sigma}}} \cdot \overline{\underline{\underline{W}}} = \underline{\underline{Q}}^{T} \cdot (\dot{\underline{\underline{\sigma}}} + \underline{\underline{W}}^{T} \cdot \underline{\underline{\sigma}} + \underline{\underline{\sigma}} \cdot \underline{\underline{W}}) \cdot \underline{\underline{Q}} \tag{A.46}$$

and since $\underline{\underline{W}}^{T} = -\underline{\underline{W}}$ the above equation can be written as

$$\dot{\underline{\underline{\sigma}}} + \overline{\underline{\underline{W}}}^{T} \cdot \overline{\underline{\underline{\sigma}}} + \overline{\underline{\underline{\sigma}}} \cdot \overline{\underline{\underline{W}}} = \underline{\underline{Q}}^{T} \cdot (\dot{\underline{\underline{\sigma}}} + \underline{\underline{W}} \cdot \underline{\underline{\sigma}} + \underline{\underline{\sigma}} \cdot \underline{\underline{W}}) \cdot \underline{\underline{Q}} \tag{A.47}$$

Therefore, the Jaumann stress rate is an objective rate. By similar procedures this can be shown for all corotational stress rates.

Appendix B

Elastic tests - Objective stress rates

B.1 Simple shear using objective stress rates in hypoelasticty

Considering the simplest hypoelastic equation to finite deformation

$$\underline{\underline{\sigma}}^{\nabla} = 2\mu\underline{\underline{D}} + \lambda tr(\underline{\underline{D}})\underline{\underline{I}} \tag{B.1}$$

- Definition of the simple shear test

$$x_1 = X_1 + k(t)X_2, \quad x_2 = X_2, \quad x_3 = X_3 \tag{B.2}$$

$$u_1 = kX_2, \quad u_2 = u_3 = 0 \tag{B.3}$$

$$\underline{\underline{F}} = \begin{pmatrix} 1 & k & 0 \\ 0 & 1 & 0 \\ 0 & 0 & 1 \end{pmatrix} \qquad det(\underline{\underline{F}}) = 1(Incompressible) \tag{B.4}$$

$$\underline{\underline{\dot{F}}} = \begin{pmatrix} 0 & \dot{k} & 0 \\ 0 & 0 & 0 \\ 0 & 0 & 0 \end{pmatrix} \quad \underline{\underline{F}}^{-1} = \begin{pmatrix} 1 & -k & 0 \\ 0 & 1 & 0 \\ 0 & 0 & 1 \end{pmatrix} \tag{B.5}$$

$$\underline{\underline{L}} = \begin{pmatrix} 0 & \dot{k} & 0 \\ 0 & 0 & 0 \\ 0 & 0 & 0 \end{pmatrix} \tag{B.6}$$

$$\underline{\underline{D}} = \begin{pmatrix} 0 & \frac{\dot{k}}{2} & 0 \\ \frac{\dot{k}}{2} & 0 & 0 \\ 0 & 0 & 0 \end{pmatrix} \quad \underline{\underline{W}} = \begin{pmatrix} 0 & \frac{\dot{k}}{2} & 0 \\ -\frac{\dot{k}}{2} & 0 & 0 \\ 0 & 0 & 0 \end{pmatrix} \tag{B.7}$$

Therefore considering the constitutive equation for finite deformations

$$\underline{\underline{\sigma}}^{\triangledown} = 2\mu \underline{\underline{D}} \quad since \quad tr(\underline{\underline{D}}) = 0 \tag{B.8}$$

- Jaumann stress rate (corotational)

The Jaumann stress rate is defined as

$$\underline{\underline{\sigma}}^{*} = \frac{\partial}{\partial t}(\underline{\underline{\sigma}}) - \underline{\underline{W}} \cdot \underline{\underline{\sigma}} + \underline{\underline{\sigma}} \cdot \underline{\underline{W}} \tag{B.9}$$

Considering the simple shear test it can be the written from the constitutive equation that

$$\underline{\underline{\sigma}}^{*} = \frac{\partial}{\partial t}(\underline{\underline{\sigma}}) - \underline{\underline{W}} \cdot \underline{\underline{\sigma}} + \underline{\underline{\sigma}} \cdot \underline{\underline{W}} = 2\mu \underline{\underline{D}} \tag{B.10}$$

Since the simple shear test is 2D the stress tensor is given by

$$\underline{\underline{\sigma}} = \begin{pmatrix} \sigma_{11} & \sigma_{12} & 0 \\ \sigma_{21} & \sigma_{22} & 0 \\ 0 & 0 & 0 \end{pmatrix} \tag{B.11}$$

The components of the equation can be determined

$$\underline{\underline{\sigma}} \cdot \underline{\underline{W}} = \begin{pmatrix} -\frac{\dot{k}}{2}\sigma_{12} & \frac{\dot{k}}{2}\sigma_{11} & 0 \\ -\frac{\dot{k}}{2}\sigma_{22} & \frac{\dot{k}}{2}\sigma_{12} & 0 \\ 0 & 0 & 0 \end{pmatrix} \qquad -\underline{\underline{W}} \cdot \underline{\underline{\sigma}} = \underline{\underline{\sigma}} \cdot \underline{\underline{W}}^{T} = \begin{pmatrix} -\frac{\dot{k}}{2}\sigma_{12} & -\frac{\dot{k}}{2}\sigma_{22} & 0 \\ \frac{\dot{k}}{2}\sigma_{11} & \frac{\dot{k}}{2}\sigma_{12} & 0 \\ 0 & 0 & 0 \end{pmatrix} \tag{B.12}$$

Again referring to the constitutive equation it can be shown that

$$\frac{\partial \sigma_{11}}{\partial t} = \dot{k}\sigma_{12}, \qquad \frac{\partial \sigma_{22}}{\partial t} = -\dot{k}\sigma_{12} \tag{B.13}$$

$$\begin{aligned} \frac{\partial \sigma_{12}}{\partial t} &= \dot{k}\mu + \frac{\dot{k}}{2}\sigma_{22} - \frac{\dot{k}}{2}\sigma_{11} \\ &= \dot{k}\mu - \frac{\dot{k}}{2}(\sigma_{11} - \sigma_{22}) \end{aligned} \tag{B.14}$$

By differenciating the above equation the ordinary differential equation is obtained

$$\begin{aligned} \frac{\partial^2 \sigma_{12}}{\partial^2 t} &= -\frac{\dot{k}}{2}\frac{\partial}{\partial t}\left[\sigma_{11} - \sigma_{22}\right] \\ &= -\dot{k}^2 \sigma_{12} \end{aligned} \tag{B.15}$$

of which the general solution is

$$\sigma_{12} = A \cdot sin(k) + B \cdot cos(k) \tag{B.16}$$

where $k = 2\int_0^t D_{12}\, dt$ is the shear strain

Considering the boundary condition

$$\underline{\underline{\sigma}}(t=0) = \underline{\underline{0}} \quad \Longrightarrow \quad B = 0 \tag{B.17}$$

To determine A it must be considered that the constitutive equation is valid at every instant t

$$\frac{\partial \sigma_{12}}{\partial t} - \frac{\dot{k}}{2}\sigma_{22} + \frac{\dot{k}}{2}\sigma_{11} = \dot{k}\mu \tag{B.18}$$

where

$$\frac{\partial \sigma_{12}}{\partial t} = \dot{k} A cos(k) \tag{B.19}$$

therefore considering t=0 it can be seen that

$$\sigma_{11} = -\sigma_{22}, \quad A = \mu, \quad \Longrightarrow \quad \sigma_{12} = \mu sin\, k \tag{B.20}$$

To determine σ_{11} and σ_{22} the following equation is re-considered

$$\frac{\partial \sigma_{11}}{\partial t} = \dot{k}\sigma_{12} = \dot{k}\mu sin(k) \tag{B.21}$$

and by integrating the equation

$$\sigma_{11} = \dot{k}\mu \cdot \left[-\frac{1}{\dot{k}} cos(k) + n\right] \tag{B.22}$$

finally, considering the boundary condition $\underline{\underline{\sigma}}(t=0) = \underline{\underline{0}}$

$$n = \mu \quad \Longrightarrow \quad \sigma_{11} = -\sigma_{22} = \mu(1 - cos\, k) \tag{B.23}$$

- Green-McInnis or Green-Naghdi stress rate (corotational)

The Green-McInnis or Green-Naghdi rate is defined as

$$\underline{\underline{\sigma}}^{*} = \frac{\partial}{\partial t}(\underline{\underline{\sigma}}) - \underline{\underline{W}}^{*} \cdot \underline{\underline{\sigma}} + \underline{\underline{\sigma}} \cdot \underline{\underline{W}}^{*} \tag{B.24}$$

where $\underline{\underline{W}}^{*}$ is the angular velocity defined as

$$\underline{\underline{W}}^{*} = \dot{\underline{\underline{R}}} \cdot \underline{\underline{R}}^{T} \tag{B.25}$$

Then $\underline{\underline{\sigma}}$ can be determined using similar procedures as before

$$\sigma_{11} = -\sigma_{22} = 4\mu(cos\,(2\theta)\,ln(cos\theta) + \theta sin\,(2\theta) - sin^{2}\theta) \tag{B.26}$$

$$\sigma_{12} = 2\mu cos\,(2\theta)\,(2\theta - 2\,tan\,(2\theta)\,ln(cos\theta) - tan\theta) \tag{B.27}$$

where $\theta = tan^{-1}(\frac{k}{2})$

- Cotler-Rivlin stress rate (non-corotational)

The Cotler-Rivlin rate is defined as

$$\underline{\underline{\sigma}}^{*} = \frac{\partial}{\partial t}(\underline{\underline{\sigma}}) + \underline{\underline{L}}^{T} \cdot \underline{\underline{\sigma}} + \underline{\underline{\sigma}} \cdot \underline{\underline{L}} \tag{B.28}$$

Considering the simple shear test it can be the written from the constitutive equation that

$$\underline{\underline{\sigma}}^{*} = \frac{\partial}{\partial t}(\underline{\underline{\sigma}}) + \underline{\underline{L}}^{T} \cdot \underline{\underline{\sigma}} + \underline{\underline{\sigma}} \cdot \underline{\underline{L}} = 2\mu \underline{\underline{D}} \tag{B.29}$$

Since the simple shear test is 2D the stress tensor is given by

$$\underline{\underline{\sigma}} = \begin{pmatrix} \sigma_{11} & \sigma_{12} & 0 \\ \sigma_{21} & \sigma_{22} & 0 \\ 0 & 0 & 0 \end{pmatrix} \tag{B.30}$$

The components of the equation can be determined

$$\underline{\underline{L}}^{T} \cdot \underline{\underline{\sigma}} = \begin{pmatrix} 0 & \dot{k}\sigma_{11} & 0 \\ 0 & \dot{k}\sigma_{21} & 0 \\ 0 & 0 & 0 \end{pmatrix} \tag{B.31}$$

$$\underline{\underline{\sigma}} \cdot \underline{\underline{L}} = \begin{pmatrix} 0 & 0 & 0 \\ \dot{k}\sigma_{11} & \dot{k}\sigma_{12} & 0 \\ 0 & 0 & 0 \end{pmatrix} \tag{B.32}$$

Again referring to the constitutive equation it can be shown that

$$\frac{\partial \sigma_{11}}{\partial t} = 0, \qquad \frac{\partial \sigma_{22}}{\partial t} = -2\dot{k}\sigma_{12} \tag{B.33}$$

$$\frac{\partial \sigma_{12}}{\partial t} = \dot{k}\mu - \dot{k}\sigma_{11} \tag{B.34}$$

Therefore, $\underline{\underline{\sigma}}$ can be determined

$$\sigma_{11} = 0, \quad \sigma_{12} = \mu k, \quad \sigma_{22} = \mu k^2 \tag{B.35}$$

- Oldroyd's and Truesdell stress rate (non-corotational)

For the specific problem of simple shear the Oldroyd's and the Truesdell stress rates are one and the same since $tr(\underline{\underline{D}}) = 0$ The Oldroyd's rate is defined as

$$\underline{\underline{\sigma}}^* = \frac{\partial}{\partial t}(\underline{\underline{\sigma}}) - \underline{\underline{L}} \cdot \underline{\underline{\sigma}} - \underline{\underline{\sigma}} \cdot \underline{\underline{L}}^T \tag{B.36}$$

Considering the simple shear test it can be the written from the constitutive equation that

$$\underline{\underline{\sigma}}^* = \frac{\partial}{\partial t}(\underline{\underline{\sigma}}) - \underline{\underline{L}} \cdot \underline{\underline{\sigma}} - \underline{\underline{\sigma}} \cdot \underline{\underline{L}}^T = 2\mu \underline{\underline{D}} \tag{B.37}$$

Since the simple shear test is 2D the stress tensor is given by

$$\underline{\underline{\sigma}} = \begin{pmatrix} \sigma_{11} & \sigma_{12} & 0 \\ \sigma_{21} & \sigma_{22} & 0 \\ 0 & 0 & 0 \end{pmatrix} \tag{B.38}$$

The components of the equation can be determined

$$\underline{\underline{L}} \cdot \underline{\underline{\sigma}} = \begin{pmatrix} \dot{k}\sigma_{21} & \dot{k}\sigma_{22} & 0 \\ 0 & 0 & 0 \\ 0 & 0 & 0 \end{pmatrix} \tag{B.39}$$

$$\underline{\underline{\sigma}} \cdot \underline{\underline{L}}^T = \begin{pmatrix} \dot{k}\sigma_{12} & 0 & 0 \\ \dot{k}\sigma_{22} & 0 & 0 \\ 0 & 0 & 0 \end{pmatrix} \tag{B.40}$$

Again referring to the constitutive equation it can be shown that

$$\frac{\partial \sigma_{11}}{\partial t} = +2\dot{k}\sigma_{12}, \qquad \frac{\partial \sigma_{22}}{\partial t} = 0 \tag{B.41}$$

$$\frac{\partial \sigma_{12}}{\partial t} = \mu\dot{k} + \dot{k}\sigma_{22} \tag{B.42}$$

Therefore, $\underline{\underline{\sigma}}$ can be determined

$$\sigma_{22} = 0, \quad \sigma_{12} = \mu k, \quad \sigma_{11} = \mu k^2 \tag{B.43}$$

- Logarithimic stress rate (corotational)

Taking the grade zero constitutive equation for the logarithmic stress rate

$$\underline{\underline{\sigma}} = 2\mu\, ln\underline{\underline{V}} + \lambda tr(ln\underline{\underline{V}})\underline{\underline{I}} \tag{B.44}$$

The left Cauchy-Green tensor $\underline{\underline{B}}$ for simple shear is

$$\underline{\underline{B}} = \begin{pmatrix} 1+k^2 & k & 0 \\ k & 1 & 0 \\ 0 & 0 & 1 \end{pmatrix} \quad \underline{\underline{V}} = \begin{pmatrix} \frac{1+sin^2(arctan(\frac{k}{2}))}{cos(arctan(\frac{k}{2}))} & sin(arctan(\frac{k}{2})) & 0 \\ sin(arctan(\frac{k}{2})) & cos(arctan(\frac{k}{2})) & 0 \\ 0 & 0 & 1 \end{pmatrix} \tag{B.45}$$

$$ln\underline{\underline{V}} = ln(\frac{1+sin(arctan(\frac{k}{2}))}{cos(arctan(\frac{k}{2}))}) \begin{pmatrix} sin(arctan(\frac{k}{2})) & cos(arctan(\frac{k}{2})) & 0 \\ cos(arctan(\frac{k}{2})) & -sin(arctan(\frac{k}{2})) & 0 \\ 0 & 0 & 1 \end{pmatrix} \tag{B.46}$$

It can be show that $\underline{\underline{\sigma}}$ is defined by

$$\sigma_{11} = -\sigma_{22} = 2\mu sin(\theta) ln\, \frac{1+sin(\theta)}{cos(\theta)} \tag{B.47}$$

$$\tag{B.48}$$

$$\sigma_{12} = 2\mu cos(\theta) ln\, \frac{1+sin(\theta)}{cos(\theta)} \tag{B.49}$$

where $\theta = arctan(\frac{k}{2})$

Having described hypoelasticity in an Eulerian formulation for finite deformation considering some objective rates it is now possible to draw the relation between shear strain and the different stress tensor components

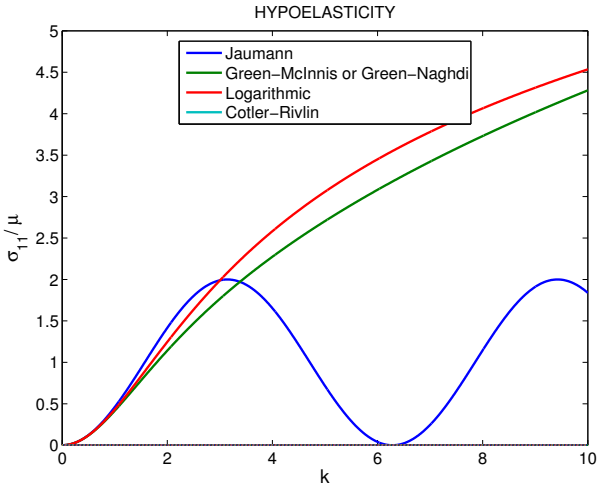

Figure 1: Simple shear in hypoelasticity for various objective stress rates

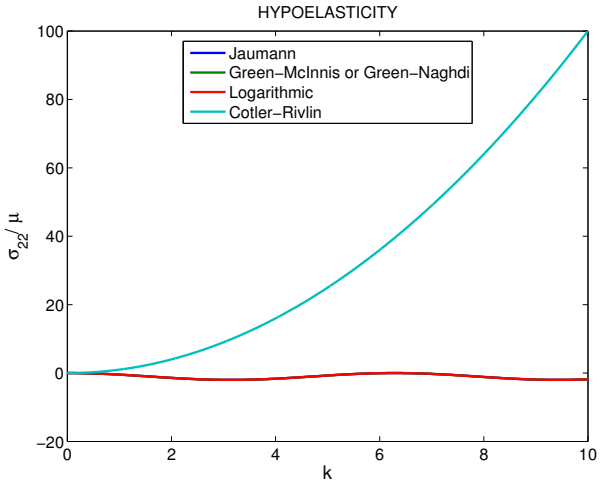

Figure 2: Simple shear in hypoelasticity for various objective stress rates

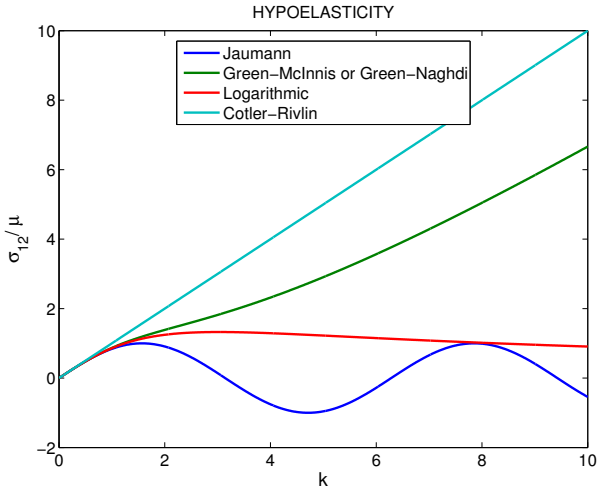

Figure 3: Simple shear in hypoelasticity for various objective stress rates

B.2 Elastic deformation cycles using objective stress rates in hypoelasticty

Considering the simplest hypoelastic equation to finite deformation

$$\underline{\underline{\sigma}}^{\nabla} = 2\mu\underline{\underline{D}} + \lambda tr(\underline{\underline{D}})\underline{\underline{I}} \tag{B.50}$$

- Definition of the elastic deformation cycles ([77])

$$x_1 = X_1 + \frac{(1 - cos\Phi)\cdot r/H}{1 + sin\Phi\cdot r/H}X_2, \quad x_2 = (1 + sin\Phi\cdot r/H)\cdot X_2, \quad x_3 = X_3 \tag{B.51}$$

$$\underline{\underline{F}} = \begin{pmatrix} 1 & \frac{(1-cos\Phi)\cdot r/H}{1+sin\Phi\cdot r/H} & 0 \\ 0 & 1 + sin\Phi\cdot r/H & 0 \\ 0 & 0 & 1 \end{pmatrix} \tag{B.52}$$

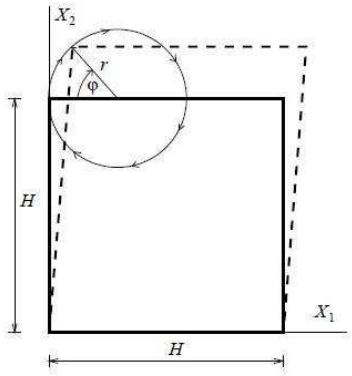

Figure 4: Deformation cycles ([77])

These repeated elastic deformation cycles were performed considering different rigid-body corrections (different objective stress rates) namely the Jaumann, Green-Naghdi and the Logarithmic corrections and also when no correction was considered. Two different ratios r/H are considered, $r/H = 0,5$ for large elastic deformations and $r/H = 0,01$ for small elastic deformations.

The relation between the number of cycles and the different stress tensor components for different stress rates is presented below. The ratio r/H is considered 0,5 which represent large elastic deformations.

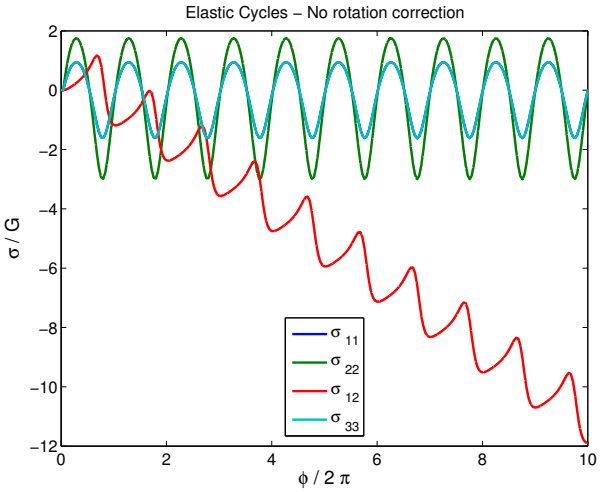

Figure 5: Elastic deformation cycles - No rigid-body motion correction

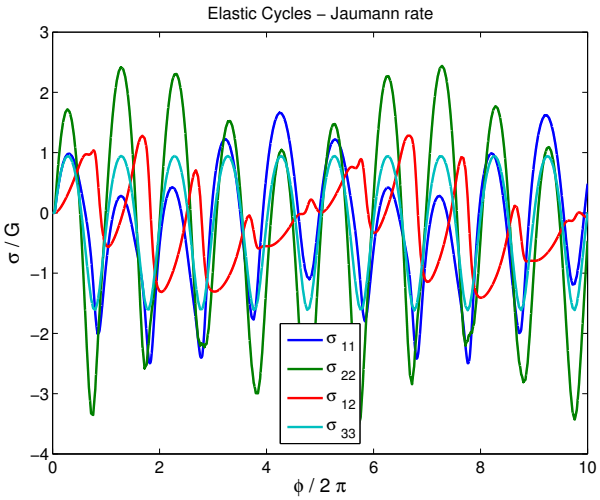

Figure 6: Elastic deformation cycles - Jaumann stress rate

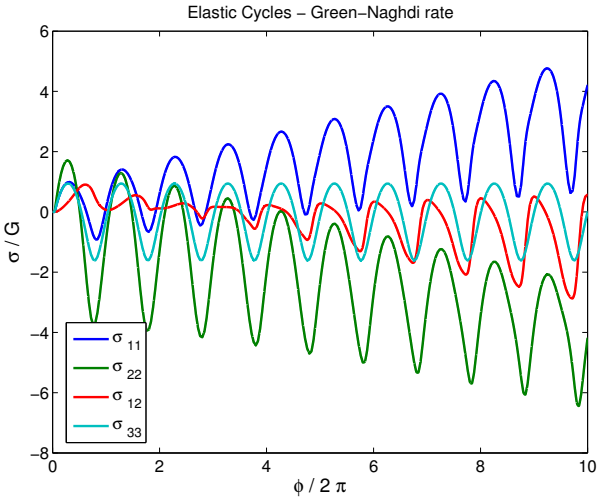

Figure 7: Elastic deformation cycles - Green-Naghdi stress rate

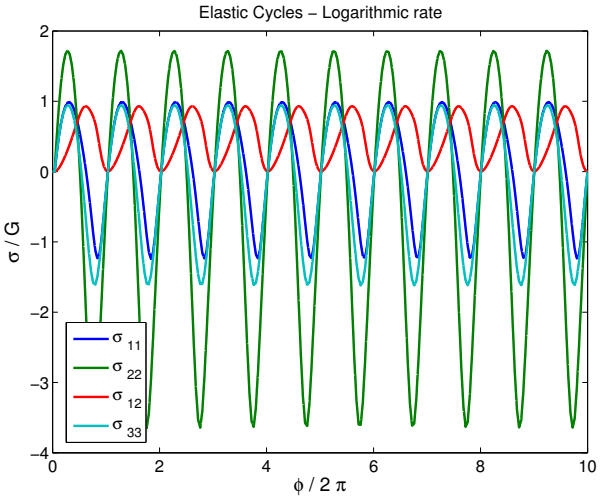

Figure 8: Elastic deformation cycles - Logarithmic stress rate

Appendix C

Derivation of constitutive relations

C.1 ECP constitutive model - Monotonic behaviour

Adopting the soil mechanics sign convention (compression is positive) the deviatoric yield surface for a monotonic mechanism of the k plane considering the altered ECP constitutive model is given by

$$f = q_k - p_k \cdot M \cdot r_k \cdot (1 - b \cdot log(\frac{p_k}{p_c})) = 0 \tag{C.1}$$

where

$$\dot{r_k} = \dot{\Lambda} \frac{(1 - r_k)^2}{a} \quad , \quad \dot{p_c} = p_c \beta tr(\underline{\underline{D}}^p) \tag{C.2}$$

The plastic multiplier $\dot{\gamma}$ is determined from the consistency equation. The consistency condition is written as follows:

$$\dot{f} = \frac{\partial f}{\partial \underline{\underline{\sigma}}} : \underline{\underline{\dot{\sigma}}} + \frac{\partial f}{\partial r_k} \dot{r_k} + \frac{\partial f}{\partial p_c} \dot{p_c} = 0 \tag{C.3}$$

and developing this equation it can be found that

$$\dot{\gamma} = \frac{K\, tr(\underline{\underline{D}})(-M \cdot r_k \cdot (1 - b \cdot (1 + log(\frac{p_k}{p_c})))) + 2G \cdot \frac{\underline{\underline{s_k}} : \underline{\underline{D}}^D}{q_k}}{H} \tag{C.4}$$

where H is the hardening modulus that can be positive (hardening behaviour) or negative (softening behaviour). Explicitly H is given by:

$$H = H_\sigma + H_r + H_v \tag{C.5}$$

where

$$H_\sigma = K(M - \frac{q_k}{p_k}) \cdot (-M \cdot r_k \cdot (1 - b \cdot (1 + log(\frac{p_k}{p_c})))) + 2G \cdot \frac{\overline{\overline{s_k}} : \overline{\overline{s_k}}}{q_k^2} \tag{C.6}$$

$$H_r = p_k \, M \, (1 - b \cdot log(\frac{p_k}{p_c})) \, \frac{(1 - r_k)^2}{a} \tag{C.7}$$

$$H_v = -p_k \cdot M \cdot r_k \cdot b \cdot \beta \cdot (M - \frac{q_k}{p_k}) \tag{C.8}$$

C.2 ECP constitutive model - Cyclic behaviour

The yield criterion for a cyclic loading can be expressed as

$$f^c = 0 \tag{C.9}$$

$$\begin{aligned} f^c &= q_k^c - p_k \cdot M \cdot r_k^c \cdot (1 - b \cdot log(\frac{p_k}{p_c})) \\ &= \frac{q_k^c}{p_k \cdot M \cdot (1 - b \cdot log(\frac{p_k}{p_c}))} - r_k^c \end{aligned} \tag{C.10}$$

where the variables are hereby defined as

$$q_k^c = ||\underline{\underline{s_k^c}}|| \quad , \quad \underline{\underline{s_k^c}} = s_k - p_k \cdot M \cdot (1 - b \cdot log(\frac{p_k}{p_c})) \cdot (\underline{\underline{X}}^H + r_k^c \cdot \underline{\underline{t}}^H) \tag{C.11}$$

$$\underline{\underline{X}}^H = \frac{\underline{\underline{s_k^H}}}{p_k^H \cdot M \cdot (1 - b \cdot log(\frac{p_k^H}{p_c^H}))} \quad , \quad \underline{\underline{t}}^H = \frac{\underline{\underline{s_k^{cH}}}}{q_k^c} \tag{C.12}$$

The memory tensor $\underline{\underline{X}}^H$ defines the point of tangential contact between the monotonic loading yield surface and the cyclic loading yield surface. Also, the vector $\underline{\underline{t}}^H$ defines the direction of loading prior to the change in the loading direction.

The flow rule can be expressed as

$$\underline{\underline{D}}_p = \dot{\gamma} \cdot \frac{\partial g}{\partial \underline{\underline{\sigma}}} = \dot{\gamma} \, [\frac{\underline{\underline{s_k^c}}}{q_k^c} + \frac{1}{2}(M - \frac{\underline{\underline{s_k^c}} : \underline{\underline{s_k^c}}}{q_k^c \cdot p_k})\underline{\underline{I}}] \tag{C.13}$$

The plastic multiplier $\dot{\gamma}$ is determined from the consistency equation. Therefore, for a non-associated flow rule and considering the normality rule, differentiating the yield surface equation gives

$$\begin{aligned} \dot{f} &= \frac{\partial f}{\partial \underline{\underline{\sigma}}} : \dot{\underline{\underline{\sigma}}} + \frac{\partial f}{\partial r_k^c}\dot{r_k^c} + \frac{\partial f}{\partial p_c}\dot{p_c} = 0 \\ &= K(tr(\underline{\underline{D}}) - \dot{\gamma}(M - \frac{\underline{\underline{s_k^c}} : \underline{\underline{s_k^c}}}{q_k^c \cdot p_k})) \cdot (- M \cdot r_k^c \cdot (1 - b \cdot (1 + log(\frac{p_k}{p_c})))) \cdot \\ &\cdot \quad tr((r_k^c - (\underline{\underline{X}}^H + \underline{\underline{t}}^H \cdot r_k^c) \cdot \frac{\underline{\underline{s_k^c}}}{q_k^c}) \cdot \underline{\underline{I}}) + \\ &+ \quad 2G(\underline{\underline{D}}^D - \dot{\gamma}\frac{\underline{\underline{s_k^c}}}{q_k^c}) \cdot \frac{\underline{\underline{s_k^c}}}{q_k^c} + \\ &+ \quad (-p_k \, M \, (1 - b \cdot log(\frac{p_k}{p_c}))) \, (1 - \frac{\underline{\underline{s_k^c}} : \underline{\underline{t}}^H}{2 \cdot q_k^c}) \, \dot{\gamma} \, \frac{(1 - r_k^c)^2}{2 \cdot a} + \\ &+ \quad (+\dot{\gamma} \, p_k \cdot M \cdot b \cdot \beta \cdot tr((r_k^c - (\underline{\underline{X}}^H + \underline{\underline{t}}^H \cdot r_k^c) \cdot \frac{\underline{\underline{s_k^c}}}{q_k^c}) \cdot \underline{\underline{I}}) \cdot (M - \frac{\underline{\underline{s_k^c}} : \underline{\underline{s_k^c}}}{q_k^c \cdot p_k})) \end{aligned} \tag{C.14}$$

where it was considered

$$\dot{p}_c = p_c \beta tr(\underline{\underline{D}}_p) = \dot{\gamma}\, p_c \beta (M - \frac{\underline{\underline{s}}_k^c : \underline{\underline{s}}_k^c}{q_k^c \cdot p_k}) \quad , \quad \dot{r_k^c} = \dot{\gamma}\, \frac{(1 - r_k^c)^2}{2 \cdot a} \tag{C.15}$$

The consistency condition can be solved to obtain

$$\dot{\gamma} = \frac{K\, tr(\underline{\underline{D}})(M r_k^c (1 - b(1 + log(\frac{p_k}{p_c})))) \cdot tr((r_k^c - (\underline{\underline{X}}^H + \underline{\underline{t}}^H r_k^c) \frac{\underline{\underline{s}}_k^c}{q_k^c}) \underline{\underline{I}}) + 2G \cdot \frac{\underline{\underline{s}}_k^c : \underline{\underline{D}}^D}{q_k^c}}{H} \tag{C.16}$$

where

$$\begin{aligned} H &= K(M - \frac{\underline{\underline{s}}_k^c : \underline{\underline{s}}_k^c}{q_k^c \cdot p_k}) \cdot (- M \cdot (1 - b \cdot (1 + log(\frac{p_k}{p_c})))) \cdot \\ &\cdot \quad tr((r_k^c - (\underline{\underline{X}}^H + \underline{\underline{t}}^H \cdot r_k^c) \cdot \frac{\underline{\underline{s}}_k^c}{q_k^c}) \cdot \underline{\underline{I}}) + \\ &+ \quad 2G \cdot \frac{\underline{\underline{s}}_k^c : \underline{\underline{s}}_k^c}{q_k^c \cdot q_k^c} + \\ &- \quad p_k\, M\, (1 - b \cdot log(\frac{p_k}{p_c})) \cdot (1 - \frac{\underline{\underline{s}}_k^c : \underline{\underline{t}}^H}{2 \cdot q_k^c}) \cdot \frac{(1 - r_k^c)^2}{a} + \\ &+ \quad p_k \cdot M \cdot b \cdot \beta \cdot tr((r_k^c - (\underline{\underline{X}}^H + \underline{\underline{t}}^H \cdot r_k^c) \cdot \frac{\underline{\underline{s}}_k^c}{q_k^c}) \cdot \underline{\underline{I}}) \cdot (M - \frac{\underline{\underline{s}}_k^c : \underline{\underline{s}}_k^c}{q_k^c \cdot p_k}) \end{aligned} \tag{C.17}$$

The constitutive law for a Mohr-Coulomb model with isotropic hardening is therefore given by

$$\underline{\underline{\sigma}}^{\triangledown} = K(tr(\underline{\underline{D}}) - \dot{\gamma}(M - \frac{\underline{\underline{s}}_k^c : \underline{\underline{s}}_k^c}{q_k^c \cdot p_k}))\, \underline{\underline{I}} + 2G\, [\underline{\underline{D}}^D - \langle \dot{\gamma} \rangle \frac{\underline{\underline{s}}_k^c}{q_k^c}\,] \tag{C.18}$$

where $\langle \dot{\gamma} \rangle = \begin{cases} \dot{\gamma}, & \text{if } \dot{\gamma} \geq 0 \\ 0, & \text{if } \dot{\gamma} < 0 \end{cases}$ which depends on the loading.

C.3 Revised ECP constitutive model

Adopting the soil mechanics sign convention (compression is positive) the deviatoric yield surface for a monotonic mechanism of the k plane considering the altered ECP constitutive model is given by

$$f = q_k - p_k \cdot M \cdot r_k \cdot r_{br_k} \cdot (1 - b \cdot log(\frac{p_k}{p_c})) = 0 \tag{C.19}$$

where

$$\dot{r_k} = \dot{\Lambda}\,\frac{(1-r_k)^2}{a} \quad , \quad \dot{r}_{br_k} = -\dot{\Lambda}(a^{br} \cdot r_{br_k}) \quad , \quad \dot{p_c} = p_c \beta tr(\underline{\underline{D}}^p) \tag{C.20}$$

The plastic multiplier $\dot{\gamma}$ is determined from the consistency equation. The consistency condition is written as follows:

$$\dot{f} \;=\; \frac{\partial f}{\partial \underline{\underline{\sigma}}} : \dot{\underline{\underline{\sigma}}} + \frac{\partial f}{\partial r_k}\dot{r_k} + \frac{\partial f}{\partial p_c}\dot{p_c} + \frac{\partial f}{\partial r_{br_k}}\dot{r_{br_k}} = 0 \tag{C.21}$$

and developing this equation it can be found that

$$\dot{\gamma} = \frac{K\,tr(\underline{\underline{D}})(-M \cdot r_k \cdot r_{br_k} \cdot (1 - b \cdot (1 + log(\frac{p_k}{p_c})))) + 2G \cdot \frac{\underline{\underline{s_k}} : \underline{\underline{D}}^D}{q_k}}{H} \tag{C.22}$$

where H is the hardening modulus that can be positive (hardening behaviour) or negative (softening behaviour). Explicitly H is given by:

$$H = H_\sigma + H_r + H_v + H_{br} \tag{C.23}$$

where

$$H_\sigma = K(M - \frac{q_k}{p_k}) \cdot (-M \cdot r_k \cdot r_{br_k} \cdot (1 - b \cdot (1 + log(\frac{p_k}{p_c})))) + 2G \cdot \frac{\underline{\underline{s_k}} : \underline{\underline{s_k}}}{q_k^2} \tag{C.24}$$

$$H_r = p_k\, M\, r_{br_k}\, (1 - b \cdot log(\frac{p_k}{p_c}))\, \frac{(1-r_k)^2}{a} \tag{C.25}$$

$$H_v = -p_k \cdot M \cdot r_k \cdot r_{br_k} \cdot b \cdot \beta \cdot (M - \frac{q_k}{p_k}) \tag{C.26}$$

$$H_{br} = p_k\, M\, r_k\, (1 - b \cdot log(\frac{p_k}{p_c}))\, (-a^{br} \cdot r_{br_k}) \tag{C.27}$$

Appendix D

Derivation of free energy and dissipation functions

D.1 ECP constitutive model

- Stress invariants definition

$$p = (\lambda + \frac{2}{3}\mu)(\epsilon_v - \epsilon_v^p) = K(\epsilon_v - \epsilon_v^p) \tag{D.1}$$

$$\underline{\overline{\sigma}} = 2\mu(\underline{\overline{\epsilon}} - \underline{\overline{\epsilon}}^p) \tag{D.2}$$

$$q = ||\underline{\overline{\sigma}}|| \tag{D.3}$$

- Free energy function

$$\rho\psi = \frac{1}{2}(\lambda + \frac{2}{3}\mu)(\epsilon_v - \epsilon_v^p)^2 + \mu(||(\underline{\overline{\epsilon}} - \underline{\overline{\epsilon}}^p)||)^2 - \frac{p_{c0}}{\beta}\, exp[-\beta(\epsilon_v^p + \varpi(r))] \tag{D.4}$$

where,

$$r = \frac{M \int_0^t ||\underline{\dot{\overline{\epsilon}}}^p||\, dt}{a + M \int_0^t ||\underline{\dot{\overline{\epsilon}}}^p||\, dt} \tag{D.5}$$

$$\varpi(r) = \int_r \frac{a\,\alpha(r)}{1-r}\, dr\,, \quad 0 < r < 1 \tag{D.6}$$

$$\alpha(r) = M\,\eta\, r\,(1-r)^m\,, \quad 1 \geq m \geq 0; \quad \eta \geq 0 \tag{D.7}$$

- Dissipation function

$$\begin{aligned}\rho\phi &= -[\, M\,||\dot{\underline{\underline{\epsilon}}}^p||\, b\,\alpha\, r\, exp[-\frac{1}{b\,M\,r}(\,\frac{\dot{\epsilon}_v^p}{||\dot{\underline{\underline{\epsilon}}}^p||\,\alpha} + M\,(1-r)\,)\,] + \dot{\epsilon}_v^p + \Theta(r)\,\dot{r}\,] \qquad \text{(D.8)}\\ & \quad p_{c0}\, exp[-\beta(\epsilon_v^p + \varpi(r))\,] + [\,2\,G\,||(\underline{\underline{\epsilon}} - \underline{\underline{\epsilon}}^p)||\,(1-\alpha) - \alpha\, M\,(1-r\,b)\,K\,(\epsilon_v - \epsilon_v^p)\,]\,||\dot{\underline{\underline{\epsilon}}}^p||\end{aligned}$$

where

$$\Theta(r) = \frac{a\,\eta\,r\,M}{(1-r)^{1-m}} \qquad \text{(D.9)}$$

- Consistency relationship

$$\rho(\delta_{\epsilon_v^p}\psi + \delta_{\dot{\epsilon}_v^p}\phi + \delta_r\psi + \delta_{\dot{r}}\phi)\underline{\underline{I}} + \rho(\delta_{\underline{\underline{\epsilon}}^p}\psi + \delta_{\dot{\underline{\underline{\epsilon}}}^p}\phi) = 0 \qquad \text{(D.10)}$$

- Isotropic terms

$$\begin{aligned}\delta_{\epsilon_v^p}\psi &= \frac{1}{2}(\lambda+\frac{2}{3}\mu)\frac{\delta}{\delta_{\epsilon_v^p}}\left[\,(\epsilon_v-\epsilon_v^p)^2\,\right]-\frac{p_{c0}}{\beta}\,\frac{\delta}{\delta_{\epsilon_v^p}}\left(exp[\,-\beta(\epsilon_v^p+\varpi(r))\,]\right) \\ &= \frac{1}{2}(\lambda+\frac{2}{3}\mu)\,[-2]\,(\epsilon_v-\epsilon_v^p)+p_{c0}\,exp[\,-\beta(\epsilon_v^p+\varpi(r))\,] \\ &= -\,(\lambda+\frac{2}{3}\mu)\,(\epsilon_v-\epsilon_v^p)+p_{c0}\,exp[\,-\beta(\epsilon_v^p+\varpi(r))\,] \\ &= -\,p+p_{c0}\,exp[\,-\beta(\epsilon_v^p+\varpi(r))\,]\end{aligned} \tag{D.11}$$

$$\begin{aligned}\delta_r\psi &= -\,\frac{p_{c0}}{\beta}\,\frac{\delta}{\delta_r}\left(exp[\,-\beta(\epsilon_v^p+\varpi(r))\,]\right) \\ &= \frac{\delta}{\delta_r}\,(\varpi(r))\,p_{c0}\,exp[\,-\beta(\epsilon_v^p+\varpi(r))\,] \\ &= \frac{a\,\alpha}{1-r}\,p_{c0}\,exp[\,-\beta(\epsilon_v^p+\varpi(r))\,]\end{aligned} \tag{D.12}$$

$$\begin{aligned}\delta_{\dot{\epsilon}_v^p}\phi &= -\,[\,M\,||\dot{\underline{\underline{\epsilon}}}^p||\,b\,\alpha\,r\,exp[\,-\frac{1}{b\,M\,r}(M\,(1-r))\,]\,\frac{\delta}{\delta_{\dot{\epsilon}_v^p}}\,[\,exp(-\frac{1}{b\,M\,r}\,(\frac{\dot{\epsilon}_v^p}{||\dot{\underline{\underline{\epsilon}}}^p||\,\alpha})\,) \\ &+ \frac{\delta}{\delta_{\dot{\epsilon}_v^p}}\,(\dot{\epsilon}_v^p)\,]\,p_{c0}\,exp[\,-\beta(\epsilon_v^p+\varpi(r))\,] \\ &= -\,[\,1-exp[\,-\frac{1}{b\,M\,r}(\,\frac{\dot{\epsilon}_v^p}{||\dot{\underline{\underline{\epsilon}}}^p||\,\alpha}+M\,(1-r)\,)\,]\,]\,p_{c0}\,exp[\,-\beta(\epsilon_v^p+\varpi(r))\,]\end{aligned} \tag{D.13}$$

$$\begin{aligned}\delta_{\dot{r}}\phi &= -\,\frac{\delta}{\delta_{\dot{r}}}\,[\,p_{c0}\,exp[\,-\beta(\epsilon_v^p+\varpi(r))\,]\,\Theta(r)\,\dot{r}\,] \\ &= -\,p_{c0}\,exp[\,-\beta(\epsilon_v^p+\varpi(r))\,]\,\Theta(r)\end{aligned} \tag{D.14}$$

Notice that the definition of $\Theta(r)$ in which $\delta_r\psi+\delta_{\dot{r}}\phi=0$ is verified is

$$\Theta(r)=\frac{a\,\eta\,r\,M}{(1-r)^{1-m}} \tag{D.15}$$

which is the same definition taken at the start, therefore, $\delta_{\dot{r}}\phi+\delta_r\psi=0$ is true. This results in that, considering solely the isotropic terms,

$$\rho(\delta_{\epsilon_v^p}\psi+\delta_{\dot{\epsilon}_v^p}\phi)=0 \tag{D.16}$$

which results in

$$p=p_{c0}\,exp[\,-\beta(\epsilon_v^p+\varpi(r))\,]\,exp[\,-\frac{1}{b\,M\,r}(\,\frac{\dot{\epsilon}_v^p}{||\dot{\underline{\underline{\epsilon}}}^p||\,\alpha}+M\,(1-r)\,)\,] \tag{D.17}$$

- Deviatoric terms

$$\begin{aligned} \delta_{\underline{\underline{\dot{\epsilon}}}^p}\psi &= 2\mu\,||(\underline{\underline{\epsilon}}-\underline{\underline{\epsilon}}^p)|| \\ &= \underline{\underline{\sigma}} \end{aligned} \tag{D.18}$$

$$\begin{aligned} \delta_{\underline{\underline{\dot{\epsilon}}}^p}\phi &= -\,[\,M\,b\,\alpha\,r\,exp(-\frac{1}{b\,M\,r}\,(M(1-r)))\frac{\delta}{\delta_{||\underline{\underline{\dot{\epsilon}}}^p||}}\,(||\underline{\underline{\dot{\epsilon}}}^p||\,exp(-\frac{1}{b\,M\,r}\,(\frac{\dot{\epsilon}_v^p}{||\underline{\underline{\dot{\epsilon}}}^p||\,\alpha})))\,] \\ &\quad p_{c0}\,exp[-\beta(\epsilon_v^p+\varpi(r))\,]+[\,2\,G\,||(\underline{\underline{\epsilon}}-\underline{\underline{\epsilon}}^p)||\,(1-\alpha)-\alpha\,M\,(1-r\,b)\,K\,(\epsilon_v-\epsilon_v^p)\,]\,\frac{\delta}{\delta_{||\underline{\underline{\dot{\epsilon}}}^p||}}\,(||\underline{\underline{\dot{\epsilon}}}^p||) \\ &= -\,[\,M\,b\,\alpha\,r\,exp(-\frac{1}{b\,M\,r}\,(M(1-r)))\,[\,(-\frac{\underline{\underline{\dot{\epsilon}}}^p}{||\underline{\underline{\dot{\epsilon}}}^p||})\,exp(-\frac{1}{b\,M\,r}\,(\frac{\dot{\epsilon}_v^p}{||\underline{\underline{\dot{\epsilon}}}^p||\,\alpha}))\;+\;||\underline{\underline{\dot{\epsilon}}}^p||\,\frac{\dot{\epsilon}_v^p}{\alpha\,b\,M\,r} \\ &\quad exp[-\frac{1}{b\,M\,r}(\,\frac{\dot{\epsilon}_v^p}{||\underline{\underline{\dot{\epsilon}}}^p||\,\alpha}+M\,(1-r)\,)\,]\,\frac{\delta}{\delta_{||\underline{\underline{\dot{\epsilon}}}^p||}}(\frac{1}{||\underline{\underline{\dot{\epsilon}}}^p||})\,]\,] \\ &\quad p_{c0}\,exp[-\beta(\epsilon_v^p+\varpi(r))\,]+[\,2\,G\,||(\underline{\underline{\epsilon}}-\underline{\underline{\epsilon}}^p)||\,(1-\alpha)-\alpha\,M\,(1-r\,b)\,K\,(\epsilon_v-\epsilon_v^p)\,]\,(-\frac{\underline{\underline{\dot{\epsilon}}}^p}{||\underline{\underline{\dot{\epsilon}}}^p||}) \\ &= M\,b\,\alpha\,r\,exp[-\frac{1}{b\,M\,r}(\,\frac{\dot{\epsilon}_v^p}{||\underline{\underline{\dot{\epsilon}}}^p||\,\alpha}+M\,(1-r)\,)\,]\,p_{c0}\,exp[-\beta(\epsilon_v^p+\varpi(r))\,] \\ &\quad \frac{\underline{\underline{\dot{\epsilon}}}^p}{||\underline{\underline{\dot{\epsilon}}}^p||}\,[\,1+\frac{1}{b\,M\,r\,\alpha}\,(-\frac{\dot{\epsilon}_v^p}{||\underline{\underline{\dot{\epsilon}}}^p||})\,]-\;[\,\underline{\underline{\sigma}}\,(1-\alpha)-\alpha\,M\,(1-rb)\,p\,]\,(\frac{\underline{\underline{\dot{\epsilon}}}^p}{||\underline{\underline{\dot{\epsilon}}}^p||}) \end{aligned} \tag{D.19}$$

Replacing $p = p_{c0}\,exp[-\beta(\epsilon_v^p+\varpi(r))\,]\,exp[-\frac{1}{b\,M\,r}(\,\frac{\dot{\epsilon}_v^p}{||\underline{\underline{\dot{\epsilon}}}^p||\,\alpha}+M\,(1-r)\,)\,]$

$$\begin{aligned} \delta_{\underline{\underline{\dot{\epsilon}}}^p}\phi &= M\,b\,\alpha\,r\,p\,\frac{\underline{\underline{\dot{\epsilon}}}^p}{||\underline{\underline{\dot{\epsilon}}}^p||}\,[\,1+\frac{1}{b\,M\,r\,\alpha}\,(-\frac{\dot{\epsilon}_v^p}{||\underline{\underline{\dot{\epsilon}}}^p||})\,] \\ &\quad -\,[\,\underline{\underline{\sigma}}\,(1-\alpha)-\alpha\,M\,(1-rb)\,p\,]\,(\frac{\underline{\underline{\dot{\epsilon}}}^p}{||\underline{\underline{\dot{\epsilon}}}^p||}) \end{aligned} \tag{D.20}$$

Considering the deviatoric terms

$$\rho(\delta_{\underline{\underline{\dot{\epsilon}}}^p}\psi+\delta_{\underline{\underline{\dot{\epsilon}}}^p}\phi)=0 \tag{D.21}$$

and then taking the norm since $q=||\underline{\underline{\sigma}}||$

$$q\;+\;M\,b\,\alpha\,r\,p\,[\,1+\frac{1}{b\,M\,r\,\alpha}\,(-\frac{\dot{\epsilon}_v^p}{||\underline{\underline{\dot{\epsilon}}}^p||})\,]\;-q\,(1-\alpha)+\alpha\,M\,(1-rb)\,p=0 \tag{D.22}$$

The flow rule is then given by

$$-\alpha\,(M-\frac{q}{p}) = \frac{-\dot{\epsilon}_v^p}{||\dot{\underline{\underline{\epsilon}}}^p||} \tag{D.23}$$

Inverting $p = p_{c0}\,exp[-\beta(\epsilon_v^p + \varpi(r))\,]\,exp[-\frac{1}{b\,M\,r}(\,\frac{\dot{\epsilon}_v^p}{||\dot{\underline{\underline{\epsilon}}}^p||\,\alpha} + M\,(1-r)\,)\,]$ so that it yields

$$-\frac{\dot{\epsilon}_v^p}{||\dot{\underline{\underline{\epsilon}}}^p||} = \alpha\,[\,ln(\frac{p}{p_c})\,(b\,M\,r) - M\,(1-r)\,] \tag{D.24}$$

where $p_c = p_{c0}\,exp[-\beta(\epsilon_v^p + \varpi(r))\,]$. Replacing $-\frac{\dot{\epsilon}_v^p}{||\dot{\underline{\underline{\epsilon}}}^p||}$ in the flow rule the yield function is obtained and is given as

$$q + M\ p\,r(1 - b\,ln\frac{p}{p_c}) = 0 \tag{D.25}$$

D.2 Revised ECP constitutive model

- Stress invariants definition

$$p = (\lambda + \frac{2}{3}\mu)(\epsilon_v - \epsilon_v^p) = K(\epsilon_v - \epsilon_v^p) \tag{D.26}$$

$$\overline{\underline{\sigma}} = 2\mu(\overline{\underline{\epsilon}} - \overline{\underline{\epsilon}}^p) \tag{D.27}$$

$$q = ||\overline{\underline{\sigma}}|| \tag{D.28}$$

- Free energy function

$$\rho\psi = \frac{1}{2}(\lambda + \frac{2}{3}\mu)(\epsilon_v - \epsilon_v^p)^2 + \mu(||(\overline{\underline{\epsilon}} - \overline{\underline{\epsilon}}^p)||)^2 - \frac{p_{c0}}{\beta}\, exp[-\beta(\epsilon_v^p + \varpi(r) + \varpi(r_{br}))] \tag{D.29}$$

where,

$$r = \frac{M \int_0^t ||\dot{\overline{\underline{\epsilon}}}^p||\, dt}{a + M \int_0^t ||\dot{\overline{\underline{\epsilon}}}^p||\, dt} \tag{D.30}$$

$$\varpi(r) = \int_r \frac{a\,\alpha(r)}{1-r}\, dr\,, \quad 0 < r < 1 \tag{D.31}$$

$$\alpha(r) = M\,\eta\, r\,(1-r)^m\,, \quad 1 \geq m \geq 0; \quad \eta \geq 0 \tag{D.32}$$

$$r_{br} = r_{br_0} - exp[\,a^{br} \cdot \int_0^t ||\dot{\overline{\underline{\epsilon}}}^p||\, dt\,], \quad 1 \geq r_{br_0} \geq 0 \tag{D.33}$$

$$\varpi(r_{br}) = \int_{r_{br}} a^{br}(r_{br})\,(\,r_{br_0} - r_{br}\,)\, dr_{br}\,, \quad 0 < r_{br} \leq 1 \tag{D.34}$$

$$a^{br}(r_{br}) = a_0^{br} - [(1 - r_{br}) \cdot a_0^{br}]^{m_a^{br}}\,, \quad a_0^{br} \geq 0; \quad 1 \geq m_a^{br} \geq 0 \tag{D.35}$$

- Dissipation function

$$\begin{aligned}\rho\phi &= -[\,M\,||\dot{\underline{\underline{\epsilon}}}^p||\,b\,\alpha\,r\,r_{br}\,exp[-\frac{1}{b\,M\,r\,r_{br}}(\,\frac{\dot{\epsilon}_v^p}{||\dot{\underline{\underline{\epsilon}}}^p||\,\alpha}+M\,(1-r\,r_{br})\,)\,]+\dot{\epsilon}_v^p \\ &+ \Theta(r)\,\dot{r}\;+\Theta(r_{br})\,\dot{r_{br}}\,]\,p_{c0}\,exp[-\beta(\epsilon_v^p+\varpi(r)+\varpi(r_{br}))\,] \\ &+ [\,2\,G\,||(\underline{\underline{\epsilon}}-\underline{\underline{\epsilon}}^p)||\,(1-\alpha)-\alpha\,M\,(1-r\,r_{br}\,b)\,K\,(\epsilon_v-\epsilon_v^p)\,]\,||\dot{\underline{\underline{\epsilon}}}^p||\end{aligned} \tag{D.36}$$

where

$$\Theta(r)=\frac{a\,\eta\,r\,M}{(1-r)^{1-m}} \tag{D.37}$$

$$\Theta(r_{br})=(a_0^{br}-[(1-r_{br})\,a_0^{br}]^{m_a^{br}}\,)\,(\,r_{br_0}-r_{br}\,) \tag{D.38}$$

- Consistency relationship

$$\rho(\delta_{\epsilon_v^p}\psi+\delta_{\dot{\epsilon}_v^p}\phi+\delta_r\psi+\delta_{\dot{r}}\phi+\delta_{r_{br}}\psi+\delta_{\dot{r_{br}}}\phi)\underline{\underline{I}}+\rho(\delta_{\underline{\underline{\epsilon}}^p}\psi+\delta_{\dot{\underline{\underline{\epsilon}}}^p}\phi)=0 \tag{D.39}$$

- Isotropic terms

$$\begin{aligned}\delta_{\epsilon_v^p}\psi &= \frac{1}{2}(\lambda+\frac{2}{3}\mu)\frac{\delta}{\delta_{\epsilon_v^p}}\,[\,(\epsilon_v-\epsilon_v^p)^2\,]-\frac{p_{c0}}{\beta}\,\frac{\delta}{\delta_{\epsilon_v^p}}\,(exp[-\beta(\epsilon_v^p+\varpi(r)+\varpi(r_{br}))\,]) \\ &= \frac{1}{2}(\lambda+\frac{2}{3}\mu)\,[-2]\,(\epsilon_v-\epsilon_v^p)+p_{c0}\,exp[-\beta(\epsilon_v^p+\varpi(r)+\varpi(r_{br}))\,] \\ &= -\,(\lambda+\frac{2}{3}\mu)\,(\epsilon_v-\epsilon_v^p)+p_{c0}\,exp[-\beta(\epsilon_v^p+\varpi(r))\,] \\ &= -\,p+p_{c0}\,exp[-\beta(\epsilon_v^p+\varpi(r)+\varpi(r_{br}))\,]\end{aligned} \tag{D.40}$$

$$\begin{aligned}\delta_r\psi &= -\frac{p_{c0}}{\beta}\,\frac{\delta}{\delta_r}\,(exp[-\beta(\epsilon_v^p+\varpi(r)+\varpi(r_{br}))\,]) \\ &= \frac{\delta}{\delta_r}\,(\varpi(r))\,p_{c0}\,exp[-\beta(\epsilon_v^p+\varpi(r)+\varpi(r_{br}))\,] \\ &= \frac{a\,\alpha}{1-r}\,p_{c0}\,exp[-\beta(\epsilon_v^p+\varpi(r)+\varpi(r_{br}))\,]\end{aligned} \tag{D.41}$$

$$\begin{aligned}\delta_{r_{br}}\psi &= -\frac{p_{c0}}{\beta}\,\frac{\delta}{\delta_{r_{br}}}\,(exp[-\beta(\epsilon_v^p+\varpi(r)+\varpi(r_{br}))\,]) \\ &= \frac{\delta}{\delta_r}\,(\varpi(r_{br}))\,p_{c0}\,exp[-\beta(\epsilon_v^p+\varpi(r)+\varpi(r_{br}))\,] \\ &= a^{br}\,(\,r_{br_0}-r_{br}\,)\,p_{c0}\,exp[-\beta(\epsilon_v^p+\varpi(r)+\varpi(r_{br}))\,]\end{aligned} \tag{D.42}$$

$$\begin{aligned}\delta_{\dot{\epsilon}_v^p}\phi &= -\,[\,M\,||\dot{\underline{\underline{\epsilon}}}^p||\,b\,\alpha\,r\,r_{br}\,exp[-\frac{1}{b\,M\,r\,r_{br}}(M\,(1-r\,r_{br}))\,] \\ &\quad \frac{\delta}{\delta_{\dot{\epsilon}_v^p}}\,[\,exp(-\frac{1}{b\,M\,r\,r_{br}}\,(\frac{\dot{\epsilon}_v^p}{||\dot{\underline{\underline{\epsilon}}}^p||\,\alpha})\,)\,] + \frac{\delta}{\delta_{\dot{\epsilon}_v^p}}\,(\dot{\epsilon}_v^p)\,]\,p_{c0}\,exp[-\beta(\epsilon_v^p+\varpi(r)+\varpi(r_{br}))\,] \\ &= -\,[\,1-exp[-\frac{1}{b\,M\,r\,r_{br}}(\,\frac{\dot{\epsilon}_v^p}{||\dot{\underline{\underline{\epsilon}}}^p||\,\alpha}+M\,(1-r\,r_{br})\,)\,]\,]\,p_{c0}\,exp[-\beta(\epsilon_v^p+\varpi(r)+\varpi(r_{br}))\,]\end{aligned} \tag{D.43}$$

$$\begin{aligned}\delta_{\dot{r}}\phi &= -\frac{\delta}{\delta_{\dot{r}}}\,[\,p_{c0}\,exp[-\beta(\epsilon_v^p+\varpi(r)+\varpi(r_{br}))\,]\,\Theta(r)\,\dot{r}\,] \\ &= -\,p_{c0}\,exp[-\beta(\epsilon_v^p+\varpi(r)+\varpi(r_{br}))\,]\,\Theta(r)\end{aligned} \tag{D.44}$$

$$\begin{aligned}\delta_{\dot{r_{br}}}\phi &= -\frac{\delta}{\delta_{\dot{r_{br}}}}\,[\,p_{c0}\,exp[-\beta(\epsilon_v^p+\varpi(r)+\varpi(r_{br}))\,]\,\Theta(r_{br})\,\dot{r_{br}}\,] \\ &= -\,p_{c0}\,exp[-\beta(\epsilon_v^p+\varpi(r)+\varpi(r_{br}))\,]\,\Theta(r_{br})\end{aligned} \tag{D.45}$$

Notice that the definition of $\Theta(r)$ in which $\delta_r\psi+\delta_{\dot{r}}\phi=0$ is verified is

$$\Theta(r)=\frac{a\,\eta\,r\,M}{(1-r)^{1-m}} \tag{D.46}$$

which is the same definition taken at the start, therefore, $\delta_{\dot{r}}\phi+\delta_r\psi=0$ is true.

The same can be said for $\Theta(r_{br})$ where $\delta_{r_{br}}\psi+\delta_{\dot{r_{br}}}\phi=0$ is verified when

$$\Theta(r_{br})=(a_0^{br}-[(1-r_{br})\,a_0^{br}]^{m_a^{br}}\,)\,(\,r_{br_0}-r_{br}\,) \tag{D.47}$$

This results in that, considering solely the isotropic terms,

$$\rho(\delta_{\epsilon_v^p}\psi+\delta_{\dot{\epsilon}_v^p}\phi)=0 \tag{D.48}$$

which gives

$$p=p_{c0}\,exp[-\beta(\epsilon_v^p+\varpi(r)+\varpi(r_{br}))\,]\,exp[-\frac{1}{b\,M\,r\,r_{br}}(\,\frac{\dot{\epsilon}_v^p}{||\dot{\underline{\underline{\epsilon}}}^p||\,\alpha}+M\,(1-r\,r_{br})\,)\,] \tag{D.49}$$

- Deviatoric terms

$$\begin{aligned} \delta_{\underline{\underline{\dot{\epsilon}}}^p}\psi &= 2\mu\,||(\underline{\underline{\epsilon}}-\underline{\underline{\epsilon}}^p)|| \\ &= \underline{\underline{\sigma}} \end{aligned} \tag{D.50}$$

$$\begin{aligned} \delta_{\underline{\underline{\dot{\epsilon}}}^p}\phi &= -[\,M\,b\,\alpha\,r\,r_{br}\,exp(-\frac{1}{b\,M\,r}\,(M(1-r\,r_{br})))\frac{\delta}{\delta_{||\underline{\underline{\dot{\epsilon}}}^p||}}\,(||\underline{\underline{\dot{\epsilon}}}^p||\,exp(-\frac{1}{b\,M\,r}\,r_{br}\,(\frac{\dot{\epsilon}_v^p}{||\underline{\underline{\dot{\epsilon}}}^p||\,\alpha})))\,] \\ & p_{c0}\,exp[-\beta(\epsilon_v^p+\varpi(r)+\varpi(r_{br}))\,]+[\,2\,G\,||(\underline{\underline{\epsilon}}-\underline{\underline{\epsilon}}^p)||\,(1-\alpha)-\alpha\,M\,(1-r\,r_{br}\,b) \\ & K\,(\epsilon_v-\epsilon_v^p)\,]\,\frac{\delta}{\delta_{||\underline{\underline{\dot{\epsilon}}}^p||}}\,(||\underline{\underline{\dot{\epsilon}}}^p||) \end{aligned} \tag{D.51}$$

$$\begin{aligned} &= -[\,M\,b\,\alpha\,r\,r_{br}\,exp(-\frac{1}{b\,M\,r\,r_{br}}\,(M(1-r\,r_{br})))\,[\,(-\frac{\underline{\underline{\dot{\epsilon}}}^p}{||\underline{\underline{\dot{\epsilon}}}^p||})\,exp(-\frac{1}{b\,M\,r\,r_{br}}\,(\frac{\dot{\epsilon}_v^p}{||\underline{\underline{\dot{\epsilon}}}^p||\,\alpha})) \\ &+ ||\underline{\underline{\dot{\epsilon}}}^p||\,\frac{\dot{\epsilon}_v^p}{\alpha\,b\,M\,r\,r_{br}}\,exp[-\frac{1}{b\,M\,r\,r_{br}}(\,\frac{\dot{\epsilon}_v^p}{||\underline{\underline{\dot{\epsilon}}}^p||\,\alpha}+M\,(1-r\,r_{br})\,)\,]\,\frac{\delta}{\delta_{||\underline{\underline{\dot{\epsilon}}}^p||}}(\frac{1}{||\underline{\underline{\dot{\epsilon}}}^p||})\,]\,] \\ & p_{c0}\,exp[-\beta(\epsilon_v^p+\varpi(r)+\varpi(r_{br}))\,]+[\,2\,G\,||(\underline{\underline{\epsilon}}-\underline{\underline{\epsilon}}^p)||\,(1-\alpha)-\alpha\,M\,(1-r\,r_{br}\,b) \\ & K\,(\epsilon_v-\epsilon_v^p)\,]\,(-\frac{\underline{\underline{\dot{\epsilon}}}^p}{||\underline{\underline{\dot{\epsilon}}}^p||}) \\ &= M\,b\,\alpha\,r\,r_{br}\,exp[-\frac{1}{b\,M\,r\,r_{br}}(\,\frac{\dot{\epsilon}_v^p}{||\underline{\underline{\dot{\epsilon}}}^p||\,\alpha}+M\,(1-r\,r_{br})\,)\,]\,p_{c0}\,exp[-\beta(\epsilon_v^p+\varpi(r)+\varpi(r_{br}))\,] \\ & \frac{\underline{\underline{\dot{\epsilon}}}^p}{||\underline{\underline{\dot{\epsilon}}}^p||}\,[\,1+\frac{1}{b\,M\,r\,r_{br}\,\alpha}\,(-\frac{\dot{\epsilon}_v^p}{||\underline{\underline{\dot{\epsilon}}}^p||})\,]-\,[\,\underline{\underline{\sigma}}\,(1-\alpha)-\alpha\,M\,(1-r\,r_{br}\,b)\,p\,]\,(\frac{\underline{\underline{\dot{\epsilon}}}^p}{||\underline{\underline{\dot{\epsilon}}}^p||}) \end{aligned}$$

Replacing $p = p_{c0}\,exp[-\beta(\epsilon_v^p+\varpi(r)+\varpi(r_{br}))\,]\,exp[-\frac{1}{b\,M\,r\,r_{br}}(\,\frac{\dot{\epsilon}_v^p}{||\underline{\underline{\dot{\epsilon}}}^p||\,\alpha}+M\,(1-r\,r_{br})\,)\,]$

$$\begin{aligned} \delta_{\underline{\underline{\dot{\epsilon}}}^p}\phi &= M\,b\,\alpha\,r\,r_{br}\,p\,\frac{\underline{\underline{\dot{\epsilon}}}^p}{||\underline{\underline{\dot{\epsilon}}}^p||}\,[\,1+\frac{1}{b\,M\,r\,r_{br}\,\alpha}\,(-\frac{\dot{\epsilon}_v^p}{||\underline{\underline{\dot{\epsilon}}}^p||})\,] \\ &\quad -[\,\underline{\underline{\sigma}}\,(1-\alpha)-\alpha\,M\,(1-r\,r_{br}\,b)\,p\,]\,(\frac{\underline{\underline{\dot{\epsilon}}}^p}{||\underline{\underline{\dot{\epsilon}}}^p||}) \end{aligned} \tag{D.52}$$

Considering the deviatoric terms

$$\rho(\delta_{\underline{\underline{\dot{\epsilon}}}^p}\psi+\delta_{\underline{\underline{\dot{\epsilon}}}^p}\phi)=0 \tag{D.53}$$

and then taking the norm since $q = ||\underline{\underline{\sigma}}||$

$$-q = M\,b\,\alpha\,r\,r_{br}\,p\,[\,1+\frac{1}{b\,M\,r\,r_{br}\,\alpha}\,(-\frac{\dot{\epsilon}_v^p}{||\underline{\underline{\dot{\epsilon}}}^p||})\,]\,-q\,(1-\alpha)+\alpha\,M\,(1-r\,r_{br}\,b)\,p \tag{D.54}$$

The flow rule is then given by

$$-\alpha\,(M-\frac{q}{p}) = \frac{-\,\dot{\epsilon}_v^p}{||\dot{\underline{\underline{\epsilon}}}^p||} \tag{D.55}$$

Inverting $p = p_{c0}\,exp[-\beta(\epsilon_v^p + \varpi(r) + \varpi(r_{br}))\,]\,exp[-\frac{1}{b\,M\,r\,r_{br}}(\,\frac{\dot{\epsilon}_v^p}{||\dot{\underline{\underline{\epsilon}}}^p||\,\alpha} + M\,(1-r\,r_{br})\,)\,]$ so that it yields

$$-\frac{\dot{\epsilon}_v^p}{||\dot{\underline{\underline{\epsilon}}}^p||} = \alpha\,[\,ln(\frac{p}{p_c})\,(b\,M\,r\,r_{br}) - M\,(1-r\,r_{br})\,] \tag{D.56}$$

where $p_c = p_{c0}\,exp[-\beta(\epsilon_v^p + \varpi(r) + \varpi(r_{br}))\,]$. Replacing $-\frac{\dot{\epsilon}_v^p}{||\dot{\underline{\underline{\epsilon}}}^p||}$ in the flow rule the yield function is obtained and is given as

$$q + M\;p\,r\,r_{br}\,(1 - b\,ln\frac{p}{p_c}) = 0 \tag{D.57}$$

Appendix E

Interface elements

E.1 Mechanical formulation

The mechanical formulation for the interface is written in terms of relative displacements and stress vector increments considering only 2 directions, normal and tangential. In terms of displacements it can be written that

$$u_n = \underline{u} \cdot \underline{n} \tag{E.1}$$

$$\tag{E.2}$$

$$u_t = \underline{u} \cdot \underline{t} \tag{E.3}$$

where $\underline{n}$ and $\underline{t}$ are unit vectors normal and tangential, respectively, to the interface element alignment. In terms of stress components and considering $\underline{T}$ the stress vector with respect to the interface

$$\underline{T} = \underline{\underline{\sigma}} \cdot \underline{n} \tag{E.4}$$

in can then be written

$$\sigma_n = \underline{T} \cdot \underline{n} = \underline{n} \cdot \underline{\underline{\sigma} n} \tag{E.5}$$

$$\tag{E.6}$$

$$\tau = (\,\underline{T} - \sigma_n \cdot \underline{n}\,) \cdot \underline{t} \tag{E.7}$$

where σ_n and τ represent the normal and shear stress respectively.

E.2 Interface model formulation

The isotropic nonlinear elastic behaviour is represented in the model by an evolution of the elastic variables with the normal compressive effective stress. The elastic and shear modulus, K and G, are determined as

$$E(\sigma'_n) = E_{ref}(\frac{\sigma'_n}{\sigma'_{ref}})^{n_e} \tag{E.8}$$

$$G(\sigma'_n) = G_{ref}(\frac{\sigma'_n}{\sigma'_{ref}})^{n_e} \tag{E.9}$$

where E_{ref} and G_{ref} are the moduli measured at the reference pressure σ'_{ref} and n_e is the degree of non-linearity ($n_e = 0$ corresponds to linear elasticity).
Considering the plastic range, the monotonic yield function is given by

$$f = \tau - \sigma_n \cdot tan\,\phi_{pp} \cdot r \cdot r_{br} \cdot (1 - b \cdot \ln(\frac{\sigma_n}{\sigma_c})) = 0 \tag{E.10}$$

where

$$\dot{r} = \dot{\Lambda}\,\frac{(1-r)^2}{a} \quad , \quad \dot{\sigma}_c = \sigma_c \beta \dot{u}_n^p \quad , \quad \dot{r}_{br} = -\dot{\Lambda}(a^{br} \cdot r_{br}) \tag{E.11}$$

and

$$a = a_1 + (a_2 - a_1)\alpha(r) \tag{E.12}$$

where $\alpha(r)$ evolves depending on the interval where the value of r is

$$\alpha(r) = \begin{cases} 0 & \text{if } r < r_{hys} & \text{pseudo-elastic domain} \\ (\frac{r - r_{hys}}{r_{mob} - r_{hys}})^m & \text{if } r_{hys} < r < r_{mob} & \text{hysteretic domain} \\ 1 & \text{if } r_{mob} < r < 1 & \text{mobilized domain} \end{cases}$$

and similarly as before

$$a^{br} = a_0^{br} - [(1 - r_{br_k}) \cdot a_0^{br}]^{m_a^{br}} \tag{E.13}$$

Finally, the flow rule gives that

$$\dot{u}_n^p = \dot{\Lambda}\,(\,tan\phi_{pp} - \frac{\tau}{\sigma_n}\,) \tag{E.14}$$

Appendix F

Model Parameters

Model parameters			
Sand type	Ottawa sand	Illinois River sand	Toyoura sand
Elasticity			
$K_{ref}(MPa)$	285.0	300.0	296.0
$G_{ref}(MPa)$	215.0	230.0	222.0
n_e	0.00	0.00	0.40
$p_{ref}(MPa)$	1.0	1.0	1.0
Critical State and Plasticity			
$\phi'_{pp}(^\circ)$	33	34	30
β	52	45	17
d	2.00	2.00	3.50
b	0.22	0.25	0.22
$p_{co}(MPa)$	0.45	0.40	4.90
Flow Rule and Isotropic Hardening			
$\psi(^\circ)$	33	34	30
α_ψ	1.00	1.00	1.00
a_1	0.0001	0.0001	0.0001
a_2	0.0100	0.0150	0.0150
c_1	0.0600	0.0600	0.0600
c_2	0.0300	0.0300	0.0300
m	1.00	1.00	1.00
Threshold Domains			
r^{ela}	0.005	0.005	0.005
r^{hys}	0.030	0.030	0.030
r^{mob}	0.800	0.800	0.800
r^{ela}_{iso}	0.0001	0.0001	0.0001
Breakage parameters			
a^{br}_0	0.01	0.006	n.a.
m^{br}_a	0.89	0.88	n.a.
$b_{W_p}(MPa)$	80	120	n.a.

Table F.1: ECP model's parameters for Ottawa, Illinois River and Toyoura sand

Appendix G

Ring shear test: Illinois River sand

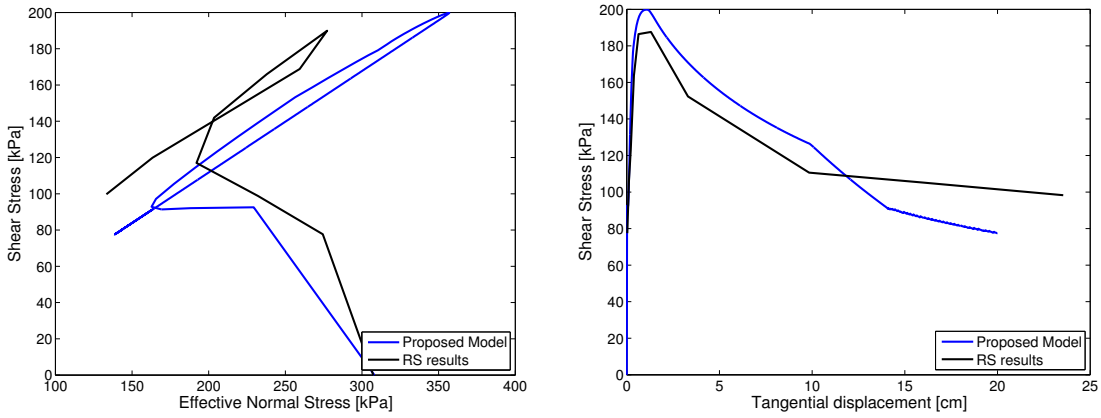

Figure 1: Illinois River sand : σ'_n - τ and u_T - τ

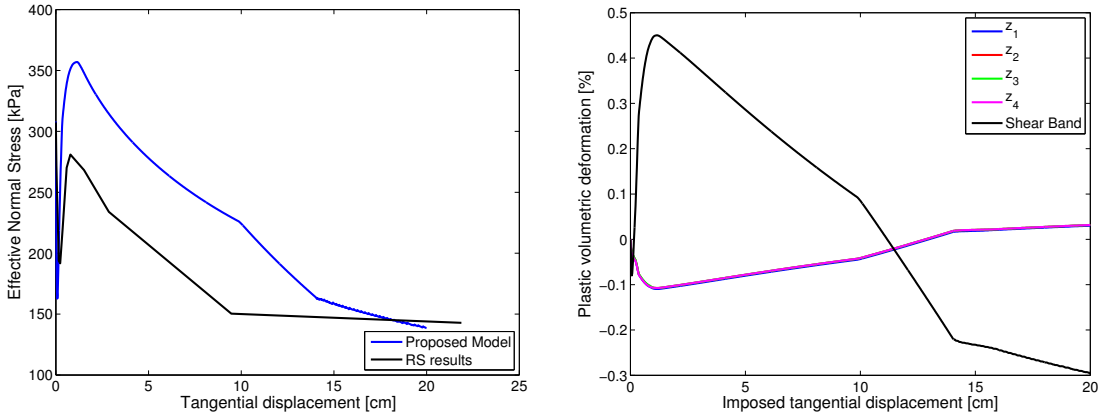

Figure 2: Illinois River sand : u_T - σ'_n and u_T - $\dot{J}^p$

Appendix H

Standard mechanical tests in soil mechanics using the ECP constitutive model

H.1 Ottawa sand (OT) (D_r=25%)

H.1.1 Ottawa sand: Drained triaxial tests

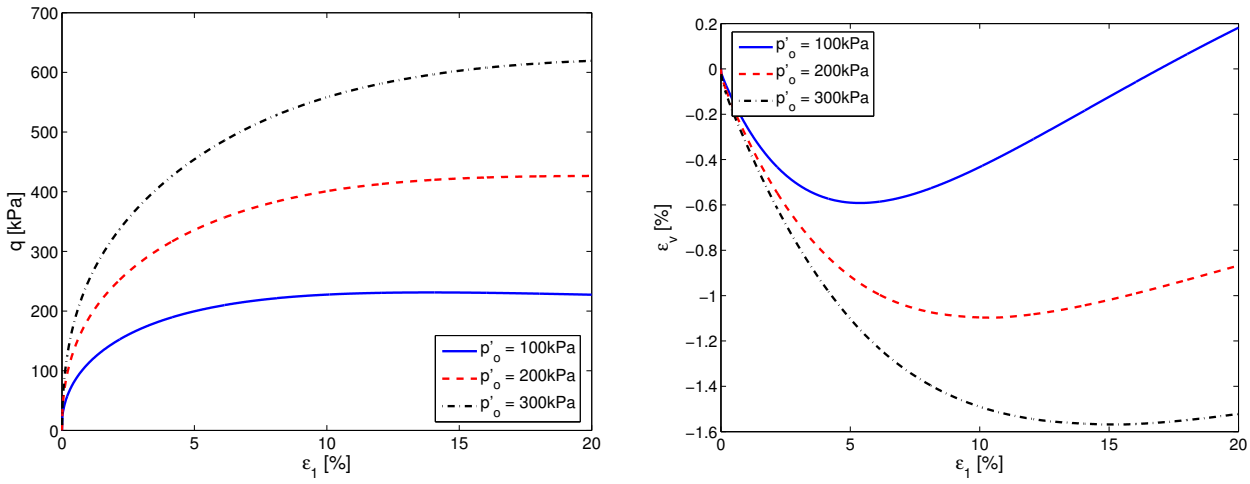

Figure 1: ϵ_1 - q and ϵ_1 - ϵ_v

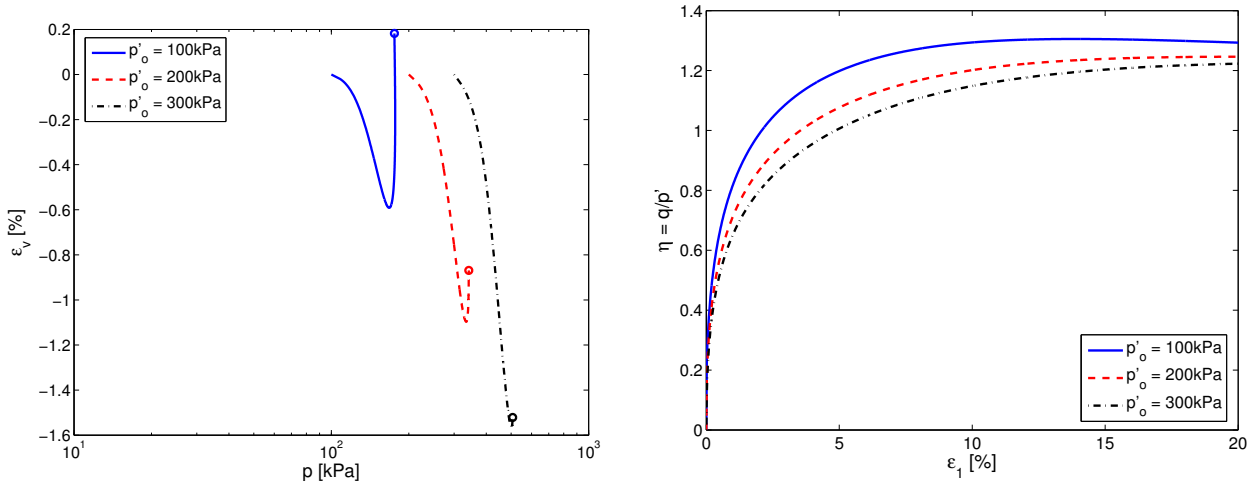

Figure 2: p' - ϵ_v and ϵ_1 - $\eta = \frac{q}{p'}$

H.1.2 Ottawa sand: Undrained triaxial tests

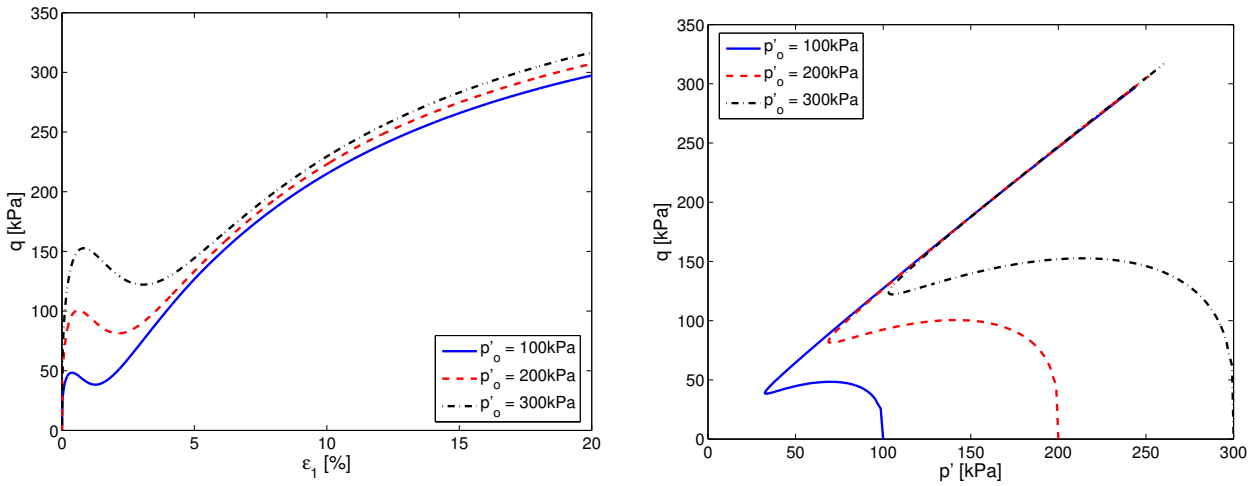

Figure 3: q - ϵ_1 and p' - q

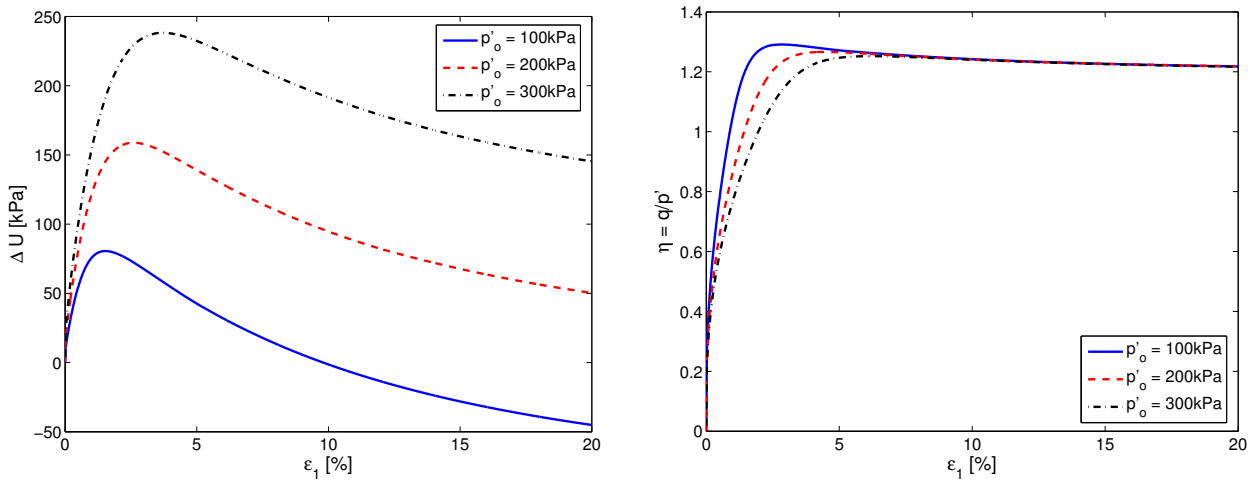

Figure 4: ϵ_1 - ΔU and ϵ_1 - $\eta = \frac{q}{p'}$

H.1.3 Ottawa sand: Consolidation tests

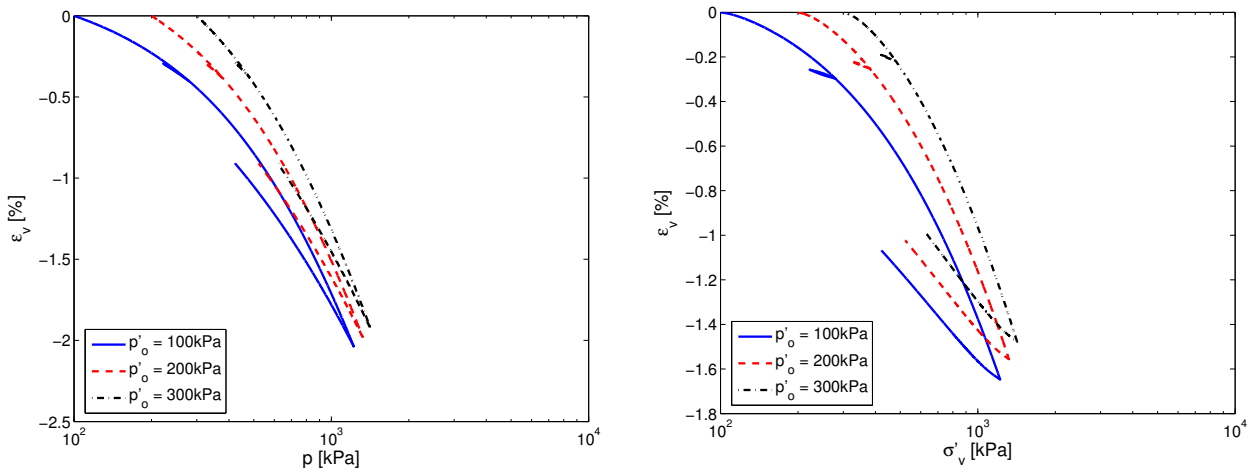

Figure 5: p' - ϵv and p' - σ'_v

H.1.4 Ottawa sand: Drained cyclic strain-controlled shear test

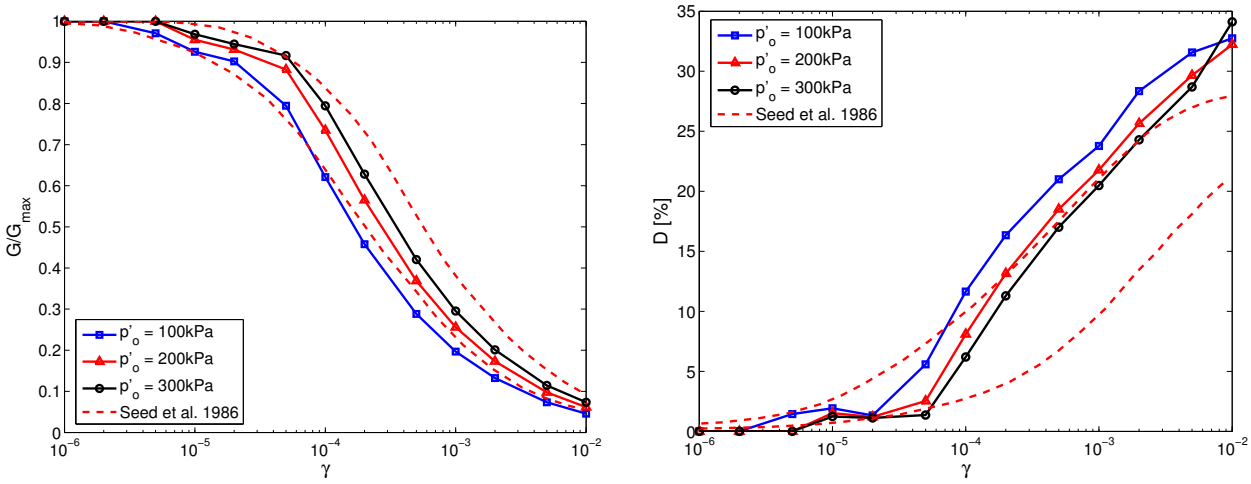

Figure 6: γ - G/G_{max} and γ - D

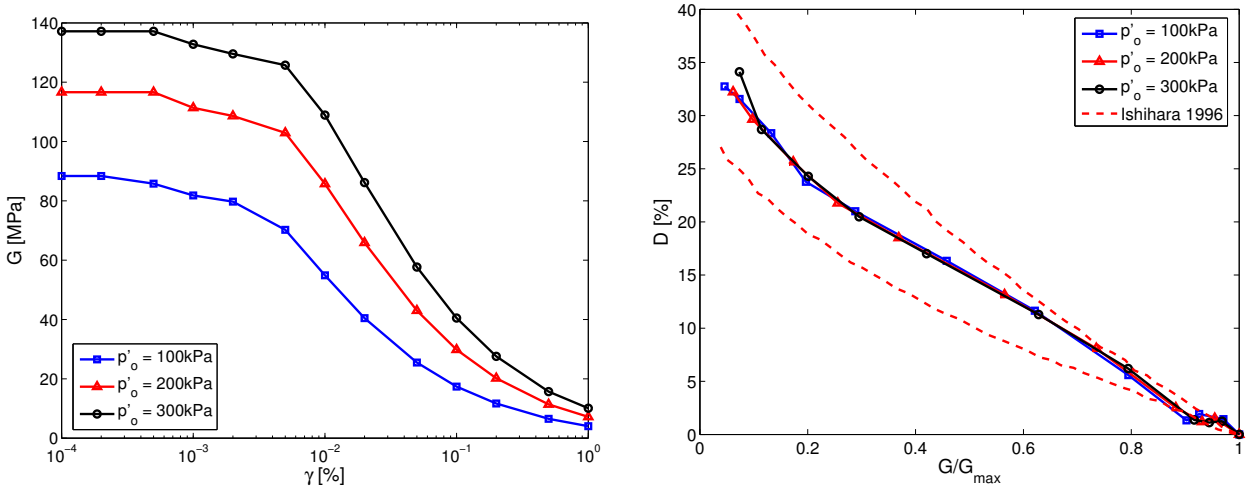

Figure 7: γ - G and G/G_{max} - D

H.2 Illinois River sand (IR) (D_r=30%)

H.2.1 Illinois River sand: Drained triaxial tests

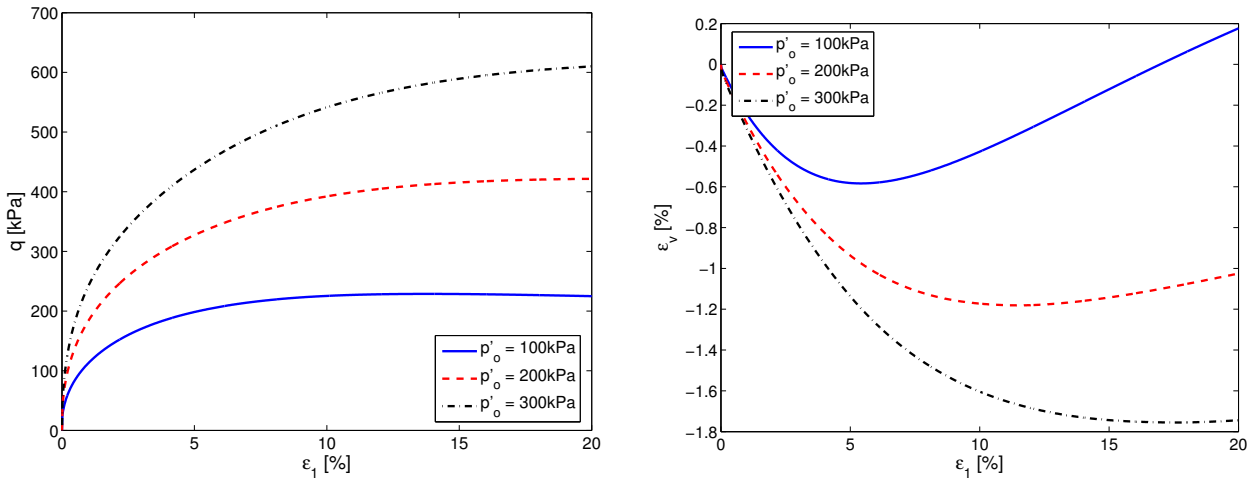

Figure 8: ϵ_1 - q and ϵ_1 - ϵ_v

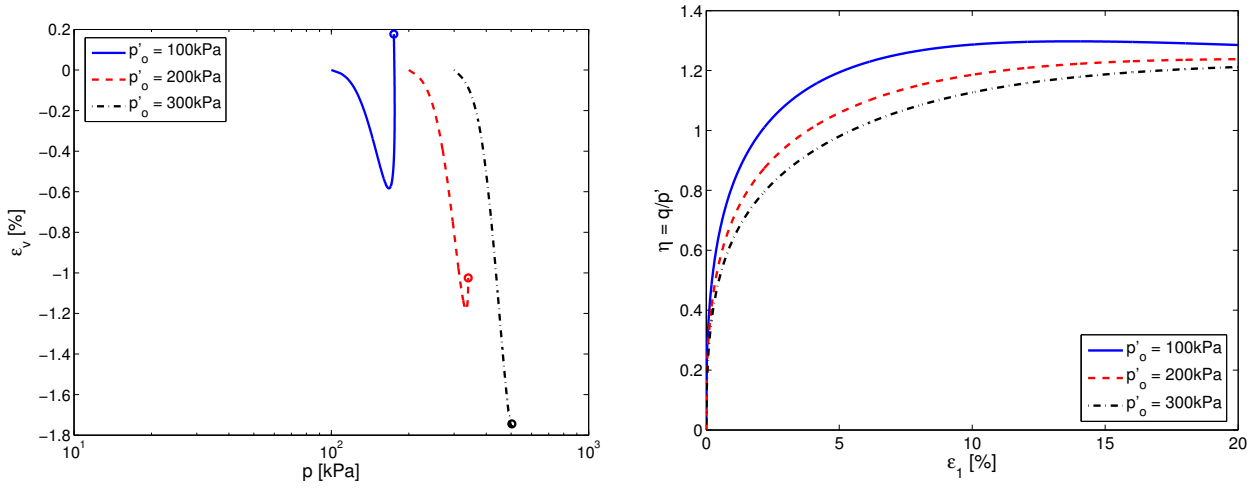

Figure 9: p' - ϵ_v and ϵ_1 - $\eta = \frac{q}{p'}$

H.2.2 Illinois River sand: Undrained triaxial tests

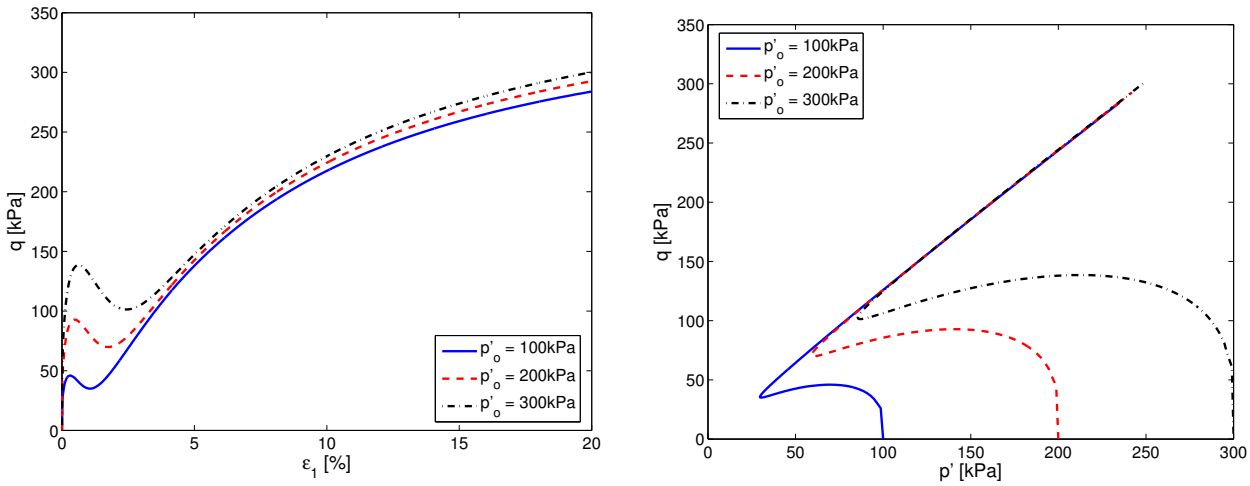

Figure 10: q - ϵ_1 and p' - q

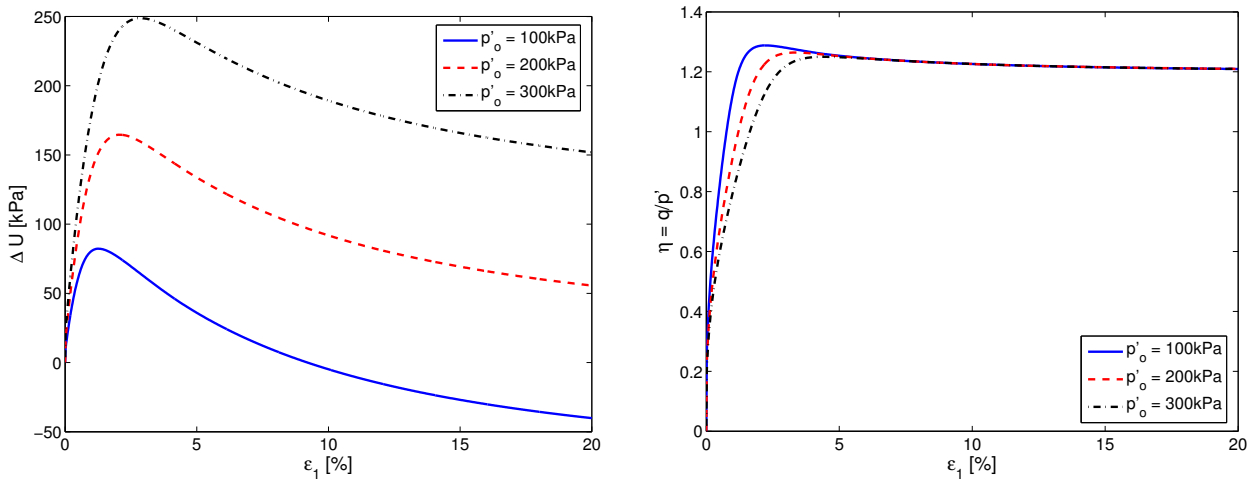

Figure 11: ϵ_1 - ΔU and ϵ_1 - $\eta = \frac{q}{p'}$

H.2.3 Illinois River sand: Consolidation tests

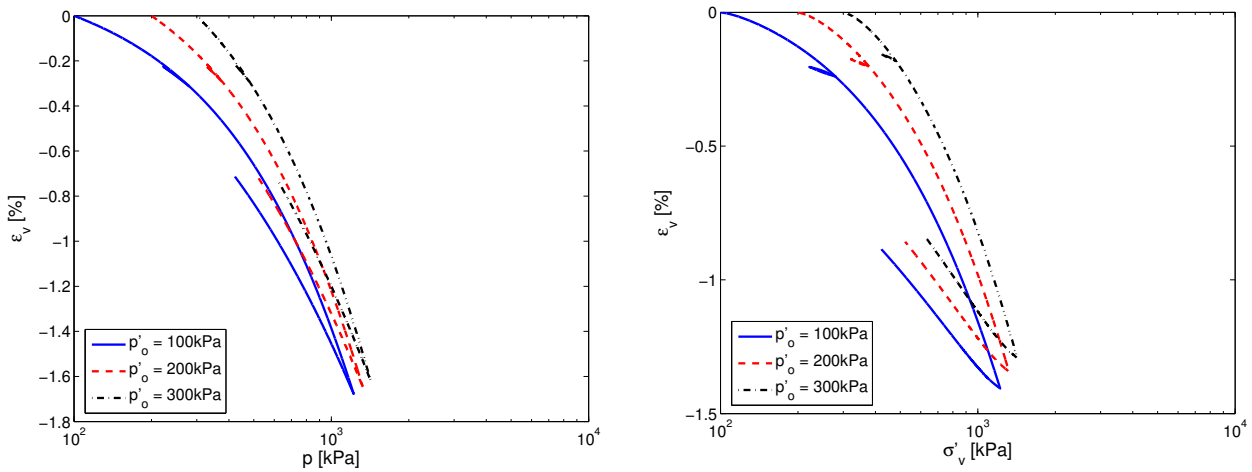

Figure 12: p' - ϵv and p' - σ'_v

H.2.4 Illinois River sand: Drained cyclic strain-controlled shear test

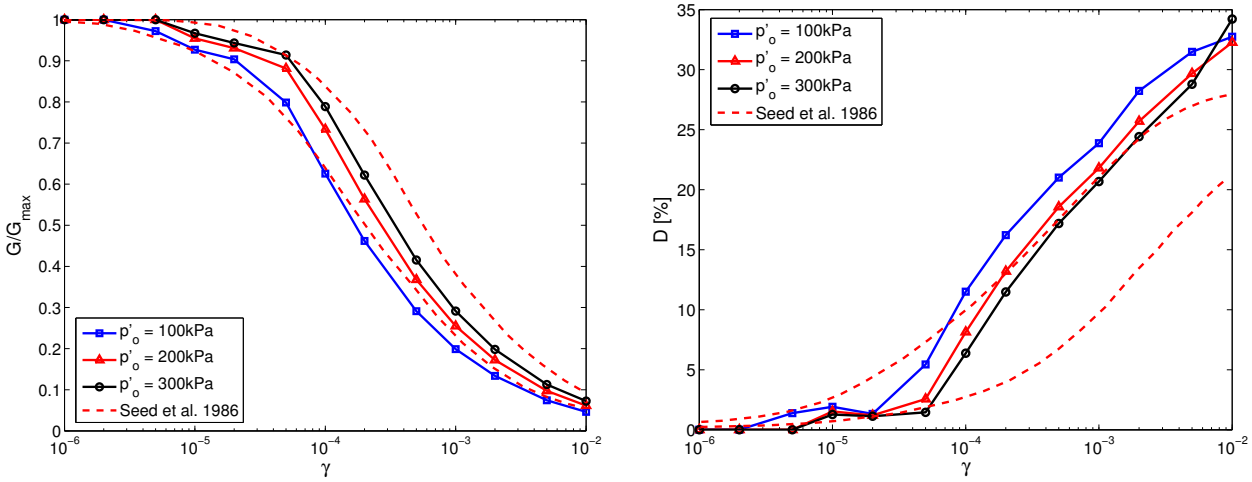

Figure 13: γ - G/G_{max} and γ - D

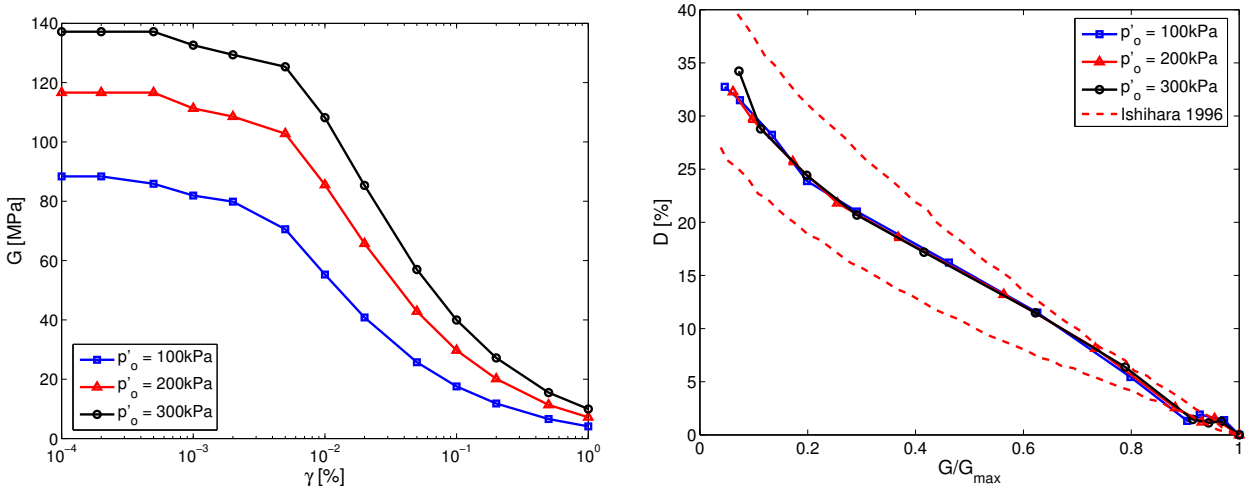

Figure 14: γ - G and G/G_{max} - D

H.3 Toyoura sand (TY) (D_r=93%)

H.3.1 Toyoura sand: Drained triaxial tests

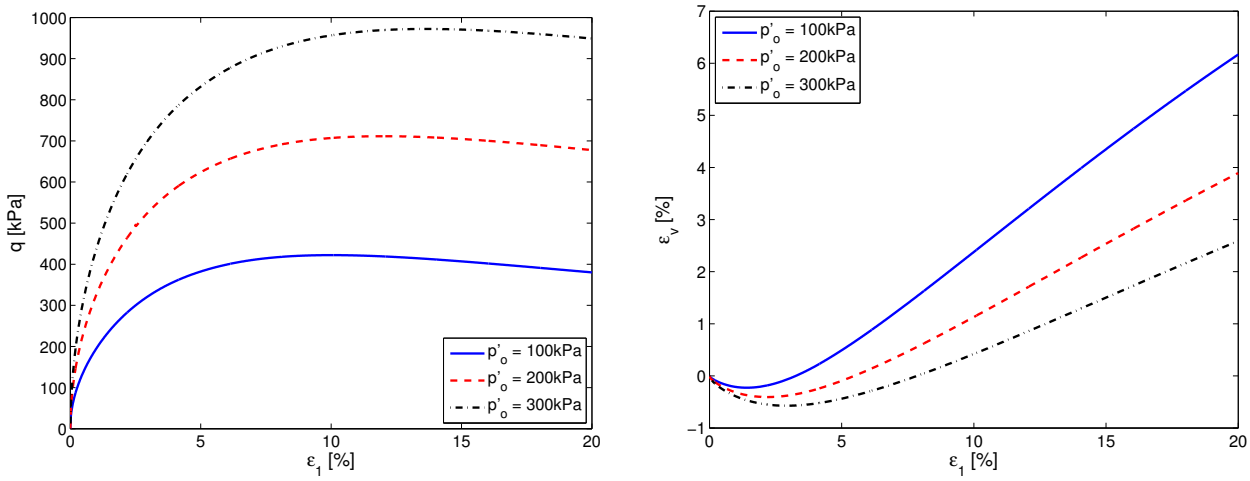

Figure 15: ϵ_1 - q and ϵ_1 - ϵ_v

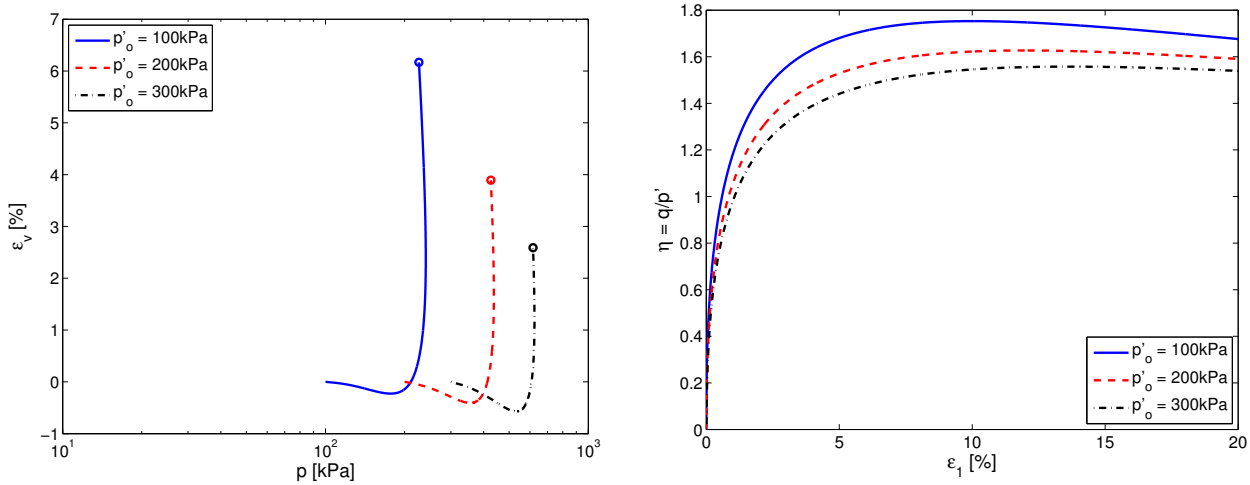

Figure 16: p' - ϵ_v and ϵ_1 - $\eta = \frac{q}{p'}$

H.3.2 Toyoura sand: Undrained triaxial tests

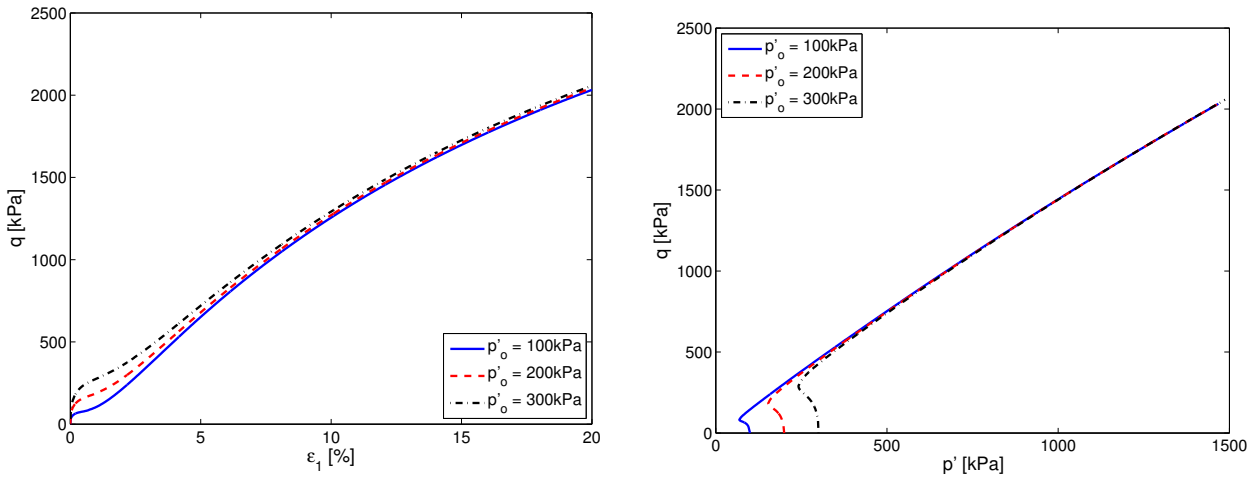

Figure 17: q - ϵ_1 and p' - q

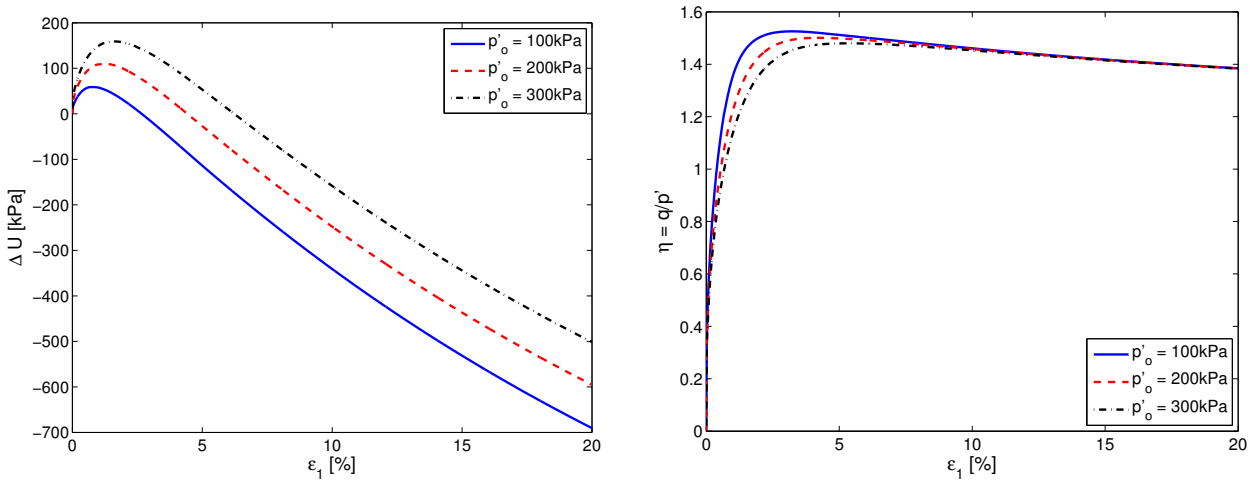

Figure 18: ϵ_1 - ΔU and ϵ_1 - $\eta = \frac{q}{p'}$

H.3.3 Toyoura sand: Consolidation tests

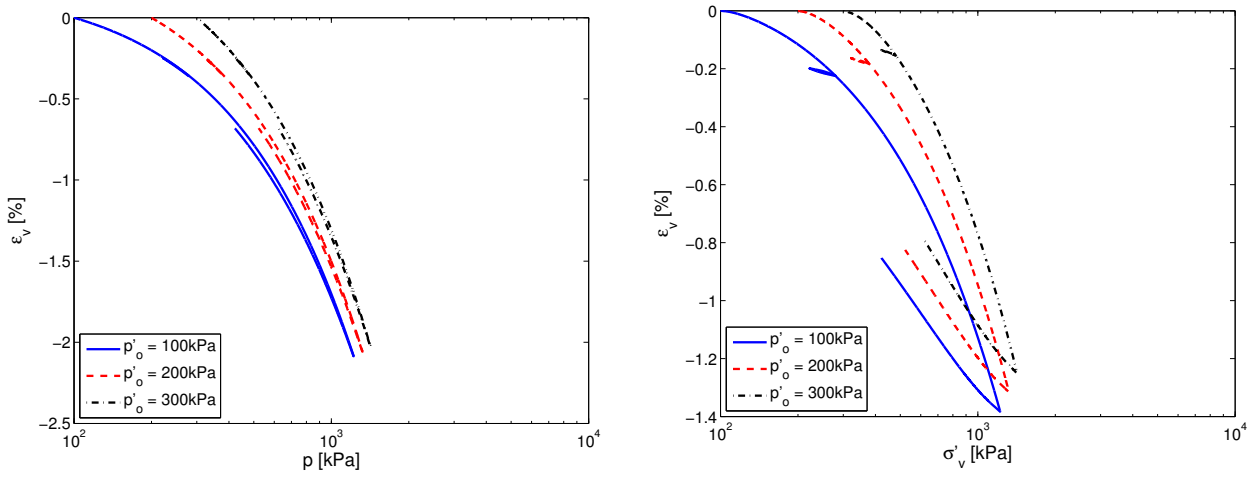

Figure 19: p' - ϵv and p' - σ'_v

H.3.4 Toyoura sand: Drained cyclic strain-controlled shear test

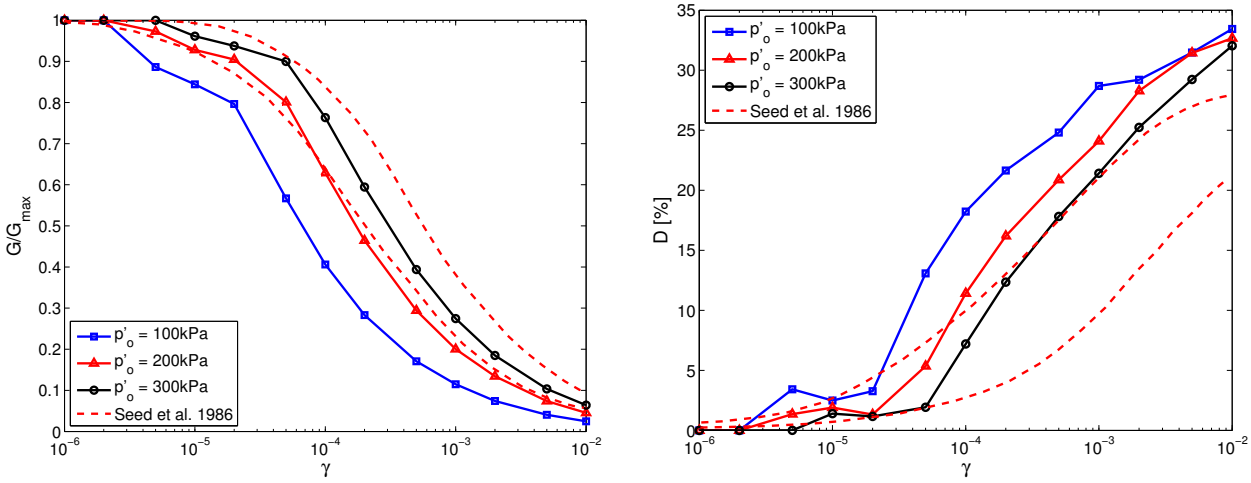

Figure 20: γ - G/G_{max} and γ - D

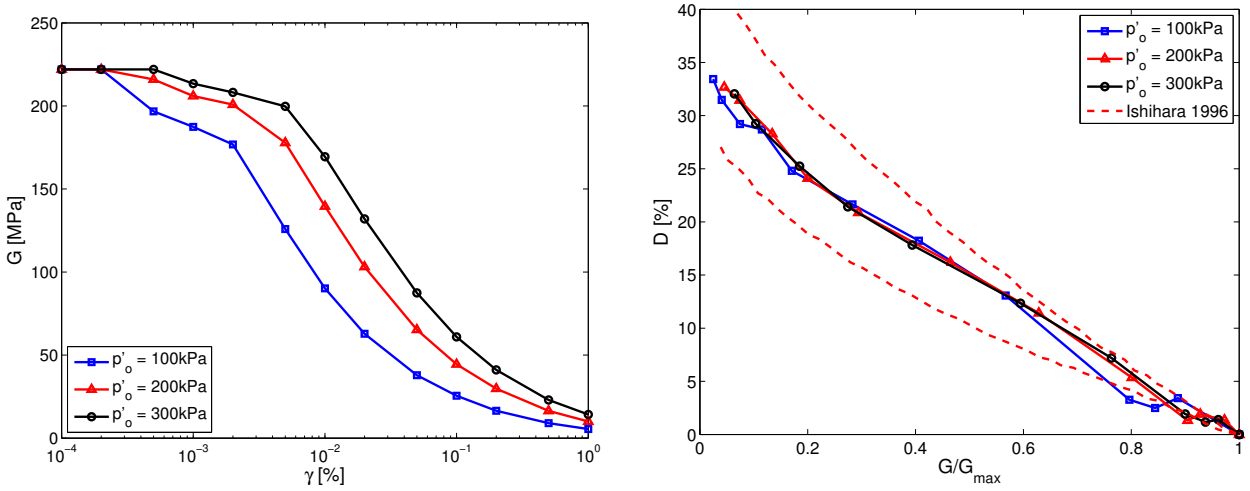

Figure 21: γ - G and G/G_{max} - D

Bibliography

[1] A. S. Alawneh. Modelling load-displacement response of driven piles in cohesionless soils under tensile loading. *Computers and Geotechnics*, 32:578–586, 2005.

[2] D. Aubry, J. C. Hujeux, F. Lassoudière, and Y. Meimon. A double memory model with multiple mechanisms for cyclic soil behavior. In *International Symposium on Numerical Methods in Geomechanics*, pages 3–13, 1982.

[3] D. Aubry, A. Modaressi, and H. Modaressi. A constitutive model for cyclic behaviour of interfaces with variable dilatancy. *Computers and Geotechnics*, 9:47–58, 1990.

[4] B. Baharom and S. E. Stallebrass. A constitutive model combining the microscopic and macroscopic behaviour of sand in shear and volumetric deformation. In *Proc. 4th Eur. Conf. on Numerical Methods in Geotech. Engng, Udine, 1998*, pages 263–273. Springer-Verlag Wien, New York, 1998.

[5] K. J. Bathe. *Finite Element Procedures*. Prentice Hall, New Jersey, 1996.

[6] K.J. Bathe and H. Ozdemir. Elasto-plastic large deformation static and dynamic analysis. *Computers and Structures*, 6:81–92, 1976.

[7] A. J. Bond and R. J. Jardine. Effects of installing displacement piles in a high ocr clay. *Géotechnique*, 41(3):341–363, 1991.

[8] M. Boulon, V.N. Ghionna, and G. Mortara. A strain-hardening elastoplastic model for sand-structure interface under monotonic and cyclic loading. *Mathematical and Computer Modelling*, 37(5-6):623630, 2003.

[9] P. W. Bridgman. The thermodynamics of plastic deformation and generalized entropy. *Rev. Mod. Phys.*, 22:56, 1950.

[10] O.T. Bruhns, H. Xiao, and A. Meyers. Self-consistent eulerian rate type elasto-plasticity models based upon the logarithmic stress rate. *Int. J. Plasticity*, 15: 479520, 1999.

[11] O.T. Bruhns, H. Xiao, and A. Meyers. Large simple shear and torsion problems in kinematic hardening elasto-plasticity with logarithmic rate. *International Journal of Solids and Structures*, 38:8701–8722, 2001.

[12] J.L.E. Campos, E.A. Vargas Jr., G. Bernardes, J.P. Ibanez, and R.Q. Velloso. Numerical experiments with discrete elements to simulate pile penetration in granular soils. In *Proceedings of the XXVI Iberian Latin-American Congress on Computational Methods in Engineering*, 2005.

[13] A. Cavalieri. *The interface friction behaviour of sands.* Masters dissertation, University of Trento, Italy, 2000.

[14] M. Cecconi, A.o DeSimone, C. Tamagnini, and G.M.B. Viggiani. A constitutive model for granular materials with grain crushing and its application to a pyroclastic soil. *International Journal for Numerical and Analytical Methods in Geomechanics*, 26:1531–1560, 2002.

[15] C. Cekerevac, S. Girardin, G. Klubertanz, and L. Laloui. Calibration of an elastoplastic constitutive model by a constrained optimisation procedure. *Computers and Geotechnics*, 33:432–443, 2006.

[16] J. Chakrabarty. *Theory of plasticity.* Butterworth-Heinemann, 2006.

[17] M.R. Coop, K.K. Sorensen, T. Bodas Freitas, and G. Georgoutsos. Particle breakage during shearing of a carbonate sand. *Géotechnique*, 54(3):157163, 2004.

[18] Y.F. Dafalias. A missing link in the macroscopic constitutive formulation of large plastic deformations. *In: Plasticity today, modelling, methods and applications*, page 135151, 1985.

[19] S. C. D'Aguiar, A. Modaressi-Farahmand-Razavi, J. A. dos Santos, and F. Lopez-Caballero. Elastoplastic constitutive modelling of soil-structure interfaces under monotonic and cyclic loading. *Computers and Geotechnics*, 38:430–447, 2011.

[20] S.C. D'Aguiar. *Numerical modelling of soil-pile axial load transfer mechanisms in granular soils.* PhD dissertation, Ecole Centrale Paris and Instituto Superior Técnico, 2008.

[21] S.C. D'Aguiar, F. Lopez-Caballero, A. Modaressi-Farahmand-Razavi, and J.A. Santos. Piles under cyclic loading : study of the friction fatigue and its importance in piles. In *17th International Conference on Soil Mechanics and Geotechnical Engineering, Egypt, Alexandria*, pages 1313–1316, 2009.

[22] A. Daouadji, P.-Y. Hicher, and A. Rahma. An elastoplastic model for granular materials taking into account grain breakage. *Eur. J. Mech. A/Solids*, 20:113137, 2001.

[23] E.A. de Souza, D. Peric, and D.R.J. Owen. *Computational methods for plasticity. Theory and Applications.* Wiley, 2008.

[24] C. S. Desai and Y. Ma. Modelling of joints and interfaces using the disturbed state concept. *International Journal for Numerical and Analytical Methods in Geomechanics*, 16:623–653, 1992.

[25] J. Dijkstra, W. Broere, and A.F. van Tol. Numerical investigation into stress and strain development around a displacement pile in sand. *Numerical Methods in Geotechnical Engineering*, pages 595–600, 2006.

[26] J. Dijkstra, K.E. Anaraki, W. Broere, and F. van Tol. Numerical simulation of pile installation in sand. In *Proceedings of the Tenth International Symposium on Numerical Models in Geomechanics*, 2007.

[27] J. Dijkstra, W. Broere, A. Bezuijen, and A.F. van Tol. Density changes near an advancing displacement pile in sand. *Foundations*, 8:545–554, 2008.

[28] J. Dijkstra, W. Broere, and A.F. van Tol. Eulerian simulation of the installation process of a displacement pile. *Geotechnical Special Publication*, pages 135–142, 2009.

[29] J. Dijkstra, W. Broere, and O/M/ Heeres. Numerical simulation of pile installation. *Computers and Geotechnics*, 38(5):612–622, 2011.

[30] D. C. Drucker. Soil mechanics and plastic analysis of limit design. *Q. Appl. Math*, 10:157–165, 1952.

[31] D. C. Drucker. A definition of stable inelastic material. *J. Appl. Mech.*, 26:101–186, 1959.

[32] K. Fakharian and E. Evgin. Cyclic simple-shear behavior of sand-steel interfaces under constant normal stiffness condition. *J. Geotech. Geoenviron. Eng.*, 123(12): 1096–1105, 1997.

[33] J. Fish and K. Shek. Finite deformation plasticity based on the additive split of the rate of deformation and hyperelasticity. *Comput Methods Appl Mech Eng*, 190: 75–93, 2000.

[34] E. Foerster. *Evaluation des méthodes meshfree pour les simulations géomécaniques en transformations finies*. PhD dissertation, Ecole Centrale Paris, 2003.

[35] M.S. Gadala. Recent trends in ale formulation and its applications in solid mechanics. *Comput Methods Appl Mech Eng*, 193:4247–4275, 1998.

[36] M.S. Gadala and J. Wang. Ale formulation and its application in solid mechanics. *Comput Methods Appl Mech Eng*, 167:33–55, 1998.

[37] M.S. Gadala and J. Wang. Computational implementation of stress integration in fe analysis of elasto-plastic large deformation problems. *Finite Elements in Analysis and Design*, 35(4):379–396, 2000.

[38] V. De Gennaro and R. Frank. Elasto-plastic analysis of the interface behaviour between granular media and structure. *Computers and Geotechnics*, 29:547–572, 2002.

[39] R. C. Gomes. Effect of stress disturbance induced by construction on the seismic response of shallow bored tunnels. *Computers and Geotechnics*, 49:338351, 2013.

[40] A.E. Green and P.M. Naghdi. A general theory of an elastic-plastic continuum. *Arch. Rat. Mech. Anal.*, 18:251–281, 1965.

[41] A.E. Green and P.M. Naghdi. Some remarks on elastic-plastic deformation at finite strain. *Int. J. Engng Sci.*, 9:1219–1229, 1971.

[42] G. Gudehus. A comprehensive constitutive equation for granular materials. *Soils and Foundations*, 36(1):1–12, 1996.

[43] M. Gui. Numerical modeling of an advancing hydraulically-driven pile in sand. *Journal of Zhejiang University SCIENCE A*, 12(1):15–23, 2011.

[44] R. Haase. *Thermodynamics of Irreversible Processes*. Addison-Wesley, Reading, MA, 1969.

[45] M. M. Hagerty, D. R. Hite, C. R. Ullrich, , and D. J. Hagerty. One-dimensional high-pressure compression of granular media. *Journal of Geotechnical Engineering*, 119(1):1–18, 1993.

[46] K. Hamadi, A. Modaressi-Farahmand-Razavi, and F. Darve. Bifurcation and instability modelling by a multimechanism elasto-plastic model. *International Journal for Numerical and Analytical Methods in Geomechanics*, 32:461–492, 2008.

[47] S. Henke and J. Grabe. Numerical modeling of pile installation. In *International Conference on Soil Mechanics and Geotechnical Engineering*, pages 1321–1324. Perth, Australia, 2005.

[48] S. Henke and J. Grabe. Simulation of pile driving by 3-dimensional finite-element analysis. In *Proceedings of 17th European Young Geotechnical Engineers' Conference*. V.Szavits-Nossan, Croatian Geotechnical Society, 2006.

[49] P. Hicher and A. Rahma. Micro-macro correlations for granular media. application to the modelling of sands. *European Journal of Mechanics. A/Solids*, 13(6):763–781, 1994.

[50] P.-Y. Hicher. *Multiscale Geomechanics*. Wiley, John & Sons, 2011.

[51] R. Hill. A general theory of uniqueness and stability in elastic-plastic solids. *J. Mech. Phys. Solids*, 6:236–249, 1958.

[52] G. T. Houlsby. The derivation of theoretical models for soils from thermodynamics. *Rep. Cambridge Univ. Eng. Dept.*, 1980.

[53] G. T. Houlsby. *A study of plasticity theories and their applicability to soils*. PhD dissertation, University of Cambridge, 1981.

[54] G. T. Houlsby. A derivation of the small-strain incremental theory of plasticity from thermodynamics. *Soil. Mech. Rep. SM020//GTH/81, OUEL Rep. 1371/81, University of Oxford*, 1981.

[55] W. Hu, Z. Yin, C. Dano, and P.Y.Hicher. A constitutive model for granular materials considering grain breakage. *Science China - Technological Sciences*, 54(8):21882196, 2011.

[56] T.J.R. Hughes, W.K. Liu, and T.K. Zimmermann. Lagrangian-eulerian finite element formulation for incompressible viscous flow. *Computer Methods in Applied Mechanics and Engineering*, 58:19–36, 1981.

[57] J. C. Hujeux. A critical state type stressstrain law for monotonous and cyclic loading. In *Symposium on Implementation of Computer Procedures and StressStrain Laws in Geot, Chicago*, pages 3–13, 1982.

[58] M.B. Jamiolkowski. Axial load capacity of a bored pile in coarse grained soils. *Unpublished lecture, Turin Technical University*, 2004.

[59] R. J. Jardine, F. C. Chow, R. Overy, and J. Standing. Icp design methods for driven piles in sands and clays. *Thomas Telford Ltd*, 2005.

[60] R. J. Jardine, B. T. Zhu, P. Foray, and Z. X. Yang. Measurement of stresses around closed-ended displacement piles in sand. *Géotechnique*, 63(1):1–17, 2013.

[61] R.J. Jardine and F.C. Chow. New design methods for offshore piles. Mtd96/103, London: Marine Technology Directorate, 1996.

[62] R.J. Jardine and R.J. Standing. Pile load testing performed for hse cyclic loading study at dunkirk, france. Health and safety executive, london, Offshore Technology Report OTO2000 0007, 2000.

[63] G.C. Johnson and D.J. Bammann. A discussion of stress rates in finite deformation problems. *International Journal of Solids and Structures*, 20(8):725–737, 1984.

[64] R. Kelly. *Development of a large diameter ring shear apparatus and its use for interface testing*. PhD dissertation, University of Sidney, 2001.

[65] E.U. Klotz and M.R. Coop. An investigation of the effect of soil state on the capacity of driven piles in sands. *Géotechnique*, 51(9):733–751, 2001.

[66] P. V. Lade and L. B. Ibsen. A study of the phase transformation and the characteristic lines of sand behaviour. In *Symposium on Deformation and Progressive Failure in Geomechanics, Nagoya, Japan*, 1997.

[67] B.M. Lehane and D.J. White. Lateral stress changes and shaft friction for model displacement piles in sand. *Canadian Geotechnical Journal*, 42(4):1039–1052, 2005.

[68] J. Lemaitre, J.-L. Chaboche, A. Benallal, and R. Desmorat. *Mécanique des matériaux solides*. Dunod, 2009.

[69] C. Liangsen, Z. Xinghua, and F. Minfu. The simple shear oscillation and the restrictions to elastic-plastic constitutive relations. *Applied Mathematics and Mechanics*, 20(6):593–603, 1999.

[70] C.-S. Liu and H.-K. Hong. Non-oscillation criteria for hypoelastic models under simple shear deformation. *Journal of Elasticity*, 57:201–241, 1999.

[71] H. Liu, E. Song, and H. I. Ling. Constitutive modeling of soil-structure interface through the concept of critical state soil mechanics. *Mechanics Research Communications*, 33:515–531, 2006.

[72] F. Lopez-Caballero, A. Modaressi-Farahmand-Razavi, and F. Elmi. Identification of an elasto-plastic mode parameters using laboratory and in situ tests. *In: In Di Benedetto et al, editor, Deformation Characteristics of Geomaterials IS Lyon, Balkema*, pages 1183–1190, 2003.

[73] F. Lopez-Caballero, A. Modaressi-Farahmand-Razavi, and H. Modaressi. Non-linear numerical method for earthquake site response analysis i - elastoplastic cyclic model and parameter identification strategy. *Bull Earthquake Eng*, 5:303–323, 2007.

[74] L. Luzzani and M. R. Coop. On the relationship between particle breakage and the critical state of sands. *Soils and Foundations*, 42(2):71–82, 2002.

[75] R. J. Marsal. Large scale testing of rockfill materials. *Journal of the Soil Mechanics and Foundations Division, ASCE*, 93(SM2):27–43, 1967.

[76] G. R. McDowell, M. D. Bolton, and D. Robertson. The fractal crushing of granular materials. *J. Mech. Phys. Solids*, 44(12):2079–2102, 1996.

[77] A. Meyers, H. Xiao, and O.T. Bruhns. Elastic stress ratchetting and corotational stress rates. *Technische Mechanik*, 23(2-4):92–102, 2003.

[78] A. Meyers, O. Bruhns, and H. Xiao. Objective stress rates in repeated elastic deformation cycles. In *PAMM Proc. Appl. Math. Mech*, pages 249–250, 2005.

[79] A. Modaressi. *Dossier d'Habilitation à Diriger des Recherches*. Hdr, Ecole Centrale Paris, 2003.

[80] H. Modaressi and A. Modaressi. Thermoplastic constitutive models respecting thermodynamic restrictions. In *International Workshop on Hydro-Thermo-Mechanics of Engineered Clay Barriers and Geological barriers, Montreal, Quebec, Canada*, 1995.

[81] H. Modaressi, L. Laloui, and D. Aubry. Thermodynamical approach for cam-clay-family models with roscoe-type dilatancy rules. *International Journal for Numerical and Analytical Methods in Geomechanics*, 18:133–138, 1994.

[82] J. J. Moreau. Sur les lois de frottement, de plasticité et de viscosité. . *R. Acad. Sci. Paris*, Série A. 271:608–611, 1970.

[83] G. Mortara, M. Boulon, and V. N. Ghionna. A 2-d constitutive model for cyclic interface behaviour. *International Journal for Numerical and Analytical Methods in Geomechanics*, 26(11):10711096, 2002.

[84] R. Naghdabadi, M. Yeganeh, and A.R. Saidi. Application of corotational rates of the logarithmic strain in constitutive modeling of hardening materials at finite deformations. *International Journal of Plasticity*, 21:1546–1567, 2005.

[85] P.M. Naghdi. A critical review of the state of finite plasticity. *ZAMP*, 41:315–394, 1990.

[86] M. Nazem. *Numerical algorithms for large deformation problems in geomechanics.* PhD dissertation, University of Newcastle, 2006.

[87] A. Niemunis and I. Herle. Hypoplastic model for cohesionless soils with elastic strain range. *Mechanics of cohesive-frictional materials*, 2:279–299, 1997.

[88] R. Nova. Controllability of the incremental response of soil specimens subjected to arbitrary loading programmes. *Journal of the Mechanical Behaviour of Materials*, 5(2):193–203, 1994.

[89] Y. Okada, K. Sassa, and H. Fukuoka. Undrained shear behaviour of sands subjected to large shear displacement and estimation of excess pore-pressure generation from drained ring shear tests. *Canadian Geotechnical Journal*, 42:787–803, 2005.

[90] G. Qiu, S. Henke, and J. Grabe. Application of a coupled eulerian-lagrangian approach on geomechanical problems involving large deformations. *Computers and Geotechnics*, 38(1):30–39, 2011.

[91] M.F. Randolph, J. Dolwin, and R. Beck. Design of driven piles in sand. *Géotechnique*, 44(3):427–448, 1994.

[92] J. R. Rice. The localization of plastic deformation. *Theoretical and Applied Mechanics, Koiter WT*, pages 207–220, 1979.

[93] R. S. Rivlin. Comments on some recent researches in thermodynamics. *Recent Advances in Engineering Science*, 8:1, 1973.

[94] K. H. Roscoe, A. N. Schofield, and C. P. Wroth. On the yielding of soils. *Géotechnique*, 8(1):22–53, 1958.

[95] A. Russell and N. Khalili. A bounding surface plasticity model for sands exhibiting particle crushing. *Canadian Geotechnical Journal*, 41:1179–1192, 2004.

[96] A. Sadrekarimi and S.M. Olson. Shear band formation observed in ring shear tests on sandy soils. *Journal of Geotechnical and Geoenvironmental Engineering*, 136(2): 366–375, 2010.

[97] A. Sadrekarimi and S.M. Olson. Particle damage observed in ring shear tests. *Canadian Geotechnical Journal*, 47:497–515, 2010.

[98] A. Sadrekarimi and S.M. Olson. Yield strength ratios, critical strength ratios, and brittleness of sandy soils from laboratory tests. *Canadian Geotechnical Journal*, 48: 493–510, 2011.

[99] A. Sadrekarimi and S.M. Olson. Critical state friction angle of sands. *Géotechnique*, 61(9):771–783, 2011.

[100] W. Salim and B. Indraratna. A new elastoplastic constitutive model for coarse granular aggregates incorporating particle breakage. *Canadian Geotechnical Journal*, 41: 657–671, 2004.

[101] I. Shahrour and F. Rezaie. An elastoplastic constitutive relation for the soil-structure interface under cyclic loading. *Computers and Geotechnics*, 21(1):2139, 1997.

[102] V. Shakhirev, J.P. Magnan, and H. Ejjaaouani. Etude experimentale du comportement du sol lors du fonage des pieux. *Bulletin des laboratoires des Ponts et Chaussées*, 206:95–116, 1996.

[103] D. Sheng, K.D. Eigenbrod, and P. Wriggers. Finite element analysis of pile installation using large-slip frictional contact. *Computers and Geotechnics*, 32:17–26, 2005.

[104] D. Sheng, P. Wriggers, and S. Sloan. Improved numerical algorithms for frictional contact in pile penetration analysis. *Computers and Geotechnics*, 33:341–354, 2006.

[105] S. Sica, L. Pagano, and A. Modaressi. Influence of past loading history on the seismic response of earth dams. *Computers and Geotechnics*, 35:61–85, 2008.

[106] Z. Sikora and G. Gudehus. Numerical simulation of penetration in sand based on fem. *Computers and Geotechnics*, 9(1/2):73–86, 1990.

[107] J.C. Simo and K. S. Pister. Remarks on rate constitutive equations for finite deformation problems: Computational implications. *Comput. Meth. Appl. Mech. Engng*, 46:201–215, 1984.

[108] S. Sloan, A. Abbo, and D. Sheng. Refined explicit integration of elastoplastic models with automatic error control. *Engineering Computations*, 18(1/2):121–154, 2001.

[109] C. Truesdell. Hypo-elasticity. *J. Rat. Mech. Anal.*, 4:83–133, 1955.

[110] C. H. C. Tsuha, P. Foray, R. J. Jardine, Z. X. Yang, M. Silva, and S. Rimoy. Behavior of displacement piles in sand under cyclic axial loading. *Soils and Foundations*, 52 (3):393–410, 2012.

[111] P. van den Berg. *Analysis of soil penetration*. PhD dissertation, Technische Universiteit Delft, 1994.

[112] P.A. von Wolffersdorff. A hypoplastic relation for granular materials with a predefined limit state surface. *Mechanics of cohesive-frictional materials*, 1:251–271, 1996.

[113] J. Wang. *Arbitrary Lagrangian-Eulerian method and its application in solid mechanics*. PhD dissertation, University of British Columbia, 1998.

[114] J. Wang and M.S. Gadala. Formulation and survey of ale method in nonlinear solid mechanics. *Finite Elements in Analysis and Design*, 24:253–269, 1997.

[115] D.J. White. A general framework for shaft resistance on displacement piles in sand. In *1st International Symposium on Frontiers in Offshore Geotechnics, ISFOG 2005*. Perth, Australia, 2005.

[116] D.J. White and M.D. Bolton. Observing friction fatigue on a jacked pile. In *International Workshop on Constitutive and Centrifuge Modelling: Two Extremes*. Monte Verita, Switzerland, 2002.

[117] D.J. White and M.D. Bolton. Displacement and strain paths during plane-strain model pile installation in sand. *Géotechnique*, 54(6):375–397, 2004.

[118] D.J. White and B.M. Lehane. Friction fatigue on displacement piles in sand. *Géotechnique*, 54(10):645–658, 2004.

[119] Z. Wieckowski. The material point method in large strain engineering problems. *Computer Methods in Applied Mechanics and Engineering*, 193:4417–4438, 2004.

[120] H.-C. Wu. *Continuum mechanics and plasticity*. Chapman and Hall, 2005.

[121] H.-C. Wu. On stress rate and plasticity constitutive equations referred to a body-fixed coordinate system. *International Journal of Plasticity*, 23(9):1486–1511, 2007.

[122] H. Xiao, O.T. Bruhns, and A. Meyers. Logarithmic strain, logarithmic spin and logarithmic rate. *Acta Mechanica*, 124:89–105, 1997.

[123] H. Xiao, O.T. Bruhns, and A. Meyers. A consistent finite elastoplasticity theory combining additive and multiplicative decomposition of the stretching and the deformation gradient. *International Journal of Plasticity*, 16:143–177, 2000.

[124] H. Xiao, O.T. Bruhns, and A. Meyers. Elastoplasticity beyond small deformations. *Acta Mechanica*, 182:31–111, 2006.

[125] Z. X. Yang, R. J. Jardine, B. T. Zhu, P. Foray, and C. H. C. Tsuha. Sand grain crushing and interface shearing during displacement pile installation in sand. *Géotechnique*, 60(6):469–482, 2010.

[126] H.-S. Yu. *Plasticity and Geotechnics*. Springer, 2006.

[127] H. Ziegler and C. Wehrli. The derivation of constitutive relations from the free energy and dissipation function. *Academic, New York*, pages 183–238, 1987.